A New Continuous Process For Dihydroxyacetone Production Through Glycerol Catalytic Oxidation

Thesis presented to the Faculty of Engineering of the University of Porto for the Ph.D. degree in Chemical and Biological Engineering

by

Pedro Monteiro Walgode

Supervisor: Professor Alírio Egídio Rodrigues

Co-supervisor: Dr. Rui Pedro Vieira Faria

LSRE-LCM, ALiCE, Faculty of Engineering, University of Porto, Portugal

May 2025

FEUP-LSRE/LCM - Universidade do Porto

“Success is a science; if you have the conditions, you get the result”

Oscar Wilde

This work was financially supported by: UID/50020 of LSRE-LCM - Laboratory of Separation and Reaction Engineering – Laboratory of Catalysis and Materials - funded by Fundação para a Ciência e a Tecnologia, I.P. /MCTES through national funds; and ALiCE, LA/P/0045/2020 (DOI: 10.54499/LA/P/0045/2020).

The student Pedro Walgode gratefully thanks the Foundation for Science and Technology (FCT, Portugal) for the doctoral grant (SFRH/BD/143916/2019).

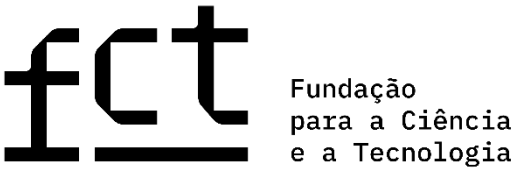

Acknowledgements

2019 to 2025. Six intense and meaningful years at LSRE-LCM and FEUP shaped this PhD journey, years marked by moments of genuine joy and fulfilment when results (finally!) aligned with expectations, but also by setbacks, uncertainty, and frustration.

Even with the mental and physical resilience I had built over twenty years of artistic roller skating, balancing a PhD with a competitive sports career was highly demanding. During this PhD, I became World Champion twice, European Champion three times, and the winner of the World Games 2022. These were childhood dreams I never stopped chasing until they came true, just like this PhD.

Despite the obstacles and delays, I moved forward step by step. My belief and the support of those around me pushed me to go further and do better. I would be naive to think I could have come this far without professors, colleagues, friends, coaches, and family. To everyone who stood by me, thank you. As the saying goes: *"If you want to go fast, go alone; if you want to go far, go together."* I am deeply grateful to many people and wish to acknowledge them here.

First, my institutional acknowledgements: I am grateful to Fundação para a Ciência e Tecnologia for the doctoral grant, to Fundação Luso-Americana para o Desenvolvimento for funding to disseminate part of this work, and to my lab, LSRE-LCM – ALiCE at DEQ, FEUP, for providing the environment in which this research was carried out.

To my supervisor, Professor Alírio Rodrigues, thank you for your wise guidance, timely advice, high standards, and above all, for supporting me through the double challenge of being both a PhD student and an elite athlete, with all the restrictions and flexibility that came with it.

To my co-supervisor, Dr. Rui Faria: thank you for your sharp intuition, insightful guidance, humour, and kindness. For always being there, sitting beside me at the computer to figure things out, rolling up your sleeves in the lab, and enduring long days and nights helping me operate the FlexSMB. So much of this PhD was only possible because of you.

To Professor Alexandre Ferreira, thank you for your encouragement and for always being willing to help, even when wrapped in your sharp and sarcastic humour.

To my colleagues from office E406 and the lab, especially Ana Pereira, Albertina Rios, Rafael Dias, Rute Seabra, and Carina Costa, thank you for your help, shared experiences, and laughter. To Isabella Correa, who shared this path under the same supervisory team, and to Lucas Coelho, who began part of the project I had the chance to explore in this thesis. I cannot forget Maria Enes and Magda Dias, from my master's days, even if life now makes it harder for us to meet often.

Friends are the family we choose, and mine made all the difference. Some have been by my side since childhood: Rui Pedro, Ricardo Filipe, Vanessa Nuno, and Inês Pinhal. To Joana Silva, childhood friend, fellow FEUP student, and long-distance PhD companion, I hold you especially close to my heart. Just like you, Filipe Marques, my dearest friend, I am so grateful to have you in my life. Jorge Menezes, thank you for being there and reminding me of my capabilities during this journey.

I also want to acknowledge my skating family from Rolar Matosinhos, especially coaches Hugo Chapouto and Fernanda Ferreira, who inspired me through this journey.

To my family, thank you from the bottom of my heart. Your love, support, and care have been everything. To my mum, Fátima Monteiro, and my sister, Ana Walgode: "thank you" doesn't even begin to cover it. You stood by me through exhaustion, frustration, and doubt. You celebrated my victories and kept me grounded when my head was in the clouds. You are my foundation, greatest strength, and inspiration to keep going. Words fall short to describe what we share and how deeply I love you. I am forever grateful to have *us*.

And finally, to my dad, Vítor Walgode, who studied at this same faculty. You only had time to share the beginning of my PhD with me. How I wish you were here. I would love to celebrate this achievement, and so many others, with you. I know it would have filled your heart with pride and love. I dedicate this work to you, Dad.

Abstract

The main objective of this PhD thesis is to develop an efficient process for glycerol valorisation through catalytic oxidation and chromatographic separation to produce high-purity dihydroxyacetone (DHA). This approach addresses the growing surplus of glycerol generated by the biodiesel industry. Among glycerol oxidation products, DHA stands out due to its high market value and strong demand in the cosmetics industry, where it is widely used as the main active ingredient in sunless tanning formulations.

Currently, DHA is produced via bio-fermentation processes, which are limited by low yields and long production times. A review of the literature identified bismuth-promoted platinum nanoparticles supported on carbon materials as benchmark catalysts for DHA production by glycerol oxidation operating under aqueous, base-free conditions, mild temperatures (30–90 °C) and oxygen pressures (1–5 bar). Recently, gold nanoparticles supported on metal oxides, particularly ZnO and CuO, have also shown potential for DHA production. However, most reported studies rely on lab-scale catalysts, and almost no research addresses the downstream separation of DHA from glycerol oxidation products, a crucial step for commercial implementation.

In the first part of this work, four commercial catalysts were screened in a fed-batch reactor operating at 353 K under base-free conditions: one Pt/AC, two Bi-promoted Pt-Bi/AC, and one Au/ZnO catalyst. The platinum-based catalysts were tested at an oxygen pressure of 4.5 bar, while the gold-based catalyst was at 6.5 bar. Pt5-Bi1.5/AC (Johnson Matthey) and Au1/ZnO (Strem Chemicals) performed best, achieving DHA yields of 36% and 27%, respectively, with DHA selectivity around 45%. These two catalysts were selected for kinetic studies, which were successfully described by a Langmuir–Hinshelwood–Hougen–Watson model. The estimated activation energies were 16 kJ mol^{-1} for Pt5-Bi1.5/AC and 52 kJ mol^{-1} for Au1/ZnO. Catalyst deactivation was attributed to the strong adsorption of reaction by-products, particularly organic acids.

For the downstream separation of DHA, equilibrium and kinetic adsorption data were obtained for glycerol, DHA, and key by-products (glyceric, glycolic, tartronic, and oxalic acids) at 293 K using the frontal analysis method in a fixed-bed column packed with a strong cation exchange resin (DOWEX® 50WX-2) in both H^+ and Ca^{2+} forms. The mobile phases were 5 mM H_2SO_4 and water, respectively. In the resin in H^+ form, all species followed linear adsorption isotherms except oxalic acid, which was best described by a Freundlich model. In the Ca^{2+} form, DHA and glycerol also followed linear isotherms, with higher retention factors compared to the H^+ resin. The separation selectivity between DHA and GLY increased from 1.04 in the H^+ resin to 1.28 in

the Ca^{2+} resin. DHA was the most retained species in both cases. Multi-component breakthrough experiments confirmed negligible competitive adsorption under the tested conditions.

These data supported the design of a two-step SMB cascade, which was experimentally validated on a FlexSMB-LSRE® unit equipped with six columns in a 1-2-2-1 configuration, operating at 293 K and an average pressure of 20 bar. The first SMB unit, packed with the H^+ resin, separated DHA from the organic acids. The second SMB unit, packed with the Ca^{2+} resin, separated DHA from the remaining glycerol. The process produced DHA with 98.6% purity and 77.5% recovery, a productivity of 21.7 kg_{DHA} $(m^3_{adsorbent} \cdot day)^{-1}$ and an eluent consumption of 9.0 $m_{eluent}^3 \cdot kg_{DHA}^{-1}$.

This work demonstrates the feasibility of an integrated process for producing high-purity DHA from glycerol catalytic oxidation using commercial catalysts, followed by continuous chromatographic separation, offering a scalable alternative to current production methods.

Graphical Abstract

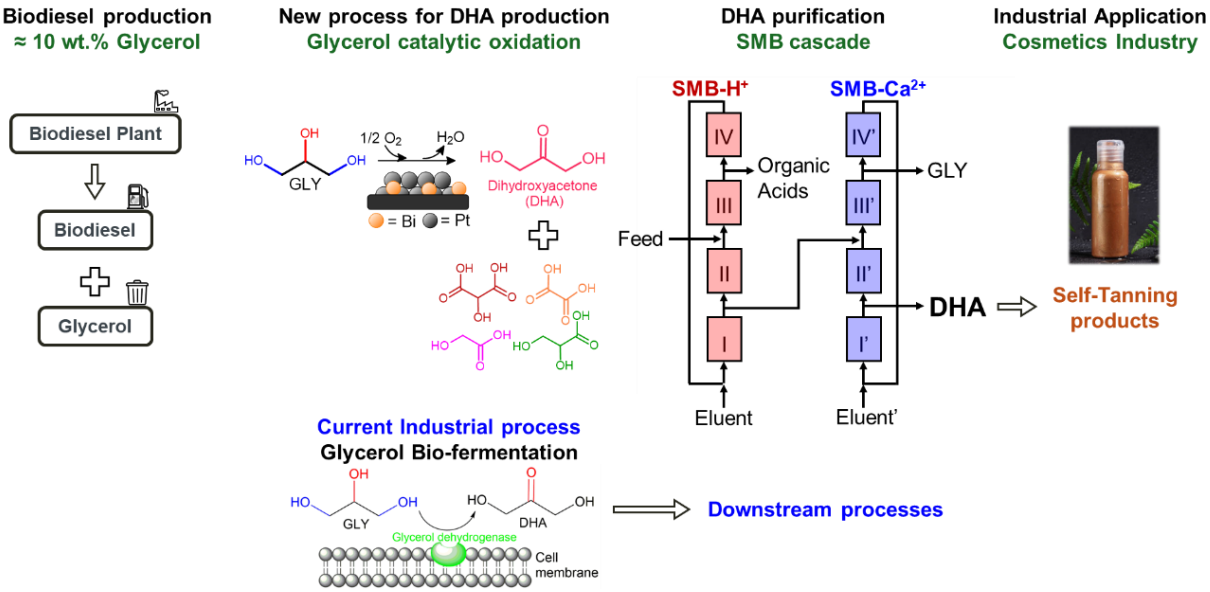

Resumo

A crescente produção de biodiesel resultou num excedente de glycerol, cujo valor diminuiu significativamente, tornando a sua valorização relevante. O principal objetivo desta tese de doutoramento consiste em desenvolver um processo eficiente para a valorização do glicerol através da sua oxidação catalítica, com vista à produção de dihidroxiacetona (DHA). A DHA destaca-se entre os diversos produtos de reação pelo seu elevado valor de mercado e procura, particularmente pela indústria cosmética. Atualmente a DHA é produzida por bio-fermentação do glicerol, um processo que apresenta algumas restrições, nomeadamente baixos rendimentos de reação e longos tempos de operação.

A oxidação catalítica do glicerol apresenta-se como uma alternativa viável. Na literatura destacam-se as nanopartículas de platina dopadas com bismuto suportadas em materiais de carbono, consideradas catalisadores de referência, operando em condições suaves de temperatura (30 a 90 °C), pressão de oxigénio (1 a 5 bar) e sem a presença de bases fortes como o hidróxido de sódio). Recentemente, nanopartículas de ouro suportadas em óxidos metálicos, tais como o ZnO e o CuO, também demonstraram resultados promissores. Contudo, a maioria dos estudos utiliza catalisadores sintetizados em laboratório. Por outro lado, praticamente não existem estudos sobre a separação da DHA dos produtos da oxidação do glicerol, uma etapa crucial para a sua posterior comercialização.

Na primeira parte deste trabalho, quatro catalisadores comerciais foram testados num reator agitado semi-fechado: um catalisador de platina suportado em carvão ativado (Pt/AC), dois de platina dopados com bismuto (Pt-Bi/AC) e um catalisador de ouro em óxido de zinco (Au/ZnO). Os catalisadores Pt5-Bi1.5/AC (Johnson Matthey) e Au1/ZnO (Strem Chemicals) demonstraram os melhores desempenhos, com rendimentos de DHA de 36% e 27%, respetivamente, e seletividades em torno de 45%. Estes foram selecionados para estudos cinéticos detalhados. O modelo de Langmuir–Hinshelwood–Hougen–Watson descreveu com sucesso as cinéticas de reação, sendo estimadas energias de ativação de 16 kJ mol^{-1} (Pt5-Bi1.5/AC) e 52 kJ mol^{-1} (Au1/ZnO) para a produção de DHA. A desativação catalítica, particularmente do Au1/ZnO, foi atribuída à forte adsorção de subprodutos, nomeadamente ácidos orgânicos.

Na segunda parte deste trabalho foi estudada a separação da DHA dos produtos da oxidação do glicerol. Iniciou-se o estudo com a obtenção de dados de equilíbrio e cinética de adsorção do glicerol, DHA e principais subprodutos (ácido glicérico, glicólico, tartrónico e oxálico) a 293 K, através do método de análise frontal em coluna de leito fixo empacotada com uma resina de permuta catiónica forte, a DOWEX® 50WX-2, nas formas H^+ e Ca^{2+}, utilizando como fases móveis, respetivamente, ácido sulfúrico (5 mM) e água. No caso da resina na forma ácida, todos

os compostos seguiram isotérmicas lineares, exceto o ácido oxálico, que foi melhor descrito por uma isotérmica de Freundlich. Já na forma Ca^{2+}, apenas o glicerol e a DHA foram testados, tendo a adsorção destes sido bem descrita por isotérmicas lineares. Em ambos os casos, a DHA foi sempre a espécie mais adsorvida, seguida do glicerol. Além disso, a seletividade para a separação entre a DHA e o glicerol é superior na resina em forma cálcio, verificando-se um aumento do fator de separação de 1.04 para 1.28. A ausência de adsorção competitiva foi confirmada pela análise de curvas de rutura multicomponente.

Os dados obtidos permitiram o desenvolvimento de um processo de purificação baseado numa cascata composta por duas unidades de leito móvel simulado (SMB), o qual foi experimentalmente validado na unidade FlexSMB-LSRE® com a configuração de colunas 1-2-2-1. O primeiro SMB (resina H^{+}) permitiu a separação pseudo-binária da DHA dos ácidos orgânicos, enquanto no segundo SMB (resina Ca^{2+}) separou-se a DHA do glicerol. O processo resultou na produção de DHA com 98,6% de pureza, apresentando uma recuperação de DHA de 77,5%, uma produtividade de 21,7 $kg_{DHA}\,(m^3_{adsorvente}\cdot dia)^{-1}$ e um consumo de eluente de 9,0 $m^3_{eluente}\cdot kg_{DHA}^{-1}$.

O trabalho desenvolvido nesta tese demonstra a viabilidade de um processo de produção e purificação da DHA a partir da oxidação catalítica do glicerol com catalisadores comerciais e da separação cromatográfica contínua, constituindo uma alternativa aos métodos de produção atuais for bio-fermentação.

Outputs

During this PhD, part of the work was published in three peer-reviewed international journals, with two additional manuscripts under submission, and disseminated through oral and poster presentations at national and international conferences, as listed:

International Journals

1. **A review of aerobic glycerol oxidation processes using heterogeneous catalysts: a sustainable pathway for the production of dihydroxyacetone.**

Catalysis Reviews - Science and Engineering, Taylor and Francis, 2021

Pedro M. Walgode; Rui. P. V. Faria; Alírio E. Rodrigues

DOI: 10.1080/01614940.2020.1747253

2. **Dihydroxyacetone Production: From Glycerol Catalytic Oxidation with Commercial Catalysts to Chromatographic Separation.**

Industrial & Engineering Chemistry Research, 2021

Pedro M. Walgode; Lucas C. D. Coelho; Rui P. V. Faria; Alírio E. Rodrigues

DOI: 10.1021/acs.iecr.1c00275

3. **Pseudo-Ternary Chromatographic Separation of Dihydroxyacetone from the Glycerol Oxidation Byproducts on a Simulated Moving Bed Cascade.**

Chemical Engineering Journal, 2023

Pedro M. Walgode; Rui. P. V. Faria; Alírio E. Rodrigues

DOI: 10.1016/j.cej.2023.146447

4. **Reaction kinetics and modelling of glycerol selective oxidation into dihydroxyacetone with a platinum-bismuth catalyst.**

Pedro M. Walgode, Rui. P. V. Faria, Alírio E. Rodrigues. Under submission in 2025

5. **Gold-catalysed oxidation of glycerol into dihydroxyacetone: Reaction kinetics and modelling.**

Pedro M. Walgode; Rui. P. V. Faria; Alírio E. Rodrigues. Under submission in 2025

Conferences

Oral presentation

1. Doctoral Congress in Engineering (DCE19), Porto, Portugal, 27-28 June 2019

Glycerol oxidation into dihydroxyacetone: perspectives and solutions

Pedro M. Walgode, Rui. P. V. Faria, Alírio E. Rodrigues

https://paginas.fe.up.pt/≈dce/2019/wp-content/uploads/2019/09/DCE-BoA-PDEQB.pdf

2. Doctoral Congress in Engineering (DCE21), Porto, Portugal, 28-29 June 2021

Dihydroxyacetone production by glycerol oxidation over Pt commercial catalysts and purification by Simulated Moving Bed Chromatography

Pedro M. Walgode, Rui. P. V. Faria, Alírio E. Rodrigues

https://drive.google.com/file/d/1Pw5S14ET_QcSMCAZdRmDuEJ65Rb99Uh7/view

3. 2021 AIChE Annual Meeting, Boston, USA, 7-11 November 2021

Dihydroxyacetone Separation from Glycerol Catalytic Oxidation Products by Simulated Moving Bed Technology

Pedro M. Walgode, Rui. P. V. Faria, Alírio E. Rodrigues

www.aiche.org/academy/conferences/aiche-annual-meeting/2021/proceeding/paper/412d-dihydroxyacetone-separation-glycerol-catalytic-oxidation-products-simulated-moving-bed

4. Doctoral Congress in Engineering (DCE23), Porto, Portugal, 15-16 June 2023

Dihydroxyacetone Separation from Glycerol Catalytic Oxidation Products in a Simulated Moving Bed Cascade: Proof-of-Concept

Pedro M. Walgode, Rui. P. V. Faria, Alírio E. Rodrigues

https://paginas.fe.up.pt/≈dce/2023/wp-content/uploads/2023/07/eqb_merged.pdf

5. 2023 AIChE Annual Meeting, Orlando, FL, USA, 5-10 November 2023

Separation of Dihydroxyacetone from Glycerol Catalytic Oxidation Products in a Simulated Moving Bed Cascade: From Concept to Proof-of-Concept

Pedro M. Walgode, Rui. P. V. Faria, Alírio E. Rodrigues

https://aiche.confex.com/aiche/2023/meetingapp.cgi/Paper/670319

6. **Fundamentals of Adsorption (FOA15), Porto, Portugal, 18-23 May 2025**

A Simulated Moving Bed Cascade for Enhanced Separation of Dihydroxyacetone from Glycerol Oxidation Mixtures.

Pedro M. Walgode, Rui. P. V. Faria, Alírio E. Rodrigues

https://media.sci-meet.com/foa15.events.chemistry.pt/fa1d4c98-c8ae-4913-9c94-78db515f63c7/Program_FOA_OralSession.pdf

7. **9th European Process Intensification Conference (EPIC2025), Athens, Greece, 4-6 June 2025**

Simulated Moving Bed Cascade for Efficient DHA Separation: from Batch to Continuous

Pedro M. Walgode, Rui. P. V. Faria, Alírio E. Rodrigues

https://epic-2025.com/scprogram

Poster presentation

1. **2019 AIChE Annual Meeting, Orlando, FL, USA, 10-15 November 2019**

Sustainable Solutions for Selective Glycerol Oxidation into Dihydroxyacetone Using Commercial Catalysts

Pedro M. Walgode, Rui. P. V. Faria, Alírio E. Rodrigues

aiche.org/conferences/aiche-annual-meeting/2019/proceeding/paper/560aq-sustainable-solutions-selective-glycerol-oxidation-dihydroxyacetone-using-commercial-catalysts

2. **43 Reunião Ibérica Adsorção (RIA43), Porto, Portugal, 1-4 September 2024**

Simulated Moving Bed Cascade for the Separation of Dihydroxyacetone from Glycerol Catalytic Oxidation Products

Pedro M. Walgode, Rui. P. V. Faria, Alírio E. Rodrigues

https://media.sci-meet.com/ria43.events.chemistry.pt/85d09180-a36b-4586-8633-9683526ca30d/BookofAsbtracts.pdf

Table of Contents

List of Figures

List of Tables

1. Introduction

This chapter presents the motivation and relevance of addressing glycerol valorisation and the potential of glycerol catalytic oxidation to produce dihydroxyacetone. It outlines the main objectives of this Thesis on developing a new alternative process, from catalytic oxidation to adsorption-based separation processes.

1.1. Motivation and Relevance

The growing global demand for energy and the urgent need for green and sustainable solutions have accelerated the expansion of renewable energy industries. This transition aims to address the energy crisis, tackle climate change, and develop safer, cleaner, and more sustainable processes for producing energy and chemical commodities. These efforts align with the United Nations' 2030 Agenda for Sustainable Development, particularly Goal 7. *Ensure access to affordable, reliable, sustainable and modern energy* [1].

Biodiesel plays a significant role in this transition as a biodegradable and non-toxic alternative to fossil diesel. Its global production more than doubled from 20 Mm^3 in 2010 to 45 Mm^3 in 2022, with projections indicating continued growth or stabilisation until 2050 [2, 3]. However, this expansion has led to a surplus of glycerol (GLY), the main byproduct, constituting approximately 10 wt.% of biodiesel production. Valorising glycerol is essential for enhancing the economic and environmental sustainability of the biodiesel industry, aligning with global efforts towards a circular economy and with the United Nations' Sustainable Development Goals, specifically Goal 12. *Ensure sustainable consumption and production patterns*, and Goal 13. *Take urgent action to combat climate change and its impacts*.

Glycerol is a promising feedstock for chemical synthesis, with several valorisation routes, including oxidation, hydrogenolysis, dehydration, pyrolysis, gasification, steam reforming, etherification, and polymerization [4-6]. However, only a few of these routes have reached the commercial stage [7]. Among them, catalytic oxidation stands out as an effective route to produce high-value compounds such as organic acids (e.g., glyceric acid, hydroxypyruvic acid, tartronic acid, glycolic acid, oxalic acid) and dihydroxyacetone (DHA) [7-9]. Controlling the reaction selectivity is fundamental to obtain the desired product [10-12].

DHA is particularly notable due to its high demand in the cosmetics industry, as the active ingredient in sunless tanning lotions. These products have gained popularity as a safer alternative to traditional sunbathing or tanning beds, which are associated with health risks [13, 14]. DHA itself is considered safe for skin application [14, 15].

Currently, microbial fermentation of glycerol using *Gluconobacter oxydans* is the industrial state-of-the-art for DHA production. However, this biotechnological process is costly [16] and presents limitations such as low productivity and long reaction times [7, 10, 17-20]. In contrast, catalytic oxidation offers a promising alternative with potential advantages in efficiency and scalability. Since the first reports in the early 1990s demonstrating glycerol's selective oxidation into DHA using Pt-based catalysts [21, 22], significant progress has been made in catalyst development and process optimisation. Nevertheless, challenges persist, particularly in achieving high DHA yield with catalyst stability [6, 12, 23].

On the other hand, research on DHA purification from glycerol oxidation products is minimal despite its critical importance in developing a viable alternative DHA production process [24].

1.2. Objectives and Outline

The main objective of this Thesis is to develop an alternative and efficient process for dihydroxyacetone (DHA) production, integrating glycerol catalytic oxidation and downstream DHA purification. This research focused on selecting a suitable commercial catalyst for the selective oxidation of glycerol, studying reaction kinetics, and designing adsorption-based separation processes to help establish a commercially viable DHA production process that meets the demands of a growing market.

This Thesis is structured into seven chapters, covering the contextual background, literature review, experimental work, and final conclusions related to catalyst selection, reaction kinetics, and DHA purification via simulated moving bed (SMB) technology.

1. **Chapter 1. Introduction** outlines the motivation and relevance of developing a new process for glycerol catalytic oxidation into DHA and its purification.
2. **Chapter 2. State-of-the-art** provides an overview of biodiesel production, glycerol valorisation routes, and potential applications of DHA. It reviews the current DHA production methods, their limitations, and provides a comprehensive analysis of glycerol catalytic oxidation strategies and adsorption-based purification processes. Relevant patents on DHA production and separation technologies are also discussed.
3. **Chapter 3. Catalyst screening for Glycerol Selective Oxidation into Dihydroxyacetone** reports the investigation of commercial and pre-commercial catalysts, focusing on platinum- and gold-based materials, evaluating their performance in terms of glycerol conversion, DHA selectivity and stability.
4. **Chapter 4. Glycerol Oxidation Kinetics** presents a kinetic study of the glycerol oxidation network using the most promising catalysts identified in Chapter 3.
5. **Chapter 5. Adsorption Equilibrium and Kinetics** explores the adsorption of the main compounds obtained during glycerol catalytic oxidation. Equilibrium data was obtained via frontal analysis, performing single- and multi-component adsorption breakthrough experiments on a fixed-bed column. Polystyrene divinylbenzene resins were used as the stationary phase, and water/H_2SO_4 aqueous solution as the mobile phase.
6. **Chapter 6. SMB Separation of Dihydroxyacetone** details the design of a simulated moving bed process for DHA separation from glycerol oxidation products. A two-stage unit is proposed and experimentally validated using the FlexSMB-LSRE® lab-made pilot unit.

7. **Chapter 7. Conclusions and Suggestions for Future Work** summarises the key findings and provides further research and process improvements recommendations.

1.3. References

1. United Nations General Assembly A/RES/70/1, *Transforming our world, the 2030 Agenda for Sustainable Development*. 2015: New York, USA.
2. IEA, *World Energy Outlook 2022*. 2022: IEA, Paris.
3. IEA, *Renewables 2020*. 2020, IEA, Paris.
4. Xiao, Y., Greeley, J., Varma, A., Zhao, Z.J., and Xiao, G., *An experimental and theoretical study of glycerol oxidation to 1, 3-dihydroxyacetone over bimetallic Pt-Bi catalysts.* AIChE Journal, 2017. **63**(2): p. 705-715.
5. Quispe, C.A., Coronado, C.J., and Carvalho Jr, J.A., *Glycerol: production, consumption, prices, characterization and new trends in combustion.* Renewable and Sustainable Energy Reviews, 2013. **27**: p. 475-493.
6. Zhou, C.-H.C., Beltramini, J.N., Fan, Y.-X., and Lu, G.M., *Chemoselective catalytic conversion of glycerol as a biorenewable source to valuable commodity chemicals.* Chemical Society Reviews, 2008. **37**(3): p. 527-549.
7. Katryniok, B., Kimura, H., Skrzyńska, E., Girardon, J.-S., Fongarland, P., Capron, M., Ducoulombier, R., Mimura, N., Paul, S., and Dumeignil, F., *Selective catalytic oxidation of glycerol: perspectives for high value chemicals.* Green Chemistry, 2011. **13**(8): p. 1960-1979.
8. Dodekatos, G., Schünemann, S., and Tüysüz, H., *Recent Advances in Thermo-, Photo-, and Electrocatalytic Glycerol Oxidation.* ACS Catalysis, 2018. **8**(7): p. 6301-6333.
9. Kosamia, N.M., Samavi, M., Uprety, B.K., and Rakshit, S.K., *Valorization of biodiesel byproduct crude glycerol for the production of bioenergy and biochemicals.* Catalysts, 2020. **10**(6): p. 609.
10. Hirasawa, S., Watanabe, H., Kizuka, T., Nakagawa, Y., and Tomishige, K., *Performance, structure and mechanism of Pd–Ag alloy catalyst for selective oxidation of glycerol to dihydroxyacetone.* Journal of catalysis, 2013. **300**: p. 205-216.
11. Lee, S., Kim, H.J., Lim, E.J., Kim, Y., Noh, Y., Huber, G.W., and Kim, W.B., *Highly selective transformation of glycerol to dihydroxyacetone without using oxidants by a PtSb/C-catalyzed electrooxidation process.* Green Chemistry, 2016. **18**(9): p. 2877-2887.
12. Hu, W. and Varma, A. *Catalytic Oxidation of Glycerol to High-Value Chemical Dihydroxyacetone*. in *21st North American Catalysis Society Meeting, San Francisco, CA*. 2009.
13. Mogensen, M. and Jemec, G.B., *The potential carcinogenic risk of tanning beds: clinical guidelines and patient safety advice.* Cancer management and research, 2010: p. 277-282.
14. Ciriminna, R., Fidalgo, A., Ilharco, L.M., and Pagliaro, M., *Dihydroxyacetone: An Updated Insight into an Important Bioproduct.* ChemistryOpen, 2018. **7**(3): p. 233-236.
15. *Opinion on Dihydroxyacetone (DHA) CAS N° 96-26-4*. 03-04 March 2020, Scientific Committee on Consumer Safety.
16. *1,3-Dihydroxyacetone Market Analysis in Global Industry, Demands, Perspective, Insights, Research and Forecast 2019-2026.* Mynewsdesk.
17. Garcia, A.C., Birdja, Y.Y., Tremiliosi-Filho, G., and Koper, M.T., *Glycerol electro-oxidation on bismuth-modified platinum single crystals.* Journal of Catalysis, 2017. **346**: p. 117-124.
18. Hu, W., Knight, D., Lowry, B., and Varma, A., *Selective oxidation of glycerol to dihydroxyacetone over Pt− Bi/C catalyst: optimization of catalyst and reaction conditions.* Industrial & Engineering Chemistry Research, 2010. **49**(21): p. 10876-10882.

19. Li, M.-h., Wu, J., Liu, X., Lin, J.-p., Wei, D.-z., and Chen, H., *Enhanced production of dihydroxyacetone from glycerol by overexpression of glycerol dehydrogenase in an alcohol dehydrogenase-deficient mutant of Gluconobacter oxydans.* Bioresource technology, 2010. **101**(21): p. 8294-8299.

20. Bagheri, S., Julkapli, N.M., and Yehye, W.A., *Catalytic conversion of biodiesel derived raw glycerol to value added products.* Renewable and Sustainable Energy Reviews, 2015. **41**: p. 113-127.

21. Kimura, H., Tsuto, K., Wakisaka, T., Kazumi, Y., and Inaya, Y., *Selective oxidation of glycerol on a platinum-bismuth catalyst.* Applied Catalysis A: General, 1993. **96**(2): p. 217-228.

22. Kimura, H., *Selective oxidation of glycerol on a platinum-bismuth catalyst by using a fixed bed reactor.* Applied Catalysis A: General, 1993. **105**(2): p. 147-158.

23. Li, Y. and Zaera, F., *Sensitivity of the glycerol oxidation reaction to the size and shape of the platinum nanoparticles in Pt/SiO 2 catalysts.* Journal of Catalysis, 2015. **326**: p. 116-126.

24. Skrzyńska, E., Wondołowska-Grabowska, A., Capron, M., and Dumeignil, F., *Crude glycerol as a raw material for the liquid phase oxidation reaction.* Applied Catalysis A: General, 2014. **482**: p. 245-257.

2. State-of-the-Art

This chapter discloses glycerol as a versatile building block, focusing on its production and valorisation routes. It comprehensively reviews glycerol valorisation by selective oxidation into dihydroxyacetone, summarising key advancements in catalyst development and reaction engineering. Finally, DHA separation and purification methods are presented, particularly chromatographic techniques, which offer promising solutions for obtaining high-purity DHA.

This Chapter was adapted from Walgode, P. M., Faria, R. P., & Rodrigues, A. E. (2021). A review of aerobic glycerol oxidation processes using heterogeneous catalysts: a sustainable pathway for the production of dihydroxyacetone. *Catalysis Reviews*, *63*(3), 422-511.

2.1. Introduction

Dihydroxyacetone (DHA, 1,3-dihydroxy-2-propanone) is the simplest ketose and an important intermediate in carbohydrate metabolism, naturally formed during glycolysis in higher plants and animals. DHA is a dimer with a dioxane structure in its solid state, which dissociates into free carbonyl and hydrated monomers upon dissolution. Commercially, DHA is predominantly produced via microbial fermentation of glycerol using acetic acid bacteria [1].

DHA was first reported in the 19th century, but its widespread applications were only realised decades later [2]. In the 1920s, DHA was used in medical trials in patients with diabetes, resulting in unexpected yellow staining of their gums. Subsequent studies in the 1950s by Wittgenstein and Berry confirmed that DHA reacts with amino groups in skin proteins via the Maillard reaction, forming melanoidins responsible for skin browning [1]. This discovery laid the foundation for its use in self-tanning products, which started in the 1960s and gained increasing commercial relevance in the late 20th century until today, driven by increasing awareness of ultraviolet radiation risks and advancements in product formulations. DHA remains the key ingredient in sunless tanning formulations, approved by the US Food and Drug Administration. Besides aesthetic purposes, DHA formulations offer a safe and effective therapeutic option for patients with vitiligo [3].

Beyond cosmetics, DHA has gained attention as a versatile bio-based building block, with potential applications in biocompatible and biodegradable polymers. Research is underway to develop more efficient synthetic pathways for DHA production, moving beyond microbial fermentation to alternative catalytic, photo- and electro-oxidation routes. The economic feasibility of such approaches remains challenging, particularly due to the reliance on noble metal catalysts. However, the growing demand for high-purity DHA has intensified research into cost-effective and scalable processes [1, 4].

This chapter comprehensively reviews the state of the art regarding DHA production and purification. The first part focuses on the catalytic oxidation of glycerol as an alternative route for DHA synthesis, summarising key advancements in catalyst development and reaction engineering. The second part examines DHA separation and purification methods, particularly chromatographic techniques, which offer promising solutions for obtaining high-purity DHA.

2.2. From Glycerol to Dihydroxyacetone

2.2.1. Biodiesel Industry and Glycerol Surplus

The global demand for energy and chemical commodities remains largely reliant on fossil fuels. The transport sector accounts for approximately 20% of global energy consumption, a figure projected to rise due to ongoing population and economic growth [5]. This sector is also responsible for 25% of energy-related carbon dioxide emissions, with 95% originating from crude fossil oil [5]. Concerns regarding fossil fuel depletion, geopolitical dependencies, and the environmental impact of fossil fuel extraction and exploration have driven the transition towards renewable energy sources. This shift has been reinforced by government policies, such as the European Union's directive targeting 20% renewable energy consumption by 2020, including a share of 10% liquid biofuels in the transport sector [6].

Biodiesel and bioethanol are the most significant biofuels [5]. Biodiesel is attractive due to its renewability, biodegradability, low toxicity, and fuel properties comparable to fossil diesel. Initially used in road transport, its application has expanded since the early 2000s to aviation, maritime transport, and electricity generation [7-9]. It can be used either in pure form or blended with fossil diesel. Global biodiesel production increased from 20 Mm^3 in 2010 [10] to 45 Mm^3 in 2019 and has remained relatively stable since [11, 12]. Historically, the European Union has been the leading producer and consumer, followed by the United States (Figure 2.1).

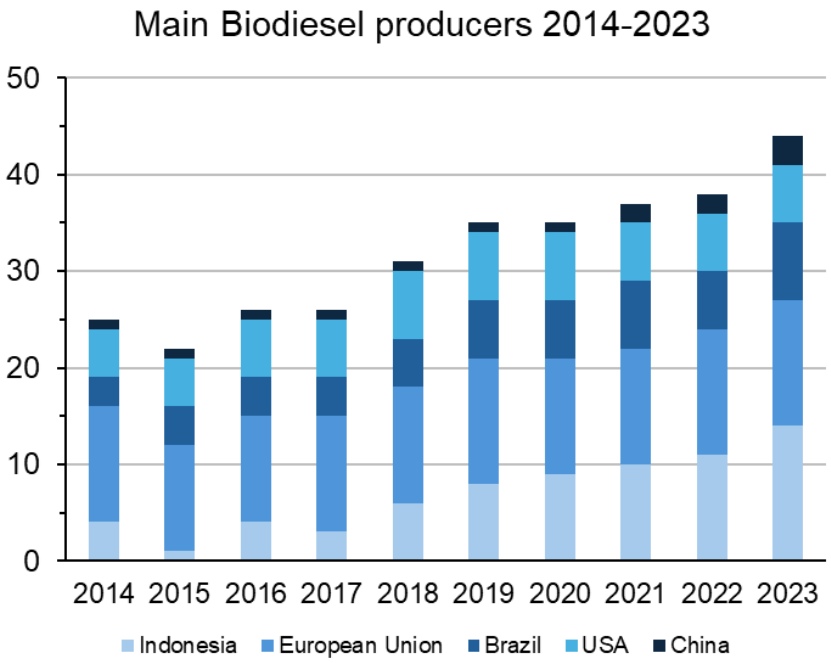

Figure 2.1. Top biodiesel-producing countries, 2014–2023.

However, production and demand have slowed in advanced economies while increasing in emerging markets, particularly Brazil, Indonesia, and India. Since 2023, Indonesia has become the world's leading producer, with 14 Mm^3 (primarily from palm oil), followed by the EU at 13 Mm^3 (mainly from rapeseed and used cooking oil) and Brazil at 8 Mm^3 (mainly from soybeans) [5, 11, 12]. However, biodiesel remains 1.5–2 times more expensive than fossil diesel in the EU and the USA [13].

Besides the slowdown in diesel car sales in favour of gasoline and electric cars, a key factor contributing to the slowdown in biodiesel growth is the increasing interest in hydrotreated vegetable oil (HVO), also known as renewable diesel. It is a "drop-in" fuel, fully compatible with existing diesel engines in pure and blended forms without the blending constraints of biodiesel. Hydrotreated vegetable oil has a lower aromatic content than fossil diesel and superior cold-weather performance compared to biodiesel and conventional diesel. Still, its production is more expensive and complex than biodiesel [12, 14].

Biodiesel, or Fatty Acid Methyl Ester, is primarily produced through the transesterification of vegetable oils or animal fats (triglycerides) with a short-chain alcohol, typically methanol or ethanol, in the presence of a homogeneous alkaline catalyst such as NaOH.

The major by-product of this process is glycerol, which accounts for approximately 10 wt.% of total biodiesel output [15, 16]. The crude glycerol obtained contains several impurities, including water, inorganic salts, methanol, fatty acids, and esters, resulting in a 40–88 wt.% purity range, depending on the feedstock and production process. This level of purity is significantly lower than that of technical-grade (88 – 98 wt.%) and pharmaceutical-grade (>98 wt.%) glycerol, limiting its commercial value [7, 9, 17].

Crude glycerol impurities, particularly unreacted methanol or ethanol, can be recovered and recycled into biodiesel production, especially in large-scale operations [6]. Various purification techniques have been developed to obtain higher-purity glycerol, including conventional filtration, membrane-based microfiltration and ultrafiltration, simple and vacuum distillation, chemical and physical treatments, ion exchange, and adsorption processes [15, 16].

Glycerol, formally propane-1,2,3-triol (IUPAC), is commonly known as glycerine. It is a colourless, odourless, and highly viscous liquid with a syrupy texture at room temperature (866 cP at 293 K). As a C3 compound with three hydrophilic hydroxyl groups, glycerol is hygroscopic and highly miscible in water, alcohols, and other polar compounds [15, 17]. In the mid-20th century, it was reported to have as many as 1,500 potential commercial applications, particularly in the pharmaceutical and cosmetics industries [16].

Glycerol is primarily produced as a by-product of saponification and hydrolysis in oleochemical plants and from the transesterification reaction in biodiesel production [15, 16]. It

is widely used across multiple industries, including pharmaceuticals, cosmetics, food, paper, and textiles, as a solvent, sweetener, stabiliser, lubricant, and humectant [15-17]. However, the oversupply of glycerol has led to a continuous decline in its market price, with refined glycerol averaging ≈600 €/ton and crude glycerol around ≈300 €/ton. Prices have fallen as low as 50–100 €/ton in the late 2000s [15, 17]. Recent data on the average cost of refined and crude glycerol in different regions in 2020 [18] is presented in Figure 2.2.

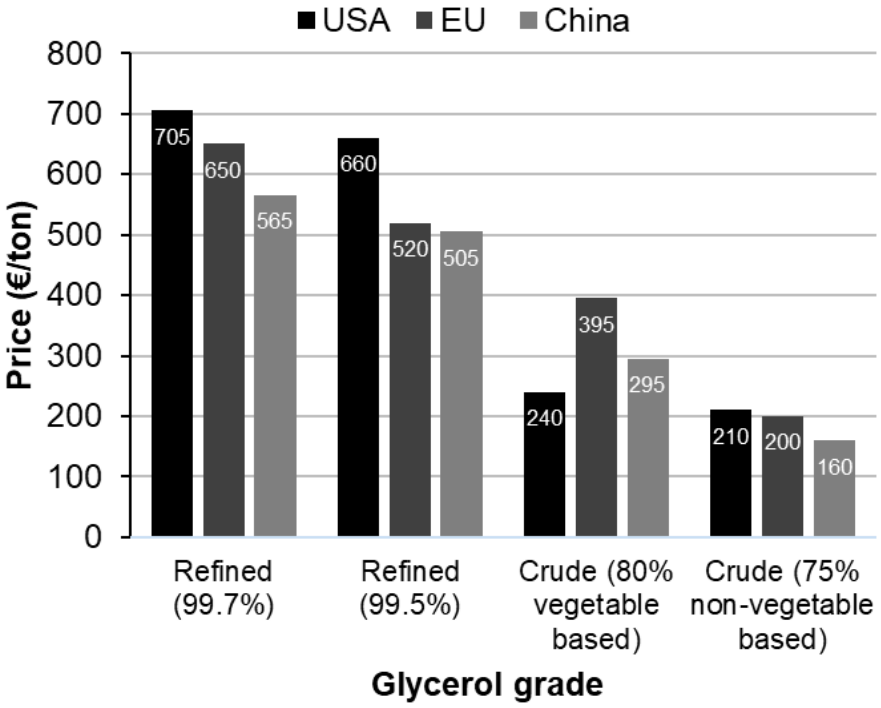

Figure 2.2. Average glycerol prices by region (2020, 2nd semester) and grade: 99.7% kosher, 99.5% technical, 80% vegetable-based crude, 75% non-vegetable-based crude.

Crude glycerol was often treated as a waste product and incinerated for energy recovery. It cannot be directly used as a fuel additive due to its tendency to decompose and polymerise, which could cause engine damage [7, 9, 16, 17, 19].

The valorisation of glycerol into higher-value products is crucial for enhancing the economic and environmental sustainability of the biodiesel industry. Beyond its traditional applications, glycerol is a versatile chemical feedstock due to its low cost and ability to undergo various chemical transformations [20-22]. It can be converted through oxidation, hydrogenolysis, dehydration, cyclisation, halogenation, pyrolysis, gasification, steam reforming, thermal reduction to syngas, etherification, oligomerisation, polymerisation, carboxylation, and transesterification [17, 23, 24], as summarised in Figure 2.3.

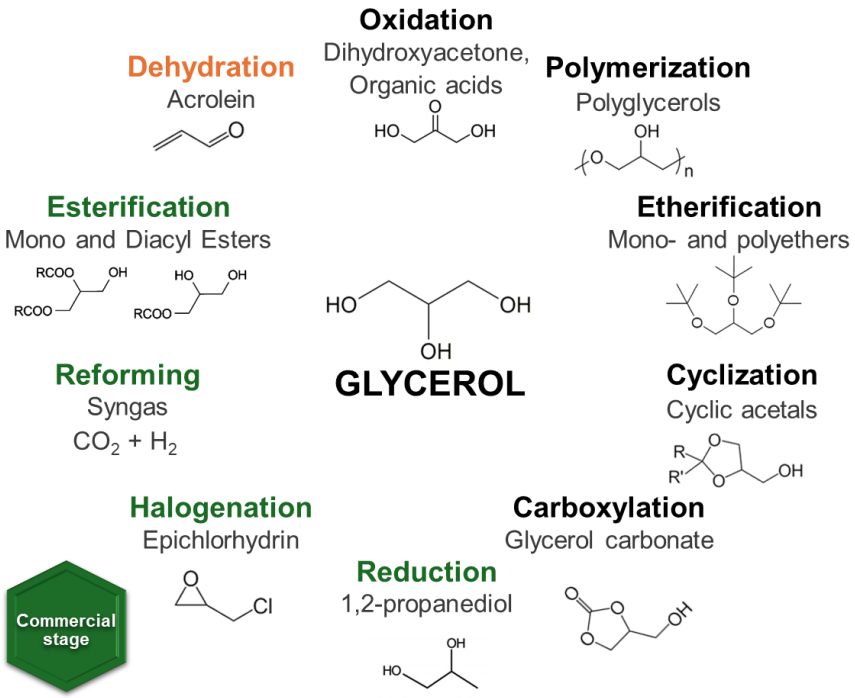

Figure 2.3. Main glycerol valorisation routes to high-value products. Green: commercialised; Orange: near-commercial; Black: non-commercialised.

Some of these valorisation routes are already at a commercial stage, including glycerol reforming to produce syngas, glycerol chlorination to yield epichlorohydrin (a key intermediate for epoxy resins), and glycerol esterification to produce monoacyl and diacyl esters (e.g., glycerol acetates or fatty acid esters) [4, 16]. Glycerol dehydration to acrolein has been technologically ready for commercialisation since the 2010s; however, the bio-based process remains economically uncompetitive compared to the conventional petrochemical route [16].

2.2.2. Glycerol Oxidation

Glycerol oxidation can yield various products depending on the reaction conditions. Oxidation of hydroxyl (-OH) groups leads to the formation of carbonyl (-C=O) or carboxyl (-COOH) functional groups. The selective oxidation of the secondary hydroxyl group results in ketones, whereas oxidation of primary hydroxyl groups initially forms aldehydes, which may further oxidise into carboxylic acids in aqueous media [25, 26]. This process enables the production of high-value chemicals such as dihydroxyacetone (DHA), glyceraldehyde (GLAD), glyceric acid (GCA), hydroxypyruvic acid (HPA), tartronic acid (TTA), glycolic acid (GCO), and oxalic acid (OXA) [20-22]. The reaction scheme, illustrating different pathways and product selectivity depending on catalyst type and reaction conditions, is presented in Figure 2.4.

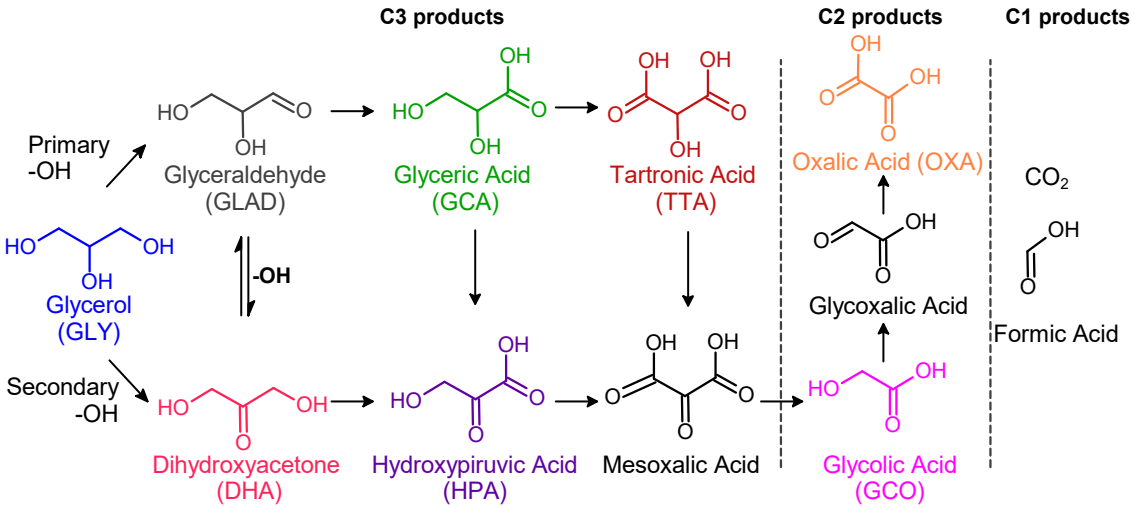

Figure 2.4. Glycerol oxidation pathways. GLAD–DHA interconversion occurs under basic conditions.

Traditional oxidation methods rely on hazardous oxidants such as chromium-based reagents, TEMPO, benzoquinone, and permanganates [4, 27]. To align with green chemistry principles, milder and more sustainable oxidants, such as molecular oxygen or hydrogen peroxide, are preferred [25]. Due to glycerol's high boiling point (290 °C), oxidation typically occurs in the aqueous phase [20, 24, 28].

Both homogeneous and heterogeneous catalysts have been studied extensively, with heterogeneous catalysts particularly advantageous due to their recyclability and process efficiency. Platinum-based catalysts, in particular, enable high glycerol conversion and selective oxidation under mild conditions, though catalyst deactivation remains a key challenge [25-27, 29-31]. The earliest report of aerobic glycerol oxidation using metal catalysts dates to the 1970s, with palladium supported on carbon selectively oxidising the primary hydroxyl groups to produce GCA and TTA [32]. In 1992, a patent described using Pt/C and Pd/C catalysts for glycerol oxidation [4].

Glycerol conversion and reaction selectivity are strongly influenced by catalyst properties (e.g., metal type, particle size, support) and reaction conditions (e.g., temperature, pressure, substrate concentration, oxidant type, solvent). Reaction kinetics are complex, with the product's selectivity changing significantly over the reaction time [4, 6, 27, 32-46]. pH plays a crucial role: under acidic conditions, oxidation of the secondary hydroxyl group is favoured, producing DHA, whereas under basic conditions, primary hydroxyl oxidation predominates, yielding GLAD [47]. Alkaline media typically enhances reaction rates by facilitating dehydrogenation and/or acid desorption from the catalyst surface [28]. However, DHA is unstable under basic conditions and undergoes interconversion into GLAD [40, 48], a mechanism also observed in the enzymatic oxidation of glycerol [4, 40].

2.2.3. Dihydroxyacetone: Challenges and Opportunities

DHA exists in a dimeric form but readily dissociates into its monomeric form in water. Its carbonyl group is responsible for its primary application as a self-tanning agent via the Maillard reaction, where it reacts with amino acids in the skin's stratum corneum to produce temporary pigmentation. This feature has established DHA as a key ingredient in sunless tanning products, including lotions, sprays, and professional treatments [1-4].

The global DHA market has experienced steady growth due to increasing awareness of the risks associated with UV exposure and rising demand for safer tanning alternatives. DHA production was approximately 2,000 tons in 2007, primarily derived from microbial fermentation of glycerol using *Gluconobacter oxydans* [49]. Since 2011, the market value has grown from USD 135 million and is projected to reach USD 220 million by 2028. Europe and North America dominate the DHA market (35% share each), followed by Asia-Pacific (27%) [50].

Beyond cosmetics, DHA holds significant commercial value in pharmaceuticals and fine chemical synthesis. In the pharmaceutical sector, DHA is a precursor in the synthesis of D,L-serine and other biologically relevant compounds [1, 4]. Cosmetic-grade DHA production must comply with strict quality and regulatory standards to meet Good Manufacturing Practices [51].

Currently, microbial fermentation remains the only commercially viable method for DHA production. However, this process has limitations such as low substrate concentrations, extended fermentation times, and low productivity (≈ 3 g L^{-1} h^{-1} in a two-stage repeated fed-batch system over 77 hours) [4, 20, 34, 52-54]. Patents related to DHA production are summarised in Table 2.1, with key producers including Merck KGaA, Adina, Hubei Marvel-Bio Medicine, and Changxing Pharmaceutical [55].

Table 2.1. Patented processes for DHA production via glycerol oxidation.

Catalyst	Summary of Invention	Inventor (Year) Patent number
Acetobacter suboxydans	Glycerol bioconversion under aerobic conditions (pH ≈4, 24-48 h). Y_{DHA} = 75-90%.	Charney, W. [56] 1978 US4076589
(i) Acid catalysts (ii) O_2/chromium trioxide complex	(i) GLY acetal formation over acid catalysts (H_2SO_4, p-Toluenesulfonic acid, cation exchange resin); (ii) oxidation; (iii) hydrolysis. S_{DHA} ≈ 99%.	Wang & Yu [57] 2009 CN101412706
(i) Acid catalyst (acetal formation) (ii) homogeneous catalysts or Pt-Bi/AC	(i) GLY acetal formation with acetaldehyde or 1,1-diethoxyethane over acid catalysts (H_2SO_4, cation exchange resin), (ii) cis-6 isomer separation by distillation, (iii) oxidation over Ru, Cr, hypohalite salts with strong oxidants, or Pt-Bi/AC with O_2, (iv) hydrolysis. Moderate DHA yields	Miller et al. [58] 2012 US8735633
TEMPO	Indirect DHA production (i) GLY reaction with boric acid to protect primary -OH (ii) secondary -OH oxidation with TEMPO, (iii) hydrolysis.	Ai, Y. [59] 2014 CN104098455
Cu/HT H_2O_2	Cr, Mn, Fe, Co, Ni, and Cu-based hydrotalcite (HT). Cu/HT preferred. H_2O_2 as oxidant. GLY 80 wt.%. Y_{DHA} ≈ 60%, 12 h, 60 ºC.	Fang et al. [60] 2012, CN102432445
Precursors of positive halogens and Lewis acids	Glycerol oxidation with halogen precursors (trichloroisocyanuric acid, inorganic hypochlorites) and Lewis acids ($AlCl_3$, zeolites). Y_{DHA} ≈ 90%. Suitable for crude glycerol feed.	Spanu & Ulgheri [61] 2014 WO2014102840
Au on ZnO, Cu-Al spinel or HT O_2	GLY oxidation under base-free conditions (80°C, 10-20 bar O_2, 2-3 h). S_{DHA} = 75-98%, Y_{DHA} 75%	Dong et al. [62] 2016 CN105439831
Au/Cu-ZrO_2 O_2	0.1 M GLY oxidation under base-free conditions (3 bar, 60 °C, activated at 200 °C under airflow). Y_{DHA} up to 80% (X_{GLY} up to 80%, S_{DHA} ≈95%).	Zhao et al. [63] 2019 CN109806886
Au/HT (Zn-Ga preferred) O_2	Au/HT (2-5 nm) prepared by deposition-precipitation (DP) with urea, calcinated at 300°C. X_{GLY} = 98%, 56% S_{DHA} = 56% (80°C, 5 bar, 4 h).	He et al. [64] 2019 CN110252298
Au/CuO-SnO_2 O_2	Au/mesoporous CuO-SnO_2 (3 wt.%) DP-prepared, calcinated at 200°C. Cu:Sn molar ratio 3:1 preferred. X_{GLY} = 100%, S_{DHA} = 95% (80°C, 1-2 bar O_2, 4 h).	Ke et al. [65] 2020 CN111013605
Pt/Bi-modified porous carbon O_2	Bi is dispersed on a porous carbon skeleton by calcinating mechanically mixed Bi salts and organic precursors. Pt or Pd was loaded and reduced. X_{GLY} ≈ 90%, S_{DHA} ≈ 95% (40°C, 1 bar O_2), excellent reusability.	Leng et al. [66] 2020 CN111774087
MgOx/Au/HT O_2	MOx/Au/HT (M = Cu, Mg, Zn, Ca; 0.5-5 wt.% Au). MgAl-HT precursor was preferred. Metal hydroxide cluster-Au formation by thermally induced Al substitution. Y_{DHA} ≈ 70% (X_{GLY} ≈ 80%, S_{DHA} ≈ 85%) at 60°C, 3 bar O_2, 4 h, GLY:Au of 200:1 molar.	Feng et al.[67] 2022 CN115445611

Catalytic glycerol oxidation presents a promising alternative to fermentation, offering advantages in efficiency, scalability, and raw material utilisation. Platinum-based catalysts efficiently oxidise glycerol but typically favour primary hydroxyl oxidation. The first report of high DHA selectivity via catalytic oxidation was published in 1993 by Kimura et al. [32], demonstrating that Pt-Bi/C under acidic conditions could enhance DHA selectivity. Subsequent studies confirmed that incorporating promoters improved Pt catalytic activity, stability, and selectivity for secondary hydroxyl oxidation [29, 68].

π-electron donor metals such as bismuth (Bi), antimony (Sb), and lead (Pb), when incorporated into Pt-group catalysts, shift oxidation selectivity toward the secondary hydroxyl group. While Pt nanoparticles supported in activated carbon (AC) preferentially oxidised the primary hydroxyl group of glycerol to produce glyceric acid, the bismuth-doped catalyst, Pt-Bi/AC, improved DHA selectivity from 10% to 80% [32]. Since then, extensive research has explored noble metal catalysts (Pt, Au, Pd, Ag), along with doping strategies, support modifications, and advanced preparation and activation methods to enhance performance. Efforts to reduce costs have also focused on developing non-noble or low-metal-loaded catalysts [4, 69, 70].

Despite significant advancements, challenges remain in optimising reaction selectivity, catalyst activity and stability, and process scalability and cost-efficiency. The high cost of noble metal catalysts accounts for approximately 95% of process expenses, even with catalyst recycling [69]. However, the low price of raw materials, glycerol (0.30–0.50 €/kg) and oxygen (atmospheric air), combined with DHA's high market value (≈130 €/kg), makes the catalytic route highly attractive [4]. Although catalytic oxidation of glycerol to DHA is still under development, it represents a potential alternative to microbial fermentation.

The following Sections review recent advances in catalyst design, reaction conditions, and process optimisation for selective glycerol oxidation to DHA. Literature reviews on this topic are available [69, 71, 72], including very recent ones [73]. Various noble metal catalysts, including Pt, Pd, Au, and Ag, have been investigated to improve conversion rates and selectivity, with bimetallic and promoted catalysts showing promising enhancements in DHA selectivity while enhancing stability and activity [4, 69, 74].

This chapter focuses on aerobic glycerol oxidation using heterogeneous metal catalysts, which operate under mild conditions and allow the use of air as the oxidant, the most economical and environmentally benign stoichiometric oxidant. Although solvents can enhance reaction performance, only aqueous-phase processes are considered. Studies involving other oxidants rather than molecular oxygen (pure or diluted, i.e., air) or emerging technologies such as photo- or electro-catalysis are addressed elsewhere [69, 70, 75, 76]. While these methods show

potential, few studies have been done on the subject, and their technological maturity is lower than that of catalytic thermo-oxidation.

2.3. Catalysts for Glycerol Oxidation into DHA

Since the first report of catalytic glycerol aerobic oxidation to DHA in 1993 using Pt/AC and Pt-Bi/AC catalysts, research has focused on improving glycerol conversion, DHA selectivity, and catalyst stability. Most studies have investigated aqueous-phase reactions under basic or base-free conditions.

The reaction mechanism and selectivity depend on the catalyst composition and reaction conditions. Metal-catalysed aerobic oxidation generally involves glycerol and oxygen adsorption, hydroxyl and carbonyl dehydrogenation, water formation, and product desorption [23]. Under alkaline conditions, Au-based catalysts exhibit high activity, with the catalytic trend Au ≫ Pt > Pd > Ag for nanoparticles supported on Al_2O_3 [77, 78]. However, due to DHA's instability, alkaline media favour glyceric acid over DHA. NaOH also promotes C-C bond cleavage, increasing the formation of C2 and C1 products. Pt and Pd catalysts also suffer from metal leaching, and organic acid salt formation and precipitation complicate industrial implementation [79].

Base-free conditions are preferred for DHA production, as DHA remains stable in an acidic environment [4]. Under these conditions, Pt/AC exhibited higher glycerol oxidation rates than Au/AC and Pd/AC [79], while Ag and Pd supported on carbon black showed minimal activity [78].

Most studies focus on noble metals: Pt, Pd, Au, and Ag, due to their superior catalytic activity. Metals with redox potentials lower than Pt exhibit high oxygen surface coverage and low organic substrate adsorption, reducing their catalytic activity [28]. Other platinum-group metals (Ru, Rh, Os, Ir) have shown limited success, as metals with redox potentials lower than Pt exhibit high oxygen surface coverage and low organic substrate adsorption, reducing their catalytic activity [28]. Pd is less active than Pt, while Ru and Re are nearly inactive due to oxygen poisoning [28, 32]. Rh/AC showed some activity under basic conditions but deactivated rapidly [80]. Ru/Al_2O_3 and Ru/Hydrotalcite **(**HT) demonstrated high activity for secondary alcohol oxidation but were inactive for glycerol oxidation [26, 81-83].

Transition metals have been explored as active phases or promoters for glycerol oxidation. Ni, Zn, Cu, and Co supported on MgAl, CeO_2, ZrO_2, and Ce-Zn oxide (CZ) were active under alkaline conditions, yielding up to 69% GCA (Cu/MgAl), though no DHA was formed [84-86]. In the gas phase at 350°C, Fe supported on alumina-free MFI zeolite achieved a DHA yield of 71% [87].

However, iron catalysts were inactive in liquid-phase oxidation at mild temperatures due to strong Fe–O bonds and inflexible lattice oxygens [88].

Beyond the scope of this thesis, DHA-selective oxidation has been studied using transition metal catalysts with H_2O_2 [89, 90] and metal-free catalysts with stronger oxidants [91-93]. Additionally, metallic catalysts incorporating N- and P-containing compounds have been investigated [44, 94-98].

Given the complexity of glycerol oxidation and catalyst deactivation, research continues to optimise catalyst formulations. This chapter focuses on metal-catalysed glycerol aerobic oxidation using Pt and Au catalysts, which are the most promising. Pd- and Ag-based catalysts have not demonstrated comparable DHA selectivity, and reviews on alcohol and glycerol oxidation over Ag-containing catalysts are available elsewhere [99, 100].

For consistency, catalyst notation follows the format: the base metal (typically noble) appears first, followed by promoters. Metal loadings (wt.%) refer to the total catalyst weight but are omitted for clarity. The support is listed after the active phase, separated by a slash (e.g., Pt/AC). Hyphens distinguish separate metal components (e.g., Pt-Bi), while direct alloys are written without a hyphen (e.g., AuPt).

DHA yield is prioritised alongside glycerol conversion, DHA selectivity, and reaction time when available. However, direct comparisons are challenging due to variations in performance parameter calculations [6, 20, 33, 86, 101-105], including equations (1) and (2) for glycerol conversion (X_{GLY}), and equations (3) to (5) for product selectivity (S_{prod}), where $n_{i,t}$ is amount of species at a given time t (t=0 for initial conditions), and $No.Carbon_{prod}$ is the number of carbons in each product species. When X_{GLY} and S_{prod} were detailed, DHA yields were recalculated by $Y_{prod,t} = \frac{X_{GLY,t} \times S_{prod,t}}{100}$.

$$X_{GLY}(t) = \frac{n_{GLY,0} - n_{GLY,t}}{n_{GLY,0}} \quad (1)$$

$$X_{GLY}(t) = \frac{\sum(n_{prod,t} \times No.Carbon_{prod})}{3\, n_{GLY,0}} \quad (2)$$

$$S_{prod}(t) = \frac{n_{prod,t}}{n_{GLY,0} - n_{GLY,t}} \quad (3)$$

$$S_{prod}(t) = \frac{n_{prod,t}}{\sum n_{prod,t}} \quad (4)$$

$$S_{prod}(t) = \frac{n_{prod,t} \times No.Carbon_{prod}}{\sum(n_{prod,t} \times No.Carbon_{prod})} \quad (5)$$

2.3.1. Platinum-based Catalysts

The selective oxidation of glycerol into DHA using Pt-based catalysts has been extensively studied under acid/base-free conditions. In basic media, glyceraldehyde and glyceric acid formation are favoured, DHA stability is compromised, and Pt may leach, leading to catalyst deactivation [4, 28, 32].

Pt surface structure strongly influences product distribution. Pt nano-cubes with Pt(100) facets have higher catalytic activity and stability for glycerol oxidation than Pt nano-tetrahedrons with Pt(111) facets [106]. However, Pt(100) preferentially oxidises the primary hydroxyl group, yielding glyceraldehyde (red pathway in Figure 2.5), while Pt(111) enables oxidation of both primary and secondary hydroxyl groups (blue pathway in Figure 2.5), and these properties hold in the presence of Pt promoters such as Bi [74].

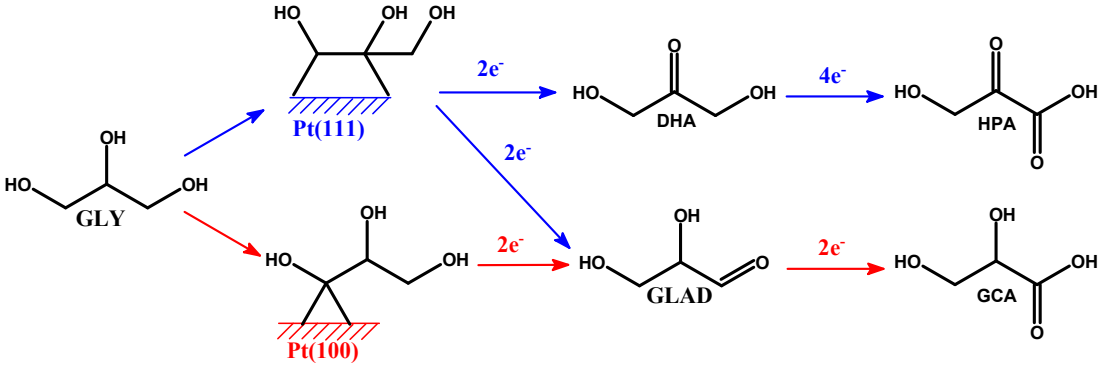

Figure 2.5. Pt (111) and (100) surface structures in glycerol oxidation in acidic media.

Density functional theory (DFT) calculations of glycerol oxidation pathways on a Pt(111) surface indicate that transition state energies for C-C bond cleavage at early reaction stages are significantly higher than for O-H or C-H scission, resulting in slow C-C bond cleavage [107]. Over time, dehydrogenated intermediates accumulate, lowering these transition state energies and increasing C_2 and C_1 product formation. These theoretical insights align with experimental findings [47, 108].

Among various platinum promoters (Bi, Te, Pb, Sb, and Se), Pt-Bi and Pt-Sb exhibit the best performance for glycerol oxidation [32]. Doping Pt with transition metals slightly improves catalytic activity, though DHA selectivity remains low (≈ 10%) [43, 109]. The main results of glycerol aerobic oxidation into DHA using Pt-based catalysts are summarised in Table 2.2.

Table 2.2. Literature review of DHA production using Pt-Bi and Pt-Sb catalysts (Pt-Bi/AC in the first part).

Catalyst	T °C	PO_2 bar	C_{GLY0} M	Rxn (h)	X_{GLY} (%)	S_{DHA} (%)	Y_{DHA} (%)	TOF[a]	Summary/Key Findings	Work et al. [Ref]
Pt5-Bi1/AC	50	1	1	4	24	80	19	n.a.	First work in the field. Acidic conditions favoured DHA production.	Kimura[32]
Pt7.4-Bi2.9/AC	60	1	1	n.a.	75	49	37	52	Optimised pH, load, and preparation. Y_{DHA}=31% with a commercial Pt5-Bi5/AC	Garcia[28]
Pt9-Bi5/AC	55	1	1	6/8	82	40	33	n.a.	Optimised metal load (Au, Pt, Bi) and preparation/activation methods.	Yanli[110]
Pt5-Bi5.4/AC	120	1	2	n.a.	59	51	30	519	Studied Bi load at fixed Pt (5 wt.%) and the impact of initial pH and GLY/Pt ratio.	Brandner[48]
Pt3-Bi0.6/AC	80	2.4	1	2	80	60	48	372	Optimised T, $P(O_2)$, pH, catalyst preparation, metal load, and AC pore size.	Hu[34]
Pt5-Bi5/AC	30	1	1	6	92	49	45	n.a.	Studied the Bi load effect on catalyst properties and performance.	Liang[111]
Pt5-Bi1/AC	80	3	0	3	80	35	28	914	Commercial catalyst. Bi leach and performance decreased after five runs.	Villa[38]
Pt4Sb3/MWCNT	60	1	1	/	90	51	46	878	PtSb outperformed Pt and Pt-Bi, benefiting from the PtSb metallic alloy, while Pt and Bi were segregated. The PtSb catalyst was stable during recycling tests.	Nie[33]
Pt5Bi4/MWCNT	60	1	1	/	80	36	32	501		
Pt4.6-Sb1/NCNT*	60	1	1	6	46	43	20	84 [b]	Compared preloaded vs. in-situ PtSb and Pt-Bi/NCNT catalysts. Higher initial rates for preloaded Pt-Bi/NCNT. Studied catalyst deactivation via leaching and product adsorption. *in-situ prepared.	Ning[33]
Pt5-Bi5/NCNT*	60	1	1	6	29	64	19	65 [b]		
Pt5-Bi5/NCNT	60	1	1	6	30	56	17	107 [b]		
Pt3-Bi0.6/MCM41	75	2.4	1	4	83	65	54	260	MCM-41 crystalline microporous-free structure was preferable. Bi_2O-Pt was identified as the active site. Proposed reaction mechanisms. Doping Bi into the support reduced Pt-Bi site formation.	Xiao[23]
Pt3-Bi0.6/AC	75	2.4	1	2.4	77	61	47	316		
Pt3-Bi0.6/ZSM5	75	2.4	1	3.6	80	41	33	209		
Pt7-(CZB)16/SBA16	30	1	0	4	90	84	76	n.a.	Pt and Bi-doped ceria (CZB) loaded into mesoporous silica. CZ improved oxygen storage, and Bi shifted selectivity to DHA.	Choi[112]
Pt7-Sb4/CNT	60	1	1	2	69	75	52	n.a.	DFT studies clarified Sb' s role. Larger SbOx-Pt/CNT particles had higher activity and DHA selectivity.	Duan[113]
Pt5-Bi7/HT	70	1	1	6	25	81	20	n.a.	Optimised Bi load and reaction conditions. Proposed a hydrogen bonding mechanism between chloride anions from the HT and GLY' s terminal -OH.	Xue[104]

2.3.1.1. Bi as a Pt promoter

Doping Pt with π-electron donating metals like Bi and Sb shifts selectivity from glycerol's primary to secondary hydroxyl group oxidation [28, 29, 68]. Glycerol oxidation with Pt-Bi preferentially produces DHA, while Pt alone favours GLAD, which oxidises into glyceric acid and potentially poisons active sites, reducing DHA yield [114]. A schematic comparison of glycerol oxidation over Pt/AC and Pt-Bi/AC is presented in Figure 2.6.

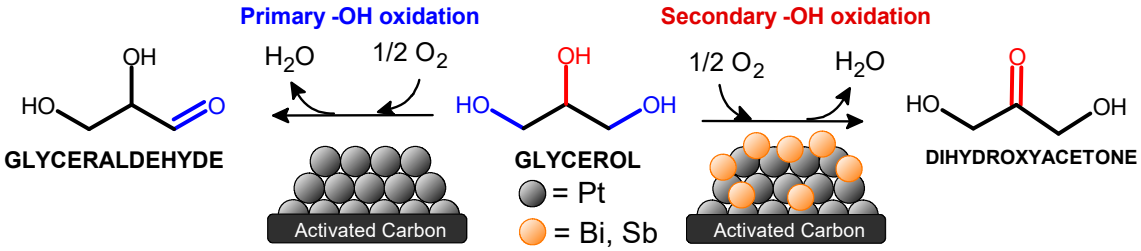

Figure 2.6. Glycerol oxidation scheme: Pt/AC selective to GLAD; Pt-Bi/AC selective to DHA.

Kimura et al. [32] were the first to demonstrate that Bi incorporation significantly enhanced DHA selectivity, increasing it from 10% to 80% when doping Pt5/C with 1 wt.% Bi. This improvement is attributed to geometric effects rather than electronic modifications, as Bi selectively blocks primary hydroxyl oxidation while favouring secondary hydroxyl oxidation via a chelation effect, forming surface complexes between glycerol, surface Pt atom, and a neighbouring positively charged Bi adatom [26, 32, 96]. Additionally, Bi mitigates catalyst deactivation by binding with carboxylic acids, preventing their adsorption and subsequent reaction on Pt sites [111, 115].

The optimal Bi surface coverage on Pt(111) corresponds to a ($\sqrt{3} \times \sqrt{3}$) R30° structure at 0.33 monolayer, as Bi preferentially occupies high-energy step sites on Pt(111) before spreading to terrace sites [32]. Upon reduction, Bi is predominantly metallic, though its oxidation state during reaction varies with catalyst preparation and conditions, existing as oxides [32, 34], carbonates [33, 48, 111], metahydroxides [96], oxychlorides [104], or metallic Bi [96]. Recent DFT studies suggest that Bi_2O is thermodynamically favoured rather than Bi_2O_3 at mild oxygen pressures, forming Bi_2O-Pt(111) active sites [23]. Bi oxides strongly chemisorb O_2 dissociatively, with Bi effectively adsorbing oxygen via π-electron donation [116]. While Pt remains metallic [32, 48], minor amounts of PtO_2 may coexist [34], but no Pt-Bi alloy formation was detected [96, 111].

Catalyst Optimisation

Pt-Bi/AC is one of the most well-studied catalysts. Optimisation studies have focused on metal load, preparation and activation methods, type of AC and reaction conditions (temperature, O_2 pressure, and pH) to maximise DHA yield using Pt-Bi/AC catalysts. Optimised metal loads are presented in the first part of Table 2.2.

Commercial Pt-Bi catalysts were tested for benchmarking against self-prepared catalysts, with moderate DHA yields, reaching 30% (X_{GLY} = 40%, S_{DHA} = 75%) with a commercial Pt5-Bi5/AC catalyst (source unspecified) and 28% (X_{GLY} = 80%, S_{DHA} = 35%, 6 h) with a Johnson Matthey Pt5-Bi1/AC catalyst [28, 38].

Preparation methods, including ion exchange [28], sequential impregnation [28, 34, 110], co-impregnation [28, 34, 48, 110], and activation methods [28, 34, 110], significantly influence catalytic performance. The comparison between different studies is not straightforward, though some general trends can be identified graphically in Figure 2.7.

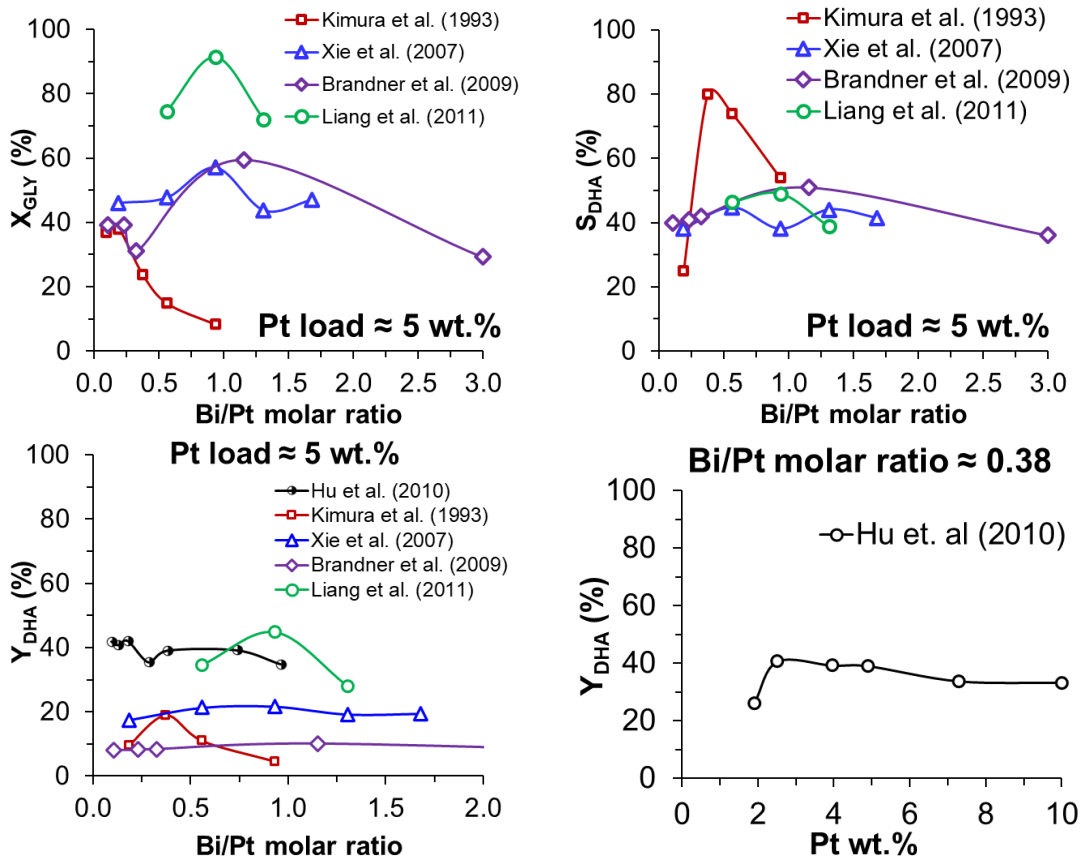

Figure 2.7. Effect of Bi loading on glycerol oxidation with Pt5–Bi/AC under base-free conditions: a) glycerol conversion, b) DHA selectivity, c) DHA yield. d) Effect of Pt loading at Bi/Pt molar ratio ≈ 0.38.

Key trends include:

- **Particle Size**: Small Pt nanoparticles enhance performance, though excessively small particles (≤ 2 nm) may lower DHA yield [34].
- **Bi/Pt Ratio**: The optimal ratio varies (0.2–1.2) [32, 34, 48, 110, 111] and generally influences glycerol conversion more than DHA selectivity (Figure 2.7). Excessive Bi load (Bi/Pt > 1) forms Bi particles that increase metal particle size, limit Bi-Pt interactions, and block active sites, reducing activity [111].

- **Reaction Conditions**: Highly acidic environments enhance DHA production [28, 34]. Good performances are achieved at moderate temperatures of ≈ 80-90 °C [34, 104] and low oxygen pressure of ≈ 2.5 bar [34], with good results also under atmospheric pressure [32, 48, 110, 111].

The highest DHA yield of 48% was achieved with a 2.5 wt.% Pt loading (2-10 wt.%, Figure 2.7 d) at a low Bi/Pt ratio of ≈0.38 [34].

Platinum dispersion is influenced by the nature of the catalyst support, with mesoporous materials typically promoting higher metal dispersion due to their increased surface area and accessible pore network. Additionally, low bismuth loadings have been reported to enhance platinum dispersion, likely by preventing the formation of large Pt–Bi aggregates and preserving the active surface area [23, 32, 48, 111]. Recent advances in the development of Pt–Bi catalysts include:

- **MCM-41**: Pt3-Bi0.6/MCM-41 achieved the highest DHA yield of 54%, outperforming Pt3-Bi0.6/AC (45%) and Pt3-Bi0.6/ZSM-5 (28%), due to its mesoporous structure without micropores, unlike ZSM-5, and its crystalline framework, unlike amorphous AC [23].
- **Carbon Nanotubes (CNT)**: Pt-Bi/CNT showed DHA yields of 32% (multi-walled CNT) and 17% (N-doped CNT), with in situ Bi^{3+} adsorption outperforming preloaded Pt-Bi/NCNT [33, 96].
- **SBA-16 mesoporous silica:** Doping Pt with a CeO_2-ZrO_2-Bi_2O_3 promoter resulted in an exceptional DHA yield of 76% (Pt7-CZB16/SBA-16) at 30 °C and atmospheric pressure [112]. CeO_2-ZrO_2-Bi_2O_3-SnO_2 as a promoter was less effective (Y_{DHA} =54%) [117].
- **Hydrotalcite** (HT): Pt-Bi supported on double-layered magnesium aluminium hydroxycarbonate (Pt5-Bi7/HT) yielded 28% DHA and showed stable performance. Bi-O-Cl is formed, with chlorine from the support strongly binding to glycerol's hydroxyl group via hydrogen bonds, unlike carbon-supported catalysts. For higher Bi loadings, DHA selectivity decreased while glycerol conversion remained largely unaffected, similar to Pt-Bi/AC catalysts [104].

2.3.1.2. Sb as a Pt promoter

While Pt-Bi catalysts enhance DHA selectivity, achieving high conversion and selectivity remains challenging. Antimony (Sb), similar to Bi in electronic properties, enhances alcohol oxidation activity [68] and offers a cost-effective alternative, as Sb oxides and metal are cheaper than Bi counterparts [108, 118, 119].

PtSb/MWCNT outperformed Pt-Bi/MWCNT, achieving higher DHA yield (46% vs. 32%) at 90% glycerol conversion with stable performance over five reactions [33]. Structural analysis

confirmed that Sb incorporates homogeneously into Pt, forming a PtSb alloy [33], unlike Bi, which remains oxidised [23, 32, 48, 111].

Pt3.8-Bi5/NCNT and Pt4.6-Sb1/NCNT showed a similar DHA yield of 20%, with Pt-Bi being more selective to DHA, while Pt-Sb exhibited higher activity [96]. Pt6.5-Sb3.9/CNT catalyst, optimised for metal loading (Pt: 2–8 wt.%, Sb: 1.2–4.8 wt.%), achieved a DHA yield of 52% [113], closely matching the best Pt-Bi catalyst (Pt3-Bi0.6/MCM-41, 54% [23]) but with higher selectivity and shorter reaction times [113]. Like Pt-Bi/CNT, Pt remained metallic, while Sb was present as an oxide [113]. DFT and X-ray Photoelectron Spectroscopy studies suggested that Sb promotes DHA selectivity via geometric effects, enabling both primary and secondary hydroxyl adsorption on Pt(111)-SbOx surfaces, improving catalytic performance [113]. Although Pt-Sb catalysts demonstrated promising performance, they are not commercially available.

2.3.2. Gold Catalysts

The deactivation issues associated with Pt- and Pd-based catalysts motivated the search for more stable alternatives for alcohol aerobic oxidation. Prati and co-workers [120] first demonstrated the potential of catalysts with gold nanoparticles for alcohol oxidation, including diols. Inspired by this, Hutchings group [39] conducted a systematic study of glycerol oxidation under basic conditions, using Au nanoparticles (0.25-1 wt.%) supported on activated carbon (AC) and graphite. These catalysts were highly active and fully selective to glyceric acid. Notably, Au-based catalysts exhibited greater resistance to oxygen poisoning than Pt and Pd-based catalysts, enabling operation at higher oxygen pressures and achieving superior catalytic performance [39].

Glycerol Oxidation Under Basic Conditions

Initially, adding a strong base (e.g., NaOH) was considered mandatory to initiate glycerol oxidation via dehydrogenation of glycerol's hydroxyl groups, but this favoured the oxidation of the primary hydroxyl group, leading to GLAD and its overoxidation products, with no DHA production [27, 37, 39, 47, 86, 121-124]. High NaOH/GLY molar ratios (> 4) further promoted GCA oxidation to TTA [37]. Au nanoparticles supported on metal oxides (Fe, Ti, Ce, Mg, V, Nb, Ta, Al) [37, 46, 79, 124-128] and carbon materials (graphite, carbon nanofibers, carbon nanospheres, carbon black) [27, 46, 125] failed to produce DHA. Unexpectedly, DHA formation was reported in three studies using Au/C, Au/CeO_2 [27, 46] and Au/TiO_2 catalysts [124], though the underlying mechanisms were not fully elucidated.

Glycerol oxidation under base-free conditions

Since DHA is unstable in basic media, base-free conditions are required for its selective production. In 2010, Prati and co-workers [79] pioneered Au-catalysed glycerol oxidation under

base-free conditions, showing that Au nanoparticles (1 wt.%) supported on materials with different isoelectric points exhibited increasing glycerol conversion in the order: AC (3%) < H-mordenite (5%) < $MgAl_2O_4$ (6%) < TiO_2 (8%), highlighting the role of the support. While no DHA was produced, Au/H-mordenite achieved the highest GCA selectivity (70%) and the lowest C1 selectivity (5%), attributed to its superior ability to decompose H_2O_2, a reaction byproduct that promotes C–C bond cleavage [79]. Following these findings, studies explored additional supports and doping Au with other metals [128-132].

Au nanoparticles supported on metal oxides (Al_2O_3, TiO_2, NiO, ZrO_2, MgO, SiO_2) were unsuitable for DHA production [128, 129]. Au/SiO_2 prepared by a one-pot aerosol-assisted SOL method (Au nanoparticles ≈3 nm) and thermally-oxidative activated under static air (550 °C, 6 h) achieved a DHA yield of 18% under harsher conditions (140 °C, 30 bar air) [133].

A milestone study by Liu et al. [128] was the first to report Au-catalysed glycerol selective oxidation to DHA under base-free conditions with high yields. A systematic investigation of metal oxide supports (Al_2O_3, TiO_2, ZrO_2, NiO, CuO) identified Au_2/CuO as the most active and selective catalyst. These catalysts required activation via oxidative thermal treatment (200–300 °C in airflow). After optimizing reaction conditions (30–100 °C, 5–20 bar O_2, pH 4–7, 1–10 h reaction time, GLY/Au = 10–100), a maximum DHA yield of 80% (X_{GLY} = 98%, S_{DHA} = 82%) was achieved at 50 °C, 20 bar O_2, and 4 h [128]. To the best of our knowledge, this remains the highest reported DHA yield for glycerol aerobic oxidation in a batch process.

Expanding on these findings, Meng et al. [129] investigated the influence of metal oxide supports (Au1/MOx, M = Zn, Cu, Ti, Si, Mg, Al) using both theoretical and experimental approaches. ZnO and CuO exhibited superior oxygen activation due to their ability to stretch the O–O bond. Under conditions similar to those used by Liu et al. [128], Au1/ZnO and Au1/CuO exhibited DHA selectivity of 85% (X_{GLY} = 24%) and 83% (X_{GLY} = 22%), respectively. Au/ZnO maintained DHA selectivity over two reuse cycles, though glycerol conversion declined from 26% to 20% [129].

Further advances were made by Pan et al. [105], who studied Au1.5/ZnO catalysts, focusing on preparation and activation methods. Au–O–Zn active site and oxygen vacancies on ZnO were identified as key factors for high catalytic activity and DHA selectivity. Kinetic studies and a reaction mechanism were proposed [105]. The best performance (Y_{DHA} of 51%, X_{GLY} of 86%, S_{DHA} of 60%, 5 h) was achieved with an $Au_{1.5}$/ZnO catalyst prepared via deposition-precipitation (DP) method and thermally activated under an oxidative atmosphere. Catalyst reuse led to a conversion drop (82% to 60%) due to zinc oxalate formation, disrupting the Au/ZnO interface. Performance was partially restored via oxidative thermal treatment [105].

A schematic representation of glycerol oxidation over Au catalysts is shown in Figure 2.8. When supported on carbon materials and operated under basic conditions (NaOH), Au nanoparticles predominantly yield GLAD (blue pathway). In contrast, Au/ZnO catalysts promote DHA formation under base-free conditions (red pathway). Au/ZnO requires thermal activation in an oxidative atmosphere to induce ZnO species migration onto the Au surface, generating oxygen vacancies that enhance catalytic performance.

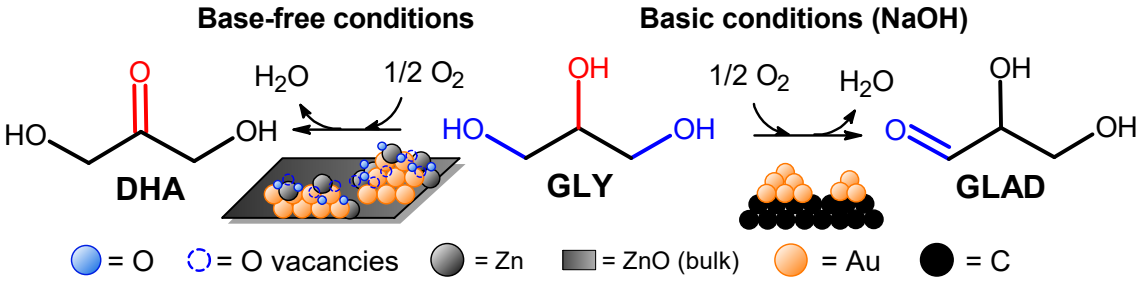

Figure 2.8. Glycerol oxidation schemes: Au/AC (basic conditions) selective to GLAD; oxidative thermal activated Au/ZnO (base-free conditions) selective to DHA.

Mixed-Oxide Supports

Among various DP-prepared catalysts (activated at 200 °C in air for 5 h), Au-supported metal oxides, Au2.5/MOx (M = Zn, Cu, Al, Fe, Ni) [134] and Au1.5/CuO-Al_2O_3 [135], were evaluated for glycerol oxidation. Au/CuO–Al_2O_3 exhibited the highest DHA yield of 75% (X_{GLY} = 77%, S_{DHA} = 97%, Cu/Al = 5:1, 10 bar O_2, 80 °C), closely followed by Au/CuO (Y_{DHA} = 74%, X_{GLY} = 89%, S_{DHA} = 83%, 80 °C, 10 bar O_2) and Au/ZnO (74%, 83%). Au/NiO (20%, 81%) showed moderate activity, while the remaining catalysts were nearly inactive. The superior performance of these catalysts was attributed to their small Au particle size (≈2 nm), which enhanced secondary C–H bond cleavage and metal-support interactions, improving lattice oxygen reducibility and increasing oxygen mobility. Mechanistic studies suggested that glycerol oxidation proceeds via metal alkoxide formation, β-H elimination at Au sites, and subsequent oxidation via lattice oxygens. However, stability tests revealed severe deactivation of Au/CuO–Al_2O_3, Au/ZnO, and Au/CuO over three cycles (rinsed with water between runs) due to Au particle growth and byproduct adsorption, with Cu–Al leaching further contributing to deactivation in the former case [134, 135].

Further work on CuO–ZrO mixed oxides as supports yielded an Au2/$Cu_{0.9}Zr_{0.1}$ catalyst with high DHA selectivity (95%) and a 70% DHA yield (50 °C, 2 bar O_2, 4 h) [136]. Cu-rich supports promoted smaller Au particles (≈2.1 nm) and an optimal number of basic sites, resulting in a glycerol conversion 18 times higher than Au/ZrO_2 and 2.5 times higher than Au/CuO. Under optimised conditions (GLY/Au = 50, 60 °C, 3 bar O_2, 8 h), the DHA yield reached 80%, similar to results obtained with Au/CuO [128]. The catalyst exhibited stable DHA selectivity over four cycles, though glycerol conversion declined due to product adsorption [136]. Extending this work

to mineral-derived CuO-ZnO supports, the rosasite-derived catalyst achieved a 70% DHA yield with remarkable stability over five cycles, outperforming its aurichalcite-derived counterpart (20% DHA yield) [137].

Hydrotalcite-derived supports with varying compositions (Zn_2Fe-, Co_2Al-, Zn_2Al-, Zn_2Ga-, and Mg_2Al-), resulting in different surface basic densities and hydroxyl vacancies, were tested as support for Au nanoparticles. Au1/Zn_2Ga-HT exhibited the highest DHA selectivity (64%) at a glycerol conversion of 73%, attributed to strong metal-support interactions at Zn^{2+}-O-Au^{3+} active sites. Despite stable selectivity over five cycles, glycerol conversion declined due to metal leaching caused by acidic byproducts [138]. The main results obtained with Au catalysts for DHA production are summarised in Table 2.3. Notably, conflicting results have been reported for Au/TiO_2-catalysed glycerol oxidation under both basic and base-free conditions [37, 79, 124, 127-129].

Table 2.3. Literature review on glycerol oxidation to DHA with gold catalysts.

Catalyst	T °C	PO_2 bar	C_0 M	Rxn h	X_{GLY} %	S_{DHA} %	Y_{DHA} %	Summary/Key Findings	Author et al. (Year) [Ref]
Au1/AC*	60	1	1.5	2	50	26	13	Used basic conditions. AuPt/AC outperformed Au/AC. SOL-prepared and oxidative thermal activation were preferable.	Demirel (2005/07) [27, 46, 125]
Au1/CeO_2*	60	1	1.5	2	40	25	10		
Au0.8/C *, **	60	3	0.3	3	100	18	18	Smaller nanoparticles with SOL-prepared catalyst were preferable.	Rodrigues (2011) [80]
Au1/TiO_2 *	60	1	0.5	24	45	64	29	Studied the impact of crude glycerol impurities on catalytic performance.	Sullivan 2014 [124]
Au2/CuO	50	20	0.1	4	98	82	80	First high DHA yield with gold catalysts. CuO preferred over Ni, Zr, Ti, Al oxides	Liu (2014) [128]
Au1/ZnO	80	10	0.1	2	24	85	20	Stronger O_2 activation using ZnO and CuO oxides. Optimised operating conditions, nanoparticle size and ZnO type. Identified H_2O_2 as an intermediate species.	Meng (2018) [129]
Au1.5/ZnO	80	1	0.1	5	86	60	51	Compared basic vs. base-free conditions, SOL vs. DP preparation and thermal activation (inert, reductive, oxidative). Proposed Au-Zn-O as the active site.	Pan et al. (2019) [105]
Au1.5/ CuO–Al_2O_3	80	10	0.1	4	77	97	75	Stability tests revealed deactivation due to Au particle growth and Cu–Al leaching.	Ke et al. (2020) [135]
Au2.5/CuO	80	10	0.1	4	89	83	74	Au/CuO and Au/ZnO are preferred over Al, Fe, Ni oxides. Small Au particle (≈2 nm) enhanced metal-support interactions, improved lattice oxygen reducibility and oxygen mobility.	Ke et al. (2020) [134]

* NaOH presence. **Commercial catalyst.

2.3.3. Noble Polymetallic Catalysts

Bimetallic noble metal catalysts, particularly AuPt and AuPd, supported on activated carbon and metal oxides (TiO_2, ZnO, CZ), exhibit higher activity and stability than their monometallic counterparts due to synergistic interactions between the metals [27, 47, 126, 127, 139, 140]. In AuPt and AuPd catalysts, alloy formation enhances catalytic performance, while even segregated phases benefit from Au's stabilisation effect [47]. For example, in AuPt/TiO_2, Au prevents the oxidation of Pt nanoparticles, improving both activity and stability [127]. Despite their high activity, these catalysts primarily promote the formation of organic acids rather than DHA under basic conditions [47, 127, 141, 142].

DHA formation remains limited under base-free conditions. AuPt nanoparticles supported on basic (MgO, NiO) and acidic (SiO_2, ZrO_2, MCM-41, H-mordenite) materials exhibited moderate activity, achieving DHA selectivity of 12–23% at 30% glycerol conversion, though glyceric acid remained the dominant product. Selectivity trends correlated with the number of acid sites, where higher acid site densities reduced activity while promoting C3 selectivity [130]. Similar studies showed that Au improved Pt and Pd performance and stability using AuPd/AC[38], AuPt/H-mordenite[79], AuPt/MgO, and AuPd/MgO[131] catalysts. PtPd/TiO_2, AuPd/TiO_2 [132], and AgPd/AC [20] achieved very low DHA yields (<5%), while AuPdPt/TiO_2 achieved a DHA yield of 13% [132], indicating limited performance for DHA production.

Pd-based catalysts are generally less active than their Pt-based counterparts, with some Pd systems being nearly 20 times less active [28]. Nonetheless, PdAg/AC emerged as the most effective Pd-based catalyst for DHA production, achieving a DHA yield of 44% (X_{GLY} = 52%, S_{DHA} = 85%, 24 h). This performance was attributed to the formation of a uniform PdAg crystalline phase that suppressed overoxidation [78]. Although PdAg/AC maintained stable DHA selectivity over multiple cycles, its catalytic activity declined with reuse. Other Pd-based catalysts doped with Ti, Mn, Ni, Re, Ir, Au, or Bi also exhibited DHA selectivity but suffered from low glycerol conversion [78].

The addition of Bi to AuPt catalysts improved DHA selectivity without compromising stability. A $Pt_3Au_3Bi_6$/AC catalyst, optimised for Pt (2–7 wt.%), Au (0.75–8 wt.%), and Bi (1.6–22.4 wt.%), achieved a maximum DHA yield of 23% (X_{GLY} = 33%, S_{DHA} = 68%) [110]. Similarly, $Bi_{0.1}(AuPt)_1$/AC maintained high DHA selectivity across multiple cycles, whereas Pt-Bi/AC suffered from Bi leaching and deactivation [38]. Doping AuPd/AC with Bi slightly increased DHA yield (16%, X_{GLY} = 30%, S_{DHA} = 52%), but catalyst deactivation remained challenging [38].

The work with the Au/ZnO catalyst [105] was extended to AuPd supported on ZnO-CuO, ZnO, and CuO [143]. AuPd/ZnO-CuO showed superior performance, reaching a DHA yield of 65% (X_{GLY} ≈ 80%, 2 h), far outperforming AuPd/CuO (13%, 4 h) and AuPd/ZnO (36%, 4 h).

This was attributed to smaller AuPd alloy nanoparticles, higher surface defect concentrations, and increased cationic Au species. Pd^{2+} acted as an additive, promoting secondary hydroxyl oxidation while suppressing DHA overoxidation and improving selectivity. A Zn/Cu ratio of 1 was optimal, with Cu atoms disrupting the ZnO structure, increasing oxygen vacancies and providing additional glycerol oxidation sites. Strong metal-support interactions stabilised AuPd nanoparticles, ensuring sustained performance over multiple cycles [143].

A distinct approach involved Pd-Ce nanoparticles supported on a functionalized Fe-MIL-101-NH_2 metal-organic framework doped with a neocuproine ligand. This system achieved a DHA yield of 55% with good stability over three cycles, though it required a CH_3CN/H_2O solvent mixture [95].

While noble polymetallic catalysts enhance activity and stability in glycerol oxidation, their selectivity towards DHA remains limited. Bi or Ag promotion can improve DHA yields, yet challenges in stability and scalability persist. The most significant results obtained with polymetallic catalysts for glycerol oxidation are summarised in Table 2.4.

Table 2.4. Literature review on DHA production using bi- and trimetallic catalysts under base-free conditions. *pH = 12

Catalyst	T °C	PO_2 bar	C_0 M	Rxn h	X_{GLY} %	S_{DHA} %	Y_{DHA} %	Summary/Key Findings	[Ref] Year
Au0.8-Pt0.2/AC*	60	1	1.5	1	50	36	18	Optimised Au/Pt for 1 wt.% total metal load.	[27] 2007
Pt3-Au3-Bi6/AC	55	1	0.5	6/8	33	68	23	Optimised metal load, preparation and activation methods.	[110] 2007
Pd2-Ag2/AC	80	3	0.6	24	52	85	44	Highest DHA yield with Pd catalysts. PdAg/metal-oxides have higher DHA selectivity but lower activity.	[20, 78] 2012/13
Au0.3-Pd0.2-Pt0.5/TiO_2	100	3	0.3	4	37	35	13	Tested basic conditions. Tested GCA, GCO, and TTA inhibition effect	[132] 2014
Bi0.1-(AuPt)1/AC	80	3	0.3	3	80	63	50	Doping AuPt with 0.1 wt.% Bi increased S_{DHA} from 4% to 63% and it is preferable to 1 wt.% Bi load and a commercial Pt-Bi/AC. Bi-AuPd/AC deactivated prematurely.	[38] 2015
Bi0.1-(AuPd)1/AC	80	3	0.3	-	30	52	16		

2.4. Reaction Mechanisms and Oxidation Kinetics

2.4.1. Alcohol Oxidation Mechanisms and Kinetics

Developing a reliable kinetic model for glycerol oxidation requires understanding the underlying reaction mechanisms. The oxidation of alcohols over platinum-group metal catalysts has been extensively studied, but the exact reaction pathways remain a topic of ongoing discussion. Comprehensive studies by Mallat and Baiker [26], further expanded by Schouten and co-workers [144], have proposed several mechanistic models for alcohol oxidation. These models provide a valuable framework for understanding the fundamental pathways and oxygen's role in glycerol oxidation. However, the complexity increases significantly for glycerol oxidation due to its three hydroxyl groups and the subsequent oxidation of its products.

The main mechanistic models proposed in the literature can be classified as follows:

Sequential dehydrogenation

In this pathway, alcohol oxidation proceeds via a two-step dehydrogenation mechanism. Initially, the alcohol adsorbs onto the metal surface, where the O–H bond cleavage forms an alkoxide intermediate. This step is followed by the β-C–H bond cleavage, often considered the rate-determining step (RDS), resulting in the formation of a carbonyl compound and the release of hydrogen atoms [26].

The presence of a base is often favourable for this mechanism as it facilitates deprotonation and enhances the formation of the alkoxide intermediate. Oxygen, or hydroxyl species in alkaline media, primarily oxidises hydrogen instead of directly participating in alcohol oxidation. Other hydrogen acceptors, such as olefins, can sometimes replace oxygen, indicating that oxygen's primary role is the removal of hydrogen rather than direct involvement in the RDS [26].

Sequential dehydrogenation with Oxidative Surface Cleaning

This model builds upon the sequential dehydrogenation mechanism but introduces a distinct role for oxygen in catalyst maintenance. Here, oxygen does not participate directly in the oxidation of the alcohol or its hydrogen coproduct. Instead, it prevents catalyst deactivation by blocking the adsorption or removing strongly adsorbed reaction byproducts, particularly carboxylic acids, which would otherwise poison the metal surface. By regenerating active sites, oxygen enhances the overall reaction rate. The acceleration of the reaction in the presence of oxygen is attributed to the oxidative removal of these adsorbed species rather than oxygen's involvement in the RDS [26].

This model is compatible with the effect of promoters (e.g., Bi or Sb), which may block a fraction of Pt active sites, preventing the formation of poisoning intermediate species. This "ensemble effect" suggests that larger active site ensembles are necessary for side reactions (e.g., C−C bond cleavage), while smaller ensembles are sufficient for alcohol dehydrogenation [26].

Reaction Between Oxidising Species and the Reactant

The reaction between adsorbed oxidising species and the adsorbed reactant or its partially dehydrogenated intermediate constitutes the RDS. This model follows a Langmuir–Hinshelwood-type kinetic behaviour, where oxygen surface coverage significantly influences the reaction rate. Oxygen or hydroxyl species adsorbed on the promoter atoms (e.g., Bi or Sb) may participate directly in the oxidation reaction [26].

Schouten and co-workers [144] proposed a mechanism involving hydride transfer from the alcohol to a free metallic site, simultaneous with the reduction of a surface hydroxyl (or oxygen) group (Figure 2.9). In this model, the formation of ketones or aldehydes occurs in a single step through simultaneous deprotonation and hydride transfer. The reaction rate increases at higher pH and with a higher catalyst potential, which favours electron-deficient metallic sites. Following the RDS, desorption of H^+ and OH^- from the surface and electron transfer through the metal occurs rapidly.

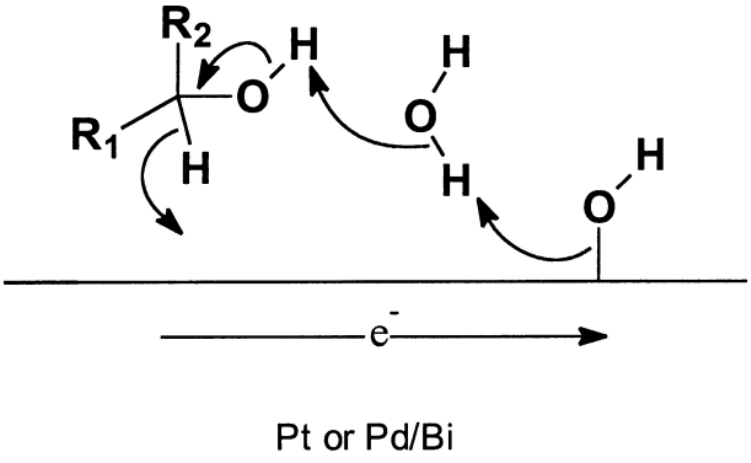

Figure 2.9. Alcohol oxidation mechanism over Pt or Pd-Bi catalysts: hydride transfer from the alcohol to a free metallic site, electron transfer through the catalyst, and surface OH reduction (H^+ migration via hydrogen bond shift). Reprinted from [144].

Kinetic Rate Expressions for Alcohol Oxidation

Alcohol dehydrogenation rates are commonly described by dual-site reaction models based on the Langmuir–Hinshelwood–Hougen–Watson (LHHW) formalism [144]. A commonly applied expression is:

$$r_{dehyd} = k\,\theta_{alcohol}\,\theta_O$$

where r_{dehyd} is the alcohol dehydrogenation rate, k is the reaction kinetic constant, $\theta_{alcohol}$ and θ_O represents the surface coverage by alcohol and oxygen species, respectively.

In some cases, the availability of free metallic sites is crucial, and a more accurate description of the data includes the fraction of surface vacant sites fraction θ_v:

$$r_{dehyd} = k\,\theta_{alcohol}\,\theta_O\,\theta_v$$

While not an actual three-site model, this expression accounts for the need for a free site for the reaction to proceed [144]. The surface composition of the catalyst is determined by the equilibrium adsorption of the alcohol and the products, a balance between dissociative oxygen adsorption and alcohol dehydrogenation, and the degree of over-oxidation.

For example, the latter model effectively described the oxidation of methyl-glucopyranoside over Pt/graphite. This model also accounted for catalyst deactivation and subsequent reactivation, as the catalyst activity was restored by temporarily stopping the oxygen flow, allowing the alcohol to reduce the surface species [144].

Similarly, the selective oxidation of ethanol to acetaldehyde and further products (e.g., acetic acid and ethyl acetate) over Au/TiO_2 was well described by an LHHW-type model, assuming that hydrogen abstraction by surface hydroxyl species is the RDS and that oxygen adsorption was dissociative [145].

In another study, the oxidation of 2-octanol to 2-octanone over a Pt–Bi/AC catalyst was successfully modelled using LHHW kinetics. The reaction rate was highest at the lowest ketone adsorption coefficient, corresponding to an optimal solvent composition of 16–18% dioxane in heptane. This solvent combination prevented excessive ketone adsorption, thus maintaining active sites and restoring catalytic activity [146].

These kinetic models and mechanisms offer valuable insights for developing glycerol oxidation kinetics, essential for optimising reaction conditions, designing efficient catalysts, and enhancing overall process performance. Glycerol oxidation kinetics are mainly described using the Langmuir–Hinshelwood–Hougen–Watson (LHHW) methodology. Experimental data collected under various operating conditions underwent verification to rule out mass transfer limitations, ensuring that the reaction proceeds within the kinetic regime [105, 114, 147, 148].

The resulting kinetic data provide a deeper understanding of catalyst efficiency, reaction pathways, and underlying mechanisms.

2.4.2. Glycerol Oxidation Kinetics - Basic Conditions

Kinetic studies of glycerol oxidation under basic conditions showed that Au catalysts exhibited lower activation energy than Pt-based catalysts for glycerol oxidation into GCA, but none provided detailed insights into DHA formation due to its minimal yield [149-151].

Demirel et al. [147] conducted the first systematic kinetic study using Au/AC under basic conditions, applying a Langmuir–Hinshelwood mechanism incorporating species and NaOH concentrations. Significant adsorption of GLY, GCA, and TTA was observed, while DHA and GLAD interconversion remained negligible. OXA formation proceeded predominantly through GCO oxidation rather than TTA oxidation, consistent with findings from Au/graphite catalysts [149].

Following this work, other studies were performed. A study on Au/Al_2O_3 introduced two types of active sites on the LHHW model: the Au metal surface and the support surface. Water's strong affinity for the support influenced the formation of reactive oxygen species, impacting oxidation behaviour [152]. Another study proposed a dual mechanism model, combining a Langmuir–Hinshelwood model for the catalysed reaction, with surface reaction as the RDS, and a power-law model for the non-catalysed reaction. Without a catalyst, C–C cleavage prevailed, forming glycolic and formic acids, whereas Au/Al_2O_3 promoted GCA and subsequent TTA and OXA formation. Organic acids had the highest adsorption constants since the carboxylic group interacts with the catalyst surface by chelation [150].

Further insights into the reaction mechanism were obtained using in-situ Raman spectroscopy of unsupported Au nanoparticles. It was observed that glycerolate anions (deprotonated glycerol) did not adsorb directly on the Au surface but instead underwent a reaction before returning as carboxylates. Glycerate surface species rapidly formed in the presence of O_2, supporting an Eley−Rideal mechanism with adsorbed O_2. In the absence of O_2, neither glycerol nor glycerolate adsorbed directly on the catalyst surface. High alkalinity activated glycerol through deprotonation, while negatively charged Au nanoparticles weakened the O_2 bond, further promoting the oxidation reaction [153].

Pt group catalysts demonstrated similar trends. Glycerol oxidation using Pt-Pd-Bi/AC, described by LHHW kinetics, selectively produced GCA with a low activation energy of 39 kJ/mol [154]. For Pd/AC, strong product and reactant adsorption led to catalyst inhibition [155].

A comparative kinetic analysis using a power-law model was performed on Ag/Al_2O_3, Pt/Al_2O_3, and Au/Al_2O_3 catalysts. This study included a deactivation term described by a simple power-law equation with time and temperature (Arrhenius-type) dependence. Pt and Au catalysts exhibited higher rate constants, particularly for GCA formation, with smaller metal particles leading to increased reaction rates. While Pt catalysts showed significant deactivation, Au and Ag demonstrated greater resistance [151].

2.4.3. Glycerol Oxidation Kinetics - Base-free Conditions

Under base-free conditions, glycerol oxidation follows a distinct pathway. For monometallic Pt/CNT catalysts, LHHW kinetics combined with solvent effect measurements, DFT calculations, and kinetic isotopic analyses suggested that water-assisted O_2 dissociation forms active OH* intermediates in equilibrium, rather than serving as the RDS. OH*-assisted C-H bond cleavage of glycerol was identified as the likely RDS, favouring GLAD formation, as expected for monometallic Pt catalysts [156].

Pt/CNT with different Pt sizes and metal load showed similar reaction orders for GLY and O_2 as well as activation energy for the productions of either GLAD/GCA or DHA, so the data was fitted by a Michaelis–Menten kinetic model. Sb addition enhanced DHA selectivity by forming interfacial Pt–SbO sites along with partial Sb incorporation into Pt lattice, inhibited primary hydroxyl activation, evidenced by a negative GLY reaction order of -0.8 for GLAD formation and a positive reaction order of 0.5 for DHA production [157].

2.4.3.1. Pt-Bi Catalysts

Worz et al. [114] studied the kinetics and selective deactivation of Pt-Bi/AC catalysts by applying a dual-site (Pt and Pt-Bi) kinetic model and considering four species (GLY, DHA, GLAD, and GCA). The dual-site model effectively described concentration profiles, while the single-site model failed to describe DHA formation. Catalyst deactivation was attributed to strong GCA adsorption on Pt-Bi sites, leading to site blocking. Experimental data confirmed that the initial glycerol reaction rate decreased by approximately 50% upon GCA addition. At higher glycerol concentrations (5 M), deviations from model predictions were noted, likely due to the unaccounted adsorption of other organic acids [114].

To extend Worz et al.'s findings [114], which considered only three steps and low glycerol conversion data (X_{GLY} < 30%), Hu et al. [148] conducted a microkinetic study considering additional intermediates (HPA, TTA, GCO, OXA, and CO_2). A single-site kinetic model was used, assuming that each oxidation reaction required two vacant sites. The glycerol oxidation network was decomposed into five progressively larger sub-networks with different intermediates

as initial reactants for proper parameter estimation. Strong adsorption of intermediates was identified as the primary cause of catalyst inhibition, corroborating previous results [114], but identifying TTA (GCA oxidation product) strong adsorption as responsible for catalyst inhibition. While a comprehensive network provided deeper mechanistic insights, a simplified four-step kinetic model accurately predicted GLY, DHA, and GCA concentrations, making it preferable for reactor modelling and process optimisation in terms of DHA production [148].

The mechanism of glycerol oxidation selective to DHA over Pt-Bi/AC catalysts was elucidated using DFT calculations [23]. Under oxidative conditions, Bi oxidised preferentially over Pt, forming Bi_2O clusters that promoted glycerol's secondary hydroxyl oxidation. The Bi_2O-Pt(111) active site, formed through O_2 dissociative adsorption, facilitated glycerol adsorption in a favourable spatial orientation for secondary hydroxyl group oxidation, lowering the activation energy. The most favourable pathway involved simultaneous dehydrogenation of the middle C-H and O-H under Bi_2O and Pt cooperation, rather than sequential dehydrogenation, while water formation occurred over Bi sites rather than Pt sites. Terminal hydroxyl group oxidation to produce GLAD was thermodynamically less favourable over the Pt-Bi active sites [23]. A catalytic cycle was proposed for the metallic Bi_2-Pt active site (Figure 2.10): 1) O_2 dissociative adsorption on Bi (Bi_2O-Pt), 2) GLY adsorption on the Bi_2O-Pt interface (Bi_2O-Pt + GLY*), 3) GLY simultaneous dehydrogenation (Bi_2OH + PtH + DHA*), 4) DHA desorption (Bi_2OH + PtH), and 5) H_2O formation and desorption (Bi_2-Pt) [23].

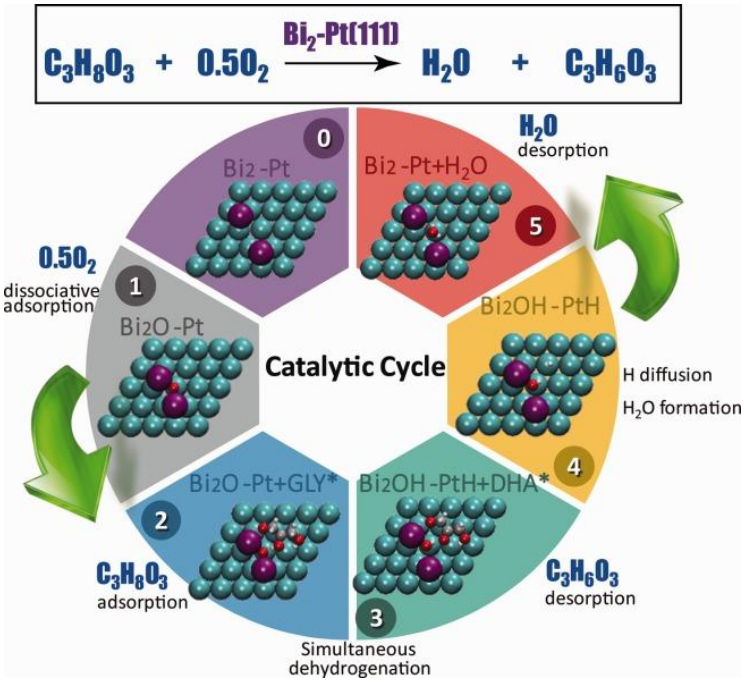

Figure 2.10. Proposed reaction mechanism for glycerol oxidation to DHA over Pt-Bi/AC under base-free conditions. Reprinted from [23].

2.4.3.2. Gold-Based Catalysts

Oxygen vacancy defects on the support played a critical role in Au/ZnO catalysts [105]. In-situ FTIR and isotope studies showed that O_2 formed OOH* species in the presence of water, while glycerol's secondary C–H abstraction at the Au/ZnO interface was the RDS. Without oxygen vacancy defects, glycerol oxidation did not proceed under base-free conditions. A detailed reaction rate law was proposed based on nine elementary steps (Figure 2.11): 1) O_2 dissociative chemisorption on Au, forming O*; 2) and 3) H_2O reaction with 2O*, producing peroxide (OOH*) and hydroxyl (OH*) species; 4) dissociative chemisorption of -OH on the oxygen vacancy defects, forming H* and alcoholate R_2CHO* species; 5) H abstraction from R_2CHO* by OOH*, yielding R_2CO* and H_2O_2*; 6) H* reaction with OH*, yielding H_2O* and (7-9) product desorption [105]. A similar mechanism was proposed for PtAu/LDH catalysts, where O_2 adsorption on negatively charged Pt atoms resulted in electron transfer to the O-O π* antibonding orbital. Glycerol dehydrogenation was facilitated by the basic LDH support, forming water and aldehydes, which readily oxidise [31, 158].

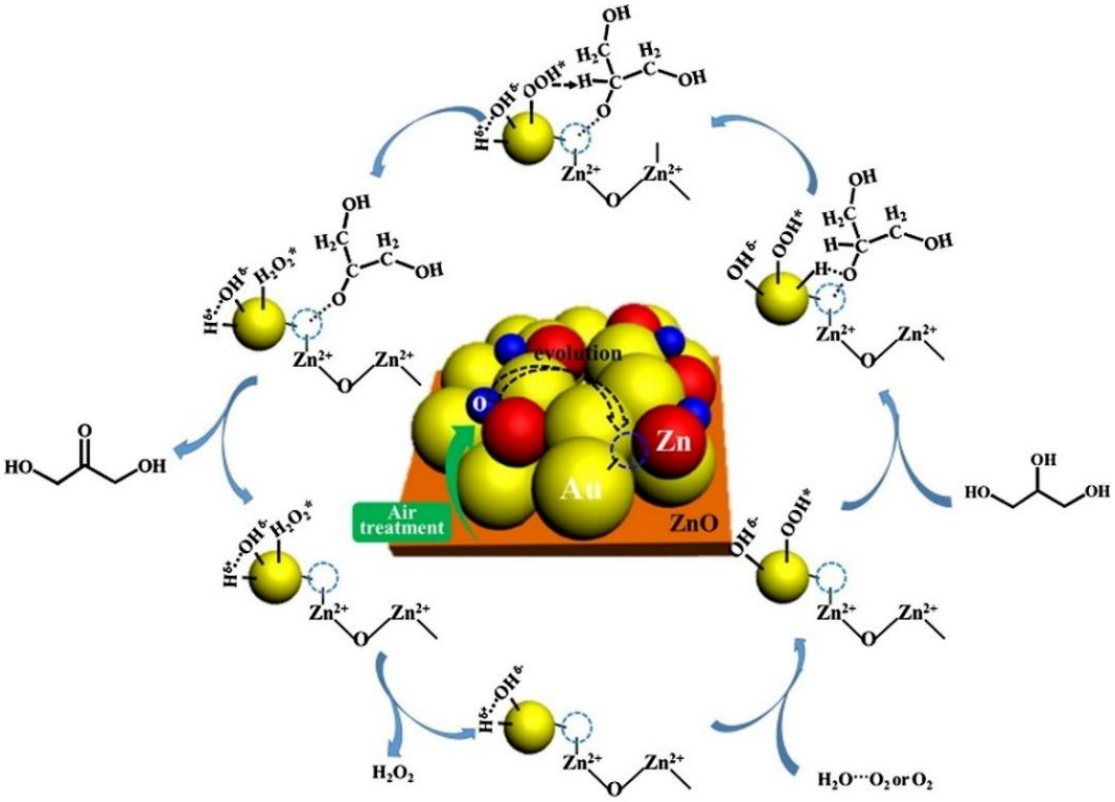

Figure 2.11. Proposed reaction mechanism for glycerol oxidation to DHA over oxidative thermal activated Au/ZnO under base-free conditions. Reprinted from [105].

Meng et al. [129] suggested a non-dissociative O_2 adsorption mechanism: 1) O_2 adsorption on Au with O-O bond activation, yielding Au/ZnO-O_2*, which 2) abstracts an H^+ from glycerol's central or terminal C-H bond, yielding OOH*; 3) OOH* abstracts an H^+ from the respective OH group, producing H_2O_2* and DHA* or GLAD* 4) products desorption. The O-O bond was

stretched like a superoxo-like (O_2-) state ion, considered a critical step in Au-catalysed alcohol aerobic oxidation [31, 129, 158], activated by electron donation into the O_2 π* antibonding orbital from Au nanoparticles negatively charged by the support and to a minor extent by water. Au/ZnO and Au/TiO_2 catalysts exhibit nearly zeroth O_2 reaction orders at different oxygen pressures, supporting an Eley-Rideal kinetic model rather than a Langmuir-Hinshelwood mechanism, which would result in a fast reaction rate drop. The Eley-Rideal model was consistent with DFT calculations, where glycerol reacted with Au/ZnO-O_2* rather than adsorbed on the Au surface. The lower H_2O_2 concentration observed during Au/ZnO catalysis indicated rapid peroxide decomposition under reaction conditions. Increasing glycerol concentration from 0.01 M to 0.1 M enhanced oxidation rate [129].

2.4.4. Summary

The activation energies (E_A) for glycerol oxidation into DHA using different catalysts are summarised in Table 2.5. Despite varying experimental operating conditions, kinetic models, and parameter determination methods, the activation energies (E_A) for glycerol oxidation into DHA using different catalysts remained comparable in the 50-70 kJ mol^{-1} range. The considerable number of estimated parameters introduced discrepancies, particularly in adsorption enthalpy estimations [114, 147, 148].

Table 2.5. Literature data of kinetic and adsorption parameters for GLY oxidation into DHA using LHHW-based models.

Catalyst	$E_{A,GLY}$ kJ mol^{-1}	$k_{0,GLY}$ min^{-1}	$\Delta H_{ads,GLY}$ kJ mol^{-1}	K_{GLY} M^{-1}	$\Delta H_{ads,DHA}$ kJ mol^{-1}	K_{DHA} M^{-1}	Ref.
Au1/AC	47	3.1×10^{-2}	/	/	/	2.4×10^{-2}	[147]
Au/ZnO	63-75	/	/	/	/	/	[159]
Pt5-Bi5/AC	53	6.0×10^{5} mol L^{-1} s^{-1}	-17	2.6×10^{-4}	/	6.8×10^{-3}	[114]
Pt3-Bi0.6/AC	58	1.9×10^{11}	-158	2.7×10^{-27}	-121	9.7×10^{-18}	[148]

2.5. Catalyst Properties and Reaction Performance

Catalyst properties, including metal particle size, dispersion, preparation and activation methods, and support characteristics, significantly influence catalytic activity, stability, and product selectivity. In glycerol oxidation, optimising these parameters is essential for improving catalytic efficiency and selectivity toward DHA. This Section examines the impact of particle size, support, and preparation methods on the performance of Pt-group and Au-based catalysts.

2.5.1. Particle Size

Metal particle size plays a crucial role in aerobic glycerol oxidation, affecting both catalytic activity and product distribution. Smaller particles generally exhibit higher activity due to an increased surface-to-volume ratio, improving glycerol access to active sites [149]. However, nanoparticles below 2 nm tend to deactivate rapidly due to strong oxygen affinity [29]. Studies indicate that for Pt and Au catalysts, the optimal particle size for high activity typically ranges from 2 to 6 nm [4, 27, 36, 111, 160, 161], highlighting the structure-sensitive nature of glycerol oxidation [46, 149]. A narrow particle size distribution further enhances metal dispersion and catalytic performance [77], though prolonged reactions can lead to particle growth and activity loss [96, 132].

2.5.1.1. Pt and Pd-based Catalysts

Both metal particle size and support porosity influence reaction selectivity for Pt catalysts. Highly microporous supports (e.g., activated carbon) can confine nanoparticles, restricting glycerol access, whereas micropore-free supports allow a more accurate assessment of particle size effects [45, 162]. Under basic conditions, Pt/AC catalysts with smaller nanoparticles (≈2.0–2.5 nm) exhibited higher glycerol conversion than larger particles (≈8 nm), though its influence on selectivity was unclear. For Pd/AC, an increase in particle size from <2 nm to 9.2 nm enhanced catalytic activity, whereas further growth to 14.5 nm led to significant deactivation [36, 163].

Under base-free conditions, Pt nanoparticles on carbon supports generally followed a volcano-shaped trend in activity concerning particle size (ranging from 1.2 nm to 26.5 nm), with an optimal diameter of approximately ≈2.5–3 nm [45, 161, 162]. Particles below 2 nm favoured DHA selectivity, though it remained low (monometallic Pt is glyceraldehyde selective [45, 161, 162]). On carbon nanotube (CNT) supports, smaller Pt particles stabilised glyceraldehyde, while larger ones promoted further oxidation to glyceric acid [45]. Figure 2.12 illustrates the effect of monometallic Pt particle size on glycerol conversion and DHA selectivity.

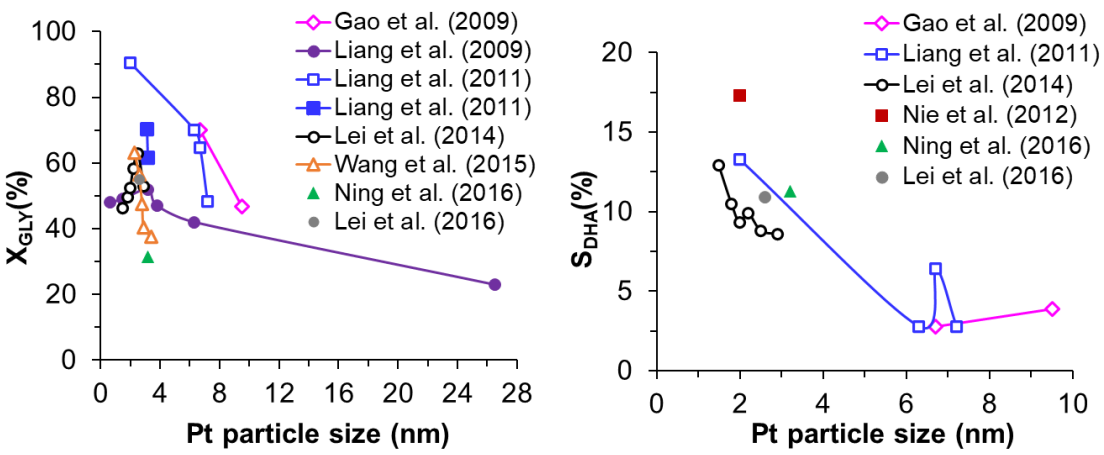

Figure 2.12. Influence of Pt nanoparticle size under base-free conditions. Left: glycerol conversion at 6 h, except [44, 113, 163]; Right: S_{DHA} at $X_{GLY} \approx 50\%$ (6 h).

Increasing the promoter/Pt ratio generally results in larger metal particles. When the ratio exceeds one, the promoter may encapsulate Pt particles, blocking active sites and reducing both glycerol conversion and DHA selectivity [104, 111]. This effect is particularly pronounced in Pt-Sb and Pt-Bi catalysts, where an optimal particle size of 3.1–3.8 nm corresponds to maximum performance. Excess promoter loading leads to severe encapsulation and performance decline [104, 111, 113].

2.5.1.2. Au-based Catalysts

Early studies on Au catalysts focused on alkaline conditions, with limited data on nanoparticle size effects in base-free media. Under alkaline conditions, Au nanoparticles on carbon supports exhibited strong size-dependent effects. Particles >50 nm were inactive, while ≈20 nm particles showed low activity but high selectivity toward glyceric acid. In contrast, smaller Au particles (≈2–6 nm) increased activity nearly tenfold due to higher metallic surface area and edge site concentration [39, 40, 108, 149, 164]. This trend was confirmed by multiple studies [4, 27, 36, 46, 139, 160, 165]. Small nanoparticles may undergo size modifications and re-dispersion during the glycerol oxidation reaction, affecting performance [149]. Reducing Au loading led to smaller nanoparticles, increasing glycerol conversion and adsorption while decreasing water desorption over the catalyst surface [166, 167].

For DHA production under base-free conditions, the most effective Au catalysts had particle sizes between 2 and 4 nm [128, 129]. Increasing Au nanoparticle size from 2.5 nm to 6.3 nm on Au/ZnO improved DHA selectivity from 82% to 92%, though at the expense of lower glycerol conversion [129]. This aligns with trends observed for glyceric acid-selective catalysts, where smaller Au particles enhance conversion, but larger ones stabilise selective oxidation pathways.

Overall, glycerol oxidation over Au catalysts follows a trend of increasing activity with decreasing particle size (see Figure 2.13). However, some studies suggest an optimal Au size of ≈3–7 nm under basic conditions [27, 46, 69].

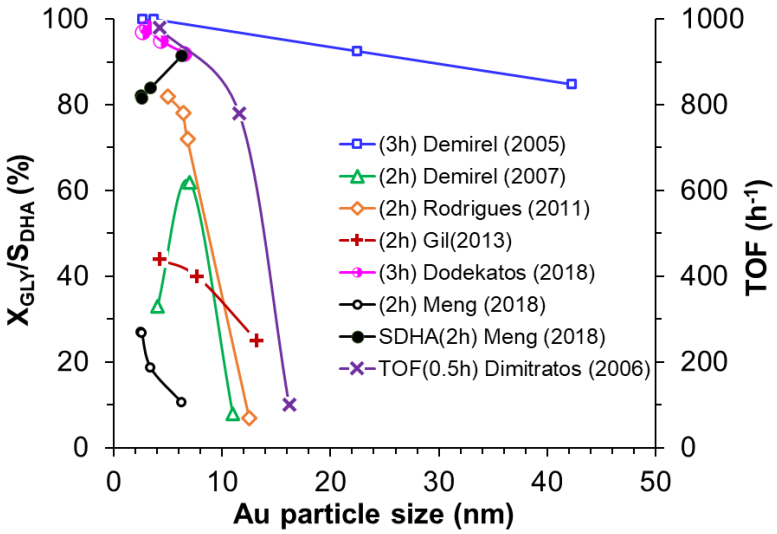

Figure 2.13. Effect of Au particle size in glycerol oxidation: basic [27, 46, 69, 101, 149] and base-free conditions [129]. TOF values (right axis) shown for purple crosses [36].

2.5.2. Support

The catalyst support provides a stable platform for metal nanoparticles and ensures that the catalyst is heterogeneous. Beyond that, the acidity, surface area, porosity, metal dispersion, crystallinity, and support-metal interactions impact catalytic activity and selectivity. Strong metal-support interactions can modify reaction pathways, making support selection essential for optimising glycerol oxidation catalysts [139, 149]. Generally, larger pores mitigate mass transfer limitations and enhance C3 selectivity [24].

Various support materials have been explored, including carbon-based materials [28, 32-35, 37, 39, 40, 43-46, 78, 80, 96, 98, 102, 108, 113, 114, 121, 125, 139, 149, 162, 168-176], hydrotalcite [41, 42, 84, 85, 104, 158, 177], zeolites, mesoporous silicas and mesoporous materials [23, 79, 87, 103, 112, 130, 177-181], metal oxides [20, 37, 46, 86, 87, 100, 105, 122, 125, 127-132, 140, 141, 177, 182-185], metal-organic frameworks [95], and ion exchange resins [186].

Carbon-Based Supports

Carbon materials, particularly activated carbon (AC), are widely studied due to their chemical stability and ease of metal recovery via combustion [28, 34, 37, 80, 102, 108, 125, 176]. The first

DHA formation by glycerol oxidation was reported using Pt/AC [32], and commercial catalysts were tested, such as Pt-Bi/AC [28, 38] and Pd-Pt-Bi/AC [154].

For Pt/AC catalysts, reducing AC particle size from 253 μm to 9 μm (keeping constant the surface area and the porous size distribution) improved glycerol conversion and GCA selectivity but decreased DHA selectivity, likely due to improved accessibility of Pt nanoparticles [176]. Reducing the microporosity of the Au/AC support enhanced glycerol conversion and GCA selectivity, though DHA selectivity slightly decreased [27, 33, 34, 37, 111]. Au catalysts on macroporous AC (34 nm pore diameter) achieved four times higher glycerol conversion than those on mesoporous AC (6 nm pore diameter), highlighting the role of porosity in catalyst performance [37]. Nonetheless, Au supported in black carbon and AC with similar micropore fractions (≈60%) showed different performances, with the former being less active but more selective to DHA [27].

Carbon support morphology also influences performance: Au supported on carbon nanospheres outperformed graphene and carbon nanofibers due to the smallest (4.2 nm) and better dispersed Au nanoparticles and curved surfaces enhancing reactive edge sites [149]. Modified carbon supports, such as nitrogen-doped materials, enhance metal dispersion, reduce particle size, and improve catalytic stability while potentially introducing new active sites [96, 98, 139, 174, 175]. CNT and multi-walled CNT (microporous free) have been tested for Pt, Pt-Sb, Pt-Bi, and Au [33, 45, 113, 121, 173], facilitating metal accessibility, improving conversion compared to AC-based catalysts [173].

For Pt-Bi/AC catalysts, larger AC pore sizes (4 nm vs. 1.6 nm) improved DHA yield (39% vs. 22%) by reducing diffusion resistance [34]. Comparing Pt-Bi/AC with mesoporous silica (MCM-41) and zeolite (ZSM-5) supports, Pt-Bi/MCM-41 achieved the highest DHA yield due to its ordered mesoporous structure, high surface area, and superior Pt dispersion, which minimised mass transfer limitations. In contrast, Pt-Bi/ZSM-5 suffered from micropore-induced diffusion constraints, leading to DHA overoxidation. Preloading Bi into the MCM-41 framework hindered the formation of active Pt-Bi sites, reducing DHA selectivity [23].

Metal Oxide Supports

Au nanoparticles supported on metal oxides generally exhibited lower activity than those on carbon supports for glycerol oxidation under basic conditions [37, 46, 125]. TiO_2, AC, and Nb_2O_5 were the most effective supports, with sol-immobilised prepared catalysts showing better dispersion and activity than those prepared via deposition-precipitation [37].

Metal oxides, such as CeO_2, ZrO_2, and CZ, are widely studied for their oxygen storage and redox properties, with an established role in alcohol oxidation in both gas [187] and liquid phases [125, 188]. They became oxygen-deficient due to lattice oxygen loss by thermal activation under

an oxidative atmosphere, enhancing catalytic activity [112]. Glycerol oxidation with Au-Ru/CZ [122], Au-Pd/CZ [140], and Au-Cu/CZ [86] (basic conditions) and Ag-Pt/CeO_2 [100] and Au-Pt/CeO_2 [123] (base-free conditions) led to high glycerol conversion but lacked DHA selectivity. Pd-Ag/CeO_2 and Pd-Ag/ZrO_2 exhibited high DHA selectivity but low activity, whereas Pd-Ag/AC proved more efficient [20].

For glycerol oxidation under base-free conditions, AuPt nanoparticles supported on acidic supports (H-mordenite, SiO_2, MCM-41, sulphated ZrO_2) favoured C3 selectivity (>95% at 30% X_{GLY}). In contrast, basic supports (MgO, NiO) were more active but promoted C-C cleavage [130]. The concentration of acid sites, rather than their type, was determinant in the activity and selectivity [130]. DHA was not produced [177].

Incorporating Bi_2O_3 into the CZ lattice (CZB) improved oxygen mobility by creating oxide ion vacancies via the substitution of Ce^{4+} and Zr^{4+} by the larger and low-valent Bi^{3+}, activating the support for low-temperature oxidation [112, 189]. This modification shifted selectivity toward DHA, with Pt7-CZB16/SBA-16 achieving a remarkable 76% DHA yield under base-free conditions [112]. Preloading Bi into the CZ lattice improved DHA selectivity over in situ loading [112]. Bi remained stable, unlike the dynamic leaching observed in Pt-Bi/NCNT [96].

Thermally activated Au/CuO and Au/ZnO (200–300°C in airflow) exhibited high DHA selectivity (≈84%) at moderate glycerol conversion (22–24%) due to their ability to activate molecular oxygen [130]. DFT calculations confirmed that ZnO and CuO facilitated oxidation by donating electrons to Au [129]. The preparation method of the ZnO support influenced catalyst performance. ZnO synthesised via a hydrothermal method using urea (ZnO-U) had fewer oxygen vacancies than ZnO prepared by precipitation with sodium carbonate (ZnO-C). Lower oxygen-vacancy concentrations in ZnO-U increased its work function, enhancing electron transfer and strengthening the Au/ZnO interface. As a result, Au/ZnO-U exhibited superior catalytic performance, achieving a higher DHA yield (56% vs. 50%) and a turnover frequency (TOF) 1.5 times greater than Au/ZnO-C. This improvement was attributed to the abundance of positively charged Au sites, which promoted OH* surface coverage and facilitated H abstraction from glycerol's O–H bond [159]. Other metal oxides (Al_2O_3, TiO_2, NiO, ZrO_2, MgO, SiO_2) remained unsuitable for DHA production [128, 129].

Other Supports

Layered double hydroxides, metal-organic frameworks, and zeolites have also been explored as catalyst supports. Pd-Ce supported on Fe-MIL-101-N=CHNeocuproine achieved a DHA yield of 55% [95]. Pt-Bi/HT showed good DHA selectivity [104]. Layered double hydroxides offer tuneable framework compositions and interlayer anions that influence catalytic performance, potentially eliminating the need for strong base addition [4, 31, 41, 42, 79, 84, 85, 104, 158, 190].

Zeolites, including HY, NaY, and ReY, have been tested for supporting Au, leading to complete glycerol oxidation under basic conditions with high selectivity for tartronic acid [179]. Pt nanoparticles supported on silicalite-1, Sn-MFI, and BEA zeolites showed limited activity in base-free conditions [178]. Pt-Bi/ZSM-5 produced DHA, but diffusion constraints resulted in lower performance than AC and mesoporous MCM-41 [23].

An alternative approach involved supporting Pt nanoparticles on macroporous weak anion exchange resins, showing high activity, stability, recyclability and GCA selectivity for glycerol oxidation under basic conditions [186].

2.5.3. Preparation and Activation Methods

The preparation and activation of catalysts play a crucial role in glycerol oxidation, directly impacting activity and selectivity toward DHA production [24, 47]. Standard preparation methods include sol immobilisation (SOL), impregnation (IMP), and deposition-precipitation (DP), while alternative techniques such as ion exchange and in-situ adsorption have also been explored. Activation treatments typically involve thermal processes under oxidative, reductive, or inert atmospheres and liquid-phase reduction using chemical agents.

2.5.3.1. Pt and Pd-based Catalysts

Pt [28, 44, 45, 161, 173, 176, 191] and Pd [28, 78, 192] catalysts are typically prepared using the aforementioned methods, with reduction normally performed using CH_2O, KBH_4, $NaBH_4$, or H_2. For Pt/AC-IMP, pretreatment of the support (e.g., with H_2O_2 or HNO_3) and the reduction temperature and reducing agent concentration significantly influence Pt particle size, ranging from ≈1 to 27 nm [161].

Sequential impregnation is commonly used for bimetallic Pt and Pd catalysts, where the promoter (e.g., Bi or Sb) is introduced after the base metal to enhance metal-metal interactions [23, 28, 33, 34, 96, 104]. In Pt-Bi/AC catalysts, co-impregnation yielded a higher DHA yield (37%) compared to sequential ion exchange (30%) and sequential impregnation (28%) [28]. However, other studies found that sequential impregnation outperformed co-impregnation [34]. The order of metal loading also influences performance: when Bi was preloaded onto MCM-41 before Pt, DHA yield was reduced due to Bi incorporation into the support structure, which hindered the formation of active Pt-Bi sites [23, 34]. The choice of reducing agent also affects performance. Pt-Bi/AC reduction with $NaBH_4$ and KBH_4 resulted in higher DHA yield compared to CH_2O or H_2 reduction [34, 110]. For Pt-Bi/CNT, increasing the reduction time and temperature of the catalysts from 250 °C (2 h) to 600 °C (12 h) resulted in better ordered Pt-Bi, increasing

slightly activity and DHA selectivity but especially its stability for long-time operation in continuous flow reactors [193].

For Pt-Bi/NCNT, Bi exhibited dynamic leaching and readsorption during the reaction, affecting catalyst stability and selectivity. Regardless of whether Bi was introduced via sequential or co-reduction, ex-situ or in-situ impregnation, homogeneous Pt-Bi nanoparticles formed. However, in situ Bi impregnation using $Bi(NO_3)_3 \cdot 5H_2O$ led to higher DHA yield than $BiCl_3$ or Bi_2O_3, and in situ catalysts generally exhibited better DHA selectivity than preloaded ones, suggesting a more straightforward preparation method with advantages in Bi concentration control [96].

A different approach studied coating CNT with Bi_2O_3 to facilitate the formation of a uniform oxide layer. Pt/Bi_2O_3-CNT was prepared by two different immobilisation methods: via atomic layer deposition or via impregnation, and the former significantly outperformed in terms of catalytic activity and DHA yield (48% vs. 21%), attributed to the uniform Pt-Bi_2O_3 interface and the positively charged Pt species in the former [194].

2.5.3.2. Au-based Catalysts

Sol immobilisation (SOL), impregnation (IMP), and deposition-precipitation (DP) methods are widely used for preparing Au-based catalysts, with significant differences in performance depending on the method and operating conditions.

For glycerol oxidation under basic conditions with carbon-supported Au catalysts, SOL generally produces catalysts with superior performance compared to IMP or DP [27, 40, 101, 149]. SOL-prepared Au/AC catalysts activated with polyvinyl alcohol (PVA) and reduced with $NaBH_4$ or tetrahydroxymethyl phosphonium chloride (THPC) exhibit smaller nanoparticles (≈4–5 nm) and higher activity than those reduced with sodium citrate or prepared by impregnation or deposition-precipitation (Au nanoparticles >10 nm) [27, 40]. A similar trend was observed for Au catalysts supported on black pearl carbon, TiO_2, and CeO_2, where SOL with THPC reduction results in higher activity than DP with urea reduction [125]. THPC is both a mild reducing and stabilising agent, while $NaBH_4$ is a strong reducing agent [195]. THPC-reduced Au/AC showed superior catalytic activity compared to $NaBH_4$-reduced counterparts [27]. Additionally, SOL-prepared Au/AC and AuPd/AC catalysts reduced with $NaBH_4$ form very small nanoparticles (2–4 nm), exhibiting increased activity compared to those reduced with $N_2H_4 \cdot 2HCl$ [36]. For Au nanoparticles supported on Al_2O_3, MgO, and $MgAl_2O_4$, preparation via DP and SOL resulted in different nanoparticle sizes (SOL: 2.6–4.0 nm; DP: 4.8–5.9 nm). For glycerol oxidation under basic conditions, DP-prepared Au/Al_2O_3 and Au/$MgAl_2O_4$ exhibited higher turnover frequency (TOF) values than their SOL-prepared counterparts, except for Au/MgO-DP, which showed the reverse trend [196].

Bimetallic AuPd/AC-SOL was synthesised using a two-step reduction process: Au nanoparticles are immobilised and reduced with $NaBH_4$, followed by Pd immobilisation and reduction with H_2 to slow down the process and prevent metal segregation. The catalytic activity (TOF, mol mol_{Au}^{-1} h^{-1}) followed the order: alloyed $(AuPd)_1$/AC (6400) > segregated $(AuPd)_1$/AC (4800) >> Au_1/AC (1000) ≈ Pd_1/AC (900), demonstrating that alloyed catalysts significantly outperform both monometallic and segregated counterparts [197].

For base-free glycerol oxidation, Au/ZnO and Au/CuO catalysts prepared via DP-urea and thermally activated under airflow exhibited exceptional performance, whereas reductive (H_2) or inert (N_2) activation resulted in poor activity [105]. During oxidation, negligible sintering occurred, with Au/ZnO-DP catalyst nanoparticle size increasing slightly from 2.6 nm to 3.5 nm. Likewise, Au/ZnO-SOL catalysts were nearly inactive unless activated by oxidative thermal treatment [105]. Characterisation studies suggest that oxidative thermal treatment facilitates electron transfer from Au nanoparticles to the ZnO support, remodelling ZnO at the Au surface. Au cations may migrate into the ZnO lattice at the Au/ZnO interface, replacing Zn^{2+} and generating Au–O–Zn active centres with oxygen vacancy defects due to charge mismatch [105]. Thus, oxidative thermal treatment is crucial for maximising DHA yields in Au catalysts supported on metal oxides under base-free conditions.

2.6. Catalyst Stability

Noble metal catalysts may deactivate during glycerol oxidation due to overoxidation, poisoning, metal leaching, and sintering. The extent of deactivation depends on catalyst composition, promoters, support material, and reaction conditions. While Au catalysts generally resist overoxidation and leaching, they are prone to product adsorption. Pt and Pd catalysts, in contrast, require stabilisation strategies to maintain long-term performance.

The most common deactivation mechanism in glycerol oxidation is catalyst poisoning, caused by the strong adsorption of oxygen species or reaction products that block active sites, reducing catalytic activity. Overoxidation results from M–O or M–OH species formation, which shifts the reaction equilibrium toward excessive surface oxidation, particularly at low substrate concentrations. High oxygen pressures enhance reaction rates but also promote catalyst poisoning [24, 28, 29]. While Au catalysts remain stable even at 20 bar [128], Pt and Pd experience surface poisoning under elevated O_2 pressures ($P(O_2) \gtrsim 5$ bar), although typically remaining metallic during glycerol oxidation, making atmospheric or slightly pressurised air preferable [6, 99].

Reaction conditions influence poisoning severity. Under acidic conditions, undissociated organic acids such as GCA, TTA and HPA strongly adsorb onto active sites, exacerbating surface

overoxidation. In basic media, these acids may precipitate as salts, reducing adsorption; however, Pt and Pd may leach [4, 28, 32]. Crude glycerol pretreatment is usually required, as impurities, such as sulphur compounds and sugars, also contribute to catalyst deactivation [29, 68, 114, 115, 198].

2.6.1. Pt and Pt-Bi Catalysts

Maintaining small nanoparticles is crucial for catalytic activity, ensuring a large active surface area [161]. However, catalyst deactivation may occur due to metal leaching and structural changes, such as nanoparticle sintering, permanently reducing performance [29, 68, 114, 198]. For glycerol oxidation, Pt exhibits negligible leaching in acidic media but dissolves irreversibly under basic conditions [4, 6, 28, 41, 42, 47, 102, 119, 161, 175]. Pd-based catalysts show minimal leaching [108], though Pd-Ag/AC (good results for DHA production) activity loss may result from product adsorption [78]. Promoters, such as Au, enhance the stability of Pd and Pt catalysts, reducing overoxidation and leaching, while Bi, Sb, and Cu promoters are more prone to dissolution [26].

Pt-Bi Catalysts

Pt-Bi catalysts suffer from Bi leaching, though stability varies by support. Minimal Bi loss was observed for Pt-Bi/AC [28, 114] and Pt-Bi/HT [104], but a commercial Pt_5-Bi_1/AC catalyst lost 30% Bi after five cycles. Au incorporation improved stability. Notably, Bi-AuPt/AC showed significantly improved stability [38].

Product adsorption was identified as the main deactivation mechanism during base-free glycerol oxidation rather than overoxidation, sintering, or metal leaching [114]. Pt active sites are selective to GLAD, while Pt-Bi active sites are selective to DHA. GLAD readily oxidises to GCA and MOXA, which strongly adsorbs onto active sites, particularly Pt-Bi actives, decreasing DHA production [114]. Similar effects were observed in other studies [148, 175].

The catalytic effect does not arise from Bi^{3+} leaching, which should be avoided, as it complexes with reaction products [96, 114] or may be reduced by alcohols to inactive Bi^0 on the Pt surface, leading to deactivation [26]. Pre-load and in-situ load of Bi onto the Pt catalysts were studied. While Bi did not leach from the CeZr lattice in Pt_7-CeZrBi_{16}/SBA-16, resulting in higher DHA yields than in situ-prepared catalysts [112], for Pt-Bi/ NCNT and Pt-Sb/NCNT, similar results were reported, exhibiting a dynamic leaching/adsorption behaviour that maintained performance [96].

2.6.2. Gold Catalysts

Gold catalysts exhibit excellent resistance to leaching and overoxidation during alcohol oxidation [198]. During glycerol oxidation under basic conditions, they show negligible metal leaching [37, 101, 120, 149], although partial deactivation occurs, likely due to nanoparticle growth over multiple reaction cycles [101]. Au also enhances the stability of Pd and Pt catalysts by preventing leaching and extending catalyst lifespan [38, 79, 97, 123, 127, 130, 192]. For example, while Pd/AC suffered deactivation, Pd-Au/AC maintained stable performance [192].

Some Au-containing catalysts deactivate due to sintering or strong adsorption of reaction products. Au-Pd-Pt/TiO_2 became unstable after two base-free oxidation tests, showing significant particle growth and some metal leaching [132]. Introducing GCA, TTA, or GCO further reduced glycerol conversion, with adsorbed species persisting despite water rinsing [132]. Similarly, AuPt/H-mordenite deactivated at higher glycerol concentrations, likely due to product adsorption [79]. In contrast, AuPt/MCM-41 performance remained stable across multiple oxidation cycles without detectable metal loss [130].

A clear example of catalyst deactivation due to product adsorption on the surface was observed for an Au/ZnO-ZrO_2 catalyst in Figure 2.14. Thermogravimetric and mass-spectrometric analysis revealed minimal mass loss for the fresh catalyst (less than 2%), while the used catalyst exhibited a significant mass loss peak (≈16%) at ≈300 °C, associated with CO_2 formation. This result suggests that carbonaceous deposits or strongly adsorbed reaction products contributed to catalyst deactivation, which could be removed by thermal treatment.

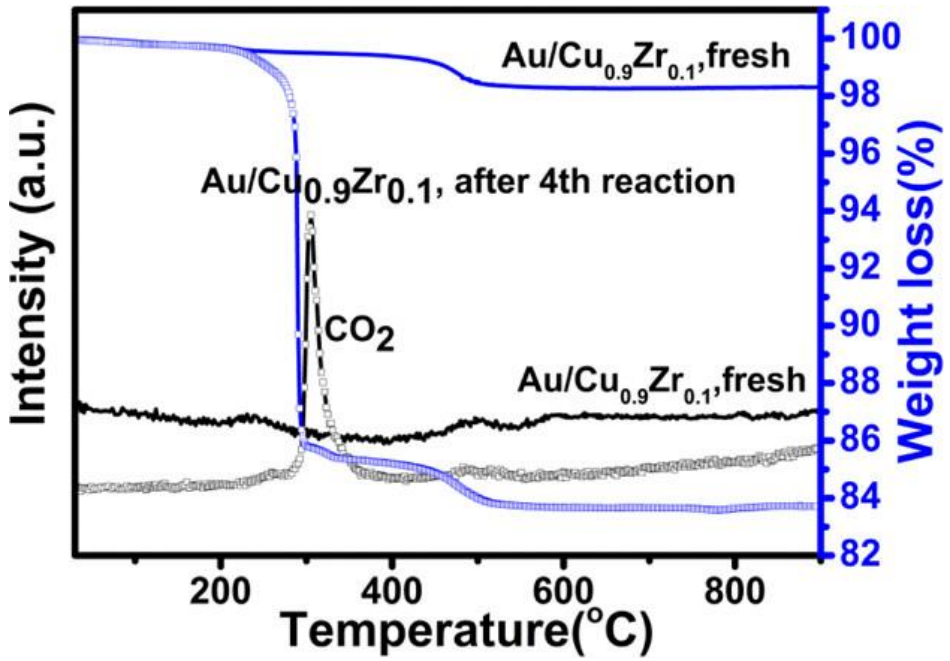

Figure 2.14. Thermogravimetric and mass-spectrometric profiles of fresh and spent Au/CuO-ZrO_2. Reprinted from [136].

2.6.3. Strategies for Enhancing Stability

Several approaches have been investigated to improve catalyst stability:

- **Promoted catalysts**: Bimetallic or promoted (e.g., Pt-Bi, Pd-Au) resist overoxidation and poisoning better than monometallic counterparts.
- **Gold doping**: Au prevents overoxidation and byproduct poisoning in Pt and Pd catalysts [38, 79, 131].
- **Controlled nanoparticle size**: Avoiding sub-2 nm nanoparticles reduces excessive oxygen affinity and deactivation [29].
- **Optimised oxygen pressure**: Lower O_2 pressures minimise surface oxidation, enhancing Pt and Pd longevity, while Au tolerates higher oxygen pressures. Monitoring electrochemical potential may help regulate oxygen supply and prevent catalyst overoxidation [24, 29].
- **Catalyst design**: Engineering catalysts to control mass transfer limitations, such as dispersing metal within porous extrudates, may reduce overoxidation, although it can also affect glycerol accessibility to active sites [24, 29].
- **Regeneration techniques**: Thermal treatments (200-300 °C) may effectively remove adsorbed intermediates and restore catalytic activity, as demonstrated for Au/ZnO [105] and Pt-Bi/NCNT [175]. Organic/alkaline washing has proven ineffective [175].

While Au catalysts generally exhibit superior stability, they remain vulnerable to byproduct adsorption. Pt and Pd catalysts require tailored stabilisation approaches, including controlled reaction conditions, promoter selection, and regeneration strategies, to maintain performance over multiple cycles.

2.7. Glycerol Oxidation - Operating Conditions

2.7.1. pH

The pH of the reaction medium significantly affects glycerol oxidation by influencing catalyst stability, activity, and product selectivity. Catalytic activity is clearly higher in alkaline media, where TOF values are often one to two orders of magnitude greater than in base-free conditions [28, 127]. Alkaline conditions promote glycerol oxidation, favouring organic acid formation [34], but present challenges for large-scale operations due to acid salt precipitation, while in acidic media, free carboxylic acids are obtained [79].

For Pt-based catalysts, different bases have been tested, with activity decreasing in the order NaOH ≫ CsOH > LiOH ≫ RbOH > $NaNO_3$ > KOH, with OH^- anions demonstrating higher catalytic efficiency than NO_3^- anions [108]. Basic conditions facilitate dehydrogenation at the C-H bond, considered the rate-determining step, but primary hydroxyl groups are preferentially oxidised over secondary ones, favouring glyceraldehyde over DHA formation [28, 32]. Furthermore, DHA is unstable under alkaline conditions and undergoes further conversion into glyceraldehyde and organic acids [40].

In contrast, acidic conditions favour DHA production and stability, enhancing selectivity [34]. While Pt-based catalysts can operate under both conditions, base-free systems are preferred to improve DHA selectivity and prevent catalyst deactivation due to metal leaching [4, 28, 32]. An optimal balance between reaction rate and selectivity is observed at neutral pH. For high DHA yields using Pt-Bi/AC, strongly acidic conditions (pH ≈2) are favourable, as depicted in Figure 2.15, naturally achieved due to the accumulation of organic acid byproducts [6, 28, 32].

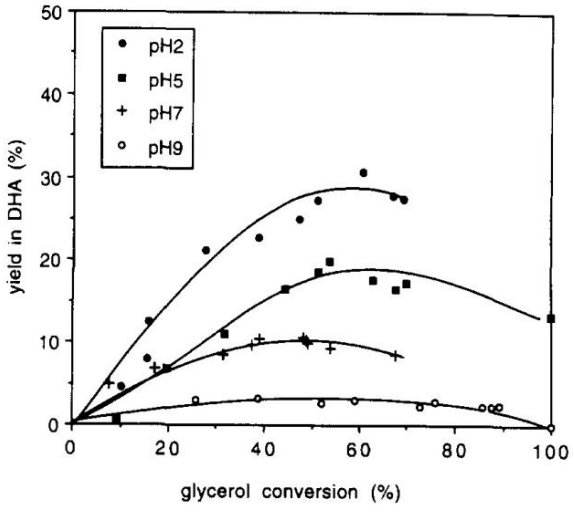

Figure 2.15. Influence of solution pH on DHA yield using a commercial Pt-Bi/AC catalyst. Reprinted from [28].

In contrast, glycerol oxidation with Au catalysts was believed to proceed only under strongly alkaline conditions, yielding GLAD and GCA as the main products with minimal DHA formation [27, 37, 39, 46, 47, 86, 121-125]. However, Villa et al. [79] demonstrated that Au nanoparticles supported on TiO_2, $MgAl_2O_4$, and H-mordenite can produce DHA formation under base-free conditions, though with very low activity. Higher DHA yields were later reported using Au nanoparticles supported on transition metal oxides such as CuO [128] and ZnO[105, 129] after thermal activation under oxidative conditions.

Bimetallic AuPt and AuPd catalysts are effective in GCA production under basic and base-free conditions, with the optimal Au/Pt ratio depending on the pH of the reaction medium. In the presence of NaOH, Au-rich catalysts exhibit higher initial activity, with Au_9Pt_1/TiO_2 achieving a TOF of 7389 mol molmetal^{-1} h^{-1}. Conversely, a higher Pt content improves activity under base-free conditions, as observed for Au_6Pt_4/TiO_2 (TOF = 301 mol molmetal^{-1} h^{-1}) [127].

2.7.2. Oxygen pressure

Oxygen pressure influences catalyst performance by increasing O_2 solubility in the liquid phase, potentially enhancing reaction rates. However, low oxygen pressures (atmospheric or slightly above) are preferred for Pt-based catalysts to prevent overoxidation. Under basic conditions, Pd/CNT performed best at 1 bar, while Pt/CNT exhibited optimal performance at 3 bar, consistent with Pd's greater susceptibility to overoxidation than Pt [43]. For base-free glycerol oxidation with Pt-Bi/AC, the optimal oxygen pressure was 2.4 bar within a tested range of 1–13.4 bar [34].

Gold nanoparticles are more resistant to overoxidation, allowing operation under higher oxygen pressures. For glycerol oxidation under basic conditions, increasing O_2 pressure from 3 to 10 bar did not affect the reaction rate, suggesting that the presence of a strong base dominated catalyst performance over oxygen pressure [46, 199]. For base-free oxidation with Au/CuO, DHA production peaked at 10–20 bar, though DHA selectivity slightly declined at higher pressures [128].

2.7.3. Temperature

The partial oxidation of glycerol to DHA and GLAD is exothermic, with estimated standard enthalpies of reaction at 25 °C of approximately - 139 kJ mol^{-1} to - 175 kJ mol^{-1}, respectively, computed from the standard enthalpy of formation of glycerol, water, glyceraldehyde [200], and dihydroxyacetone [201].

While increasing temperature reduces O_2 solubility in the liquid phase, it generally enhances reaction rates and catalytic activity for noble metal catalysts [34, 37, 43, 46, 47, 104, 108, 128, 186].

For glycerol oxidation under base-free conditions, Pt-Bi/AC activity increased near-proportionally with temperature from 30 to 90 °C, with maximum DHA yield at 80 °C [34]. Pt-Bi/HT showed optimal yield at 90 °C but slightly higher selectivity at 70 °C [104]. For Au/CuO, increasing the temperature from 30 °C to 100 °C increased conversion from ≈ 0% to 23%, though DHA selectivity dropped from 100% to 60% [128]. For PdPt/TiO_2, AuPdPt/TiO_2, and AuPd/TiO_2 catalysts, increasing the temperature from 60 to 100 °C increased glycerol conversion without affecting DHA selectivity [132]. Similar trends were observed under basic conditions, where increasing the temperature (range of 40–90 °C) boosted glycerol conversion for various catalysts, including AuPd/AC, PdPt-Bi/AC, Pt/AC, Au/CeO_2, Au/ZrO_2, and Au/CZ [36, 40, 86, 154].

2.7.4. Crude glycerol as Raw Material for Oxidation

Crude glycerol, the main by-product of biodiesel production, varies in composition depending on the feedstock and production process, typically containing 40–98 wt.% glycerol along with impurities such as methanol (≤30 wt.%), water, inorganic salts ("ash", 0.03–7 wt.%), free fatty acids, unreacted glycerides, methyl esters (0.7–22 wt.%), and other organic materials. These impurities limit its direct valorisation [6, 149].

Although catalytic oxidation could potentially accommodate crude or partially purified glycerol, some studies have investigated it [6, 77, 124, 139, 149, 202]. Ag, Au, Pd, Pt and AuPd supported in Al_2O_3, TiO_2, and carbon materials were tested under basic conditions, except Pt1/Al_2O_3, which was also tested under base-free conditions [6]. Most studies employed crude glycerol from rapeseed-based biodiesel, with one evaluating mixed waste oil feedstocks [124], including different levels of crude glycerol purification [6, 124].

Catalyst Performance with Crude Glycerol

Catalyst performance strongly depended on glycerol purity. Au/TiO_2, moderately active using pure glycerol oxidation under basic conditions, nearly deactivated with crude glycerol, shifting selectively towards formic acid. DHA and GCA selectivity increased with increasing glycerol purification degrees [124]. Similarly, carbon-supported Au catalysts showed higher glycerol conversion and GCA selectivity with higher purity (6 h reaction): crude (42%, 25%) < evaporated (46%, 32%) < evaporated and neutralised (72%, 38%) < commercial (78%, 50%) [149]. These catalysts did not produce DHA, shifting from GCO selectivity with crude glycerol to GCA with purified samples. High Au leaching (80 wt.%) occurred in the presence of CH_3ONa, a common biodiesel catalyst that reacted with Au^+, destabilising the support and causing metal loss.

Removing methanol, water, CH_3ONa, and fatty acids improved catalyst stability, restoring performance to levels comparable with commercial-grade glycerol [149].

Similar trends were observed for other catalysts. For pure glycerol oxidation, the activity of AuPd nanoparticles supported on carbon decreased in the order AC ≫ N- carbon nanofibers > CNT > carbon nanofibers > TiO_2 [139], while for Al_2O_3-supported catalysts, the trend was: Au ⋙ Pt ≫ Pd > Ag [77]. All catalysts favoured GCA production except for Ag/Al_2O_3, which was GCO-selective.

Crude glycerol impurities also influenced catalyst stability. AuPd/AC showed good and stable performance over eight cycles with commercial or purified glycerol. Using crude glycerol, AuPd/AC lost 15 wt.% metal content and saw conversion drop to 6% after eight cycles with crude glycerol, though GCA selectivity remained high [139]. Free fatty acids were identified as the primary cause of deactivation due to strong adsorption on active sites. For Al_2O_3-supported catalysts, crude glycerol reduced conversion and shifted selectivity towards GCO and FA [77]. Pd/Al_2O_3 exhibited the highest resistance, retaining 24% conversion after two hours, whereas Au/Al_2O_3 and Pt/Al_2O_3 suffered tenfold and fourfold activity losses, respectively. Ag/Al_2O_3 maintained glycerol conversion but shifted selectivity from GCO and formic acid to GCA, indicating selective blocking of oxidative cleavage sites by impurities [77].

Effects of Individual Impurities

Skrzyńska et al. [6, 77, 202] systematically evaluated the impact of individual impurities on glycerol oxidation under basic conditions (60 °C, 5 bar), illustrated for Au/Al_2O_3 and Pt/Al_2O_3 under basic and base-free conditions in Figure 2.16.

- **Methanol** (≤15 wt.%) had minor effects. It enhanced Pt/Al_2O_3 activity by increasing oxygen solubility but reduced Au/Al_2O_3 and Ag/Al_2O_3 performance. Under base-free conditions, Pt/Al_2O_3 initially benefited from methanol, but excessive amounts decreased activity. While Pd/Al_2O_3 selectivity remained unchanged, Au/Al_2O_3 and Pt/Al_2O_3 exhibited increased formic acid formation, and Ag/Al_2O_3 shifted from GCO to GCA.
- **Ash** (sulphates) increased Pd/Al_2O_3 activity but inhibited other catalysts, particularly Au/Al_2O_3, which shifted selectivity from GCO to FA. Under base-free conditions, Pt/Al_2O_3 activity declined with increasing ash content.
- **Organic matter**, a complex hydrophobic mixture of fatty acid derivatives, is strongly adsorbed onto active sites. Soap (a surfactant) delayed oxygen dissolution and caused excessive foam formation, further reducing glycerol conversion. While Pd/Al_2O_3 was the most resistant, Au/Al_2O_3 became nearly inactive.
- **Organic sulphur compounds**, especially thioglycolic acid, had the most severe poisoning effect, drastically reducing catalytic activity.

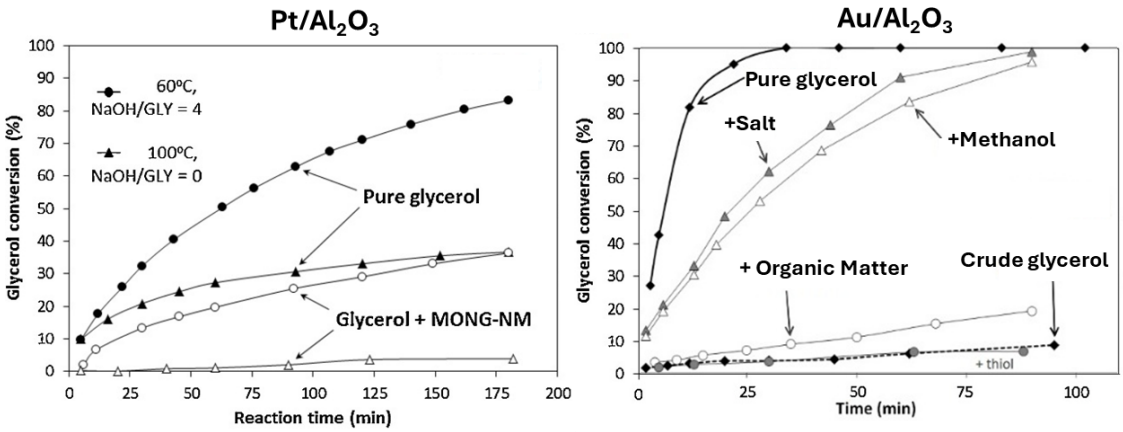

Figure 2.16. Glycerol impurities' impact on glycerol conversion. Left: Pt/Al_2O_3, basic and base-free conditions; Right: Au/Al_2O_3, basic conditions. Adapted from [6, 77].

Overall, Pd/Al_2O_3 exhibited the highest resistance, while Au/Al_2O_3 and Pt/Al_2O_3 were highly susceptible to deactivation. Organic matter and sulphur derivatives were the most detrimental impurities, necessitating removal for stable catalytic performance. Some impurities acted as unconventional selectivity modifiers, shifting oxidation pathways [6, 77, 202].

2.8. Glycerol Oxidation - Continuous Flow

From an industrial perspective, continuous processes are preferred due to their potential for higher production rates and improved process control. This Section discusses studies on continuous glycerol oxidation using Pt-Bi and Au-based catalysts, summarising key results in Table 2.6.

2.8.1. Pt and Pt-Bi Catalysts

Kimura et al. [168] proposed a continuous process using a Pt-Bi/AC catalyst to enhance DHA yield. In batch operation, a DHA yield of 20% was obtained, which increased to 53% (X_{GLY} = 75%, S_{DHA} = 70%) in a continuous fixed-bed reactor with a 6 M glycerol feed (50 wt.% aqueous solution) and a liquid hourly space velocity (LHSV) of 0.06 h^{-1}. A 1000-hour endurance test demonstrated stable catalyst performance at lower glycerol concentrations (10–20 wt.%), but mass transfer limitations became significant at higher concentrations (30–50 wt.%) [168].

Similarly, García et al. [28, 115] and Brandner et al. [48] extended their batch reactor studies, which achieved maximum DHA yields of 37% (Pt7.4-Bi2.9/AC) and 30% (Pt5-Bi5.4/AC), respectively, to continuous trickle-bed operation. García et al. [28, 115] reported higher glycerol conversion (≈90%) in continuous mode, but overoxidation reduced DHA selectivity, resulting in a maximum DHA yield of 24% (X_{GLY} = 72%, S_{DHA} = 34%). Brandner et al. [48] conducted a

1000-hour test (see Figure 2.17), finding that at a feed rate of 1 mL min^{-1}, glycerol conversion was only 18% while reducing the flow rate to 0.1 mL min^{-1} increased conversion to 90%. DHA selectivity was initially 70% but declined to 40% over the first 700 hours, stabilising thereafter. Under optimal conditions (0.1 mL min^{-1} feed rate), DHA yield initially reached 45% (X_{GLY} = 90%, S_{DHA} = 50%) but gradually decreased to 36% at 700 hours, remaining stable until 1000 hours of operation. ≈

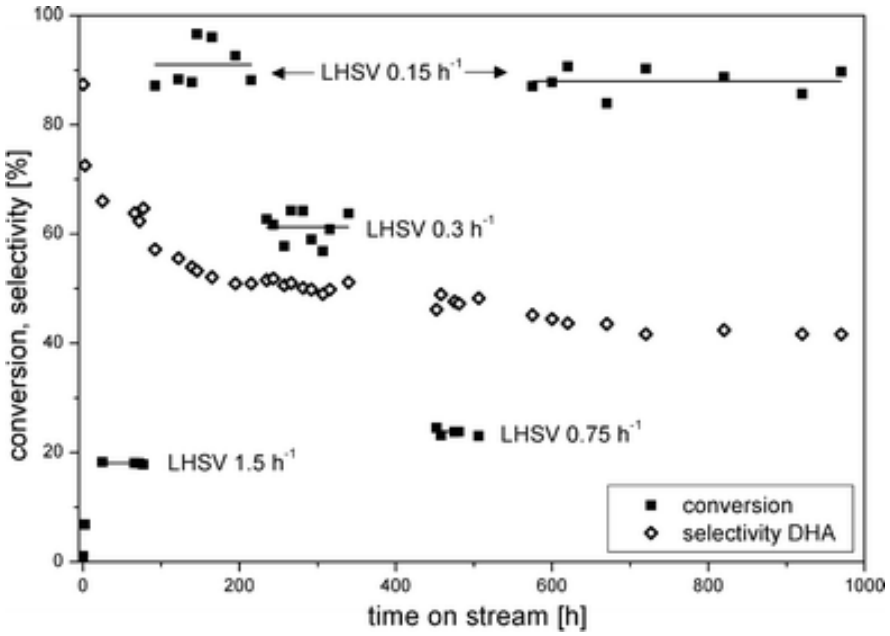

Figure 2.17. GLY conversion and DHA selectivity using Pt-Bi/AC in a continuous flow reactor at 393 K, 10 bar, $P(O_2)$ = 1 bar, C_{GLY} = 10 wt.%, Q_{feed} = 0.1 - 1 mL/min, LHSV 0.15 - 1.5 h^{-1}, O_2/GLY = 1.4 - 0.14. Reprinted from [48].

Pt@Sn-MFI catalyst, synthesised via in-situ encapsulation of Pt nanoparticles within a tin-silicalite-1 (Sn-MFI) zeolite, formed a core-shell structure that enhanced metal-support interactions while preventing Pt leaching and agglomeration. The Sn species induced an electron-deficient state in Pt, suppressing glyceraldehyde overoxidation and promoting its isomerisation to DHA. Optimising the Si/Sn ratio to 80 enhanced the catalyst's Lewis acidity and performance. A vertical fixed-bed reactor achieved 75% DHA selectivity with 44% glycerol conversion at 60 °C under atmospheric pressure [203].

2.8.2. Au-Based Catalysts

Zope et al. [204] investigated the effect of reactor configuration on Au/TiO_2 performance under basic conditions. In batch mode, the catalyst exhibited high glycerol conversion with GCA as the primary product. In a continuous flow reactor (60 °C, 10 bar, 0.3 M glycerol, 0.3 M NaOH, 1 mL min^{-1} feed), increasing the O_2 flow rate (5 to 30 STP mL min^{-1}) enhanced both TOF and glycerol conversion from 0.25 to 0.8 mol_{GLY} $molAu^{-1}$ s^{-1} and 5% to 16%, respectively, with no

further gains beyond 30 STP mL min^{-1}. Increasing pressure from 5 to 10 bar raised TOF from 0.45 to 0.75 mol_{GLY} mol_{Au}^{-1} s^{-1}, while temperature variation (35–75 °C) had minimal impact on reaction rate but altered selectivity: GCA, TTA, and OXA selectivity increased, whereas GCO selectivity decreased significantly. Higher glycerol feed rates reduced conversion but improved GCA selectivity by suppressing overoxidation.

Pollington et al. [35] studied glycerol oxidation using Au/AC in batch and continuous flow reactors, including a monolith and a slurry bubble column reactor (SBCR) with co-current gas-liquid inlets. In batch mode and with the monolith, complete GCA selectivity was observed, whereas the SBCR exhibited moderate DHA selectivity (≈55%), attributed to improved oxygen availability in the structured reactor.

Villa et al. [38] extended their base-free batch oxidation studies to a continuous fixed-bed reactor [97] over 80 hours using Au4Pt1/AC (GCA-selective) and Bi0.5-Au4Pt1/AC (DHA-selective) catalysts.

Au4Pt1/AC exhibited stable performance, maintaining 25% glycerol conversion and approximately 70% GCA selectivity. Pt and Au did not leach, and nanoparticle size remained unchanged after 80 hours. A slight variation in particle distribution was observed, likely due to the diffusion of Au from within the support pores and its subsequent redeposition on the carbon surface [97].

Bi0.5-Au4Pt1/AC achieved the highest DHA selectivity (48%) at 25% conversion (60 °C, LHSV = 0.18 h^{-1}, O_2 = 5 mL min^{-1}). Longer contact times reduced DHA and GLAD selectivity in favour of overoxidised species (HPA, FA, GCO). Lowering the temperature from 60 °C to 30 °C decreased DHA selectivity from 48% to 31%, likely due to slower DHA desorption from Bi-AuPt active sites. Higher O_2 flow rates also reduced DHA selectivity (48% to 38%) without affecting conversion. During the first 20 hours, glycerol conversion and DHA selectivity declined from 25% and 48% to 18% and 40%, respectively, before reaching steady-state conditions. While Au and Pt leaching remained comparable to Au_4Pt_1/AC, Bi leaching was significant. Nanoparticle size increased from 3.9 to 8.1 nm, indicating weaker metal-support interactions induced by Bi [97].

Table 2.6. Glycerol oxidation to DHA under continuous flow on a fixed-bed reactor; base-free unless noted (*entry #3: SBCR, basic conditions).

Catalyst	T °C	P/P_{O2} bar	O_2/GLY mol/mol	C_{GLY} (M) /Q[b]	LHSV h^{-1}	X_{GLY} %	S_{DHA} %	Y_{DHA} %	Summary/Key Findings	Work (Year) [Ref]
Pt5-Bi1/ AC	50	n.a.	2	6/ n.a.	0.06	75	70	53	Optimised carbon type, LSHV, O_2/GLY ratio, and pH. The catalyst structure changed during the initial reaction stages.	Kimura 1993 [168]
Pt4-Bi1/ AC	50	10	1	0.2/ n.a.	[d]	72	34	24	Maximum DHA yield achieved at 20 g_{Pt} h^{-1} ml^{-1} contact time	Fordham et al. 1996 [115]
Pt5-Bi5.4/AC	120	10/ 1	1.4-0.14	1.1/ 0.1-1	0.15-1.5	90-20	50	45	Increasing the feed flow rate decreased conversion without affecting selectivity. Selectivity declined from 80% to 50% after 100 h, while glycerol conversion remained unchanged.	Brandner et al. 2009 [48]
Au1/C monolith	60	5/ 1	1.4	0.6/ n.a.	5.6 [c]	30	53	16	An Au/C-coated monolith or an SBCR significantly increased reaction rates over batch reactors. SBCR enhanced DHA selectivity due to higher oxygen availability.	Pollington et al. 2009 [35]
Fe0.8/ silicalite	350	1	3.5	n.a./ 0.012	52900 [a]	99	72	71	Gas-phase oxidation. Activated catalysts with highly dispersed Fe cations or extra-framework FeOx showed Y_{DHA} at ≈70%.	Lari et al. 2015 [87]
Bi0.1-(AuPt)1/ AC	60	3	n.a.	0.55/ n.a.	0.183	25	48	12	Optimised T, O_2, and GLY flow. The catalyst structure changed over 80 h, affecting performance. $(AuPt)_1$/AC was more stable than 0.1Bi-(AuPt)1/AC.	Motta et al. 2018 [97]

[a]Gas hour space velocity; [b]Flowrate (ml/min); [c]Superficial velocity (mm s^{-1}); [d]Fixed O_2/GLY.

2.9. Separation Processes

The first part of this Chapter reviewed various catalysts, operating conditions, and continuous operations for the selective oxidation of glycerol. While high DHA selectivity has been reported in the literature, complete selectivity has not been achieved with any catalyst. Consequently, DHA must be separated from the remaining oxidation products and unreacted glycerol, as high-purity DHA is required for commercial applications, including in the cosmetics industry [51].

Downstream processes in bioindustries are inherently complex and often account for more than 50% of the total production cost in bioprocesses [205, 206]. The purification of DHA obtained from bio-fermentation is challenging and costly, including special attention to DHA sensitivity to heat and alkaline conditions [51, 207, 208]. Industrial separation processes for DHA typically involve organic solvents [208] and multiple purification steps, including filtration of the fermentation broth to remove insolubles, ion-exchange resin adsorption to eliminate inorganic cations and anions, and vacuum distillation for concentration [56].

In contrast, DHA production via chemical routes results in a mixture containing several organic acids with structural similarities, including similar molecular sizes, weights, and high boiling points. These characteristics make conventional separation techniques, such as membrane separation and distillation, challenging. Moreover, DHA decomposes before reaching its boiling point (188 °C) [51], further limiting thermal-based separation methods.

Chromatography is a promising alternative for separating DHA from glycerol oxidation products, successfully used in similar systems [209, 210], including commercial applications [211-215]. One study reported the separation of DHA from glycerol using an ion-exchange resin in calcium form, though it did not address separation from organic acids [216]. Ion-exchange resins are widely used for the purification of various compounds, including in continuous chromatographic processes, such as Simulated Moving Bed (SMB) units (discussed later) for sugar separation, glycerol desalting, and the purification of amino acids and organic acids [217-219]. These fine-mesh spherical resins offer an optimal flow rate balance, column packing efficiency, and chemical and mechanical stability, making them suitable for high-throughput separation and repeated regeneration cycles [218, 219].

Strong acid cation-exchange resins have also effectively separated glyceric acid from tartronic acid, two common glycerol oxidation products [220, 221]. A commercial polystyrene divinyl benzene resin in the acid form was used as the stationary phase at 293 K, with a 5mM H_2SO_4 aqueous solution as the mobile phase to maintain resin acidity. Lower crosslinked resins (2%) provided superior separation of GCA and TTA, demonstrating higher adsorption capacity and efficiency than those with greater crosslinking (4% and 8%) [220].

True Moving Bed (TMB) chromatography implements the concept of continuous counter-current chromatographic separation by enabling both solid and fluid phases to move counter currently, maximising adsorption driving forces between the two phases. This approach provides higher productivity, more concentrated product streams and lower mobile phase consumption than elution chromatography, allowing the efficient separation, even in the case of low separation selectivity [210, 222-224]. However, the operation of a TMB is unfeasible due to technical problems such as equipment limitations and adsorbent abrasion. Those limitations are overcome by the SMB process, which simulates counter-current movement of the liquid and solid streams by periodically shifting the inlet and outlet ports in the direction of the fluid flow. In conventional operation, all ports shift one column forward simultaneously at defined intervals, known as the switching time t^*, defined as $t^* = {}^{L}/_{u_s}$, where L is the column length and u_s is the solid velocity. When the streams return to their initial position, one SMB cycle is completed [210]. A schematic representation of a conventional SMB unit is shown in Figure 2.18.

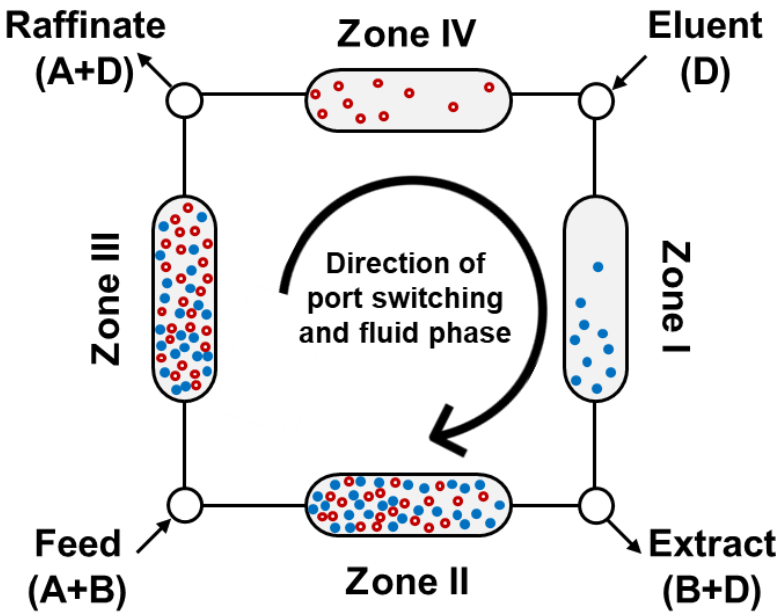

Figure 2.18. Schematic of a four-zone SMB for binary (A/B) separation. A: least retained (red); B: most retained (blue).

The conventional unit consists of two inlet streams (feed and eluent) and two outlet streams (extract and raffinate), dividing the unit into four sections (see Figure 2.18). The feed stream enters between sections II and III, and the least adsorbed species (A) move with the liquid phase and is collected in the raffinate stream, while the most adsorbed species (B) move with the solid phase and is collected in the extract stream. Sections I and IV regenerate the solid and liquid phases before recycling them, respectively. In section I, compounds should move forward with the liquid to be collected in the extract port, while in section IV, they should move back with the solid to be collected in the raffinate port.

These separations are achieved by carefully controlling flow rates in each section. The feasible separation and regeneration regions for SMB operation can be determined using various approaches, including the Equilibrium Theory, the Standing Wave Design, the Unified Design Approach, and SMB modelling with search algorithms [210, 223, 225, 226]. These methodologies will be discussed in Section 2.10.9.

SMB technology was first patented by UOP, Inc. (USA) in the 1960s with the Sorbex® process (Table 2.7, first entry). This breakthrough led to the development of several industrial applications in the 1970s, including the separation of p-xylene from C8 isomeric mixtures with high purity (Parex®, Aromax®, Eluxyl®), the separation of n-paraffins (Molex®), the separation of olefins from paraffins (Olex®), and the purification of ethylbenzene (Ebex®), among others [227, 228]. In the 1980s, UOP, Inc. extended the application of SMB technology to the sugar industry, introducing the Sarex® process for the separation of fructose from corn syrup using PS-DVB resins in calcium form (Table 2.7, third entry) [227, 228].

A new generation of SMB systems emerged in the early 1990s, driven by the need for high-purity chiral separations, which later expanded into pharmaceutical and biomolecule purification. The development of advanced stationary phases with fine particle diameters (≈20 μm) significantly enhanced separation efficiency compared to earlier SMB systems [227, 228]. This advancement enabled the separation of commercial drugs such as Prozac, Biltricide, Zoloft, and insulin, many of which involve complex chiral separations.

Originally designed for binary separations, SMB has since been adapted to handle increasingly complex separations, including ternary and multicomponent mixtures, through various process modifications and operational strategies [210, 222-224]. The biopharmaceutical industry, in particular, has driven innovations in chromatographic processes, incorporating solvent gradients and specialised process configurations. While early SMB systems operated with up to 24 large columns in fully continuous current mode, modern approaches now explore configurations with as few as two columns, with only about 25% of the process operating in continuous counter-current movement [229]. These advancements are further explored in the following Section 2.10.

Some groundbreaking patents in SMB technology are summarised in Table 2.7, alongside key patents for the separation of organic acids relevant to the process discussed in this thesis.

Table 2.7. Key patents related to SMB technology and organic acid separations.

Title Inventor/Year/Ref. Number	Summary of Invention/Key Aspects
Continuous sorption process employing fixed bed of sorbent and moving inlets and outlets. Broughton & Gerhold, 1961, US2985589 [230]	The first SMB patent, from UOP Inc., used in large-scale operations, such as the Sorbex® and Parex® processes. It introduced a continuous separation in which a fluid mixture is fed to a fixed-bed column with a solid adsorbent, with selective sorption in different zones. The cyclic flow and counter-current movement enhanced separation efficiency.
Rotary valve. Carson & Purse, 1962, US3040777 [231]	From UOP Inc., the central rotary valve was designed to synchronise the switching of inlet and outlet streams, enabling the counter-current operating in SMB units.
Sucrose separation from aqueous solutions featuring simulated moving bed Broughton, 1983, US4404037 [232]	Sarex® by UOP Inc., an SMB process for sugar purification, separating fructose from corn syrup using ion exchange resins with particle sizes of 300–500 μm at ≈ 65°C. SMB plants were ≈50% smaller than those in the petrochemical operation due to lower purity requirements (≈ 90%).
Process for separating optical isomers. Yamashita, Shoji 1992, US5126055 [233]	By Daicel Chemical Industries. Separation of optical isomers for the pharma industry. Chiral stationary phases with small particle sizes (≈20 μm) increased efficiency, enabling to separate enantiomers with high purity in smaller SMB columns (≈10 cm), though with lower productivity than petrochemical applications.
Process for separating an organic acid or acids from an organic acid-containing solution. Maeda & Nakazawa, 1993, US5245078 [234]	Describes a non-continuous chromatographic process using cation exchange resins to separate tartaric acid, citric acid, lactic acid, gluconic acid and glycolic acid from fermentation-derived solutions, using a dilute H_2SO_4 aqueous solution as a mobile phase.
Method for fractionating a solution Heikkilä et al., 2005 US6875349 [235]	Describes an SMB process for separating various organic acid-containing solutions, targeting a broad range of feedstocks, including sugar- and fermentation-derived mixtures containing molasses, vinasse, hydrolysates, whey, and/or amino acids.
Process for purifying organic acid by chromatography Theoleyre & Baudouin, 2007 FR2900654 [236]	A chromatographic separation process using an anionic resin to purify citric acid from fermentation broths through sequential processing in a multi-zone fixed bed.
SMB-System. Paananen et al., 2012, EP2316551 [237]	Industrial-scale SMB packed with small particle resins for fractionation of solutions, such as molasses, vinasse, and sulphite cooking liquors.
Process for the separation of mono- and dicarboxylic acid compounds. Archer et al., 2013, US20130345473 [238]	Details an SMB process for separating mono- and dicarboxylic acids from glucose oxidation mixtures, using anion exchange resins as the stationary phase.
Separation process Sarmala et al., 2015, US8951416 [239]	Describes an SMB process combining strong and weak acid cation exchange resins in a specific order to separate betaine and organic acids from sugar beet fermentation solutions.

2.10.Multicomponent SMB Separation Strategies

SMB technology is a highly efficient technique for continuous chromatographic separation, initially developed for binary separations in high-purity applications. Over time, advanced configurations and operating modes have been introduced to enhance its efficiency, expand its industrial applications, and enable unfeasible separations with the conventional four-zone SMB. Today, SMB is widely applied in pharmaceuticals for enantiomer separation, peptide purification, and protein refinement; in bioprocessing for the purification of sugars, amino acids, and organic acids from fermentation broths; and in the petrochemical industry for hydrocarbon separations and impurity removal [210, 229, 240].

To improve SMB performance and to meet the challenges of complex mixtures, several alternative SMB configurations and operating modes have been developed, including:

- **Alternative Configurations**: Reduced-zone SMB, Extended-zone SMB (or Parallel SMB), SMB cascades (or Tandem SMB), Double-Layer SMB.
- **Dynamic Configuration Variations**: Varicol®; Pseudo-SMB (Japan Organo process), Improved-SMB®, Sequential-SMB.
- **Flow rate modulation**: Power Feed, Partial-Feed, Partial-Discard, Partial-Withdrawal, Partial-Port-Closing (Outlet Swing Stream).
- **Concentration modulation**: ModiCon, Enriched Extract SMB.
- **Gradient operation**: Solvent gradient, temperature gradient.
- **SMB-based/Multicolumn Chromatography**: Multi-Column Solvent Gradient Process (MCSGP), Sequential Multi-Column Chromatography (SMCC), Periodic Counter-current Chromatography (PCC), among others.

The conventional four-zone SMB is unsuitable for the resolution of multicomponent mixtures (three or more compounds). Some strategies, while not directly designed for multi-component separation, have contributed significantly to the evolution of SMB technology:

- **Varicol®** (Asynchronous shifts SMB): This configuration enables asynchronous shifts of inlet and outlet ports, providing flexible section lengths and increasing productivity by up to 30% compared to conventional SMB [210, 228].
- **Three-zone open-loop SMB**: This configuration eliminates section IV and the recycling stream, preventing extract contamination and improving product purity. However, it increases eluent consumption and raffinate dilution while reducing hardware requirements and stationary phase costs [228, 241-243]. For systems following anti-Langmuir isotherms, section I (solid regeneration) can be eliminated by feeding the eluent directly into Zone II [244]. A redesigned unit by Mun et al.

rearranges SMB ports to allow operation at higher feed concentrations without compromising product recovery [245].

- **Flow Rate Modulation:** Selective inlet and outlet stream flow rates improve separation performance and internal concentration distribution [210, 228].
- **Simulated Moving Bed Reactor:** A process intensification approach that integrates chemical reactions within the SMB unit, allowing the separation to drive reversible reactions beyond equilibrium, thus improving productivity and selectivity [210, 228].

For illustration purposes, the separation of a three-component mixture (A/B/C), where A is the least adsorbed, C is the most adsorbed, and B has intermediate adsorption affinity, will be considered. Various SMB strategies can be tailored to optimise the separation efficiency of such multicomponent systems, such as Extended SMB (SMB-#, where # is the number of SMB zones, not columns), SMB Cascades, Pseudo-SMB, Improved-SMB (I-SMB), and Sequential-SMB (S-SMB) [210, 228]. These approaches vary in design complexity, operational feasibility, and separation efficiency. A comparative overview of SMB-based technologies for ternary and multicomponent separations is provided in Table 2.8.

A robust design strategy typically involves obtaining adsorption equilibrium data, starting with a simple model, identifying potential challenges and opportunities, and then refining it while accounting for limiting factors such as mass transfer, hydrodynamics, and phase heterogeneities. Nicoud [223] outlined some considerations for designing multicomponent SMB processes, including whether gradient operation should be considered when retention times significantly impact separation selectivity and whether the separation should be performed in a single step or through multiple sequential steps for a given stationary and mobile phase. Modelling and simulation tools are essential for designing and optimising SMB separation strategies, as experimental trial-and-error approaches are resource-intensive and time-consuming. Nonetheless, experimental validation remains necessary [223].

The most relevant multicomponent SMB separation strategies will be discussed in further detail throughout the following subsections.

Table 2.8. Comparison of SMB-based technologies for ternary and multicomponent separations

Feature	Continuous Counter-Current	Min. Columns	Ternary Separation	Operation Mode for Ternary Separation	Features	Drawbacks	Application
SMB Cascade	Yes	8 (6 in open loop)	Yes (3 or more). Bypass improves efficiency	SMB in series	Different stationary phases can be used for enhanced selectivity.	High capital and operational costs. High solvent consumption, high dilution, low productivity	Two SMB-4 for glucose + xylose separation from acetic and sulfuric acid- 2 SMB-3 open loop for valine separation from leucine, alanine, and ammonium sulphate
Extended SMB	Yes	SMB-5 (4 in open loop) SMB 8/9	Difficult to obtain pure B. Extended modes for ternary separations	1. SMB-5 with Partial-Collect of B; 2. Modified SMB-5 with Zone 0; 3. SMB-8 with bypass.	Single unit operation for ternary separations. High productivity. Low solvent consumption.	Complex design for ternary separations. Requires precise flow control.	1. SMB-5 for phthalates; sugars from corn-stover 2. SMB-9 for glucose/xylose from biomass. 3. SMB-8 with internal recycling for cyclic ketones
Improved-SMB	Semi-continuous	4	Yes, with its versions: 3S-ISMB, 3W-ISMB.	Switching time is divided into: 1. SMB without Zone IV, 2. Loop with closed inlet/outlets	High separation efficiency, flexible operation, suitable for multiple mixtures.	Complex design and operation.	Sugars separation. Two enantiomers separation with impurity removal
Sequential SMB	Semi-continuous	4	Yes	Switching time is divided into 1. Feed, 2. Loop, 3. Elution	High utilisation of mobile phase, reduced water consumption, suitable for industrial production.	Complex operation, difficult control, and lower utilisation of the stationary phase.	Sugars separation
Pseudo-SMB	Intermittent	4	Yes. Extendable for quaternary separation	Two steps: 1st fixed-bed operation (B) and 2nd SMB without feed (A + C)	Well-suited for ternary separations.	Difficult to extend for quaternary separations. Intermittent operation.	Sugars separation
Multi Column	Semi-continuous/ Intermittent	2/3 depending on the system	Yes (usually capture of the centre-cut species)	MCSGP, SMCC, PCC	Low number of columns. Versatile operation modes, including solvent gradients and column cleaning	Limited application, primarily for biopharmaceuticals.	Biopharmaceutical: proteins, peptides, monoclonal antibodies separations

2.10.1. Tandem/Cascade SMB

Tandem or Cascade SMB is one of the most straightforward approaches to multicomponent separation, in which multiple SMB units are linked sequentially, each dedicated to resolving a specific binary or pseudo-binary separation [246-250]. The first SMB unit separates one component, while the remaining mixture is further processed in the next SMB unit, continuing until the target components are separated.

One rule of thumb is to perform the separation in the easy-to-difficult order. When separating a ternary mixture (A/B/C), if the selectivity between A and B is higher, A is collected in the raffinate stream of the first SMB, while B and C are directed to the extract. This extract is fed into the second SMB, where B and C are further separated (see Figure 2.19). An alternative operation is possible: collecting C in the extract and directing A/B to the second SMB. Adding additional SMB units in series can extend this concept to more complex mixtures.

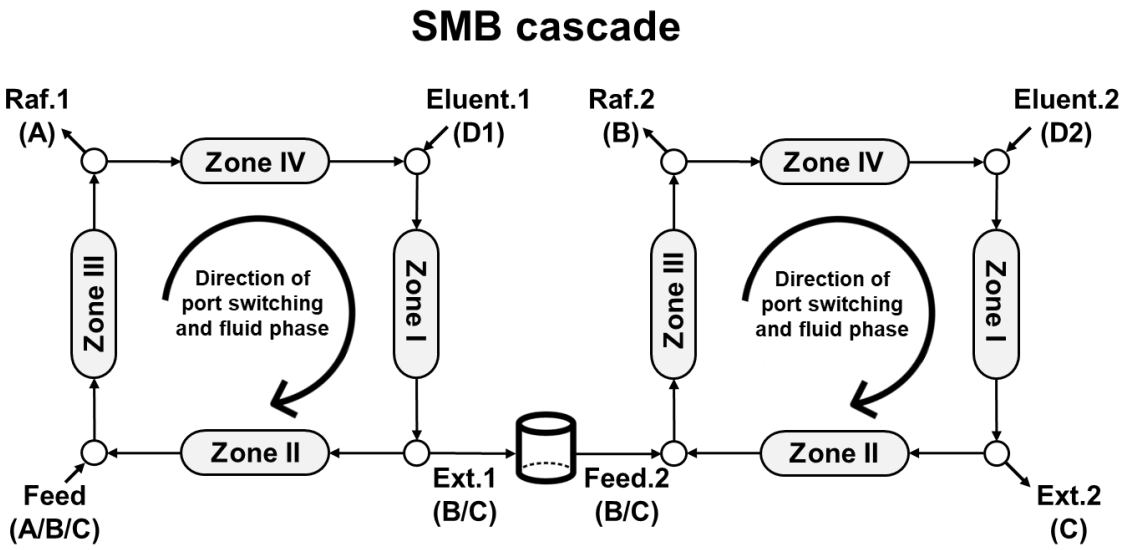

Figure 2.19. Two-unit SMB cascade for ternary separation. A is separated in the first SMB, and B/C are separated in the second SMB. A homogenization tank is used between units.

SMB cascades effectively separate mixtures with closely related properties, such as enantiomers. Unlike Parallel SMB, cascades allow independent control of each unit's switching times, temperature, and stationary phase. Different stationary phases in each SMB can enhance selectivity and productivity while reducing solvent consumption. However, careful management of mobile phase compatibility between units is required. Recent advancements include combining alternative SMB configurations in tandem. For example, a cascade of two three-zone open-loop SMB units effectively separated valine from leucine, alanine, and ammonium sulphate, outperforming conventional industrial processes [240].

Despite their effectiveness, SMB cascades involve high capital, operational costs, eluent consumption, and product dilution, which can reduce overall productivity [228]. A bypass stream strategy can mitigate this by selectively directing intermediate fractions between units [251]. A recent study demonstrated that for a two-SMB cascade, product dilution could be reduced by up to 85% by (1) increasing the column length in the SMB unit with higher mass transfer resistance (while proportionally decreasing the column length in the other unit to maintain total bed volume) and (2) allocating more columns in the zones containing the edges of the solute bands for the target component [252].

2.10.2. Extended sections SMB (Parallel SMB)

Extended SMB (or Parallel SMB) enhances multicomponent separation by introducing additional zones and intermediate withdrawal streams, improving selectivity while reducing eluent consumption. However, a key limitation is the requirement for a single switching time, which can restrict productivity. Additionally, these configurations involve higher equipment and operation complexity and costs. While effective for ternary and even quaternary separations, advanced control strategies are necessary for optimal performance [253-257].

Five-section SMB

The Five-section SMB (SMB-5) separates a ternary mixture (A/B/C) using three outlet streams: A and C are obtained as pure fractions, while B is recovered in a side stream, contaminated with either A or C. A key design decision is whether to operate with two extract streams (side stream contains B/C) or two raffinate streams (side stream contains B/A). This configuration is particularly useful when A or C are contaminants, allowing selective removal. It successfully separated dimethyl, dibutyl, and dioctyl phthalate, as well as sugars from corn-stover hydrolysate. However, achieving a pure fraction of the middle-eluting component (B) was unfeasible [258-261]. To address this, modified five-zone SMB designs have been developed (see Figure 2.20):

1. **Partial-Collect SMB:** Species B is collected only during the first fraction of the switching time, enabling high-purity separation for all components [262].
2. **Modified SMB-5**: An open-loop SMB-3 plus a "Zone 0" disconnected from the SMB-3 to collect the most retained species C, while B is collected in the extract stream and A in the raffinate. A different mobile phase can be used in Zone 0, particularly beneficial for pharmaceutical and biotechnological applications involving strongly adsorbed impurities. In such cases, an equilibration zone is required to restore the

mobile phase composition in the central SMB zones (I, II, III). This setup has been successfully applied to nucleoside separations [263, 264].

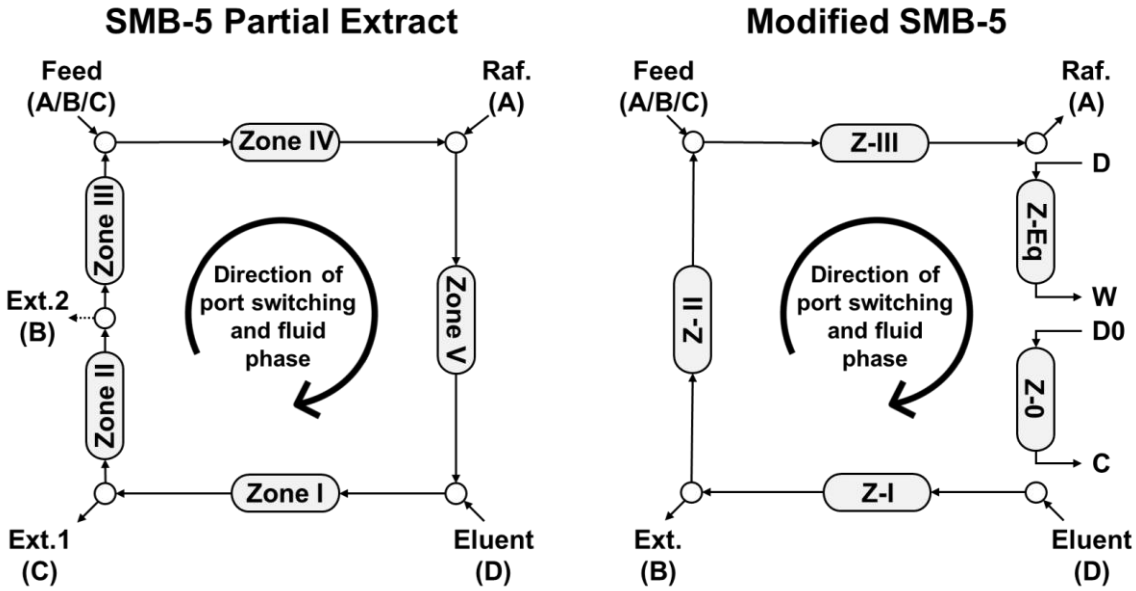

Figure 2.20. Five-zone SMB unit for ternary separation. Left: Partial-collect extract with internal recycling. Right: Modified SMB-5: open-loop SMB-3 plus two zones for regeneration and equilibration steps.

Eight- and Nine-section SMB

These configurations integrate two SMB units (e.g., SMB-4 + SMB-5) into a single system [265]. By incorporating three feed streams (one feed and two desorbent inlets), three product outlet streams, and a bypass stream, these designs enable multiple intermediate zones for enhanced control over flow rates and adsorption equilibria. They are suitable for separating complex mixtures with similar adsorption properties, such as petrochemical refining and biotechnological purification.

A nine-zone SMB (SMB-9, SMB-5 + SMB-4) operating with coupled rings successfully recovered glucose and xylose from biomass hydrolysates. In the first ring (SMB-5), sulfuric acid (fast-moving solute) was collected in the raffinate, while acetic acid (slow-moving solute) was partially recovered in the extract. Glucose and xylose (intermediate solutes), along with residual acetic acid, were fed to the second ring (SMB-4), where sugars were recovered in the raffinate and acetic acid in the extract [266].

An Eight-zone SMB unit (SMB-8, SMB-4 + SMB-4) with internal recycling enables ternary centre-cut separation (see Figure 2.21). Here, the raffinate (or the extract) stream is recycled three zones forward (or backward) relative to the fluid flow direction. The internally recycled stream contains the intermediately adsorbed component, contaminated with either the least (raffinate

recycle) or most retained (extract recycle) species. This approach was experimentally validated for separating cyclohexanone (B) from cyclopentanone and cycloheptanone. It reduces capital costs and equipment complexity while enhancing separation efficiency (pre-separation of the binary mixture internally recycled) and decreasing eluent consumption compared to a two SMB-4 cascade [240].

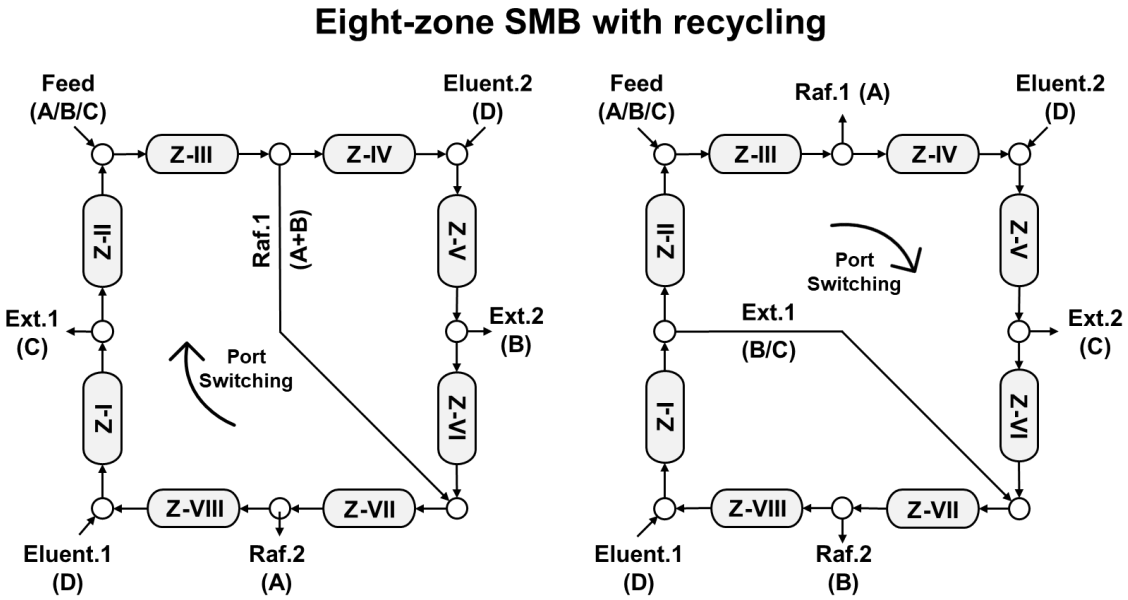

Figure 2.21. Eight-zone SMB unit (SMB-4 + SMB-4) with internal recycling. Left: raffinate recycle for A/B separation. Right: extract recycle for B/C separation.

2.10.3. Pseudo-SMB (Japan Organo Process)

Pseudo-SMB, also known as the Japan Organo (JO) process, was developed by Japan Organo Co. as an alternative SMB strategy for ternary separations [267]. Unlike conventional SMB, Pseudo-SMB operates with intermittent feed and withdrawal, operating in two distinct operation steps (Figure 2.22):

1. **Fixed-Bed Step:** The circulation flow is stopped by closing a shut-off valve, effectively transforming the system into a series of fixed-bed columns. Like a classic SMB, the feed enters Zone III, and the eluent enters Zone I. The intermediate-affinity species (B) is selectively eluted and collected at the end of Zone II.
2. **Simulated Moving Bed Step**: The shut-off valve is opened, resuming SMB operation for one cycle without additional feed input. A B-enriched region is formed, while C is collected in the extract and A in the raffinate.

This sequential operation effectively isolates the intermediate component before applying SMB separation to the remaining mixture, improving purity and reducing solvent consumption [267, 268]. It has been successfully applied to sugar separations and to fractionate beet molasses

[260, 269, 270]. Recent advancements have extended pseudo-SMB capabilities to gradient elution and modified configurations, enabling enhanced selectivity and purity in quaternary separations [271-274]. A five-section pseudo-SMB was designed for complex separations, achieving high purity even in moderately difficult systems [261].

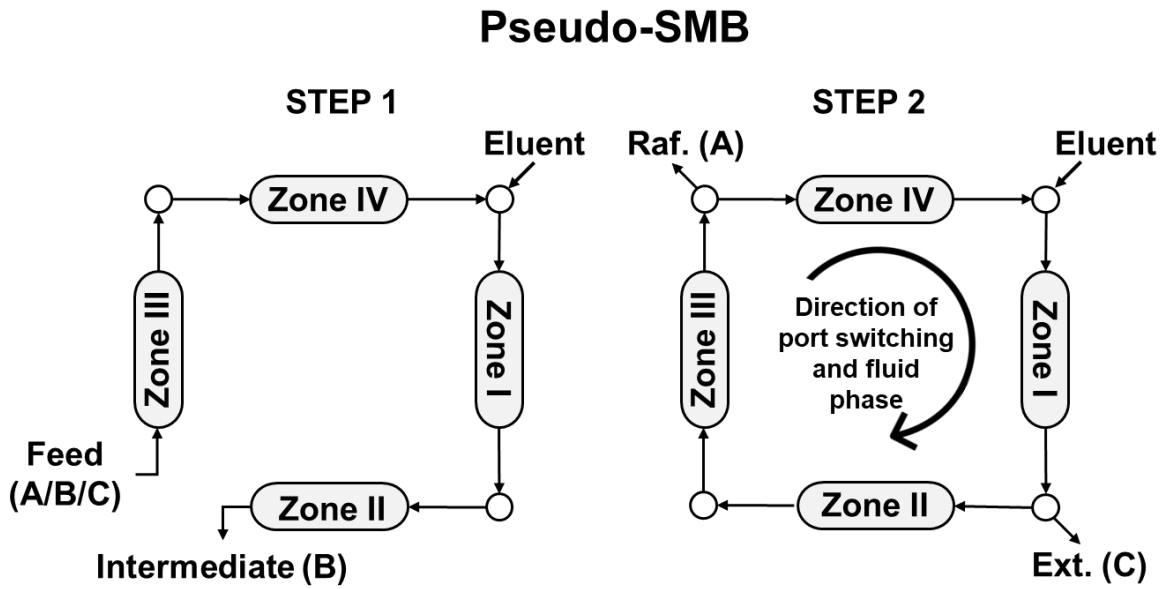

Figure 2.22. Pseudo-SMB for ternary separation. Step 1: fixed-bed operation for elution of B. Step 2: SMB operation separates A (raffinate) and C (extract) and creates a B-enriched zone.

2.10.4. Sequential-SMB

Sequential-SMB (S-SMB), developed by Novasep (France) [275], divides each switching time into three sequences, enabling efficient ternary separations with fewer columns [276]. An intermittent flow strategy enhances productivity and reduces solvent consumption compared to conventional SMB [240, 277]. This process optimises mobile phase efficiency and has been successfully applied in large-scale sugar production and other industrial separations [276]. The three operational phases of S-SMB (Figure 2.23, bottom) are:

1. Feeding Phase: Inlet and outlet ports are in the conventional SMB arrangement. C is collected in the extract, B in the raffinate, while Zones II and IV are inactive.
2. Loop Phase: All inlets and outlets close, and all columns are connected into a circular loop with internal flow to redistribute the concentration profile.
3. Elution Phase: Eluent is fed into Zone I, and A is collected in the raffinate at the end of Zone III. Zone IV is inactive, while the extract and feed streams remain closed.

2.10.5. Improved-SMB

Improved-SMB® (I-SMB), also known as Intermittent-SMB, was developed by Nippon Rensui Co. (Japan) [229, 240]. Unlike conventional SMB, where all zones operate continuously, I-SMB divides the switching cycle into two stages (Figure 2.23 top):

1. **Step 1 (SMB)** – Operates like a standard SMB, except Zone IV is inactive, preventing fluid recycling into Zone I.
2. **Step 2 (Recirculation)** – All inlet and outlet streams are closed, allowing internal recycling to redistribute solute concentration profiles before resuming the next switching cycle.

This configuration optimises solvent usage and column efficiency while maintaining productivity comparable to conventional SMB. I-SMB simplifies the S-SMB by removing the elution phase [229, 240].

I-SMB for ternary separations

Two adaptations of the I-SMB were developed for ternary separations: Ternary Strong I-SMB (3S-ISMB) and Ternary Weak I-SMB (3W-ISMB) [278]. These modifications adjust the collection strategy in step 2 to selectively recover either the least or most adsorbed species, respectively, as illustrated in Figure 2.23. Compared to the conventional SMB, these adaptations reduce the number of columns and eluent consumption by approximately 10% [229, 240, 278].

- **3S-ISMB**: In step 1, A and B are collected, following the standard I-SMB operation. In step 2, an additional extract stream at the outlet of section I collects the most strongly retained species (C).
- **3W-ISMB**: In step 1, species C is collected at Zone I, while B is collected at Zone II, which operates independently. Meanwhile, A is not collected at the raffinate but instead fed into Zone IV. In step 2, Zone I becomes inactive, and the eluent is fed into Zone II to collect A at the outlet of Zone IV.

I-SMB has been successfully applied in pharmaceutical purification and biotechnological production of building blocks such as lactic acid [240]. Comparative studies show that I-SMB and S-SMB offer similar efficiency for monosaccharide separations, outperforming conventional four-zone SMB regarding solvent savings and productivity [276]. These configurations provide a flexible and scalable solution for multicomponent separations.

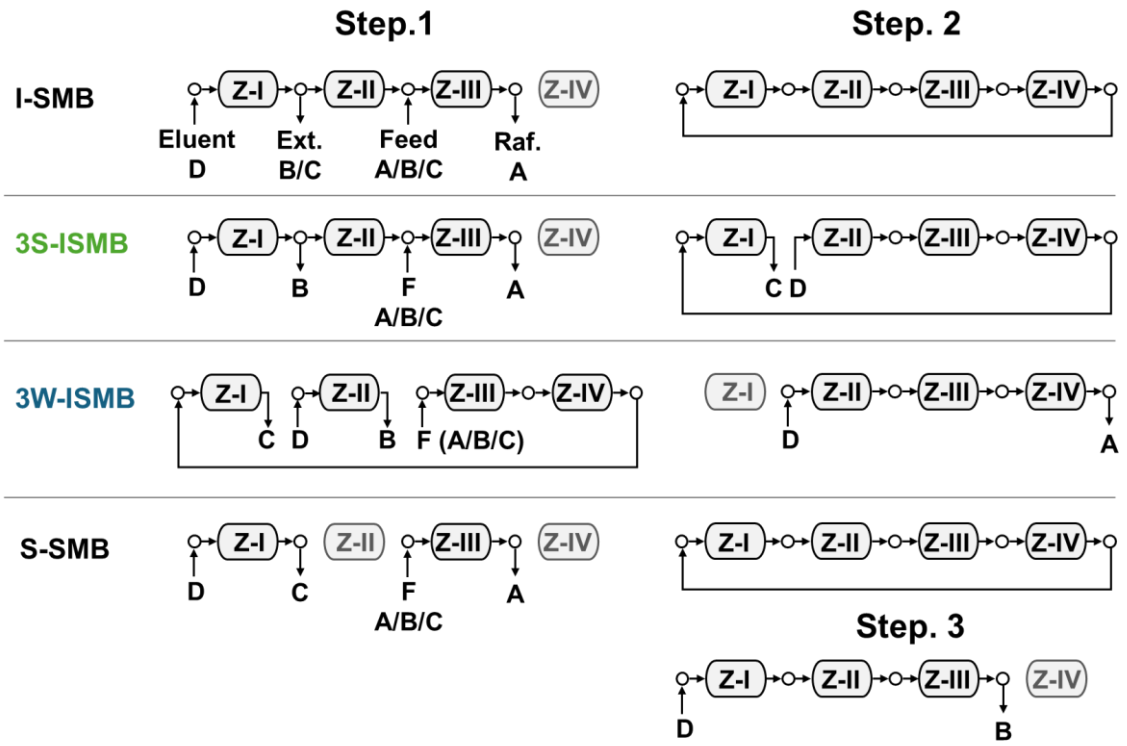

Figure 2.23. Comparison of I-SMB, 3S-ISMB, 3W-ISMB, and S-SMB. I-SMB is included for clarity, but does not enable ternary separations. Grey zones are idle.

2.10.6. Double-Layer SMB

Double-layer SMB (DL-SMB) is a novel chromatographic process introduced by Lee [279-281] for continuous ternary separations, represented in Figure 2.24. Inspired by dividing-wall distillation, DL-SMB allows ternary separation by incorporating two parallelised column layers, an upper (U) and lower (L) layer, each with six zones, requiring at least 12 columns and independent flow control for greater flexibility [279].

Zones III and IV operate independently in the upper and lower layers, while all other zones maintain the same flow rate ratios, allowing process design based on Equilibrium Theory. Feed enters between Zones III-U and IV-U, while the least- and most-retained components (A and C) are collected conventionally. The intermediate component (B) is concentrated in Zones III-L and IV-L by adjusting flow rates in Zones II and V. Except for the feed and intermediate ports, outlets from both layers are merged before being redistributed. This setup demands at least five pumps and flow splitters, or up to 10 if each split flow is managed separately [279].

While DL-SMB enhances productivity and lowers desorbent consumption for mixtures with similar A/B and B/C selectivity, its implementation is limited by complex flow control and high capital costs [280]. Alternative configurations, such as Hybrid DL-SMB and Serial DL-SMB, simplify internal flows but introduce trade-offs like increased pressure drop. The process

feasibility has been validated through Triangle Theory extensions and numerical simulations. Despite its potential, DL-SMB remains complex to implement, requiring experimental validation and configurations and flow management optimisation to enhance industrial applicability [281].

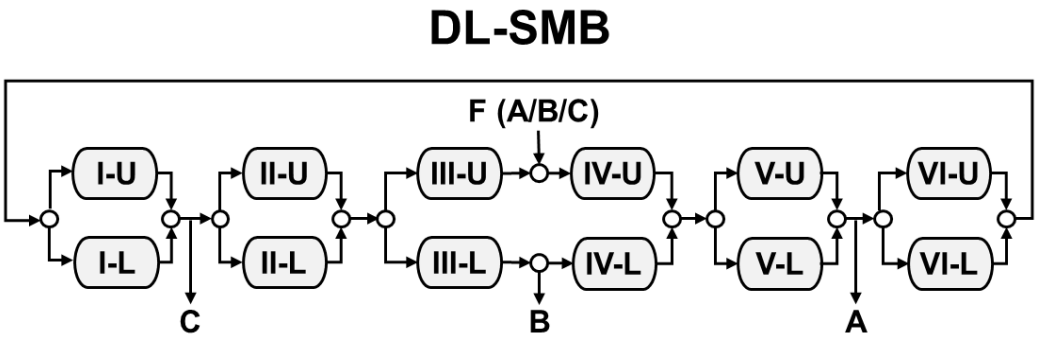

Figure 2.24. DL-SMB operation scheme for ternary separation (port direction not shown).

2.10.7. Other Multicolumn Chromatographic Units

Multicolumn chromatographic systems offer advanced separation capabilities for complex multicomponent mixtures, particularly in biopharmaceutical downstream processing, where conventional SMB struggles with ternary or pseudo-ternary separations requiring solvent gradients and intricate loading (F), washing (W), eluting (E), regeneration (R), and equilibration (Eq) steps. These systems enhance separation efficiency by integrating simulated counter-current operation with additional technologies while reducing capital costs and footprint. Some of the most relevant variants are Multicolumn Solvent Gradient Purification (MCSGP), Sequential Multicolumn Chromatography (SMCC), and Periodic Counter-current Chromatography (PCC).

2.10.7.1. Multicolumn Counter-current Solvent Gradient Purification

MCSGP combines the continuous counter-current movement of SMB with solvent gradient chromatography, enhancing selectivity and throughput for centre-cut ternary mixture separation [282, 283]. These are crucial features in biopharmaceutical production where the target compound often has intermediate adsorption strength, and weaker and stronger adsorbed impurities must be removed. MCSGP periodically switches column positions to simulate counter-current movement and recycles partially separated fractions, minimising solvent consumption while maximising yield and purity [210, 228].

The process divides the feed into five zones: (1) strongly adsorbed impurities (C), (2) product contaminated with C (B + C), (3) purified target product (B), (4) product contaminated with A (B + A), and (5) weakly adsorbed impurities (A). Pure fractions are continuously collected, while partially resolved fractions (A/B and B/C) are recycled for further separation, improving efficiency compared to batch chromatography. MCSGP rapidly reaches cyclic steady state

conditions, ensuring high reproducibility, minimal downtime, and consistent product quality [210, 228].

Initially designed as a six-column continuous unit (Figure 2.25, left), MCSGP used to require sophisticated control systems and relatively high capital investment compared to SMB. However, the reduction in solvent usage and increased productivity offset these costs. MCSGP has recently been adapted to semicontinuous two-column and three-column configurations to reduce complexity and cost. These designs separate the system into a Collect/Drain Part and a Recycling Part, maintaining high separation efficiency with fewer columns. The Twin-Column MCSGP (Figure 2.25, right) has demonstrated high yield and purity in monoclonal antibody separation, making it particularly effective for large-scale biopharmaceutical production [284]. Advanced configurations extend MCSGP's capabilities to separate more than three fractions, enabling the isolation of multiple target components in a single cycle. The method has been widely applied in biopharmaceutical purification, including protein and peptide purification, and even in rare earth element separations [210, 228].

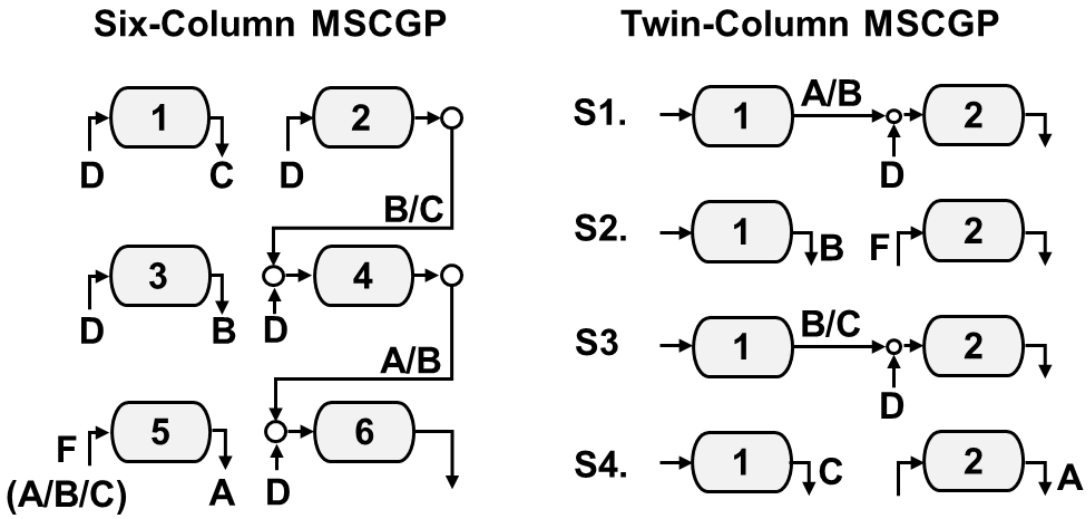

Figure 2.25. Left: six-column MCSGP (one of six steps shown). Right: first step of Twin-Column MCSGP (four sub-steps are shown; columns switch in the next step).

2.10.7.2. Sequential Multi-Column Chromatography

SMCC, patented by Novasep (France), is an open-loop multicolumn chromatography system that simulates counter-current movement by sequentially shifting inlets and outlets one column forward in the direction of the mobile phase. This quasi-continuous operation allows different buffers for the elution step, maximising dynamic binding capacity while reducing eluent consumption compared to batch chromatography. Its cyclic operation minimises downtime, making it particularly effective for multicomponent separations such as monoclonal antibody purification [210, 240, 285].

SMCC typically operates with three or more columns, progressing through the following steps (Figure 2.26, left):

1.1 Loading: Column 1 is loaded with the feed solution until near saturation.

1.2 Washing: Column 1 is washed with buffer to push non-retained products into Column 2, reducing product loss and buffer consumption.

2 Elution, Regeneration, and Equilibration: Column 1 is disconnected for elution while Column 2 continues loading.

3 Reconnection: Column 1 is reconnected and preloaded using the outlet of Column 3

When the feed returns to column 1, a cycle is completed. Detailed operation schemes are available elsewhere [286, 287]

2.10.7.3. Periodic Counter-current Chromatography

PCC, developed by GE Healthcare (United Kingdom), is a continuous capture step designed for biopharmaceutical downstream processing. It efficiently removes impurities and concentrates the target product by periodically switching inlet and outlet ports, simulating counter-current movement. PCC maximises resin utilisation by continuously loading columns up to 90% of their static binding capacity, significantly increasing productivity compared to batch chromatography [228, 240, 285]. A three-column PPC setup operation follows (Figure 2.26, right):

(1) **Loading** of Column 1 until breakthrough occurs, discarding the outlet.

(2) **Transfer** the outlet of Column 1 by connecting it to Column 2 until Column 1 reaches its target loading. The outlet of Column 2 is discarded.

(3) **Washing** Column 1 with its outlet connected to Column 3 while **Feed shifts** to Column 2.

(4) **Elution & Collection** - When the target product reaches the outlet of Column 2, it is connected to Column 3. Meanwhile, Column 1 undergoes elution, regeneration, and equilibration to recover the residual product.

(5/6) Steps 4 and 5 are applied one column ahead while column 1 is preloaded. One cycle is completed when the feed streams return to the inlet of Column 1.

Unlike SMCC, PCC operates with a continuous feed stream, differentiating it in washing steps and operational control. Typical PCC systems use three to five columns, eight-port valves, and online UV detectors for precise monitoring. Advanced variations incorporate additional columns and clean-in-place steps for improved robustness. PCC has been successfully applied in monoclonal antibody capture and other biopharmaceutical processes [228, 240, 285].

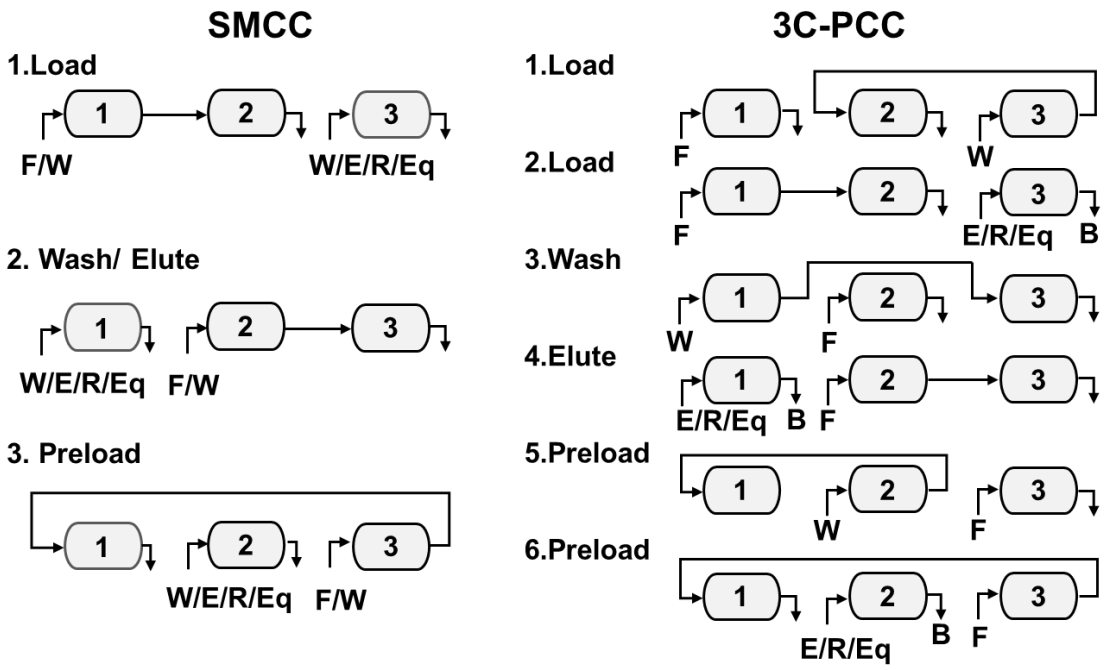

Figure 2.26. Multicolumn chromatography schemes (one cycle shown). Left: three columns SMCC; Right: three columns PCC.

2.10.8. SMB Comparison for Ternary Separations

Continuous chromatographic processes remain an evolving technology with ongoing developments. In the preface of an Alírio Rodrigues book [210], it is stated: "*Some years ago a young researcher, who did a postdoc in the SMB area in the USA, told me in one AIChE meeting "there is no future for SMB research… everything is done." I smiled - after that time, new operating modes (VARICOL, etc.) have arrived in practice in the pharmaceutical industry...*" Many of the technologies discussed earlier in this chapter were patented in the 21st century, with some still having limited presence in the open literature. Alírio Rodrigues' group also emphasises that "*New non-conventional techniques and new design/optimisation methodologies applied to both "old" and "new" applications can lead to more efficient units contributing to the relevance of SMB in the area of separation science and technology*" [227].

Nicoud highlights that the broad range of chromatographic processes makes this field both fascinating and complex. The selection of the most suitable process depends on multiple factors, including productivity, solvent consumption, capital investment, operational robustness, and footprint minimisation. No single technology is universally superior: some maximise productivity, others minimise solvent consumption, while some require higher initial investments but offer long-term economic advantages. Chromatographic processes are part of complex processes involving other operations. While equilibrium models and analytical methods provide proper initial estimations, the choice of design approach depends on system-specific constraints,

such as adsorption isotherms, mass transfer limitations, and process integration. Given the many adjustable parameters in chromatographic processes, optimisation tools are essential for process design. However, optimising chromatography remains a complex challenge that requires a structured approach, balancing practical engineering knowledge, computational efficiency, and fundamental chromatographic principles. Ultimately, the "*ability to invent and develop new and efficient chromatographic process is primarily limited by the creativity of the process engineer*" rather than by the available methodologies [223].

Despite these complexities, several studies have compared different SMB-based technologies for ternary separations, examining trade-offs between productivity, solvent consumption, complexity, and operational flexibility.

A. SMB-5 variations and SMB Cascades

For the separation of galactose, levulinic acid, and 5-hydroxymethylfurfural, a two-unit SMB-4 cascade demonstrated superior performance compared to the standard SMB-5. However, SMB-5 variations with partial feeding and partial extract collection achieved higher purities, throughput, and lower desorbent usage, resulting in a 58% increase in processing capacity than the cascade, even using fewer columns and less desorbent [250].

For the separation of amino acid mixtures, ModiCon SMB-5 variation achieved higher productivity for the intermediate species (B) compared to other SMB variations such as Varicol, Power Feed, and SMB-4 [288].

Despite the better results obtained by SMB-5 and its variations, more demanding multicomponent separations may require different stationary phases. For these cases, an SMB cascade may be the most suitable solution.

B. Pseudo-SMB and SMB Cascade

The performance of pseudo-SMB and SMB cascade was evaluated for two ternary mixtures [289]:

- **Mixture 1 (Fructose, Raffinose, Dextran T6):** The pseudo-SMB achieved higher purities due to the challenging separation between fructose and raffinose. However, an optimised SMB cascade with increased columns and optimised column configuration ultimately outperformed the pseudo-SMB.
- **Mixture 2 (Dextran T9, Dextran T6, Raffinose):** The SMB cascade outperformed the pseudo-SMB in most performance parameters and provided greater operational flexibility despite requiring additional valves and connections.

In another study, the step 1 position (fixed-bed operation) and the number of port switches in step 2 (loop) were optimised for an eight-column pseudo-SMB. The optimal position of step 1

depended on the separation selectivity of the given mixture. Maximum productivity was achieved with 2.5 cycles in step 2, increasing productivity four times compared to standard pseudo-SMB. A 16-column SMB cascade (two 8-column SMB-4) had higher productivity and required lower D/F than the pseudo-SMB process and 8-column SMB cascades (two 4-column SMB-4), but is considerably more complex [268].

C. Pseudo-SMB, SMB Cascade, SMB-8, SMB-5, SMB-4, and Generalized Model

The pseudo-SMB was exploited to a "Generalised Full Cycle" (GFC) of an SMB-4 for ternary separations. The GFC model allows two inlets (feed and desorbent) and three outlets (raffinate, extract, and an intermediate stream) per step, with adjustable flow rates and the option to deactivate specific inlets/outlets at different stages. This approach can be implemented on conventional SMB systems with minimal hardware modifications, requiring only an additional binary valve for systems using rotary valves [290].

For a given A/B/C mixture and purity requirements, the GFC model outperformed the pseudo-SMB, operating in the fixed bed to collect B in the outlet of column two (same as the standard operation) while also collecting A and C in the raffinate and extract stream outlets. In the second step, pure components C and A were recovered from the extract and raffinate stream outlets at the end of the second and fourth columns. A significant part (65%) of the total cycle duration is dedicated to steps 3 and 4 (no inlets/outlets), separating concentration profiles to be collected with high purity in the first and second steps [290]. Experimental validation of the GFC model was performed using the Semba Octave™ chromatography system to separate glucose, fructose, and maltose (10 wt.% impurity) under linear isotherm conditions. The GFC approach demonstrated a 40–50% increase in productivity compared to pseudo-SMB [291].

In addition, SMB-8 with internal recycling showed superior performance and reduced desorbent consumption compared to SMB cascades (with or without a homogenization tank), emphasising the importance of internal recycle dynamics. In contrast, SMB-5 (with three outlets) and a modified open-loop SMB-4 (which collects B at the outlet of column 1 during the first part of the switching time and C during the second part) were ineffective in achieving high purity of the intermediate component B [290].

2.10.9. Separation Design and Optimisation

The design of chromatographic separations requires careful selection of key parameters, including unit configuration (e.g., number of columns per section, column dimensions, particle size) and operational conditions (e.g., switching time, flow rates in each section, feed concentration). Model simulations can optimise these parameters, although they are computationally expensive and time-consuming. To address this, structured design

methodologies provide initial estimations of optimal operating conditions before engaging in detailed simulation [210].

Initial design methodologies relied on graphical approximation techniques such as plate theory and McCabe-Thiele diagrams or analytical solutions for SMB operation with linear adsorption isotherms without mass transfer resistances, derived using the steady-state TMB analogy [210]. These analytical methods have been extended to incorporate mass transfer resistances, reactive systems, and nonlinear adsorption isotherms (e.g., Langmuir, bi-Langmuir, and modified Langmuir models). Despite their simplifications, these models provide reliable benchmarks for detailed simulation and optimisation studies [210, 292].

2.10.9.1. Equilibrium "Triangle" Theory

A widely used SMB design method is Equilibrium Theory, often called Triangle Theory, which analytically determines dimensionless flow rates to ensure complete binary separation, represented in Figure 2.27. The method assumes instantaneous local equilibrium and negligible mass transfer effects, defining a triangular separation region based on constraints related to the transport of species between the liquid and solid phases, see [210]. The method was extended for relaxed purity requirements [293].

Equilibrium theory designs for ternary separations using different SMB configurations (SMB-4 + SMB-4, SMB-5 + SMB-4, SMB-8, SMB-9) are available, considering linear isotherms [294, 295] and Langmuir isotherms [265]. Further refinements include the separation volume approach, which extends the two-dimensional separation area to a three-dimensional separation volume using a steady-state TMB model. This approach incorporates axial dispersion, plug flow assumptions, and intraparticle mass transfer models, providing a more detailed but computationally demanding design framework [210].

The Triangle Theory application is limited in systems with significant mass transfer resistances, where it only provides initial feasibility estimates. The separation region is reduced when mass transfer resistances become relevant. For these cases, numerical simulations are required to define accurate separation and regeneration regions [210].

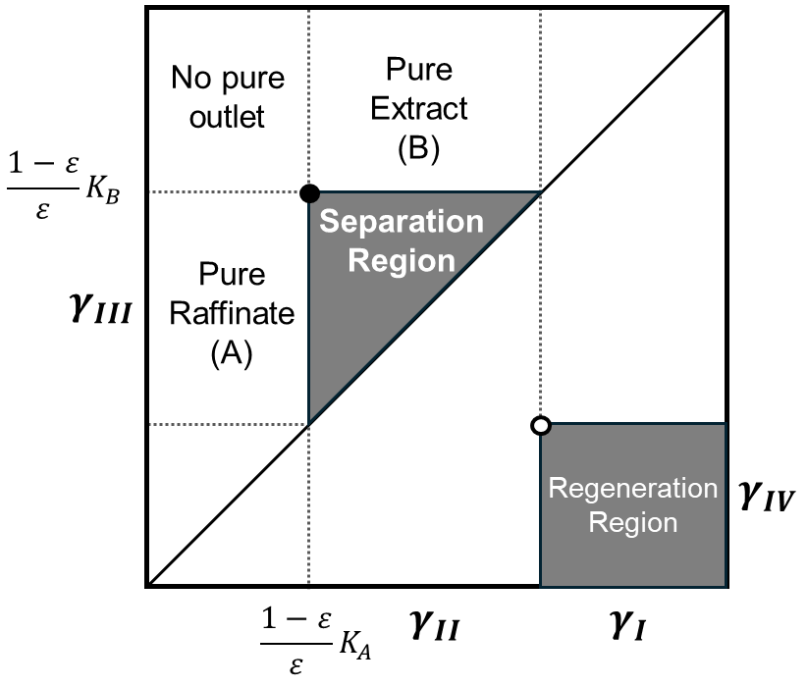

Figure 2.27. Triangle Theory for a binary SMB separation, considering linear isotherms and no mass transfer resistances. A: least retained; B: most retained. ●: optimal separation point; ∘: optimal regeneration point.

2.10.9.2. Standing Wave Design

The Standing Wave Design, developed by Linda Wang's group, ensures that adsorption/desorption waves remain "standing" during the switching period by travelling at the same velocity as the average port velocity [210]. Setting flow rates so that the average port velocity falls between the migration speeds of retained and non-retained species allows optimal m parameters to be estimated for target purities [210, 283].

Using the TMB-SMB equivalence, the TMB model, which requires reduced computational effort, is often used to determine the operating conditions [210]. Standing Wave Design is particularly useful for moderately nonlinear systems, offering an efficient algebraic approach for SMB design [283, 293].

Despite its advantages, Standing Wave Design has limitations, such as underestimating the feasible separation region in some cases [292]. It was extended to address nonlinear isotherms and non-isothermal SMB systems with significant mass transfer effects [296] and for non-isocratic pH-gradient SMB operations showing significantly higher productivity than Triangle Theory-based designs [297].

2.10.9.3. Unified Design Approach

The Unified Design Approach offers a generalised framework for designing and comparing chromatographic processes, whether they are discontinuous or continuous, by categorising them into three fundamental timed events:

- **Fixed-bed events** are classical batch chromatography, consisting of loading and elution steps.
- **SMB events** are similar to fixed-bed events, but the solid counter-current movement is simulated through periodic column switching.
- **Cut events** are fractionation-based separations outside the column, including product collection, waste removal, or recycling.

By describing different processes using dimensionless parameters, the Unified Design Approach enhances design flexibility, transferring operating conditions between different chromatographic modes [283, 298].

The Unified Design Approach generalises m-parameters across single-column and multicolumn processes, enabling empirical SMB design using single-column chromatography data. In linear adsorption systems, the design space is independent of the process type. However, for Langmuir isotherms, equivalence between single-column and SMB processes breaks down in Zone IV, limiting direct application [283].

Application to Ternary Separations

This framework has been extended to multicomponent separations, enabling the comparison of batch chromatography, steady-state recycling (SSR), counter-current SMB, and cross-current SMB [298]. For ternary separations, advanced multicolumn strategies include SMB cascades and single SMB units with discontinuous feeding and/or product collection. While conventional SMB cascades can be analysed using Triangle Theory or Standing Wave Design, other processes require specific design methodologies due to their complex operation schemes [298, 299].

For example, the pseudo-SMB design requires specific design methodologies [261, 268, 289]. The Unified Design Approach provides a better framework by treating the first step as batch chromatography and the second as a TMB operation, allowing direct comparison between technologies [298, 299].

The unified Design method offers a means to analyse and compare – both visually and with equations − their complete separation regions. Feasible separation regions for ternary mixtures with linear isotherms were derived and overlaid for batch chromatography, pseudo-SMB, and 3W-ISMB, demonstrating strong similarities between seemingly different process schemes. This

suggests that operating conditions can often be transferred across different processes without affecting product purity, provided column efficiency is sufficiently high [298].

The Unified Design Approach provides a comprehensive and systematic framework for chromatographic separation design, integrating various methodologies into a single dimensionless parameter space. It allows the Direct transfer of operating conditions across different separation modes and visualisation and analysis of separation feasibility for complex ternary/multicomponent processes. This methodology is particularly valuable for developing new SMB configurations, enabling the identification of optimal operating conditions for a wide range of separation strategies [298, 300, 301].

2.10.9.4. Optimisation of SMB separation

Optimising a conventional SMB unit involves selecting optimal operating conditions, such as flow rates, switching time, temperature, as well as geometric parameters like column number and dimensions. For more complex SMB systems, additional variables must be considered to maximise productivity or minimise desorbent consumption while ensuring constraints such as product purity and recovery [210].

Several optimisation strategies have been proposed. A two-level optimisation strategy first maximises productivity and then minimises desorbent consumption, using the "separation volume" concept and the TMB model, provided TMB-SMB equivalence is valid for the system [302]. Numerical optimisation methods, including evolutionary algorithms, have also been applied to handle multi-objective problems efficiently by obtaining Pareto-optimal solutions. Particle Swarm Optimisation has shown success in optimising both SMB configuration and operating conditions while reducing computational time [303, 304]. Other approaches include genetic algorithms for maximising productivity and purity in SMB and Varicol SMB [305] and Generalised Differential Evolution for optimising multi-column chromatographic ternary mixture separations [306]. A direct multiple-shooting method has also been employed to simultaneously determine optimal state trajectories and operating parameters [226].

SMB optimisation often requires extensive experimental work to determine adsorption parameters. To reduce this effort, a three-level optimisation approach has been proposed, integrating parameter estimation, isotherm definition, and the minimum number of experiments needed to develop a reliable model [307].

Despite advancements, SMB optimisation remains complex due to the interplay of operating variables and system dynamics. Future research will likely refine these optimisation techniques, integrating machine learning to enhance efficiency and industrial applicability.

2.11.Conclusions

This chapter comprehensively reviews the state-of-the-art developments in glycerol catalytic oxidation to DHA and subsequent separation processes for DHA purification. While significant progress has been made in both areas, challenges remain in transitioning from lab-scale to industrial implementation, namely in glycerol catalytic oxidation.

Since the 1990s, research has focused on catalyst development to enhance glycerol conversion, DHA selectivity, and stability. Noble metal catalysts have shown promising results, particularly Bi-doped Pt nanoparticles supported on carbon materials and Au nanoparticles supported on ZnO and CuO. The optimisation of particle size, support materials, and preparation methods has also contributed to higher DHA yields. However, catalyst deactivation due to product adsorption, metal leaching, and overoxidation remains a key limitation. Additionally, most studies have been conducted in batch reactors with diluted glycerol solutions, limiting direct scalability. While continuous flow processes have been explored to some extent, endurance tests and pilot-scale evaluations are still lacking, which is critical for assessing the commercial feasibility of DHA production via catalytic oxidation.

On the separation side, DHA purification presents considerable challenges due to the complexity of reaction mixtures. Almost no works in the literature concerning DHA purification from glycerol oxidation products exist. Chromatographic techniques, particularly SMB chromatography, may be an effective solution for DHA purification due to their continuous operation and high separation efficiency. The historical development of SMB technology, initially applied in petrochemicals and later expanded to sugar purification and pharmaceutical separations, has demonstrated its versatility and potential for DHA purification. Advances in SMB process design, including the use of fewer columns and alternative solvent strategies, have further improved efficiency and reduced operational costs, making it a promising technique for DHA recovery.

Despite these advancements, key challenges remain in both reaction and separation processes. Integrating optimised catalytic oxidation with chromatographic purification could provide a viable pathway for sustainable DHA production. Future research should focus on catalyst reusability and pilot-scale demonstrations to bridge the gap between laboratory success and industrial application.

2.12.Notation

A, B, and C	Hypothetical species with different affinity to the stationary phase: A is the least adsorbed, B has intermediate adsorption affinity, C is the most adsorbed
AC	Activated Carbon
CNT	Carbon Nanotubes
CZ	Ceria-zirconia
CZB	Ceria-zirconia-bismuth oxide
DHA	Dihydroxyacetone
DP	Deposition-Precipitation preparation method
DFT	Density Functional Theory
FA	Formic acid
GCA	Glyceric acid
GCO	Glycolic acid
GLAD	Glyceraldehyde
GLY	Glycerol
HPA	Hydroxypyruvic acid
HT	Hydrotalcite (formerly layered double hydroxide, LDH)
IMP	Impregnation method for catalyst preparation.
LHSV	Liquid Hour Space Velocity
MOXA	Mesoxalic acid
NCNT	Nitrogen-doped Carbon Nanotubes
OXA	Oxalic acid
TOF	Turnover Frequency
P_{O_2}	O_2 partial pressure (bar)
Q	Volumetric flow rate (ml/min)
SBCR	Slurry Bubble Column Reactor
SOL	Sol immobilisation for catalyst preparation
S_{Prod}	Product selectivity (%)
T	Temperature (°C)
TTA	Tartronic acid
wt.%	Mass fraction (%)
X_{GLY}	Glycerol conversion (%)
Y_{Prod}	Product yield (%)
SMB	Simulated Moving Bed
TMB	True Moving Bed

I-SMB	Improved-SMB® or Intermittent-SMB and variations for ternary separations (3S-ISMB and 3W-ISMB)
S-SMB	Sequential-SMB
DL-SMB	Double-Layer SMB
SMCC	Sequential Multi-Column Chromatography
PCC	Periodic Counter-current Chromatography
MCSGP	Multi-Column Solvent Gradient Process
GFC	Generalised Full Cycle SMB model (configuration optimisation)

2.13. References

1. Ciriminna, R., Fidalgo, A., Ilharco, L.M., and Pagliaro, M., *Dihydroxyacetone: An Updated Insight into an Important Bioproduct.* ChemistryOpen, 2018. **7**(3): p. 233-236.
2. Bricotte, L., Chougrani, K., Alard, V., Ladmiral, V., and Caillol, S., *Dihydroxyacetone: A User Guide for a Challenging Bio-Based Synthon.* Molecules, 2023. **28**(6): p. 2724.
3. Owji, S., Teklehaimanot, F., Maghfour, J., and Lim, H.W., *Properties and safety of topical dihydroxyacetone in sunless tanning products: A review.* Photodermatology, Photoimmunology & Photomedicine, 2023. **39**(6): p. 567-572.
4. Katryniok, B., Kimura, H., Skrzyńska, E., Girardon, J.-S., Fongarland, P., Capron, M., Ducoulombier, R., Mimura, N., Paul, S., and Dumeignil, F., *Selective catalytic oxidation of glycerol: perspectives for high value chemicals.* Green Chemistry, 2011. **13**(8): p. 1960-1979.
5. Agency, I.E., *World Energy Outlook 2018*. 2018.
6. Skrzyńska, E., Wondołowska-Grabowska, A., Capron, M., and Dumeignil, F., *Crude glycerol as a raw material for the liquid phase oxidation reaction.* Applied Catalysis A: General, 2014. **482**: p. 245-257.
7. Trifoi, A.R., Agachi, P.Ș., and Pap, T., *Glycerol acetals and ketals as possible diesel additives. A review of their synthesis protocols.* Renewable and Sustainable Energy Reviews, 2016. **62**: p. 804-814.
8. United Nations Conference on Trade And Development, U., *The global biofuels market: Energy security, trade and development*. October, 2014.
9. Nanda, M.R., Zhang, Y., Yuan, Z., Qin, W., Ghaziaskar, H.S., and Xu, C.C., *Catalytic conversion of glycerol for sustainable production of solketal as a fuel additive: A review.* Renewable and Sustainable Energy Reviews, 2016. **56**: p. 1022-1031.
10. IEA, *Renewables 2017*. 2017, IEA, Paris.
11. IEA, *Renewables 2020*. 2020, IEA, Paris.
12. WBA, *Global Bioenergy Statistics Report* 2024, World Bioenergy Association: Sweden.
13. IEA, *Renewable Energy Market Update - May 2022*. 2022, IEA, Paris.
14. IEA, *Renewables 2019*. 2019, IEA, Paris.
15. Tan, H.W., Abdul Aziz, A.R., and Aroua, M.K., *Glycerol production and its applications as a raw material: A review.* Renewable and Sustainable Energy Reviews, 2013. **27**: p. 118-127.
16. Pagliaro, M., *Glycerol: the renewable platform chemical*. 2017: Elsevier.
17. Quispe, C.A., Coronado, C.J., and Carvalho Jr, J.A., *Glycerol: production, consumption, prices, characterization and new trends in combustion.* Renewable and Sustainable Energy Reviews, 2013. **27**: p. 475-493.

18. Sandid, A., Spallina, V., and Esteban, J., *Glycerol to value-added chemicals: State of the art and advances in reaction engineering and kinetic modelling.* Fuel Processing Technology, 2024. **253**: p. 108008.

19. Ciriminna, R., Pina, C.D., Rossi, M., and Pagliaro, M., *Understanding the glycerol market.* European Journal of Lipid Science and Technology, 2014. **116**(10): p. 1432-1439.

20. Hirasawa, S., Watanabe, H., Kizuka, T., Nakagawa, Y., and Tomishige, K., *Performance, structure and mechanism of Pd–Ag alloy catalyst for selective oxidation of glycerol to dihydroxyacetone.* Journal of catalysis, 2013. **300**: p. 205-216.

21. Lee, S., Kim, H.J., Lim, E.J., Kim, Y., Noh, Y., Huber, G.W., and Kim, W.B., *Highly selective transformation of glycerol to dihydroxyacetone without using oxidants by a PtSb/C-catalyzed electrooxidation process.* Green Chemistry, 2016. **18**(9): p. 2877-2887.

22. Hu, W. and Varma, A. *Catalytic Oxidation of Glycerol to High-Value Chemical Dihydroxyacetone*. in *21st North American Catalysis Society Meeting, San Francisco, CA*. 2009.

23. Xiao, Y., Greeley, J., Varma, A., Zhao, Z.J., and Xiao, G., *An experimental and theoretical study of glycerol oxidation to 1, 3-dihydroxyacetone over bimetallic Pt-Bi catalysts.* AIChE Journal, 2017. **63**(2): p. 705-715.

24. Zhou, C.-H.C., Beltramini, J.N., Fan, Y.-X., and Lu, G.M., *Chemoselective catalytic conversion of glycerol as a biorenewable source to valuable commodity chemicals.* Chemical Society Reviews, 2008. **37**(3): p. 527-549.

25. Parmeggiani, C., Matassini, C., and Cardona, F., *A step forward towards sustainable aerobic alcohol oxidation: new and revised catalysts based on transition metals on solid supports.* Green Chemistry, 2017. **19**(9): p. 2030-2050.

26. Mallat, T. and Baiker, A., *Oxidation of alcohols with molecular oxygen on solid catalysts.* Chemical Reviews, 2004. **104**(6): p. 3037-3058.

27. Demirel, S., Lehnert, K., Lucas, M., and Claus, P., *Use of renewables for the production of chemicals: Glycerol oxidation over carbon supported gold catalysts.* Applied Catalysis B: Environmental, 2007. **70**(1-4): p. 637-643.

28. Garcia, R., Besson, M., and Gallezot, P., *Chemoselective catalytic oxidation of glycerol with air on platinum metals.* Applied Catalysis A: General, 1995. **127**(1-2): p. 165-176.

29. Gallezot, P., *Selective oxidation with air on metal catalysts.* Catalysis Today, 1997. **37**(4): p. 405-418.

30. Punniyamurthy, T., Velusamy, S., and Iqbal, J., *Recent advances in transition metal catalyzed oxidation of organic substrates with molecular oxygen.* Chemical Reviews, 2005. **105**(6): p. 2329-2364.

31. Feng, J., He, Y., Liu, Y., Du, Y., and Li, D., *Supported catalysts based on layered double hydroxides for catalytic oxidation and hydrogenation: general functionality and promising application prospects.* Chemical Society Reviews, 2015. **44**(15): p. 5291-5319.

32. Kimura, H., Tsuto, K., Wakisaka, T., Kazumi, Y., and Inaya, Y., *Selective oxidation of glycerol on a platinum-bismuth catalyst.* Applied Catalysis A: General, 1993. **96**(2): p. 217-228.

33. Nie, R., Liang, D., Shen, L., Gao, J., Chen, P., and Hou, Z., *Selective oxidation of glycerol with oxygen in base-free solution over MWCNTs supported PtSb alloy nanoparticles.* Applied Catalysis B: Environmental, 2012. **127**: p. 212-220.

34. Hu, W., Knight, D., Lowry, B., and Varma, A., *Selective oxidation of glycerol to dihydroxyacetone over Pt− Bi/C catalyst: optimization of catalyst and reaction conditions.* Industrial & Engineering Chemistry Research, 2010. **49**(21): p. 10876-10882.

35. Pollington, S.D., Enache, D.I., Landon, P., Meenakshisundaram, S., Dimitratos, N., Wagland, A., Hutchings, G.J., and Stitt, E.H., *Enhanced selective glycerol oxidation in multiphase structured reactors.* Catalysis Today, 2009. **145**(1-2): p. 169-175.

36. Dimitratos, N., Lopez-Sanchez, J.A., Lennon, D., Porta, F., Prati, L., and Villa, A., *Effect of particle size on monometallic and bimetallic (Au, Pd)/C on the liquid phase oxidation of glycerol.* Catalysis Letters, 2006. **108**(3-4): p. 147-153.

37. Sobczak, I., Jagodzinska, K., and Ziolek, M., *Glycerol oxidation on gold catalysts supported on group five metal oxides—A comparative study with other metal oxides and carbon based catalysts.* Catalysis Today, 2010. **158**(1-2): p. 121-129.

38. Villa, A., Campisi, S., Chan-Thaw, C.E., Motta, D., Wang, D., and Prati, L., *Bismuth modified Au-Pt bimetallic catalysts for dihydroxyacetone production.* Catalysis Today, 2015. **249**: p. 103-108.

39. Carrettin, S., McMorn, P., Johnston, P., Griffin, K., and Hutchings, G.J., *Selective oxidation of glycerol to glyceric acid using a gold catalyst in aqueous sodium hydroxide.* Chemical Communications, 2002(7): p. 696-697.

40. Porta, F. and Prati, L., *Selective oxidation of glycerol to sodium glycerate with gold-on-carbon catalyst: an insight into reaction selectivity.* Journal of Catalysis, 2004. **224**(2): p. 397-403.

41. Tsuji, A., Rao, K.T.V., Nishimura, S., Takagaki, A., and Ebitani, K., *Selective Oxidation of Glycerol by Using a Hydrotalcite-Supported Platinum Catalyst under Atmospheric Oxygen Pressure in Water.* ChemSusChem, 2011. **4**(4): p. 542-548.

42. Tongsakul, D., Nishimura, S., Thammacharoen, C., Ekgasit, S., and Ebitani, K., *Hydrotalcite-supported platinum nanoparticles prepared by a green synthesis method for selective oxidation of glycerol in water using molecular oxygen.* Industrial & Engineering Chemistry Research, 2012. **51**(50): p. 16182-16187.

43. Ribeiro, L.S., Rodrigues, E.G., Delgado, J.J., Chen, X., Pereira, M.F.R., and Orfao, J.J., *Pd, Pt, and Pt–Cu Catalysts Supported on Carbon Nanotube (CNT) for the Selective Oxidation of Glycerol in Alkaline and Base-Free Conditions.* Industrial & Engineering Chemistry Research, 2016. **55**(31): p. 8548-8556.

44. Wang, F.-F., Shao, S., Liu, C.-L., Xu, C.-L., Yang, R.-Z., and Dong, W.-S., *Selective oxidation of glycerol over Pt supported on mesoporous carbon nitride in base-free aqueous solution.* Chemical Engineering Journal, 2015. **264**: p. 336-343.

45. Lei, J., Duan, X., Qian, G., Zhou, X., and Chen, D., *Size effects of Pt nanoparticles supported on carbon nanotubes for selective oxidation of glycerol in a base-free condition.* Industrial & Engineering Chemistry Research, 2014. **53**(42): p. 16309-16315.

46. Demirel-Gülen, S., Lucas, M., and Claus, P., *Liquid phase oxidation of glycerol over carbon supported gold catalysts.* Catalysis Today, 2005. **102**: p. 166-172.

47. Bianchi, C.L., Canton, P., Dimitratos, N., Porta, F., and Prati, L., *Selective oxidation of glycerol with oxygen using mono and bimetallic catalysts based on Au, Pd and Pt metals.* Catalysis today, 2005. **102**: p. 203-212.

48. Brandner, A., Lehnert, K., Bienholz, A., Lucas, M., and Claus, P., *Production of biomass-derived chemicals and energy: chemocatalytic conversions of glycerol.* Topics in Catalysis, 2009. **52**(3): p. 278-287.

49. Pagliaro, M., Ciriminna, R., Kimura, H., Rossi, M., and Della Pina, C., *From glycerol to value-added products.* Angewandte Chemie International Edition, 2007. **46**(24): p. 4434-4440.

50. Tiong, A.N.T., Cheonh, P.Y.Y., Chua, W.F., Kolloju, N., Ting, J.M., and Thian, J.J., *Valorization of waste glycerol into value-added dihydroxyacetone via microbial fermentation: feasibility study.* Chemical Papers, 2024. **78**(10): p. 5905-5920.

51. *Opinion on Dihydroxyacetone (DHA) CAS N° 96-26-4*. 03-04 March 2020, Scientific Committee on Consumer Safety.

52. Garcia, A.C., Birdja, Y.Y., Tremiliosi-Filho, G., and Koper, M.T., *Glycerol electro-oxidation on bismuth-modified platinum single crystals.* Journal of Catalysis, 2017. **346**: p. 117-124.

53. Li, M.-h., Wu, J., Liu, X., Lin, J.-p., Wei, D.-z., and Chen, H., *Enhanced production of dihydroxyacetone from glycerol by overexpression of glycerol dehydrogenase in an alcohol dehydrogenase-deficient mutant of Gluconobacter oxydans.* Bioresource technology, 2010. **101**(21): p. 8294-8299.

54. Bagheri, S., Julkapli, N.M., and Yehye, W.A., *Catalytic conversion of biodiesel derived raw glycerol to value added products.* Renewable and Sustainable Energy Reviews, 2015. **41**: p. 113-127.

55. *1,3-Dihydroxyacetone Market Analysis in Global Industry, Demands, Perspective, Insights, Research and Forecast 2019-2026.* Mynewsdesk.

56. Charney, W. Process for the production of dihydroxyacetone. US4076589A, 1978.

57. Wang, J. and Yu, J. Novel method for preparing 1,3-dihydroxyacetone from glycerol. CN101412706, 2009.

58. Hong, X., Lira, C., McGiveron, O., and Miller, D. Methods for Making 1,3-Dihydroxyacetone (dha) from Glycerol. US2012014889A1, 2012.

59. Ai, Y. Method for preparing dihydroxyacetone through glycerol oxidation. CN104098455A, 2014.

60. Fang, Z., Gongde, W., Keqiang, D., Wen, S., Xianfeng, L., Xiaobo, S., and Xiaoli, W. Method for preparing dihydroxy acetone by selectively oxidizing glycerin with hydrogen peroxide. CN102432445A, 2012.

61. Spanu, P. and Ulgheri, F. Method For The Selective Oxidation Of Glycerol To Dihydroxyacetone. WO 2014/102840 A1, 2014.

62. Dong, W., Ke, Y., Li, D., Liu, C., and Yang, G. Method for producing 1,3-dihydroxyacetone through catalytic oxidation with supported gold catalyst. CN105439831A, 2016.

63. Zhao, N., Xiao, F., Wang, Y., Pu, Y., Li, F., Li, L.E.I., and Wang, F. Catalyst for preparing dihydroxyacetone through oxidation of glycerol and preparation method and application of catalyst. CN109806886, 2019.

64. He, J., Ma, H., An, Z.H.E., Song, H., Shu, X.I.N., and Xiang, X.U. Metal oxide supported gold catalyst for high-efficiency catalysis of preparation of DHA from glycerol and preparation method of catalyst. CN110252298, 2019.

65. Ke, Y., Wang, X.U.E., Li, J., Liu, H.A.I., and Yuan, H. Au/mesoporous CuO-SnO2 composite oxide catalyst and application of Au/mesoporous CuO-SnO2 composite oxide catalyst in catalytic oxidation of glycerol. CN111013605, 2020.

66. Leng, Y., Huang, N., Zhang, P., Dong, Y., and Jiang, P. Solid catalyst for synthesizing dihydroxyacetone by glycerol oxidation. CN111774087, 2020.

67. Feng, J., Li, D., Gao, M., Wang, Q., and Yang, Y. Catalyst for preparing dihydroxyacetone through selective oxidation of glycerol and preparation method of catalyst. CN115445611B, 2022.

68. Mallat, T. and Baiker, A., *Oxidation of alcohols with molecular oxygen on platinum metal catalysts in aqueous solutions.* Catalysis Today, 1994. **19**(2): p. 247-283.

69. Dodekatos, G., Schünemann, S., and Tüysüz, H., *Recent Advances in Thermo-, Photo-, and Electrocatalytic Glycerol Oxidation.* ACS Catalysis, 2018. **8**(7): p. 6301-6333.

70. Hu, X., Lu, J., Liu, Y., Chen, L., Zhang, X., and Wang, H., *Sustainable catalytic oxidation of glycerol: a review.* Environmental Chemistry Letters, 2023. **21**(5): p. 2825-2861.

71. Villa, A., Dimitratos, N., Chan-Thaw, C.E., Hammond, C., Prati, L., and Hutchings, G.J., *Glycerol oxidation using gold-containing catalysts.* Accounts of chemical research, 2015. **48**(5): p. 1403-1412.

72. Beltrán-Prieto, J.C., Kolomazník, K., and Pecha, J., *A review of catalytic systems for glycerol oxidation: alternatives for waste valorization.* Australian Journal of Chemistry, 2013. **66**(5): p. 511-521.

73. Li, J., Pan, Y., Yan, H., Ding, X., Liu, Y., Feng, X., and Yang, C., *Recent Advances in Pt-Based Ordered Intermetallic Catalysts for Glycerol Oxidation.* Industrial & Engineering Chemistry Research, 2025.

74. Liu, B. and Gao, F., *Navigating glycerol conversion roadmap and heterogeneous catalyst selection aided by density functional theory: a review.* Catalysts, 2018. **8**(2): p. 44.

75. Liu, Y., Zhang, B., Yan, D., and Xiang, X., *Recent advances in the selective oxidation of glycerol to value-added chemicals via photocatalysis/photoelectrocatalysis.* Green Chemistry, 2024.

76. Simões, M., Baranton, S., and Coutanceau, C., *Electrochemical Valorisation of Glycerol.* ChemSusChem, 2012. **5**(11): p. 2106-2124.

77. Skrzyńska, E., Zaid, S., Girardon, J.-S., Capron, M., and Dumeignil, F., *Catalytic behaviour of four different supported noble metals in the crude glycerol oxidation.* Applied Catalysis A: General, 2015. **499**: p. 89-100.

78. Hirasawa, S., Nakagawa, Y., and Tomishige, K., *Selective oxidation of glycerol to dihydroxyacetone over a Pd–Ag catalyst.* Catalysis Science & Technology, 2012. **2**(6): p. 1150-1152.

79. Villa, A., Veith, G.M., and Prati, L., *Selective oxidation of glycerol under acidic conditions using gold catalysts.* Angewandte Chemie International Edition, 2010. **49**(26): p. 4499-4502.

80. Rodrigues, E.G., Carabineiro, S.A.C., Chen, X., Delgado, J.J., Figueiredo, J.L., Pereira, M.F.R., and Órfão, J.J.M., *Selective Oxidation of Glycerol Catalyzed by Rh/Activated Carbon: Importance of Support Surface Chemistry.* Catalysis Letters, 2011. **141**(3): p. 420-431.

81. Sheldon, R.A., Arends, I., and Dijksman, A., *New developments in catalytic alcohol oxidations for fine chemicals synthesis.* Catalysis Today, 2000. **57**(1-2): p. 157-166.

82. Zhan, B.-Z., White, M.A., Sham, T.-K., Pincock, J.A., Doucet, R.J., Rao, K.R., Robertson, K.N., and Cameron, T.S., *Zeolite-confined nano-RuO2: a green, selective, and efficient catalyst for aerobic alcohol oxidation.* Journal of the American Chemical Society, 2003. **125**(8): p. 2195-2199.

83. Matsushita, T., Ebitani, K., and Kaneda, K., *Highly efficient oxidation of alcohols and aromatic compounds catalysed by the Ru-Co-Al hydrotalcite in the presence of molecular oxygen.* Chemical Communications, 1999(3): p. 265-266.

84. Zhou, C.-H., Beltramini, J.N., Lin, C.-X., Xu, Z.-P., Lu, G.M., and Tanksale, A., *Selective oxidation of biorenewable glycerol with molecular oxygen over Cu-containing layered double hydroxide-based catalysts.* Catalysis Science & Technology, 2011. **1**(1): p. 111-122.

85. Jin, X., Zhao, M., Zeng, C., Yan, W., Song, Z., Thapa, P.S., Subramaniam, B., and Chaudhari, R.V., *Oxidation of glycerol to dicarboxylic acids using cobalt catalysts.* Acs Catalysis, 2016. **6**(7): p. 4576-4583.

86. Kaminski, P., Ziolek, M., and van Bokhoven, J.A., *Mesoporous cerium–zirconium oxides modified with gold and copper–synthesis, characterization and performance in selective oxidation of glycerol.* Rsc Advances, 2017. **7**(13): p. 7801-7819.

87. Lari, G.M., Mondelli, C., and Pérez-Ramírez, J., *Gas-phase oxidation of glycerol to dihydroxyacetone over tailored iron zeolites.* ACS Catalysis, 2015. **5**(3): p. 1453-1461.

88. Mounzer, H., *Heterogeneous oxidation of alcohols*. 2009, University of Birmingham.

89. Jing, L., LI, H.-g., Ning, Z., Feng, W., and XIAO, F.-k., *Selective oxidation of glycerol to dihydroxyacetone over layer double hydroxide intercalated with sulfonato-salen metal complexes.* Journal of Fuel Chemistry and Technology, 2015. **43**(6): p. 677-683.

90. Crotti, C. and Farnetti, E., *Selective oxidation of glycerol catalyzed by iron complexes.* Journal of Molecular Catalysis A: Chemical, 2015. **396**: p. 353-359.

91. Gupta, N., Khavryuchenko, O., Villa, A., and Su, D., *Metal-Free Oxidation of Glycerol over Nitrogen-Containing Carbon Nanotubes.* ChemSusChem, 2017. **10**(15): p. 3030-3034.

92. Ulgheri, F. and Spanu, P., *An Efficient Chemical Conversion of Glycerol to Dihydroxyacetone.* ChemistrySelect, 2018. **3**(41): p. 11569-11572.

93. Zheng, Z., Luo, M., Yu, J., Wang, J., and Ji, J., *Novel process for 1, 3-dihydroxyacetone production from glycerol. 1. Technological feasibility study and process design.* Industrial & Engineering Chemistry Research, 2012. **51**(9): p. 3715-3721.

94. Painter, R.M., Pearson, D.M., and Waymouth, R.M., *Selective catalytic oxidation of glycerol to dihydroxyacetone.* Angewandte Chemie International Edition, 2010. **49**(49): p. 9456-9459.

95. Li, X., Tjiptoputro, A.K., Ding, J., Xue, J.M., and Zhu, Y., *Pd-Ce nanoparticles supported on functional Fe-MIL-101-NH2: An efficient catalyst for selective glycerol oxidation.* Catalysis Today, 2017. **279**: p. 77-83.

96. Ning, X., Li, Y., Yu, H., Peng, F., Wang, H., and Yang, Y., *Promoting role of bismuth and antimony on Pt catalysts for the selective oxidation of glycerol to dihydroxyacetone.* Journal of Catalysis, 2016. **335**: p. 95-104.

97. Motta, D., Trujillo, F.J.S., Dimitratos, N., Villa, A., and Prati, L., *An investigation on AuPt and AuPt-Bi on granular carbon as catalysts for the oxidation of glycerol under continuous flow conditions.* Catalysis Today, 2018. **308**: p. 50-57.

98. Yang, L., Li, X., Sun, Y., Yue, L., Fu, J., Lu, X., and Hou, Z., *Selective oxidation of glycerol in base-free conditions over N-doped carbon film coated carbon supported Pt catalysts.* Catalysis Communications, 2017. **101**: p. 107-110.

99. Torbina, V., Vodyankin, A., Ten, S., Mamontov, G., Salaev, M., Sobolev, V., and Vodyankina, O., *Ag-Based Catalysts in Heterogeneous Selective Oxidation of Alcohols: A Review.* Catalysts, 2018. **8**(10): p. 447.

100. Zaid, S., Skrzyńska, E., Addad, A., Nandi, S., Jalowiecki-Duhamel, L., Girardon, J.-S., Capron, M., and Dumeignil, F., *Development of silver based catalysts promoted by noble metal M (M= Au, Pd or Pt) for glycerol oxidation in liquid phase.* Topics in Catalysis, 2017. **60**(15-16): p. 1072-1081.

101. Rodrigues, E.G., Pereira, M.F., Chen, X., Delgado, J.J., and Órfão, J.J., *Influence of activated carbon surface chemistry on the activity of Au/AC catalysts in glycerol oxidation.* Journal of catalysis, 2011. **281**(1): p. 119-127.

102. Lei, J., Dong, H., Duan, X., Chen, W., Qian, G., Chen, D., and Zhou, X., *Insights into activated carbon-supported platinum catalysts for base-free oxidation of glycerol.* Industrial & Engineering Chemistry Research, 2016. **55**(2): p. 420-427.

103. Schünemann, S., Schüth, F., and Tüysüz, H., *Selective glycerol oxidation over ordered mesoporous copper aluminum oxide catalysts.* Catalysis Science & Technology, 2017. **7**(23): p. 5614-5624.

104. Xue, W., Wang, Z., Liang, Y., Xu, H., Liu, L., and Dong, J., *Promoting role of bismuth on hydrotalcite-supported platinum catalysts in aqueous phase oxidation of glycerol to dihydroxyacetone.* Catalysts, 2018. **8**(1): p. 20.

105. Pan, Y., Wu, G., He, Y., Feng, J., and Li, D., *Identification of the Au/ZnO interface as the specific active site for the selective oxidation of the secondary alcohol group in glycerol.* Journal of Catalysis, 2019. **369**: p. 222-232.

106. Zhou, J., Hu, J., Zhang, X., Li, J., Jiang, K., Liu, Y., Zhao, G., Wang, X., and Chu, H., *Facet effect of Pt nanocrystals on catalytical properties toward glycerol oxidation reaction.* Journal of Catalysis, 2020. **381**: p. 434-442.

107. Liu, B. and Greeley, J., *Decomposition pathways of glycerol via C–H, O–H, and C–C bond scission on Pt (111): A density functional theory study.* The Journal of Physical Chemistry C, 2011. **115**(40): p. 19702-19709.

108. Carrettin, S., McMorn, P., Johnston, P., Griffin, K., Kiely, C.J., and Hutchings, G.J., *Oxidation of glycerol using supported Pt, Pd and Au catalysts.* Physical Chemistry Chemical Physics, 2003. **5**(6): p. 1329-1336.

109. Dou, J., Zhang, B., Liu, H., Hong, J., Yin, S., Huang, Y., and Xu, R., *Carbon supported Pt9Sn1 nanoparticles as an efficient nanocatalyst for glycerol oxidation.* Applied Catalysis B: Environmental, 2016. **180**: p. 78-85.

110. Yanli, X., Zhendong, Z., Yang, B., and Yanfeng, L., *Studies on the synthesis of PtM/C multi-metallic bimetallic catalysts and their catalytic properties on the selective oxidation of glycerol [J].* Journal of Hainan Normal University (Natural Science), 2007. **3**: p. 013.

111. Liang, D., Shiyu, C., Jing, G., Junhua, W., Ping, C., and Zhaoyin, H., *Glycerol oxidation with oxygen over bimetallic Pt-Bi catalysts under atmospheric pressure.* Chinese Journal of Catalysis, 2011. **32**(11-12): p. 1831-1837.

112. Choi, P.-G., Nunotani, N., and Imanaka, N., *Efficient Production of Dihydroxyacetone from Glycerol over a Pt/CeO2-ZrO2-Bi2O3/SBA-16 Catalyst.* Journal of Asian Ceramic Societies, 2018(just-accepted).

113. Duan, X., Zhang, Y., Pan, M., Dong, H., Chen, B., Ma, Y., Qian, G., Zhou, X., Yang, J., and Chen, D., *SbOx-promoted Pt Nanoparticles Supported on CNTs as Catalysts for Base-free Oxidation of Glycerol to Dihydroxyacetone.* AIChE Journal, 2018.

114. Worz, N., Brandner, A., and Claus, P., *Platinum− Bismuth-Catalyzed Oxidation of Glycerol: Kinetics and the Origin of Selective Deactivation.* The Journal of Physical Chemistry C, 2009. **114**(2): p. 1164-1172.

115. Fordham, P., Garcia, R., Besson, M., and Gallezot, P., *Selective catalytic oxidation with air of glycerol and oxygenated derivatives on platinum metals*, in *Studies in Surface Science and Catalysis*. 1996, Elsevier. p. 161-170.

116. Hanna, T.A., *The role of bismuth in the SOHIO process.* Coordination chemistry reviews, 2004. **248**(5-6): p. 429-440.

117. Nunotani, N., Takashima, M., Choi, P.-G., Choi, Y.-B., and Imanaka, N., *Selective oxidation of glycerol to dihydroxyacetone using CeO2-ZrO2-Bi2O3-SnO2-supported platinum catalysts.* Journal of Asian Ceramic Societies, 2020. **8**(2): p. 470-475.

118. Ober, J.A., *Mineral commodity summaries 2018*. 2018, US Geological Survey.

119. Zhang, C., Wang, T., Liu, X., and Ding, Y., *Cu-promoted Pt/activated carbon catalyst for glycerol oxidation to lactic acid.* Journal of Molecular Catalysis A: Chemical, 2016. **424**: p. 91-97.

120. Prati, L. and Rossi, M., *Gold on carbon as a new catalyst for selective liquid phase oxidation of diols.* Journal of Catalysis, 1998. **176**(2): p. 552-560.

121. Rodrigues, E.G., Pereira, M.F., Delgado, J.J., Chen, X., and Órfão, J.J., *Enhancement of the selectivity to dihydroxyacetone in glycerol oxidation using gold nanoparticles supported on carbon nanotubes.* Catalysis Communications, 2011. **16**(1): p. 64-69.

122. Chinchilla, L.E., Olmos, C.M., Villa, A., Carlsson, A., Prati, L., Chen, X., Blanco, G., Calvino, J.J., and Hungría, A.B., *Ru-modified Au catalysts supported on ceria–zirconia for the selective oxidation of glycerol.* Catalysis Today, 2015. **253**: p. 178-189.

123. Purushothaman, R.K.P., Van Haveren, J., Van Es, D., Melián-Cabrera, I., Meeldijk, J., and Heeres, H., *An efficient one pot conversion of glycerol to lactic acid using bimetallic gold-platinum catalysts on a nanocrystalline CeO2 support.* Applied Catalysis B: Environmental, 2014. **147**: p. 92-100.

124. Sullivan, J.A. and Burnham, S., *The selective oxidation of glycerol over model Au/TiO2 catalysts—The influence of glycerol purity on conversion and product selectivity.* Catalysis Communications, 2014. **56**: p. 72-75.

125. Demirel, S., Kern, P., Lucas, M., and Claus, P., *Oxidation of mono-and polyalcohols with gold: Comparison of carbon and ceria supported catalysts.* Catalysis Today, 2007. **122**(3-4): p. 292-300.

126. Dimitratos, N., Lopez-Sanchez, J.A., Anthonykutty, J.M., Brett, G., Carley, A.F., Tiruvalam, R.C., Herzing, A.A., Kiely, C.J., Knight, D.W., and Hutchings, G.J., *Oxidation of glycerol using gold–palladium alloy-supported nanocrystals.* Physical Chemistry Chemical Physics, 2009. **11**(25): p. 4952-4961.

127. Villa, A., Jouve, A., Sanchez Trujillo, F.J., Motta, D., Prati, L., and Dimitratos, N., *Exploring the effect of au/pt ratio on glycerol oxidation in presence and absence of a base.* Catalysts, 2018. **8**(2): p. 54.

128. Liu, S.-S., Sun, K.-Q., and Xu, B.-Q., *Specific selectivity of Au-catalyzed oxidation of glycerol and other C3-polyols in water without the presence of a base.* Acs Catalysis, 2014. **4**(7): p. 2226-2230.

129. Meng, Y., Zou, S., Zhou, Y., Yi, W., Yan, Y., Ye, B., Xiao, L., Liu, J., Kobayashi, H., and Fan, J., *Activating molecular oxygen by Au/ZnO to selectively oxidize glycerol to dihydroxyacetone.* Catalysis Science & Technology, 2018. **8**(10): p. 2524-2528.

130. Villa, A., Campisi, S., Mohammed, K.M., Dimitratos, N., Vindigni, F., Manzoli, M., Jones, W., Bowker, M., Hutchings, G.J., and Prati, L., *Tailoring the selectivity of glycerol oxidation by tuning the acid–base properties of Au catalysts.* Catalysis Science & Technology, 2015. **5**(2): p. 1126-1132.

131. Brett, G.L., He, Q., Hammond, C., Miedziak, P.J., Dimitratos, N., Sankar, M., Herzing, A.A., Conte, M., Lopez-Sanchez, J.A., and Kiely, C.J., *Selective Oxidation of Glycerol by Highly Active Bimetallic Catalysts at Ambient Temperature under Base-Free Conditions.* Angewandte Chemie International Edition, 2011. **50**(43): p. 10136-10139.

132. Kondrat, S.A., Miedziak, P.J., Douthwaite, M., Brett, G.L., Davies, T.E., Morgan, D.J., Edwards, J.K., Knight, D.W., Kiely, C.J., and Taylor, S.H., *Base-Free Oxidation of Glycerol Using Titania-Supported Trimetallic Au–Pd–Pt Nanoparticles.* ChemSusChem, 2014. **7**(5): p. 1326-1334.

133. Van der Verren, M., Vykoukal, V., Styskalik, A., Malik, A.S., Aprile, C., and Debecker, D.P., *Airborne Preparation of Small Gold Nanoparticles Dispersed on Mesoporous Silica for the Catalytic Oxidation of Glycerol to Dihydroxyacetone.* ACS Applied Nano Materials, 2022. **5**(12): p. 18977-18985.

134. Ke, Y., Li, X., Li, J., Liu, C.-L., Xu, C., and Dong, W.-S., *Conversion of glycerol to dihydroxyacetone over Au catalysts on various supports.* Journal of Chemical Technology & Biotechnology, 2020. **95**(4): p. 1153-1162.

135. Ke, Y.-H., Wang, X., Qin, H.-Y., Liu, H., Yuan, H., Liu, C.-L., and Dong, W.-S., *Cu–Al composite oxides: a highly efficient support for the selective oxidation of glycerol to 1, 3-dihydroxyacetone.* New Journal of Chemistry, 2020. **44**(42): p. 18173-18184.

136. Wang, Y., Pu, Y., Yuan, D., Luo, J., Li, F., Xiao, F., and Zhao, N., *Selective Oxidation of Glycerol to Dihydroxyacetone over Au/CuxZr1–xOy Catalysts in Base-Free Conditions.* ACS Applied Materials & Interfaces, 2019. **11**(47): p. 44058-44068.

137. Wang, Y., Liu, W., Zhao, J., Wang, Z., and Zhao, N., *Oxidation of glycerol to dihydroxyacetone over highly stable Au catalysts supported on mineral-derived CuO-ZnO mixed oxide.* Applied Catalysis A: General, 2024. **671**: p. 119578.

138. An, Z., Ma, H., Han, H., Huang, Z., Jiang, Y., Wang, W., Zhu, Y., Song, H., Shu, X., Xiang, X., and He, J., *Insights into the Multiple Synergies of Supports in the Selective Oxidation of Glycerol to Dihydroxyacetone: Layered Double Hydroxide Supported Au.* ACS Catalysis, 2020. **10**(21): p. 12437-12453.

139. Chan-Thaw, C.E., Campisi, S., Wang, D., Prati, L., and Villa, A., *Selective oxidation of raw glycerol using supported AuPd nanoparticles.* Catalysts, 2015. **5**(1): p. 131-144.

140. Olmos, C.M., Chinchilla, L.E., Rodrigues, E.G., Delgado, J.J., Hungría, A.B., Blanco, G., Pereira, M.F., Órfão, J.J., Calvino, J.J., and Chen, X., *Synergistic effect of bimetallic Au-Pd supported on ceria-zirconia mixed oxide catalysts for selective oxidation of glycerol.* Applied Catalysis B: Environmental, 2016. **197**: p. 222-235.

141. Kaskow, I., Decyk, P., and Sobczak, I., *The effect of copper and silver on the properties of Au-ZnO catalyst and its activity in glycerol oxidation.* Applied Surface Science, 2018. **444**: p. 197-207.

142. Redina, E., Vikanova, K., Shesterkina, A., and Kustov, L., *Gold-Doped Fe/TiO 2 Catalysts: A Case of Extra-Low Gold Loading in Glycerol Oxidation.* Russian Journal of Physical Chemistry A, 2018. **92**(11): p. 2143-2147.

143. Zhao, G., Wu, G., Liu, Y., He, Y., Feng, J., and Li, D., *Preparation of AuPd/ZnO–CuO for the directional oxidation of glycerol to DHA.* Catalysis Science & Technology, 2020. **10**(18): p. 6223-6234.

144. Kluytmans, J., Markusse, A., Kuster, B., Marin, G., and Schouten, J., *Engineering aspects of the aqueous noble metal catalysed alcohol oxidation.* Catalysis Today, 2000. **57**(1-2): p. 143-155.

145. Aghaei, P. and Berger, R.J., *Reaction kinetics investigation of the selective oxidation of aqueous ethanol solutions with air over a Au/TiO2 catalyst.* Applied Catalysis B: Environmental, 2013. **132-133**: p. 195-203.

146. Mounzer, H.N., Wood, J., and Stitt, E.H., *Heterogeneous oxidation of 2-octanol on 5wt%Pt–1wt%Bi/Carbon catalyst.* Chemical Engineering Science, 2010. **65**(1): p. 179-185.

147. Demirel, S., Lucas, M., Wärnå, J., Salmi, T., Murzin, D., and Claus, P., *Reaction kinetics and modelling of the gold catalysed glycerol oxidation.* Topics in catalysis, 2007. **44**(1-2): p. 299-305.

148. Hu, W., Lowry, B., and Varma, A., *Kinetic study of glycerol oxidation network over Pt–Bi/C catalyst.* Applied Catalysis B: Environmental, 2011. **106**(1-2): p. 123-132.

149. Gil, S., Marchena, M., Fernández, C.M., Sánchez-Silva, L., Romero, A., and Valverde, J.L., *Catalytic oxidation of crude glycerol using catalysts based on Au supported on carbonaceous materials.* Applied Catalysis A: General, 2013. **450**: p. 189-203.

150. Díaz, J., Skrzyńska, E., Girardon, J.-S., Capron, M., Dumeignil, F., and Fongarland, P., *Glycerol oxidation in the liquid phase over a gold-supported catalyst: kinetic analysis and modelling.* ChemEngineering, 2017. **1**(1): p. 7.

151. Díaz, J.A., Skrzyńska, E., Zaid, S., Girardon, J.S., Capron, M., Dumeignil, F., and Fongarland, P., *Kinetic modelling of the glycerol oxidation in the liquid phase: comparison of Pt, Au and Ag AS active phases.* Journal of Chemical Technology & Biotechnology, 2017. **92**(9): p. 2267-2275.

152. Chida, T., Hiromori, K., Shibasaki-Kitakawa, N., Mimura, N., Yamaguchi, A., and Takahashi, A., *Comprehensive Study on Kinetic Modeling of Liquid-Phase Selective Oxidation Using Au-Supported Catalysts for Efficient Production of Value-Added Chemicals from Glycerol.* Industrial & Engineering Chemistry Research, 2023. **62**(18): p. 6932-6942.

153. Heck, K.N., Janesko, B.G., Scuseria, G.E., Halas, N.J., and Wong, M.S., *Using catalytic and surface-enhanced Raman spectroscopy-active gold nanoshells to understand the role of basicity in glycerol oxidation.* ACS Catalysis, 2013. **3**(11): p. 2430-2435.

154. Brainer, J., Sales, D., Medeiros, E., Lima Filho, N., and Abreu, C., *Wet oxidation of glycerol into fine organic acids: catalyst selection and kinetic evaluation.* Brazilian Journal of Chemical Engineering, 2014. **31**(4): p. 913-923.

155. Namdeo, A., Jhaveri, J.H., Mahajani, S.M., and Suresh, A.K., *Palladium catalyzed liquid phase oxidation of glycerol under alkaline conditions - Kinetic analysis and modelling.* Chemical Engineering Journal, 2022. **438**: p. 135424.

156. Ma, Y., Gan, J., Pan, M., Zhang, Y., Fu, W., Duan, X., Chen, W., Chen, D., Qian, G., and Zhou, X., *Reaction mechanism and kinetics for Pt/CNTs catalyzed base-free oxidation of glycerol.* Chemical Engineering Science, 2019. **203**: p. 228-236.

157. Chen, W., Wang, J., Zhang, Y., Zhang, J., Duan, X., Si, R., Chen, D., Qian, G., and Zhou, X., *Kinetics decoupling activity and selectivity of Pt nanocatalyst for enhanced glycerol oxidation performance.* AIChE Journal, 2021. **67**(10): p. e17339.

158. Tongsakul, D., Nishimura, S., and Ebitani, K., *Platinum/gold alloy nanoparticles-supported hydrotalcite catalyst for selective aerobic oxidation of polyols in base-free aqueous solution at room temperature.* ACS Catalysis, 2013. **3**(10): p. 2199-2207.

159. Wu, G., Zhao, G., Sun, J., Cao, X., He, Y., Feng, J., and Li, D., *The effect of oxygen vacancies in ZnO at an Au/ZnO interface on its catalytic selective oxidation of glycerol.* Journal of Catalysis, 2019. **377**: p. 271-282.

160. Ketchie, W.C., Fang, Y.-L., Wong, M.S., Murayama, M., and Davis, R.J., *Influence of gold particle size on the aqueous-phase oxidation of carbon monoxide and glycerol.* Journal of Catalysis, 2007. **250**(1): p. 94-101.

161. Liang, D., Gao, J., Wang, J., Chen, P., Hou, Z., and Zheng, X., *Selective oxidation of glycerol in a base-free aqueous solution over different sized Pt catalysts.* Catalysis Communications, 2009. **10**(12): p. 1586-1590.

162. Liang, D., Gao, J., Sun, H., Chen, P., Hou, Z., and Zheng, X., *Selective oxidation of glycerol with oxygen in a base-free aqueous solution over MWNTs supported Pt catalysts.* Applied Catalysis B: Environmental, 2011. **106**(3-4): p. 423-432.

163. Dimitratos, N., Messi, C., Porta, F., Prati, L., and Villa, A., *Investigation on the behaviour of Pt (0)/carbon and Pt (0), Au (0)/carbon catalysts employed in the oxidation of glycerol with*

molecular oxygen in water. Journal of Molecular Catalysis A: Chemical, 2006. **256**(1-2): p. 21-28.

164. Carrettin, S., McMorn, P., Johnston, P., Griffin, K., Kiely, C.J., Attard, G.A., and Hutchings, G.J., *Oxidation of Glycerol Using Supported Gold Catalysts.* Topics in Catalysis, 2004. **27**(1): p. 131-136.

165. Dimitratos, N., Villa, A., Prati, L., Hammond, C., Chan-Thaw, C.E., Cookson, J., and Bishop, P.T., *Effect of the preparation method of supported Au nanoparticles in the liquid phase oxidation of glycerol.* Applied Catalysis A: General, 2016. **514**: p. 267-275.

166. D'Agostino, C., Brett, G., Divitini, G., Ducati, C., Hutchings, G.J., Mantle, M.D., and Gladden, L.F., *Increased affinity of small gold particles for glycerol oxidation over Au/TiO2 probed by NMR relaxation methods.* ACS Catalysis, 2017. **7**(7): p. 4235-4241.

167. D'Agostino, C., Armstrong, R.D., Hutchings, G.J., and Gladden, L.F., *Product Inhibition in Glycerol Oxidation over Au/TiO2 Catalysts Quantified by NMR Relaxation.* ACS Catalysis, 2018. **8**(8): p. 7334-7339.

168. Kimura, H., *Selective oxidation of glycerol on a platinum-bismuth catalyst by using a fixed bed reactor.* Applied Catalysis A: General, 1993. **105**(2): p. 147-158.

169. Dimitratos, N., Lopez-Sanchez, J.A., and Hutchings, G.J., *Green catalysis with alternative feedstocks.* Topics in Catalysis, 2009. **52**(3): p. 258-268.

170. Yanfang, Z., Han, Y., Yuanyuan, M., Xuezhi, D., Gang, Q., and Xinggui, Z., *Reaction Characteristics for Base-free Oxidation of Glycerol with Oxygen over Pt-based Catalysts*, in *NINE - International Conference on Nanotechnology Based Innovative Applications for the Environment*. 2018: Rome/Italy.

171. Rodrigues, E.G., Pereira, M.F., Chen, X., Delgado, J.J., and Órfão, J.J., *Selective oxidation of glycerol over platinum-based catalysts supported on carbon nanotubes.* Industrial & Engineering Chemistry Research, 2013. **52**(49): p. 17390-17398.

172. Wang, D., Villa, A., Su, D., Prati, L., and Schlögl, R., *Carbon-supported gold nanocatalysts: shape effect in the selective glycerol oxidation.* ChemCatChem, 2013. **5**(9): p. 2717-2723.

173. Gao, J., Liang, D., Chen, P., Hou, Z., and Zheng, X., *Oxidation of glycerol with oxygen in a base-free aqueous solution over Pt/AC and Pt/MWNTs catalysts.* Catalysis letters, 2009. **130**(1-2): p. 185-191.

174. Zhang, M., Sun, Y., Shi, J., Ning, W., and Hou, Z., *Selective glycerol oxidation using platinum nanoparticles supported on multi-walled carbon nanotubes and nitrogen-doped graphene hybrid.* Chinese Journal of Catalysis, 2017. **38**(3): p. 537-544.

175. Ning, X., Zhan, L., Wang, H., Yu, H., and Peng, F., *Deactivation and regeneration of in-situ formed Bismuth-promoted Platinum catalyst for the selective oxidation of glycerol to dihydroxyacetone.* New Journal of Chemistry, 2018.

176. Zhang, M., Liang, D., Renfeng, N., Xiuyang, L., Ping, C., and Zhaoyin, H., *Oxidation of biodiesel glycerol over Pt supported on different sized carbon supports in base-free solution.* Chinese Journal of Catalysis, 2012. **33**(7-8): p. 1340-1346.

177. Xu, C., Du, Y., Li, C., Yang, J., and Yang, G., *Insight into effect of acid/base nature of supports on selectivity of glycerol oxidation over supported Au-Pt bimetallic catalysts.* Applied Catalysis B: Environmental, 2015. **164**: p. 334-343.

178. Cho, H.J., Chang, C.-C., and Fan, W., *Base free, one-pot synthesis of lactic acid from glycerol using a bifunctional Pt/Sn-MFI catalyst.* Green Chemistry, 2014. **16**(7): p. 3428-3433.

179. Cai, J., Ma, H., Zhang, J., Du, Z., Huang, Y., Gao, J., and Xu, J., *Catalytic oxidation of glycerol to tartronic acid over Au/HY catalyst under mild conditions.* Chinese Journal of Catalysis, 2014. **35**(10): p. 1653-1660.

180. Yan, H., Qin, H., Feng, X., Jin, X., Liang, W., Sheng, N., Zhu, C., Wang, H., Yin, B., and Liu, Y., *Synergistic Pt/MgO/SBA-15 nanocatalysts for glycerol oxidation in base-free medium: Catalyst design and mechanistic study.* Journal of Catalysis, 2019. **370**: p. 434-446.

181. Fu, J., He, Q., Miedziak, P.J., Brett, G.L., Huang, X., Pattisson, S., Douthwaite, M., and Hutchings, G.J., *The Role of Mg (OH) 2 in the So-Called "Base-Free" Oxidation of Glycerol with AuPd Catalysts.* Chemistry-A European Journal, 2018. **24**(10): p. 2396-2402.

182. Dodekatos, G., Abis, L., Freakley, S.J., Tüysüz, H., and Hutchings, G.J., *Glycerol Oxidation Using MgO-and Al2O3-supported Gold and Gold–Palladium Nanoparticles Prepared in the Absence of Polymer Stabilizers.* ChemCatChem, 2018. **10**(6): p. 1351-1359.

183. Jouve, A., Nagy, G., Somodi, F., Tiozzo, C., Villa, A., Balerna, A., Beck, A., Evangelisti, C., and Prati, L., *Gold-silver catalysts: Effect of catalyst structure on the selectivity of glycerol oxidation.* Journal of Catalysis, 2018. **368**: p. 324-335.

184. Li, Y. and Zaera, F., *Sensitivity of the glycerol oxidation reaction to the size and shape of the platinum nanoparticles in Pt/SiO2 catalysts.* Journal of catalysis, 2015. **326**: p. 116-126.

185. Silea, E., Chornajaa, S., Sergab, V., Lullea, I., Zhizhkunaa, S., Dubencova, K., and Kruminab, A., *Novel Pd/CeO2 and Pd-NiO/CeO2 nanocomposites' catalytic activity in glycerol oxidation processes.* Proceedings of the Estonian Academy of Sciences, 2015. **64**(3): p. 1-9.

186. Sánchez, B.S., Gross, M.S., and Querini, C.A., *Pt catalysts supported on ion exchange resins for selective glycerol oxidation. Effect of Au incorporation.* Catalysis Today, 2017. **296**: p. 35-42.

187. Montini, T., Melchionna, M., Monai, M., and Fornasiero, P., *Fundamentals and catalytic applications of CeO2-based materials.* Chemical reviews, 2016. **116**(10): p. 5987-6041.

188. Abad, A., Concepción, P., Corma, A., and García, H., *A collaborative effect between gold and a support induces the selective oxidation of alcohols.* Angewandte Chemie International Edition, 2005. **44**(26): p. 4066-4069.

189. Imanaka, N., Masui, T., Koyabu, K., Minami, K., and Egawa, T., *Significant Low-Temperature Redox Activity of Ce0. 64Zr0. 16Bi0. 20O1. 90 Supported on γ-Al2O3.* Advanced Materials, 2007. **19**(12): p. 1608-1611.

190. Takagaki, A., Tsuji, A., Nishimura, S., and Ebitani, K., *Genesis of catalytically active gold nanoparticles supported on hydrotalcite for base-free selective oxidation of glycerol in water with molecular oxygen.* Chemistry letters, 2011. **40**(2): p. 150-152.

191. Liang, D., Gao, J., Wang, J., Chen, P., Wei, Y., and Hou, Z., *Bimetallic Pt—Cu catalysts for glycerol oxidation with oxygen in a base-free aqueous solution.* Catalysis Communications, 2011. **12**(12): p. 1059-1062.

192. Villa, A., Campione, C., and Prati, L., *Bimetallic gold/palladium catalysts for the selective liquid phase oxidation of glycerol.* Catalysis letters, 2007. **115**(3-4): p. 133-136.

193. Sun, Y., Yu, Z., Chen, W., Cao, Y., Zhang, J., Duan, X., Qian, G., and Zhou, X., *PtBi Intermetallic Compounds with Enhanced Stability towards Base-Free Selective Oxidation of Glycerol.* Industrial & Engineering Chemistry Research, 2023. **62**(43): p. 17503-17512.

194. Yu, Z., Fang, J., Chen, W., Cao, Y., Zhang, J., Duan, X., Qian, G., and Zhou, X., *Construction of a uniform Pt-Bi2O3 interface to enhance selective oxidation of glycerol to dihydroxyacetone.* Chemical Engineering Science, 2025. **304**: p. 121113.

195. Avgouropoulos, G. and Tabakova, T., *Environmental catalysis over gold-based materials*. 2013: Royal Society of Chemistry.

196. Bogdanchikova, N., Tuzovskaya, I., Prati, L., Villa, A., Pestryakov, A., and Farías, M., *More insights into support and preparation method effects in gold catalyzed glycerol oxidation.* Current Organic Synthesis, 2017. **14**(3): p. 377-382.

197. Wang, D., Villa, A., Porta, F., Su, D., and Prati, L., *Single-phase bimetallic system for the selective oxidation of glycerol to glycerate.* Chemical Communications, 2006(18): p. 1956-1958.

198. Zope, B.N. and Davis, R.J., *Inhibition of gold and platinum catalysts by reactive intermediates produced in the selective oxidation of alcohols in liquid water.* Green Chemistry, 2011. **13**(12): p. 3484-3491.

199. Skrzyńska, E., Ftouni, J., Girardon, J.S., Capron, M., Jalowiecki-Duhamel, L., Paul, J.F., and Dumeignil, F., *Quasi-homogeneous oxidation of glycerol by unsupported gold nanoparticles in the liquid phase.* ChemSusChem, 2012. **5**(10): p. 2065-2078.

200. Diky, V., Muzny, C., Smolyanitsky, A., Bazyleva, A., Chirico, R., Magee, J., Paulechka, Y., Kazakov, A., Townsend, S., Lemmon, E., Frenkel, M., and Kroenlein, K., *NIST Standard Reference Database 103b - Thermodynamic Data for Pure Compounds.*

201. Dorofeeva, O.V., Vogt, N., Vogt, J., Popik, M.V., Rykov, A.N., and Vilkov, L.V., *Molecular structure and conformational composition of 1, 3-dihydroxyacetone studied by combined analysis of gas-phase electron diffraction data, rotational constants, and results of theoretical calculations. Ideal gas thermodynamic properties of 1, 3-dihydroxyacetone.* The Journal of Physical Chemistry A, 2007. **111**(28): p. 6434-6442.

202. Skrzyńska, E., Ftouni, J., Mamede, A.-S., Addad, A., Trentesaux, M., Girardon, J.-S., Capron, M., and Dumeignil, F., *Glycerol oxidation over gold supported catalysts–"Two faces" of sulphur based anchoring agent.* Journal of Molecular Catalysis A: Chemical, 2014. **382**: p. 71-78.

203. Wang, S., Li, T., Li, Y., Yin, H., Tian, Z., and Yu, H., *Enhanced Selective Oxidation of Glycerol to Dihydroxyacetone over Pt@Sn-MFI Zeolites.* Industrial & Engineering Chemistry Research, 2024. **63**(39): p. 16779-16788.

204. Zope, B.N., Davis, S.E., and Davis, R.J., *Influence of reaction conditions on diacid formation during Au-catalyzed oxidation of glycerol and hydroxymethylfurfural.* Topics in Catalysis, 2012. **55**(1-2): p. 24-32.

205. Cheng, K.K., Zhao, X.B., Zeng, J., Wu, R.C., Xu, Y.Z., Liu, D.H., and Zhang, J.A., *Downstream processing of biotechnological produced succinic acid.* Appl Microbiol Biotechnol, 2012. **95**(4): p. 841-50.

206. M. Walgode, P., D. Coelho, L.C., V. Faria, R.P., and E. Rodrigues, A.r., *Dihydroxyacetone Production: From Glycerol Catalytic Oxidation with Commercial Catalysts to Chromatographic Separation.* Industrial & Engineering Chemistry Research, 2021. **60**(29): p. 10551-10565.

207. Chen, Q. and Chen, J., *Review of the separation and purification of 1, 3-dihydroxyacetone.* Anhui Med Pharm J, 2013. **17**: p. 1271-1273.

208. Fakley, M.E. and Lindsay, R.J. Process for the isolation of dihydroxyacetone. EP0245976A1, 1987.

209. Sharma, D., *Simulated Moving Bed Technology: Overview and Use in Biorefineries.* Biorefineries-Selected Processes, 2021.

210. Rodrigues, A.E., Pereira, C.S.M., Minceva, M., Pais, L.S., Ribeiro, A.M., Ribeiro, A.E., Silva, M., Graça, N.S., and Santos, J.C., *Simulated moving bed technology: principles, design and process applications*. 1st Edition ed. 2015, Amsterdam: Butterworth-Heinemann. 304.

211. Binder, T., *Simulated moving bed chromatographic purification of amino acids.* Archer-Daniels-Midland Company, 2008: p. 18.

212. Kelliher, A., Morrison, A., Oroskar, A., Rema, R.V.N., and Agarwal, A. Simulated moving bed chromatographic separation process. US9790162B2, 2017.

213. Kelliher, A., Morrison, A., Oroskar, A., Rema, R.V.N., and Agarwal, A. SMB process for producing highly pure EPA from fish oil. US9695382B2, 2017.

214. Koop, E.P., Schwarz, M.J., and Desjonqueres, S. Method of treatment using peroxidized lipids. US6395779B1, 2002.

215. Kelliher, A., Morrison, A., Oroskar, A., Rema, R.V.N., and Agarwal, A. SMB process. US9370730B2, 2016.

216. Xie, Y.-l., Chen, P., Hou, Z.-y., and Zheng, X.-m., *Separation of dihydroxyacetone from partial oxidation product of glycerol by ion exchange resin.* Journal of Zhejiang University, Science Edition, 2007. **34**(1): p. 73.

217. Takamatsu, Y., Yamamoto, M., and Sato, Y. Method of purifying amino acid. WO2005097734A1, 2005.

218. Wheaton, R. and Lefevre, L., *Dowex Ion exchange resins: Fundamentals of Ion Exchange.* Dow Liquid Separations, 2000.

219. *DuPont Resins for Downstream Drug Purification* D.W. Solutions, Editor. July 2022, DuPont Water Solutions.

220. Coelho, L.C.D., Filho, N.M.L., Faria, R.P.V., Ribeiro, A.M., and Rodrigues, A.E., *Selection of a stationary phase for the chromatographic separation of organic acids obtained from bioglycerol oxidation.* Adsorption, 2017. **23**(5): p. 627-638.

221. Coelho, L.C.D., Filho, N.M.L., Faria, R.P.V., Ferreira, A.F.P., Ribeiro, A.M., and Rodrigues, A.E., *Separation of tartronic and glyceric acids by simulated moving bed chromatography.* Journal of Chromatography A, 2018. **1563**: p. 62-70.

222. Sá Gomes, P. and Rodrigues, A.E., *Simulated Moving Bed Chromatography: From Concept to Proof-of-Concept.* Chemical Engineering & Technology, 2012. **35**(1): p. 17-34.

223. Nicoud, R.-M., *Chromatographic Processes: modeling, simulation, and design*. Vol. 1. 2015, Cambridge: Cambridge University Press. 657.

224. Guiochon, G., Felinger, A., and Shirazi, D.G., *Fundamentals of preparative and nonlinear chromatography*. 2006: Academic Press.

225. Xie, Y., Mun, S., Kim, J., and Wang, N.H.L., *Standing wave design and experimental validation of a tandem simulated moving bed process for insulin purification.* Biotechnology progress, 2002. **18**(6): p. 1332-1344.

226. Toumi, A., Engell, S., Diehl, M., Bock, H.G., and Schlöder, J., *Efficient optimization of simulated moving bed processes.* Chemical Engineering and Processing: Process Intensification, 2007. **46**(11): p. 1067-1084.

227. Sá Gomes, P., Minceva, M., and Rodrigues, A.E., *Simulated moving bed technology: old and new.* Adsorption, 2006. **12**(5): p. 375-392.

228. Faria, R.P.V. and Rodrigues, A.E., *Instrumental aspects of Simulated Moving Bed chromatography.* Journal of Chromatography A, 2015. **1421**: p. 82-102.

229. Nicoud, R.-M., *The amazing ability of continuous chromatography to adapt to a moving environment.* Industrial & Engineering Chemistry Research, 2014. **53**(10): p. 3755-3765.

230. Broughton, D.B. and Gerhold, C.G. Continuous sorption process employing fixed bed of sorbent and moving inlets and outlets. US2985589A, 1961.

231. Carson, D.B. and Purse, F.V. Rotary valve. US3040777A, 1962.

232. Broughton, D.B. Sucrose extraction from aqueous solutions featuring simulated moving bed. US4404037A, 1983.

233. Yamashita, A. and Shoji, F. Process for separating optical isomers. US5126055A, 1992.

234. Maeda, T. and Nakazawa, I. Process for separating an organic acid or acids from an organic acid-containing solution. US5245078A, 1993.

235. Heikkilä, H., Hyöky, G., Kuisma, J., and Paananen, H. Method for fractionating a solution. US6875349B2, 2005.

236. Theoleyre, M.A. and Baudouin, S. Procede de purification d'un acide organique par chromatographie. FR2900654A1, 2007.

237. Paananen, H., Kuisma, J., Heikkilä, H., Ravanko, V., Lewandowski, J., and KÄRki, A. A simulated moving bed system. EP2316551A1, 2011.

238. Archer, R., Diamond, G.M., Dias, E.L., Murphy, V.J., Petro, M., and Super, J.D. Process for the separation of mono- and di-carboxylic acid compounds. US20130345473A1, 2013.

239. Sarmala, P., Paananen, H., Saari, P., Kekäläinen, K., and Kuisma, J. Separation process. US8951416B2, 2015.

240. Faria, R.P., Gonçalves, J.C., and Rodrigues, A.E., *Advances in Simulated Moving Bed Technology*, in *Advances in Chromatography, Volume 57*. 2020, CRC Press. p. 163-236.

241. Liang, M.-T. and Liang, R.-C., *Fractionation of polyethylene glycol particles by simulated moving bed with size-exclusion chromatography.* Journal of Chromatography A, 2012. **1229**: p. 107-112.

242. Song, S.-M., Park, M.-B., and Kim, I.H., *Three-zone simulated moving-bed (SMB) for separation of cytosine and guanine.* Korean Journal of Chemical Engineering, 2012. **29**: p. 952-958.

243. Wei, B. and Wang, S., *Separation of eicosapentaenoic acid and docosahexaenoic acid by three-zone simulated moving bed chromatography.* Journal of Chromatography A, 2020. **1625**: p. 461326.

244. Shen, B., Chen, M., Jiang, H., Zhao, Y., and Wei, F., *Modeling Study on a Three-Zone Simulated Moving Bed without Zone I.* Separation Science and Technology, 2011. **46**(5): p. 695-701.

245. Park, C., Nam, H.G., Kim, P.H., and Mun, S., *Experimental evaluation of the effect of a modified port-location mode on the performance of a three-zone simulated moving-bed process for the separation of valine and isoleucine.* Journal of separation science, 2014. **37**(11): p. 1215-1221.

246. Wankat, P.C., *Simulated Moving Bed Cascades for Ternary Separations.* Industrial & Engineering Chemistry Research, 2001. **40**(26): p. 6185-6193.

247. Kang, S.-H., Kim, J.-H., and Mun, S., *Optimal design of a tandem simulated moving bed process for separation of paclitaxel, 13-dehydroxybaccatin III, and 10-deacetylpaclitaxel.* Process Biochemistry, 2010. **45**(9): p. 1468-1476.

248. Heinonen, J., Laatikainen, M., and Sainio, T., *Chromatographic fractionation of a ternary mixture with an SMB cascade process: The effect of ion exchange resin cross-linkage on separation efficiency.* Separation and Purification Technology, 2018. **206**: p. 286-296.

249. Jo, S.H., Kim, J.K., Yoo, C.G., Kim, J.I., Koo, Y.M., and Mun, S., *Comparative Analysis of Single-Cascade Five-Zone and Two-Zone SMB Systems for the Separation of a Ternary Amino Acid Mixture.* The Canadian Journal of Chemical Engineering, 2007. **85**(6): p. 874-882.

250. Park, H., Kim, J.W., Lee, K.B., and Mun, S., *Comparison of the process performances of a tandem 4-zone SMB and a single-cascade 5-zone SMB for separation of galactose, levulinic acid, and 5-hydroxymethylfurfural in agarose hydrolyzate.* Separation and Purification Technology, 2020. **237**: p. 116357.

251. Kim, J.K. and Wankat, P.C., *Designs of simulated-moving-bed cascades for quaternary separations.* Industrial & engineering chemistry research, 2004. **43**(4): p. 1071-1080.

252. Kang, H.-J., Jo, C.Y., and Mun, S., *Strategies to reduce the extent of product dilution in a tandem simulated-moving-bed process for ternary separation without loss of throughput.* Applied Energy, 2023. **330**: p. 120376.

253. Masuda, T., Sonobe, T., Matsuda, F., and Horie, M., *Process for fractional separation of multi-component fluid mixture*. 1993, Google Patents.

254. Navarro, A., Caruel, H., Rigal, L., and Phemius, P., *Continuous chromatographic separation process: simulated moving bed allowing simultaneous withdrawal of three fractions.* Journal of chromatography A, 1997. **770**(1-2): p. 39-50.

255. Beste, Y.A. and Arlt, W., *Side-stream simulated moving-bed chromatography for multicomponent separation.* Chemical engineering & technology, 2002. **25**(10): p. 956-962.

256. Chiang, A.S., *Continuous chromatographic process based on SMB technology.* American Institute of Chemical Engineers. AIChE Journal, 1998. **44**(8): p. 1930.

257. Wooley, R., Ma, Z., and Wang, N.-H., *A nine-zone simulating moving bed for the recovery of glucose and xylose from biomass hydrolyzate.* Industrial & engineering chemistry research, 1998. **37**(9): p. 3699-3709.

258. Beste, Y.A. and Arlt, W., *Side-Stream Simulated Moving-Bed Chromatography for Multicomponent Separation.* Chemical Engineering & Technology, 2002. **25**(10): p. 956-962.

259. Xie, Y., Chin, C.Y., Phelps, D.S.C., Lee, C.-H., Lee, K.B., Mun, S., and Wang, N.-H.L., *A Five-Zone Simulated Moving Bed for the Isolation of Six Sugars from Biomass Hydrolyzate.* Industrial & Engineering Chemistry Research, 2005. **44**(26): p. 9904-9920.

260. Masuda, T., Sonobe, T., Matsuda, F., and Horie, M. Process for fractional separation of multi-component fluid mixture. US5198120A, 1993.

261. Borges da Silva, E.A. and Rodrigues, A.E., *Design of chromatographic multicomponent separation by a pseudo-simulated moving bed.* AIChE Journal, 2006. **52**(11): p. 3794-3812.

262. Mun, S., *Enhanced separation performance of a five-zone simulated moving bed process by using partial collection strategy based on alternate opening and closing of a product port.* Industrial & engineering chemistry research, 2010. **49**(19): p. 9258-9270.

263. Paredes, G., Abel, S., Mazzotti, M., Morbidelli, M., and Stadler, J., *Analysis of a Simulated Moving Bed Operation for Three-Fraction Separations (3F-SMB).* Industrial & Engineering Chemistry Research, 2004. **43**(19): p. 6157-6167.

264. Abel, S., U. Bäbler, M., Arpagaus, C., Mazzotti, M., and Stadler, J., *Two-fraction and three-fraction continuous simulated moving bed separation of nucleosides.* Journal of Chromatography A, 2004. **1043**(2): p. 201-210.

265. Nicolaos, A., Muhr, L., Gotteland, P., Nicoud, R.-M., and Bailly, M., *Application of the equilibrium theory to ternary moving bed configurations (4+4, 5+4, 8 and 9 zones): II. Langmuir case.* Journal of Chromatography A, 2001. **908**(1): p. 87-109.

266. Wooley, R., Ma, Z., and Wang, N.H.L., *A Nine-Zone Simulating Moving Bed for the Recovery of Glucose and Xylose from Biomass Hydrolyzate.* Industrial & Engineering Chemistry Research, 1998. **37**(9): p. 3699-3709.

267. Mata, V.G. and Rodrigues, A.E., *Separation of ternary mixtures by pseudo-simulated moving bed chromatography.* J Chromatogr A, 2001. **939**(1-2): p. 23-40.

268. Lee, J.W. and Wankat, P.C., *Design of pseudo-simulated moving bed process with multi-objective optimization for the separation of a ternary mixture: Linear isotherms.* Journal of Chromatography A, 2010. **1217**(20): p. 3418-3426.

269. Sayama, K., Kamada, T., Oikawa, S., and Masuda, T., *Production of raffinose: a new byproduct of the beet sugar industry.* 1992.

270. Mata, V.G. and Rodrigues, A.r.E., *Separation of ternary mixtures by pseudo-simulated moving bed chromatography.* Journal of Chromatography A, 2001. **939**(1): p. 23-40.

271. Borges da Silva, E.A., Pedruzzi, I., and Rodrigues, A.E., *Simulated moving bed technology to improve the yield of the biotechnological production of lactobionic acid and sorbitol.* Adsorption, 2011. **17**(1): p. 145-158.

272. Jiang, C., Huang, F., and Wei, F., *A pseudo three-zone simulated moving bed with solvent gradient for quaternary separations.* Journal of Chromatography A, 2014. **1334**: p. 87-91.

273. Wei, F., Li, M., Huang, F., Chen, M., Jiang, H., and Zhao, Y., *A novel pseudo simulated moving bed with solvent gradient for ternary separations.* Journal of Chromatography A, 2011. **1218**(20): p. 2906-2911.

274. Wei, F., Shen, B., Chen, M., and Zhao, Y., *Study on a pseudo-simulated moving bed with solvent gradient for ternary separations.* Journal of Chromatography A, 2012. **1225**: p. 99-106.

275. Beaudouin, S. and Lancrenon, X., *Désucrage des égoûts et des mélasses. Le" SSMB"(Sequential Simultaed Moving Bed ou Simulation de Lit Mobile Séquencé) est une nouvelle avancée technologique dans le développement de la chromatographie.* Industries Alimentaires et Agricoles (France), 2003. **120**(7).

276. David, L., Yun, J., and Nicoud, R.-M., *Comparing multi-column chromatographic processes for purifying monosaccharides part I: A simplified approach.* Adsorption, 2017. **23**(4): p. 577-591.

277. Zhang, X., Liu, J., Ray, A.K., and Li, Y., *Research Progress on the Typical Variants of Simulated Moving Bed: From the Established Processes to the Advanced Technologies.* Processes, 2023. **11**(2): p. 508.

278. Jermann, S., Katsuo, S., and Mazzotti, M., *Intermittent Simulated Moving Bed Processes for Chromatographic Three-Fraction Separation.* Organic Process Research & Development, 2012. **16**(2): p. 311-322.

279. Lee, J.W., *Expanding Simulated Moving Bed Chromatography into Ternary Separations in Analogy to Dividing Wall Column Distillation.* Industrial & Engineering Chemistry Research, 2020. **59**(20): p. 9619-9628.

280. Lee, J.W., *Double-Layer Simulated Moving Bed Chromatography for Ternary Separations: Serialized Layer Configurations.* Industrial & Engineering Chemistry Research, 2021. **60**(24): p. 8911-8926.

281. Lee, J.W., Zarei, S., Kienle, A., and Seidel-Morgenstern, A., *Short-Cut Design of Double-Layer Simulated Moving Bed Chromatography for Continuous Ternary Mixture Separation: Langmuir Isotherms.* Industrial & Engineering Chemistry Research, 2024. **63**(39): p. 16873-16884.

282. Ströhlein, G., Aumann, L., Mazzotti, M., and Morbidelli, M., *A continuous, counter-current multi-column chromatographic process incorporating modifier gradients for ternary separations.* Journal of Chromatography A, 2006. **1126**(1): p. 338-346.

283. Pfister, D., Nicoud, L., and Morbidelli, M., *Continuous biopharmaceutical processes: chromatography, bioconjugation, and protein stability*. 2018: Cambridge University Press.

284. Krättli, M., Steinebach, F., and Morbidelli, M., *Online control of the twin-column countercurrent solvent gradient process for biochromatography.* Journal of chromatography A, 2013. **1293**: p. 51-59.

285. Steinebach, F., Müller-Späth, T., and Morbidelli, M., *Continuous counter-current chromatography for capture and polishing steps in biopharmaceutical production.* Biotechnology Journal, 2016. **11**(9): p. 1126-1141.

286. Ng, C.K.S., Rousset, F., Valery, E., Bracewell, D.G., and Sorensen, E., *Design of high productivity sequential multi-column chromatography for antibody capture.* Food and Bioproducts Processing, 2014. **92**(2): p. 233-241.

287. Holzer, M., Osuna-Sanchez, H., and David, L., *Multicolumn chromatography.* BioProcess International, 2008. **6**(8): p. 74-84.

288. Yu, Y., Wood, K.R., and Liu, Y.A., *Simulation and Comparison of Operational Modes in Simulated Moving Bed Chromatography.* Industrial & Engineering Chemistry Research, 2015. **54**(46): p. 11576-11591.

289. Borges da Silva, E. and Rodrigues, A., *Design methodology and performance analysis of a pseudo-simulated moving bed for ternary separation.* Separation Science and Technology, 2008. **43**(3): p. 533-566.

290. Agrawal, G. and Kawajiri, Y., *Comparison of various ternary simulated moving bed separation schemes by multi-objective optimization.* Journal of Chromatography A, 2012. **1238**: p. 105-113.

291. Agrawal, G., Sreedhar, B., and Kawajiri, Y., *Systematic optimization and experimental validation of ternary simulated moving bed chromatography systems.* Journal of Chromatography A, 2014. **1356**: p. 82-95.

292. Rajendran, A., Paredes, G., and Mazzotti, M., *Simulated moving bed chromatography for the separation of enantiomers.* Journal of Chromatography A, 2009. **1216**(4): p. 709-738.

293. Li, Y., Xu, J., Yu, W., and Ray, A.K., *Multi-objective optimization of sequential simulated moving bed for the purification of xylo-oligosaccharides.* Chemical Engineering Science, 2020. **211**: p. 115279.

294. Nicolaos, A., Muhr, L., Gotteland, P., Nicoud, R.-M., and Bailly, M., *Application of equilibrium theory to ternary moving bed configurations (four+four, five+four, eight and nine zones): I. Linear case.* Journal of Chromatography A, 2001. **908**(1): p. 71-86.

295. Santos da Silva, F.V. and Seidel-Morgenstern, A., *Evaluation of center-cut separations applying simulated moving bed chromatography with 8 zones.* Journal of Chromatography A, 2016. **1456**: p. 123-136.

296. Soepriatna, N., Wang, N.H.L., and Wankat, P.C., *Standing Wave Design and Optimization of Nonlinear Four-Zone Thermal Simulated Moving Bed Systems.* Industrial & Engineering Chemistry Research, 2015. **54**(42): p. 10419-10433.

297. Harvey, D., Ding, Y., and Wang, N.-H.L., *Standing-wave Design of Three-Zone, open-loop non-isocratic SMB for purification.* BMC Chemical Engineering, 2019. **1**(1): p. 17.

298. Sainio, T., *Unified Design of chromatographic processes with timed events: Separation of ternary mixtures.* Chemical Engineering Science, 2016. **152**: p. 547-567.

299. Hritzko, B.J., Xie, Y., Wooley, R.J., and Wang, N.H.L., *Standing-wave design of tandem SMB for linear multicomponent systems.* AIChE journal, 2002. **48**(12): p. 2769-2787.

300. Siitonen, J. and Sainio, T., *Unified design of chromatographic separation processes.* Chemical Engineering Science, 2015. **122**: p. 436-451.

301. Sainio, T., *Unified design of chromatographic separation processes: Partial separations and waste fractions.* Chemical Engineering Science, 2021. **234**: p. 116457.

302. Minceva, M. and Rodrigues, A.E., *Two-level optimization of an existing SMB for p-xylene separation.* Computers & Chemical Engineering, 2005. **29**(10): p. 2215-2228.

303. Matos, J., Faria, R.P.V., Nogueira, I.B.R., Loureiro, J.M., and Ribeiro, A.M., *Optimization strategies for chiral separation by true moving bed chromatography using Particles Swarm Optimization (PSO) and new Parallel PSO variant.* Computers & Chemical Engineering, 2019. **123**: p. 344-356.

304. Matos, J., Faria, R.P.V., Loureiro, J.M., Ribeiro, A.M., and Nogueira, I.B.R., *Optimal Design of SMB Units: A Novel Strategy Based on Particles Swarm Optimization.* IFAC-PapersOnLine, 2021. **54**(3): p. 548-553.

305. Zhang, Z., Hidajat, K., Ray, A.K., and Morbidelli, M., *Multiobjective optimization of SMB and varicol process for chiral separation.* AIChE Journal, 2002. **48**(12): p. 2800-2816.

306. Heinonen, J., Kukkonen, S., and Sainio, T., *Evolutionary multi-objective optimization based comparison of multi-column chromatographic separation processes for a ternary separation.* Journal of Chromatography A, 2014. **1358**: p. 181-191.

307. Santos, R.V., Rebello, C.M., Prudente, A., Santana, V.V., Ribeiro, A.M., Rodrigues, A.E., Loureiro, J.M., Pontes, K.V., and Nogueira, I.B., *A nested loop for simultaneous model topology screening, parameters estimation, and identification of the optimal number of experiments: Application to a Simulated Moving Bed unit.* arXiv preprint arXiv:2209.09133, 2022.

3. Catalyst Screening for Glycerol Oxidation into Dihydroxyacetone

This chapter presents the screening of commercial catalysts to identify the most suitable options for the selective oxidation of glycerol into dihydroxyacetone (DHA). Four catalysts were evaluated: one platinum-based catalyst supported on activated carbon, two platinum-bismuth catalysts on activated carbon, and one gold catalyst supported on zinc oxide. Experiments were conducted under base-free conditions in a fed-batch reactor, using an aqueous glycerol solution and molecular oxygen as the oxidant.

Part of this chapter was adapted from Walgode, P. M., Coelho, L. C. D., Faria, R. P. V., & Rodrigues, A. E. (2021). Dihydroxyacetone production: from glycerol catalytic oxidation with commercial catalysts to chromatographic separation. Industrial & Engineering Chemistry Research, 60(29), 10551-10565. DOI https://doi.org/10.1021/acs.iecr.1c00275

3.1. Introduction

The partial oxidation of glycerol is a relevant valorisation route, producing high-value products, such as dihydroxyacetone (DHA), which is obtained by the selective oxidation of glycerol's secondary hydroxyl group, or glyceraldehyde, which is formed by primary hydroxyl group oxidation. These products can undergo further oxidation to generate a variety of compounds, including organic acids such as glyceric acid (GCA), hydroxypyruvic acid (HPA), tartronic acid (TTA), glycolic acid (GCO), and oxalic acid (OXA). The reaction pathway for glycerol oxidation is complex, as shown in Figure 3.1. Glyceraldehyde, hydroxypiruvic acid, mesoxalic acid and glycoxalic acid were not quantified in this chapter. Reaction selectivity is influenced by the catalyst choice, reaction conditions, such as reactant ratios, temperature, among others, and the reaction media composition (solvent, pH, etc.).

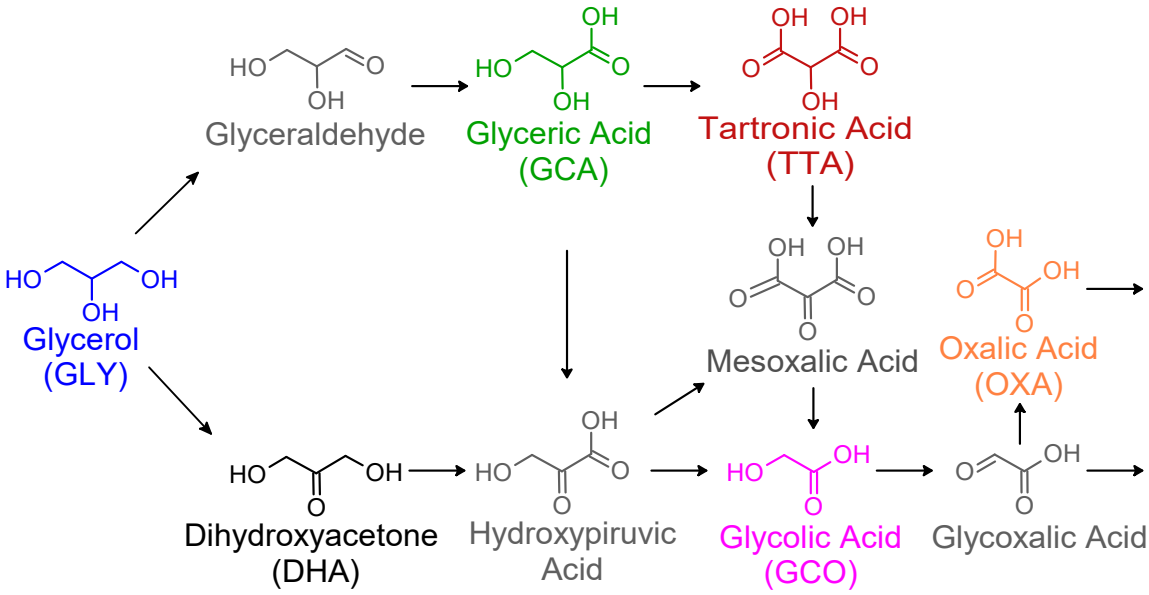

Figure 3.1. Reaction scheme of the glycerol catalytic oxidation.

Operating under base-free conditions is critical, as it suppresses terminal hydroxyl group oxidation, thereby enhancing DHA selectivity while minimising the formation of undesired byproducts such as glyceric acid [1, 2]. Additionally, base-free conditions avoid the formation of acid salts, which can precipitate, representing a challenge in industrial operation [3, 4]. Another critical factor in favour of operating under base-free conditions is that DHA is unstable at higher pH values [2, 5]. For Pt-Bi catalysts, low pH (≈ 2-4) drastically increases DHA production compared to neutral pH. These pH values are quickly attained during glycerol oxidation as the reaction byproducts are organic acids [2, 5].

The selective oxidation of glycerol can be homogeneously or heterogeneously catalysed, with the latter being more attractive for industrial applications due to the ease of separation and reuse

[6]. In a groundbreaking study in 1993, Kimura et al. demonstrated that doping Pt/C catalysts with Bi significantly increased DHA selectivity from 10% to 80% under acidic conditions [5]. Since then, Pt-Bi/AC catalysts have been among the most well-studied for DHA production, achieving yields up to 48% [5, 7-11]. Studies also explored optimising metal loadings, doping Pt with different metals, such as Sb, Pd, or Au; using different support materials, including mesoporous materials (e.g., SBA-15, MCM-41) and nitrogen-doped carbon nanotubes, and different preparation methods [1, 11-16]. These studies helped reveal the synergistic effects of electronic and morphological modifications induced by Bi or Sb on Pt to enhance DHA selectivity while minimising deactivation. Comprehensive reviews on platinum-group catalysts for glycerol oxidation provide further insights into this area [4, 17, 18].

Gold-based catalysts are another promising option for glycerol selective oxidation. Until the 1980s, gold was considered catalytically inert, as it was thought to be unable to chemisorb or dissociate O_2 or H_2 [19], when it was discovered that finely dispersed gold nanoparticles (≈ 2 to 4 nm) exhibit high catalytic activity under mild conditions, making them suitable for oxidation reactions in gas and liquid phases [19], including glycerol oxidation [20]. The catalyst preparation method is critical, with co-precipitation methods producing smaller and more active nanoparticles than conventional impregnation techniques [19]. Strong basic conditions were considered to be mandatory for glycerol oxidation with gold catalysts, with Au nanoparticles supported on carbon materials [20-30] or metal oxides (e.g., TiO_2, Al_2O_3, CeO_2) [1, 3, 27, 29-33] demonstrating excellent activity. However, since DHA is unstable under basic conditions, it was not produced, and the reaction selectivity shifted towards glyceraldehyde and its overoxidation products. These catalysts were inactive under base-free conditions [20, 29].

This barrier was overcome in 2014 when Liu et al. reported high DHA yields using Au nanoparticles supported on transition metal oxides under base-free conditions [31]. When thermally activated under oxidative conditions (airflow), metal oxide overlayers and oxygen vacancies at the Au-MOx interface formed, acting as active sites for glycerol selective oxidation. Au/ZnO and Au/CuO demonstrated superior performance due to their ability to activate O_2 effectively and stabilise intermediate species [31].

Most studies focused on lab-made catalysts, with a limited investigation on commercially available Pt-Bi/AC catalysts [2, 34]. Patents for DHA production are available, but either other oxidants rather than oxygen are used [35-37] or glycerol must react with protecting agents before oxidation to block the oxidation of the terminal hydroxyl groups [38, 39]. To the best of our knowledge, only one patent claims DHA production through glycerol aerobic oxidation, using Au nanoparticles supported in ZnO, Cu-Al hydrotalcite, or Cu-Al spinel, with DHA yields up to 75% [39].

This work aims to fill this gap by evaluating the performance of commercial catalysts for the selective oxidation of glycerol to DHA under base-free conditions, specifically, three Pt/AC with varying Bi loadings (0, 1.5, and 5 wt.%) and Au/ZnO. The study presented in this chapter aims to provide new insights into the catalytic performance, stability, and potential industrial application of these commercial catalysts, contributing to the development of efficient and scalable processes for DHA production.

3.2. Experimental Description

3.2.1. Chemicals and Materials

For the catalyst screening, glycerol (GLY ≥ 99.5%, Fisher Scientific), deionised water provided by the laboratory purification systems, N_2 (purity ≥ 99,999% Linde), and O_2 (purity ≥ 99.9995%, AIR LIQUIDE - ALPHAGAZ^{TM}) were used. For the development of the High-Performance Liquid Chromatography (HPLC) analytical method, OXA (≥ 99.5%, ACROS Organics), TTA (≥ 97%, Sigma-Aldrich), GCA (20% in water, Tokyo Chemical Industry Co., Ltd.), GCO (≥ 99%, Fisher Scientific), and DHA (≥ 98%, Merck) were used.

3.2.2. Commercial Catalysts

The catalysts tested were: 5 wt.% Pt supported in AC, denoted Pt5/AC (Figure 3.2), from Sigma-Aldrich; 5 wt.% Pt doped with 1.5 wt.% Bi, denoted Pt5-Bi1.5/AC, from Johnson-Matthey; and 5 wt.% Pt doped with 5 wt.% Bi denoted Pt5-Bi5/AC, from Evonik. These catalysts were used as received in the reduced form and powder shape.

Figure 3.2. Pt5/AC from Sigma-Aldrich in powder form.

A commercial 1 wt.% Au supported on ZnO (AURO*lite*™), supplied by Strem Chemicals, denoted Au1/ZnO, was also used. The catalyst, shipped as dark purple granulates with 1-2 mm diameter, was ground and sieved for a particle size inferior to 100 µm. After that, it was dried at 105 °C overnight and then activated under air K flow at a rate of 200 ml/min at 300°C for 4 hours (2 °C/min heat ramp). Figure 3.3 shows both fresh and activated catalysts.

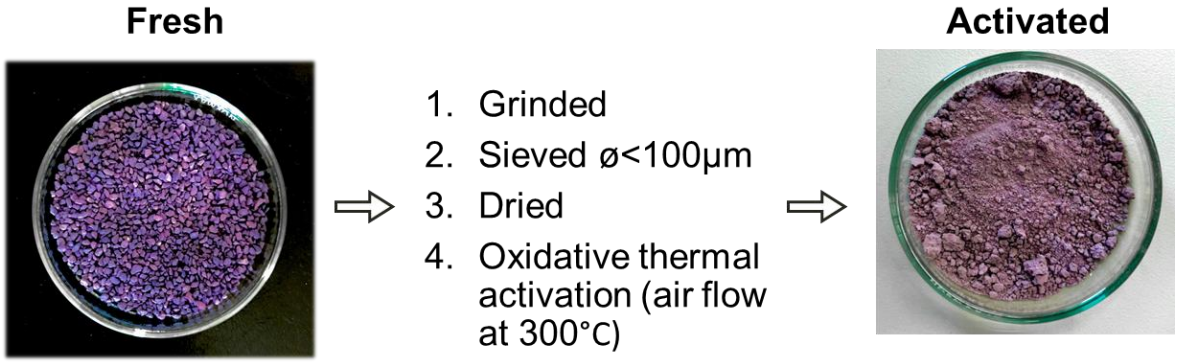

Figure 3.3. Oxidative thermal activation of Au1/ZnO from Strem Chemicals.

3.2.3. Catalysts Characterisation

The best catalysts for DHA production, Pt5-Bi1.5/AC and Au/ZnO (results discussed in Section 3.3.3), were characterised using textural, morphological, and structural analysis techniques. These characterisations were complemented by data available in the open literature.

The particle size distribution of both catalysts was determined using laser diffraction with a Beckman Coulter LS230 particle size analyser (USA), applying the Fraunhofer theory of light scattering. This analysis provided volume-based particle size distributions and average diameters.

For the Pt5-Bi1.5/AC catalyst, the textural properties of fresh and spent samples were evaluated at the *Laboratorio de Sólidos Porosos, University of Málaga*. Before analysis, samples were vacuum-dried at 150 °C for 12 h. Nitrogen adsorption-desorption isotherms were measured at 77 K using an ASAP 2420 analyser (Micromeritics, USA). The Brunauer, Emmett, and Teller (BET) method was applied to determine the specific surface area, and pore size distribution and micropore volume were calculated using the original Density Functional Theory (DFT). To further investigate microporosity, CO_2 adsorption-desorption isotherms were measured at 273 K using the same equipment.

Mercury intrusion porosimetry was used to determine the apparent particle density (ρ_p), employing an AutoPore IV 9500 Series (Micromeritics, USA) instrument operated up to 206.5 MPa with a 10 s equilibration time. The solid density (ρ_s) was obtained via helium pycnometry using an AccuPyc II 1340 (Micromeritics, USA).

For the Au1/ZnO catalyst, morphological and structural features were analysed at CICECO using scanning transmission electron microscopy (STEM). A Hitachi HD-2700 STEM microscope equipped with a 200 kV energy-dispersive spectroscopy (EDS, Bruker) detector was employed. Samples were prepared by depositing catalyst suspensions onto carbon-coated copper grids and allowing them to dry by evaporation. Detailed imaging was performed via high-resolution TEM, high-angle annular dark field STEM, and elemental mapping. Particle size histograms were generated using ImageJ software, fitting a Gaussian distribution to the dominant size peak.

3.2.4. Catalyst Screening for Glycerol Oxidation

Glycerol oxidation experiments were carried out under base-free conditions using a continuous flow of O_2 in a fed-batch stainless steel reactor. Initial trials were performed in a 400 mL reactor, but the significant catalyst mass required for each run was impractical due to the high cost of the catalysts, while small lab-made reactors available revealed time-consuming cleaning operations and sealing problems.

A custom reactor was designed and assembled by a local metalworking company to address these challenges. The fed-batch reactor unit in 316 stainless steel has a total volume of 250 mL and operates with a liquid volume from 50 to 200 mL, temperature up to 150 °C and pressure up to 30 bar. It was designed for rapid and easy cleaning between experiments while maintaining a reliable sealing system. The unit is represented in Figure 3.4.

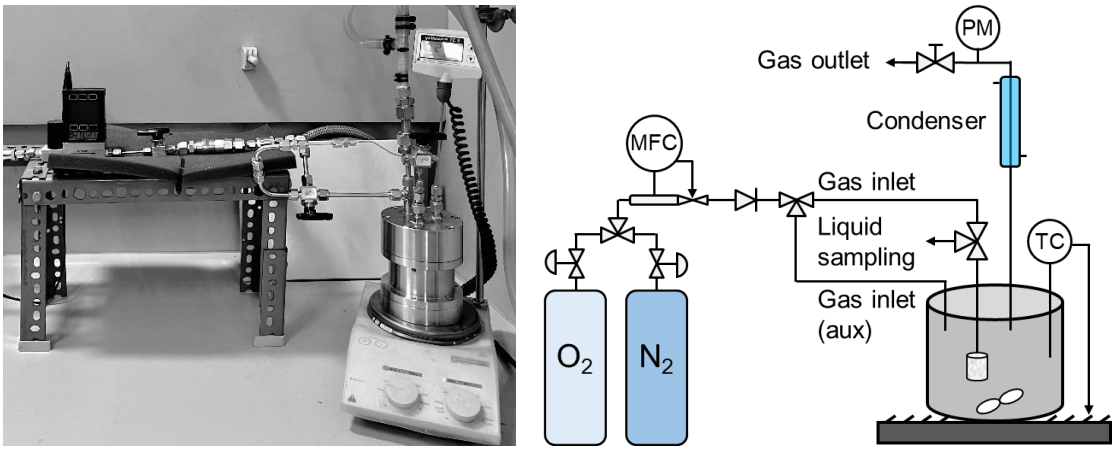

Figure 3.4. Fed-batch reactor for glycerol oxidation tests.

The inlet gas (O_2 or N_2) was selected using a three-port two-way valve, and a mass flow controller (Allicat) was used to set the desired volumetric flow. Gas was bubbled directly into the liquid medium through an inlet line with a sintered disperser. This line also served as the liquid sampling port via a three-way valve, avoiding catalyst loss and ensuring thorough cleaning. The

dead volume of the sampling line was negligible (< 200 μL). Nevertheless, the line was properly rinsed before collecting any samples.

The magnetic stirrer was set to 800 rpm. Temperature control was achieved through a heating plate connected to a thermocouple inserted into the reactor, which was wrapped in an insulation blanket to minimise heat loss and temperature gradients. The reactor pressure was monitored by a pressure gauge and manually regulated using a needle valve. A condenser in the gas outlet line minimised the loss of volatiles.

For each experiment, the reactor was charged with 100 mL of a glycerol aqueous solution and the catalyst, then sealed and purged with N_2 to ensure an inert atmosphere. The stirring and heating systems were turned on, and once the temperature (353 K) and pressure (4.5 bar for Pt catalysts; 6.5 bar for Au/ZnO) setpoints were reached, the gas was switched to O_2 at a flow rate of 200 STP mL min^{-1} to initiate the oxidation reaction. Liquid samples were periodically collected (≈ 300 μL), diluted, and analysed by HPLC. The pH of the samples was measured using a pH indicator. Sampling frequency was reduced for longer reaction times to reduce significant changes in the reaction volume.

3.2.5. HPLC Analytical Method

The main species obtained in the liquid phase from glycerol oxidation were quantified using a Prominence HPLC system (Shimadzu, Japan) equipped with a diode array detector (210 nm and 260 nm), a refraction index detector (RI), and an Alltech Organic Acid OA-1000 analytical column (7.8 x 300 mm, Hichrom, UK), kept at 333 K by a column oven. This temperature was selected as a compromise to reduce operating pressure (≈ 37 bar), enhance peak resolution, and remain within the column's maximum recommended operating temperature of 80–85 °C. The mobile phase consisted of a 5 mM H_2SO_4 aqueous solution, as recommended by the manufacturer, previously filtered and degassed, and delivered at the maximum recommended flow rate of 0.8 mL min^{-1}. A 20 μL injection loop was used for sample introduction.

Calibration curves for each compound were obtained by injecting individually prepared standard solutions at various concentrations within the appropriate working range. These standards were diluted with the eluent (1:30) before injection.

3.3. Results and Discussion

3.3.1. HPLC analytical method

The calibration method used in this study was challenging due to the wide variety of products formed during glycerol oxidation, with some studies focusing on developing and optimising HPLC analytical methods specifically tailored for this system [40-43]. The calibration curves are detailed in Appendix A.

When quantifying mixtures, most aldehydes and organic acids showed reasonably well-resolved peaks in both the RI and the UV-Vis (set at a wavelength of 210 nm) detectors. Glycerol, however, could only be detected with the RI detector, where its peak overlapped with that of DHA (see Figure A.2 in Appendix A). Notably, DHA exhibited a well-resolved peak in the UV-Vis detector at 260 nm, where almost no other compounds were detected except for oxalic acid (OXA), which elutes much earlier (see Figure A.3 in Appendix A). Therefore, GLY quantification was performed indirectly: after determining the DHA concentration via its calibration curve at 260 nm, its corresponding RI contribution was subtracted from the combined GLY+DHA signal in the RI chromatogram.

All calibration curves demonstrated excellent linearity over the studied concentration ranges ($r^2 > 0.999$). Additional compounds, namely glyoxylic acid, pyruvic acid, formic acid, and lactic acid, were injected to aid in peak identification during chromatographic analysis. However, their calibration curves were not established since these species were only detected in minor amounts.

3.3.2. Catalysts Characterisation

Figure 3.5. shows the particle size distribution of the Pt5-Bi1.5/AC and Au1/ZnO catalysts.

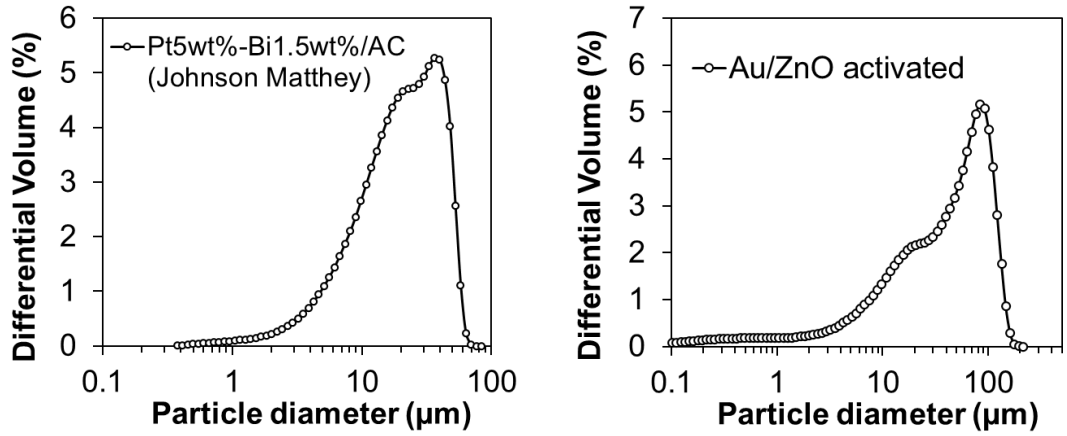

Figure 3.5. Particle size distribution: Left) Pt5-Bi1.5/AC; Right) Au1/ZnO.

The mean particle diameter for Pt5-Bi1.5/AC was 24.3 µm ± 14.8 µm, while that of Au1/ZnO was larger, 54.98 µm ± 40.91 µm. In both cases, particle sizes exceeded 0.5 µm, as confirmed by the absence of catalyst particles in the liquid samples collected from the reactor, which had a 0.5 µm filter in the sampling line. The particle size distributions were approximately monomodal for both catalysts.

Additional particle size data for Pt5-Bi5/AC and Pt5/AC are provided in Appendix B. Their mean particle diameters were 20.5 ± 12.5 µm and 28.4 ± 18.0 µm, respectively. These catalysts were not further characterised, as their performance in DHA production was less promising than that of Pt5-Bi1.5/AC and Au/ZnO, as discussed in Section 3.3.3. Additional characterisation of Pt5/AC by H_2 chemisorption and N_2 physisorption can be found elsewhere [44].

Additional characterisation data was obtained for the best-performing catalysts, Pt5-Bi1.5/AC and Au/ZnO. Because some data was already available in the open literature, the analysis performed on each catalyst was distinct to cover the information missing.

3.3.2.1. Pt5-Bi1.5/AC

The N_2 adsorption isotherms at 77 K and the corresponding pore size distributions for the Pt-Bi/AC catalyst before and after the reaction are presented in Figure 3.6.

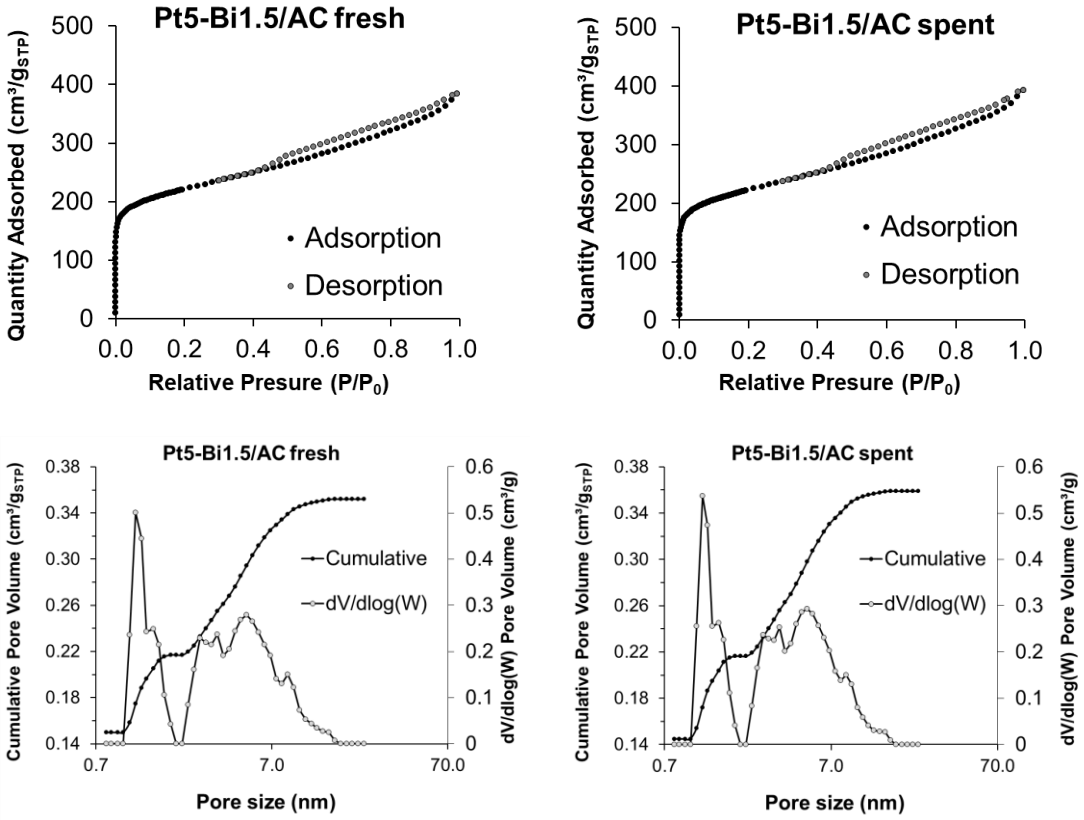

Figure 3.6. N_2 adsorption isotherms at 77 K and corresponding pore size distributions for Pt-Bi/AC: Left) fresh; Right) spent.

The N_2 isotherm (Figure 3.6) revealed a bimodal pore size distribution for the Pt-Bi/AC catalyst, with a microporous fraction (< 2 nm) contributing approximately 0.21 $cm^3\ g^{-1}$ and mesopores ranging from 2 to 16 nm accounting for an additional 0.15 $cm^3\ g^{-1}$ of the total pore volume. After testing, no significant changes in pore size distribution, total pore volume, or surface area (≈815 $m^2\ g^{-1}$) were observed on the spent catalyst. The comparison between the fresh and spent N_2 isotherms indicated that the porous structure remained intact, with no evidence of pore blockage or structural degradation, confirming the stability of the textural properties under the reaction conditions.

Given that the glycerol molecule's average and maximum projected diameters are approximately 7.0 Å and 7.9 Å, respectively, it is unlikely that glycerol can access the ultra-micropores (<0.8 nm) identified by CO_2 adsorption at 273 K. However, the presence of mesopores and larger micropores, confirmed by N_2 adsorption at 77 K, ensures sufficient pore accessibility for glycerol diffusion and interaction with the active sites required for the oxidation reaction.

3.3.2.2. Au/ZnO

TEM analysis was used to characterise the Au1/ZnO catalyst (i) fresh, (ii) activated by oxidative thermal treatment, and (iii) spent after reaction. Representative TEM images and corresponding Au nanoparticle size distributions are shown in Figure 3.7. The average Au nanoparticle diameters were 2.01 ± 0.14 nm (fresh), 1.56 ± 0.03 nm (activated), and 1.41 ± 0.44 nm (spent), based on a statistical analysis of 170, 298, and 339 particles, respectively. Additional TEM images are available in Appendix B.

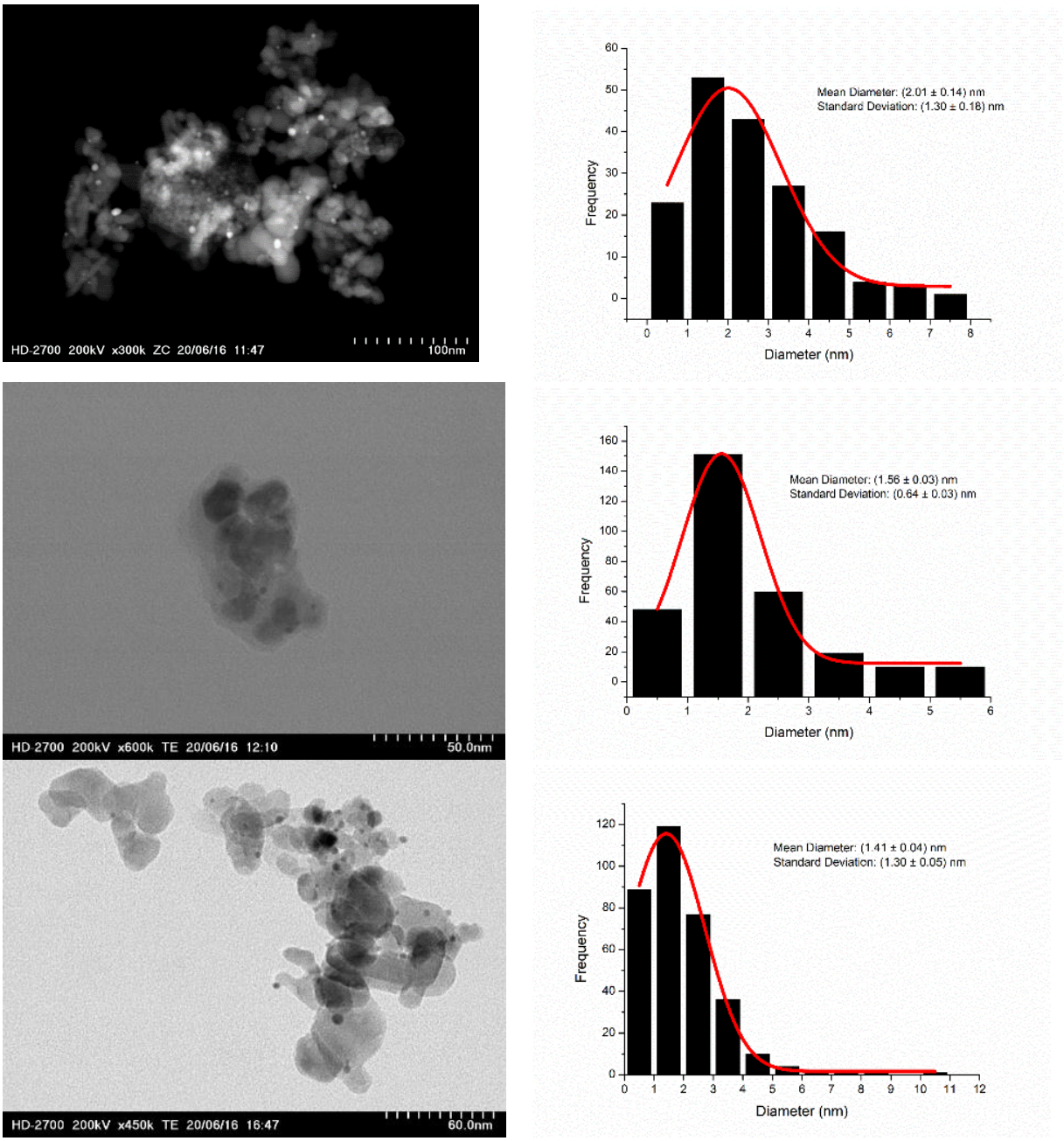

Figure 3.7. Au1/ZnO TEM analysis. Left: bright-field images; Right: particle size histograms with Gaussian fit. Top: Fresh (170 particles); Middle: Activated (298 particles); Bottom: Spent (339 particles).

Secondary-electron TEM surface imaging revealed Au nanoparticles dispersed across the ZnO surface (Figure 3.8-a). High-resolution TEM images confirmed that the Au nanoparticles were crystalline, though polymorphic (Figure 3.8-b), as suggested in the literature [45, 46].

Interestingly, a surrounding amorphous layer was observed around the Au nanoparticles in the activated sample. This material is most likely ZnO, which migrated from the bulk ZnO particles to the surface of Au nanoparticles during the oxidative thermal activation step. Similar behaviour has been reported in the literature for Au/ZnO [47, 48], AuPd/ZnO-CuO [49] and Au/CuO-ZrO

[50] catalysts submitted to oxidative thermal activation, which have shown high activity and selectivity for DHA production.

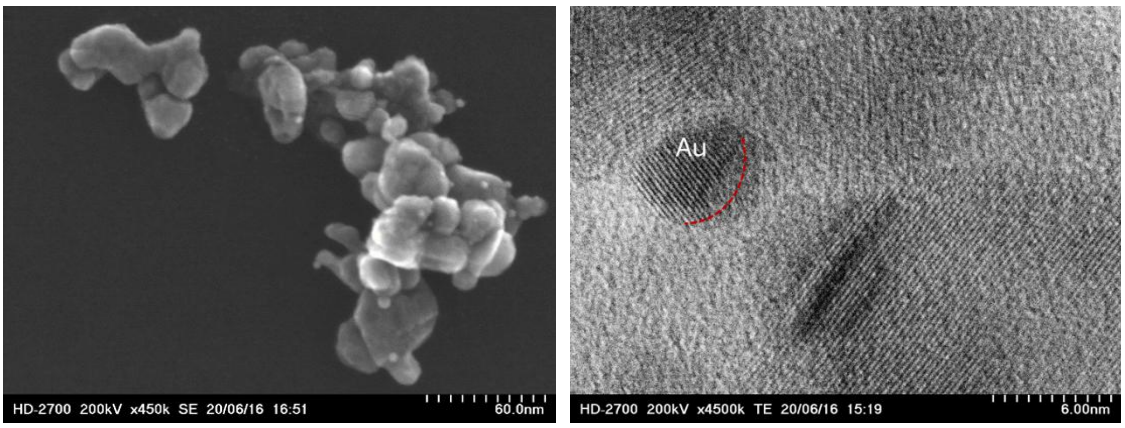

Figure 3.8. Left) Au/ZnO SE-TEM surface images. Right) HRTEM image of an Au nanoparticle.

This observation of amorphous ZnO deposition around the Au nanoparticles was further corroborated by energy-dispersive X-ray spectroscopy (EDX) elemental mapping of the fresh and thermally activated Au1/ZnO samples (Figure 3.9 a–d and Figure 3.9 e–h, respectively). The maps display the spatial distributions of Au (red), Zn (green), and O (blue). In the fresh catalyst, Au nanoparticles appeared as distinct, well-defined entities. Upon oxidative thermal activation, however, the mapping revealed the presence of ZnO surrounding the Au nanoparticles, consistent with ZnO migration from the bulk phase. This phenomenon supports the formation of Au–ZnO interfacial structures during activation, which may play a role in the catalyst's enhanced performance.

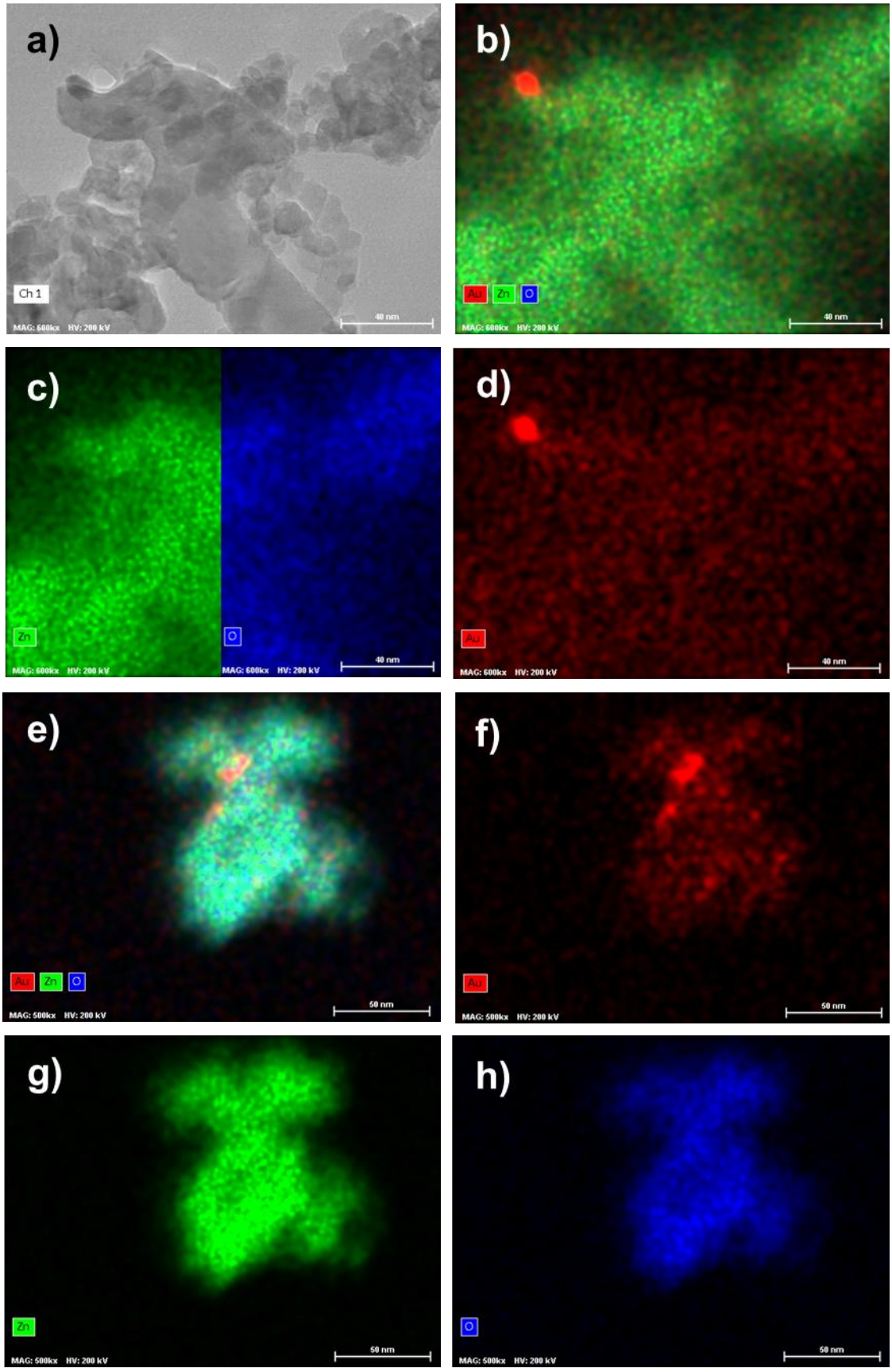

Figure 3.9. Elemental mapping of Au/ZnO: a-d) fresh; e-h) activated by oxidative thermal treatment. Au (red), Zn (green) and O (blue).

A summary of the key textural properties obtained from these analyses, along with values from the literature for both Pt5-Bi1.5/AC and Au1/ZnO, is provided in Table 3.1.

Table 3.1. Characterisation summary of Pt5-Bi1.5/AC and Au1/ZnO catalysts.

Catalyst	Pt5-Bi1.5/AC	Au1/ZnO
Pt or Au load (wt.%)	4.78	1.0 [51]
Bi load (wt.%)	1.29	-
ρs (He) (g/cm^3)	1.4204 ± 0.0062	2.72 [b]
ρap (Hg) (g/cm^3)	0.5322	1.73 [b]
εp (-)	0.63	0.36 [b]
Particle size (μm)	24.3 ± 14.8	54.9 ± 40.9
Surface area (BET) (m^2 g^{-1})	812	40…48…50 [a] [51-56]
Vp (N_2 77 K) (BJH) (cm^3 g^{-1})	0.29	0.21…0.3 [52, 55, 56]
Vp (N_2 77 K) (DFT) (cm^3 g^{-1})	0.36	0.21…0.3 [52, 55, 56]
Vp (< 7.97 Å) (cm^3 g^{-1})[c]	0.16	n.a.
Pore diameter (BJH) (nm)	4.8	19 [52, 55]
Metal size (nm)	3.6 ± 1.1 [34]	≈ 2-3[a] [53, 54]; 1.5-2.0 [This work]
Metal surface area (nm^2)	n.a.	12 [53]
Dispersion (%)	n.a.	≈50-70[a] [51, 53]
Bond Energy values (eV)	n.a.	84.0 ± 0.3 eV (Au^0) [52, 54]

[a] including data after oxidative thermal activation [51]

[b] estimated using ρb = 1.08 g/cm^3 (measured) and εb = 0.38 from correlation [57]

[c] CO_2 adsorption isotherm at 273 K.

The Pt5-Bi1.5/AC catalyst exhibited a significantly higher surface area (812 m^2 g^{-1}) and particle porosity (ε_p = 0.63) than the Au1/ZnO catalyst, which had a more compact structure (ε_p = 0.36) and a broader particle size distribution. The particle porosity was calculated based on the density by $\rho_p = (1 - \varepsilon_p)\rho_s$. The porosity data was subsequently applied in Chapter 4 to evaluate mass transfer phenomena.

Textural analysis revealed that Pt5-Bi1.5/AC possessed a primarily mesoporous structure (Barrett-Joyner-Halenda, BJH pore diameter ≈ 4.8 nm) with additional ultra-microporosity (0.16 cm^3 g^{-1} for pores <7.97 Å). In comparison, Au1/ZnO featured larger mesopores (≈19 nm), typical of oxide-based supports.

Both catalysts contained small metal nanoparticles, ranging from 1.5 to 3.6 nm in diameter, a favourable characteristic for maximising active surface area. For Au1/ZnO, a metal dispersion of

approximately 50–70% and a metal surface area of 12 nm^2 indicated a well-dispersed gold phase, in line with its high catalytic activity. Notably, the metal nanoparticle size and surface characteristics of Au1/ZnO remained unaffected by oxidative thermal treatment [51], suggesting good structural and chemical stability of the catalyst under reaction conditions.

3.3.3. Catalyst Screening: Batch Reactor

3.3.3.1. Platinum Catalysts

Three commercial Pt-based catalysts - Pt5/AC, Pt5-Bi1.5/AC, and Pt5-Bi5/AC - were tested under identical operating conditions: $C_{GLY,0}$ = 1 M; GLY/dry catalyst mass (GLY/w) = 10 wt.%; T = 80 °C; $P(O_2)$ = 4.5 bar; $Q(O_2)$ = 150 STPml min^{-1}; Stirring speed: 800 rpm. The catalysts had identical Pt loading (5 wt.%), which allowed the evaluation of the Bi loading effect on catalytic performance. Nevertheless, catalysts are from different suppliers; thus, variations in catalyst preparation, the nature of support, and metal introduction methods may influence differences in performance [8, 9, 58].

In all cases, glycerol oxidation began promptly, with the reaction medium acidifying rapidly. The pH dropped from ≈6 to ≈1 within an hour due to the formation of organic acids. This acidification is beneficial, as DHA production is significantly higher at low pH (≈2) than under neutral or basic conditions [2]. The evolution of glycerol concentration and its oxidation products over time for each catalyst is presented in Figure 3.10. The catalytic performance regarding GLY conversion, DHA selectivity, and DHA yield is summarised in Figure 3.11, with detailed results after 2 hours of reaction, as shown in Table 3.2. All catalysts achieved their maximum DHA yield within 2-3 h of reaction (Figure 3.11). Pt5-Bi1.5/AC exhibited the best performance, reaching a maximum DHA yield of 36% after 2 hours, compared to 25% for Pt5-Bi5/AC and only 9% for Pt5/AC.

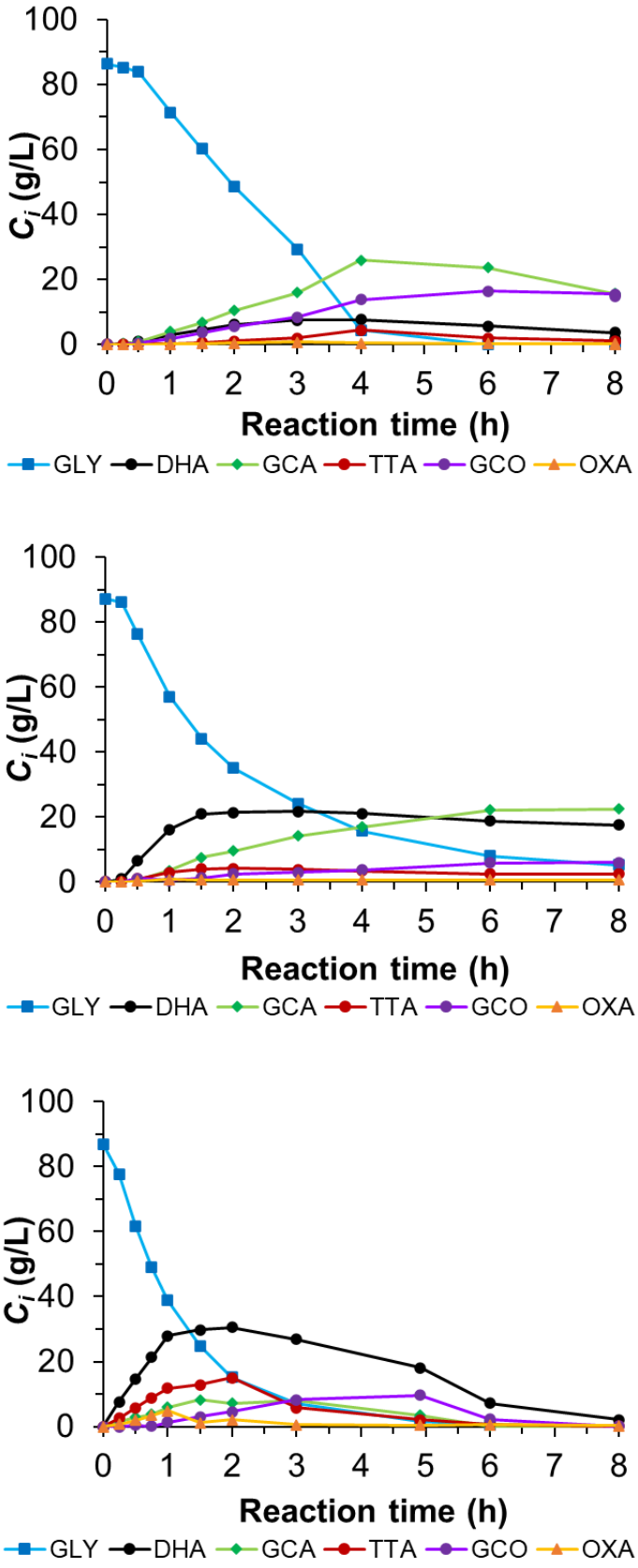

Figure 3.10. Concentration profiles of glycerol oxidation with Pt5/AC (top), Pt5-Bi1.5/AC (middle), and Pt5-Bi5/AC (bottom) catalysts. Lines are provided for visual clarity.

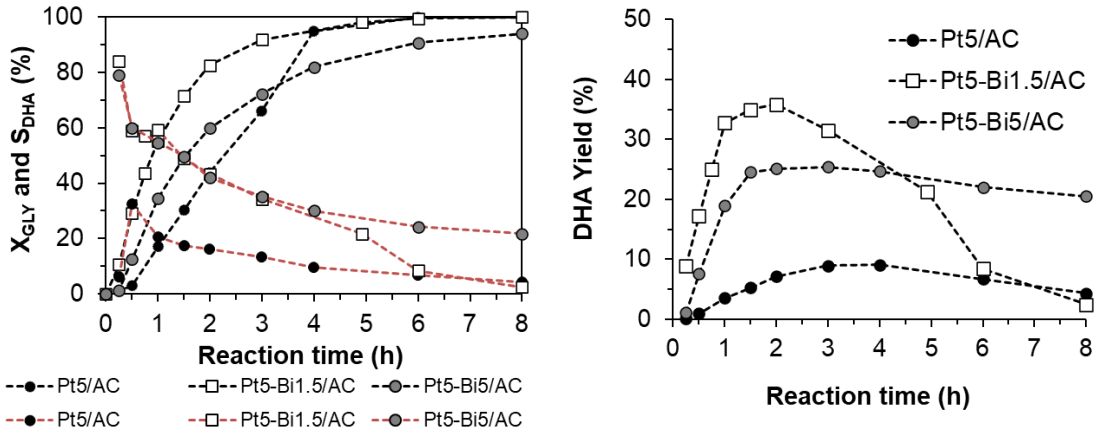

Figure 3.11. Catalytic performance of Pt5/AC (black dots), Pt5-Bi1.5/AC (white squares), and Pt5-Bi5/AC (grey dots). Left) GLY conversion (black lines) and DHA selectivity (red); Right) DHA yield. Lines are provided for visual clarity.

Table 3.2. Performance of commercial catalysts tested for glycerol oxidation.*

Catalyst	Supplier	X_{GLY} (%)	Y_{DHA} (%)	Selectivity (%)					
				DHA	GCA	TTA	GCO	OXA	Others
Pt5/AC	Sigma	44	7	16	24	2	18	1	39
Pt5-Bi1.5/AC	JM	82	36	43	9	13	8	3	25
Pt5-Bi5/AC	Evonik	60	25	42	16	5	6	1	31
Au1/ZnO	Strem	59	28	47	1	0	16	2	34

*T = 80 °C; $Q(O_2)$ = 200 STPml min^{-1}; 800 rpm, 2 h reaction. Pt catalysts: $C(GLY)_0$ = 1 M; $P(O_2)$ = 4.5 bar; GLY/w = 10 wt.%. Au1/ZnO: $C(GLY)_0$ = 0.1 M; $P(O_2)$ = 6.5 bar; GLY/w = 10 wt.%.

Pt5/AC exhibited the highest catalytic activity, achieving complete GLY conversion. However, it showed low DHA selectivity (16% after 2 hours) and a maximum DHA yield of only 9% after 3 hours, consistent with values reported in the literature [2, 5, 9]. Glyceric acid was the main oxidation product, with a maximum selectivity of 30%, lower than reported for non-commercial Pt5/AC catalysts [39, 137]. It showed a high oxidative cleavage rate, producing significant amounts of glycolic acid, formic acid, and CO_2.

Doping Pt nanoparticles with Bi modifies their electronic and geometric properties, enhancing DHA selectivity primarily through geometric effects. Bi acts as a site blocker, forming Pt-Bi active sites that control glycerol orientation, likely via a chelation effect, facilitating selective oxidation of the secondary hydroxyl group. This occurs through surface complex formation between glycerol, a Pt atom, and a neighbouring positively charged Bi adatom. Additionally, Bi selectively blocks high-energy Pt sites responsible for primary hydroxyl group oxidation, making

DHA formation the preferred catalytic route [2, 5, 13, 59]. Bi also mitigates Pt deactivation by binding with carboxylic acids, preventing their adsorption and further reaction on Pt active sites [10, 60].

Pt-Bi/AC catalysts displayed high initial DHA selectivity (≈80%), which decreased over reaction time as GLY was consumed and DHA was further oxidised. Pt5-Bi1.5/AC demonstrated the highest catalytic activity, achieving 84% conversion after 2 hours with a DHA selectivity of 42%. After four hours, DHA selectivity dropped because all GLY was completely consumed. The selectivity for TTA and GCA was low (≈ 15%). Pt5-Bi5/AC achieved only 60% GLY conversion after 2 hours but maintained higher DHA selectivity for longer reaction times due to slower DHA oxidation than Pt5-Bi1.5/AC.

These results align with the findings of the literature that lower Bi/Pt ratios optimise DHA production, though variations in preparation methods, support types, and particle sizes also influence catalytic performance [4, 5, 9, 10]. Higher DHA yields of ≈50% were reported in the literature with lab-made Pt-Bi/AC catalysts (see Table 3.3, entries 6-8).

Table 3.3. DHA production over Pt-Bi/AC catalysts (this work and literature data).

Pt wt.%	Bi wt.%	T (°C)	P (bar) Air/O_2	$C_{GLY,0}$ (M)	GLY/Pt (mol/mol)	X_{GLY} (%)	S_{DHA} (%)	Y_{DHA} (%)	Ref.
5	1	50	1 (air)	1.1	≈850	24	80	19	[5]
5	5.4	120	1 (O_2)	1.5	1755	59	51[c]	-	[8]
5	1.5	80	3 (O_2)	0.3	500	80	35	28	[34]
9	5	55	1 (air)	1.1	≈270	82	40	33	[7]
5	**1.5**	**80**	**4.5 (O_2)**	**1.0**	**425**	**82**	**43**	**36**	**This work**
7.4	2.9	60	1 (air)	1.0	n.a.	75	49	37	[2]
5	5	60	1 (O_2)	1.1	≈425	92	49	45	[10]
3	0.6	80	2.4 (O_2)	1.0	≈100	80	60	48	[9]

[a] Glycerol conversion; DHA selectivity; DHA yield

[b] commercial catalyst from Johnson Matthey

[c] at 20% conversion

The same Pt5-Bi1.5/AC commercial catalyst was tested under similar conditions (Table 3.3, entry 3), yielding comparable results: at 30% glycerol conversion, DHA selectivity was 53% [34], closely matching the 50% observed in this work. However, at ≈ 80% glycerol conversion, a significantly higher DHA selectivity (≈ 43%) was achieved in this work compared to the ≈ 23% reported in the literature [34]. The reaction temperature was the same, and the GLY/Pt ratio and the oxygen pressure were similar, with the key difference being the glycerol concentration, which was 1 M in this work vs 0.3 M in the literature [34]. Notably, while the literature reports an almost

constant DHA concentration throughout the reaction, the present study observed distinct reaction kinetics, with DHA concentration evolving differently over time.

3.3.3.2. Gold Catalysts

Gold nanoparticles are well-known for their resistance to overoxidation. Previous studies using Au nanoparticles supported on transition metal oxides, including Au/ZnO, have explored a wide range of operating conditions, including oxygen pressures from 1 to 20 bar, temperatures between 30 and 100 °C, and aqueous glycerol concentrations from 0.1 to 0.3 M [31, 47, 61, 62].

In this work, the performance of the activated Au1/ZnO catalyst was evaluated under conditions comparable to those used for Pt-based catalysts, except for a higher GLY/Au molar ratio of 2000. Under these conditions, an initial glycerol conversion of approximately 5% was achieved within 15 minutes, primarily yielding DHA. However, no further progress in conversion or selectivity was observed over the next six hours. After 80 hours of reaction, the overall glycerol conversion reached around 40%, though this was likely due to non-catalytic pathways, as the selectivity toward C_3 oxidation products was very low.

The limited activity was attributed to catalyst deactivation, likely caused by the strong adsorption of glycerol and reaction products, particularly organic acids, on the catalyst surface. This phenomenon has been reported in the literature for gold catalysts [47, 50, 62].

In subsequent trials, the initial glycerol concentration was reduced to 0.1 M to mitigate deactivation. This adjustment is also consistent with the conditions most frequently reported in the literature for Au/ZnO catalysts [47, 61, 62]. Due to the limited availability of the Au1/ZnO catalyst, now discontinued by the supplier, the reference conditions were further adjusted for subsequent experiments. The catalyst was tested with 2.0 g of dry mass and a 0.1 M aqueous glycerol solution (GLY/Au = 100 mol/mol). The corresponding results are presented in Figure 3.12.

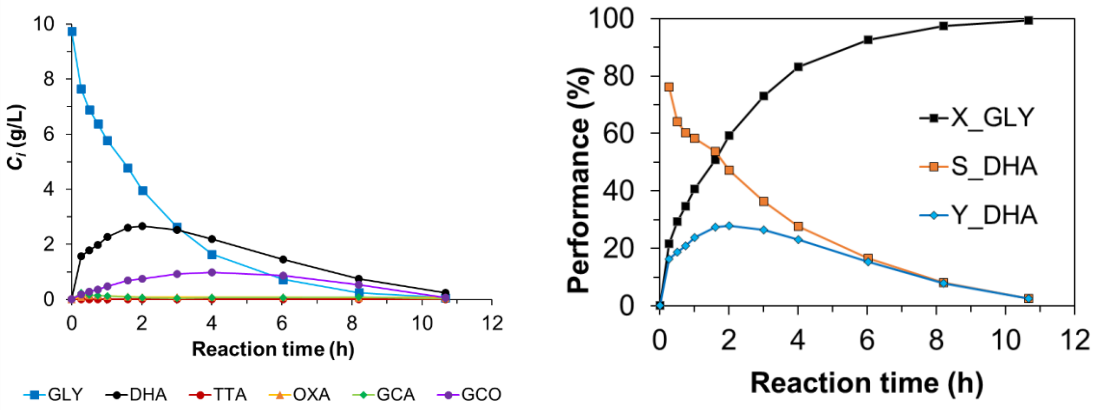

Figure 3.12. Left) species concentration profiles of GLY oxidation over Au1/ZnO. Right) catalytic performance. Lines are provided for visual clarity.

Glycerol was consumed entirely after 10 hours of reaction (see Figure 3.12). Like the Pt-Bi/AC catalysts, Au1/ZnO exhibited selectivity toward DHA, achieving a DHA yield of 27% after 1.5 hours of reaction. Glycolic acid was the main byproduct, with negligible amounts of glyceric acid and oxalic acid and no tartronic acid (TTA) detected in the liquid phase. The reaction performance of the commercial Au1/ZnO catalysts was compared in Table 3.4 with similar studies conducted with lab-made Au/ZnO catalysts [47, 61, 62]. ZnO was prepared by precipitation, and Au was introduced by deposition-precipitation in all cases, including the commercial catalyst. All of them were thermally activated under an oxidative atmosphere (airflow).

Table 3.4. DHA production over Au/ZnO catalysts (this work and literature data).

							Performance, 2 h (%)			
Au wt.%	Treatment	Activation	$P(O_2)$ (bar)	V (ml)	GLY/Au (mol/mol)	w (g)	X_{GLY}	S_{DHA}	Y_{DHA}	Ref.
1	**H_2 red 120°C 1h**	**300 °C 4 h**	**6.5***	**100**	**100**	**2.0**	**59**	**47**	**28**	**This work**
1	No	200 °C 4 h	10	12	1000	0.02	24	85	20	[61]
1.5	H_2 red. 300°C 4 h	300 °C 4 h	1	5	100	0.07	40	82	33	[47]
2.5	No	200 °C 5 h	10	24	100	0.19	74	83	61	[62]

T = 80 °C; $C(GLY)_0$ = 0.1 M; * $Q(O_2)$ = 200 STPml/min (remaining groups without gas flow).

3.3.4. Catalyst Stability

3.3.4.1. Pt5-Bi1.5/AC

Two types of active sites are responsible for glycerol oxidation over Pt-Bi/AC catalysts: Pt active sites, which are selective for glyceraldehyde production through terminal hydroxyl group oxidation, and Pt-Bi active sites, which selectively oxidise glycerol's secondary hydroxyl group, producing DHA [5, 9, 63]. Catalyst deactivation is often attributed to the strong adsorption of organic acids, such as GCA and mesoxalic acid, which poison the Pt-Bi catalyst active sites selective for DHA production [63]. Others suggest that while GCA adsorbs strongly, its oxidation product, TTA, plays a more significant role in deactivating the catalyst [64]. Pt typically remains metallic during glycerol oxidation but can suffer from oxygen poisoning under moderate oxygen pressures [65, 66]. Both Pt and Bi leaching can occur under highly acidic, alkaline, or complex environments, depending on catalyst preparation and reaction conditions [2, 23, 34, 63, 65, 67-71].

Pt5-Bi1.5/AC, the catalyst herein tested with the highest DHA yield, was subjected to stability tests across four consecutive 4-hour runs. With water washing between runs and reaction volume

adjustments to maintain a constant GLY/w, the catalyst demonstrated stable activity and selectivity, achieving ≈80% glycerol conversion and ≈45% DHA selectivity after 2 hours in each run (see Figure 3.13). These results are further supported by the characterisation results, which showed that the catalyst maintained its properties after the reaction (see Figure 3.6).

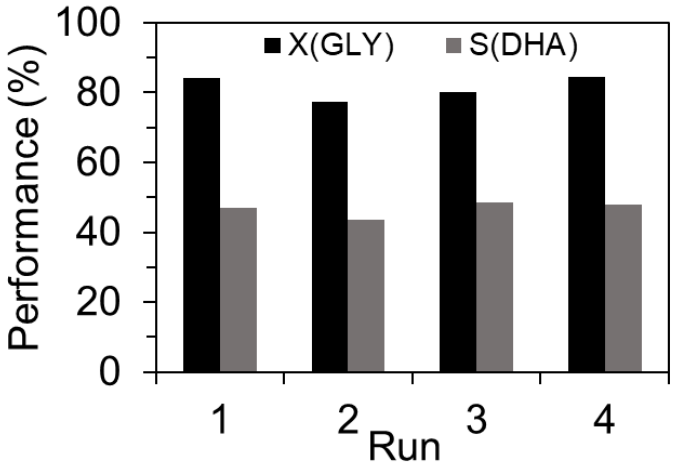

Figure 3.13. Pt5-Bi1.5/AC stability test: glycerol conversion and DHA selectivity after 2 h of reaction. $C_{GLY,0}$ = 1 M; GLY/w = 10 wt.%; 80 °C; 4.5 bar O_2; 4 h each reaction.

Literature details efforts to regenerate Pt-Bi/AC catalysts, including thermal treatment and washing with organic or alkaline solutions. Thermal treatment at 200-300 °C was the only effective regeneration method, decomposing adsorbed intermediates and restoring activity, allowing stable performance over multiple runs [71]. In this work, the long-term stability of the Pt-Bi/AC catalyst was not studied. Although this work did not assess long-term stability, previous studies indicate promising results for Pt-Bi/AC catalysts under continuous operation for 1000 h. In one case, DHA selectivity decreased from ≈80% to ≈40% after 700 h but remained stable up to 1000 hours, with glycerol conversion unaffected [8]. Another endurance test demonstrated stable performance with 10-20 wt.% glycerol solutions [58].

3.3.4.2. Au1/ZnO

Gold catalysts are known for their leach and overoxidation resistance in alcohol oxidation reactions [72]. The stability of the Au1/ZnO catalyst was evaluated over five consecutive oxidation runs:

- 1st run: fresh and activated catalyst;
- 2nd and 3rd run: washed in H_2O at 60 ºC, filtered, dried;
- 4th run: same washing protocol and reactivated (airflow, 300 °C, 4 h);
- 5th run: washed in 50% ethanol-water (V/V) at 60 ºC, filtered, and dried.

The catalyst exhibited poor stability upon reuse (see Figure 3.14). Neither washing with water nor thermal reactivation restored catalytic activity. Similarly, ethanol-water washing was

ineffective. Notably, the catalyst turned dark purple-grey after the ethanol-water washing, likely indicating a modification in the Au nanoparticles.

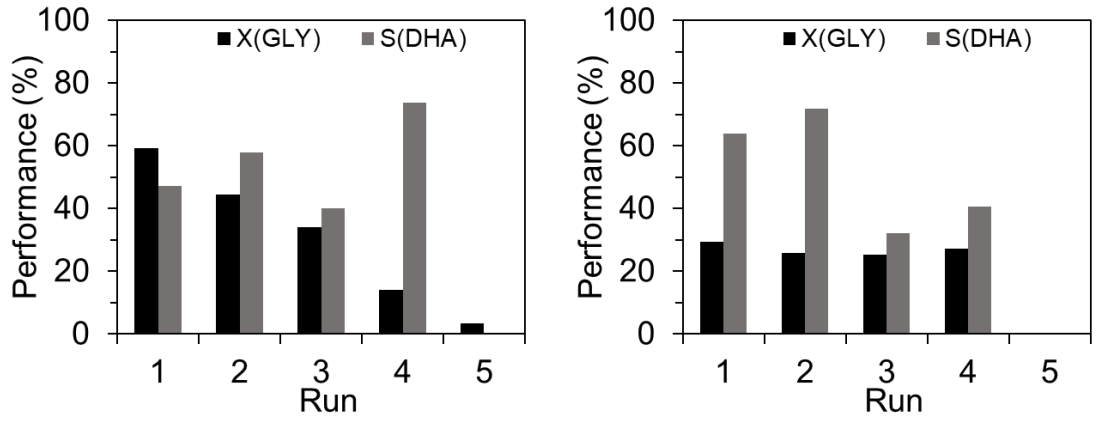

Figure 3.14. Au1/ZnO stability tests. Left: after 2 h of reaction; Right: at $X_{GLY} \approx 25\%$. $C(GLY)_0$ = 0.1 M; GLY/Au = 100 mol/mol; 80 °C; 6.5 bar O_2; 4 h each reaction.

Lab-made Au/ZnO catalysts demonstrated varying degrees of stability in glycerol oxidation. Some studies reported stable performance with reactivation between runs, achieving ≈80% glycerol conversion and ≈60% DHA selectivity over three runs, though slight Au nanoparticle growth was observed (e.g., 2.6 to 3.5 nm). Without reactivation, glycerol conversion decreased to ≈60% [47]. Other studies showed stable performance, with GLY conversion at ≈25% and DHA selectivity at ≈80% alongside minimal nanoparticle growth (2.4 to 2.9 nm) [61]. However, significant deactivation was also reported, with glycerol conversion dropping from 74% to 9% after three runs due to Au particle aggregation (2.3 to 3.3 nm) and carbon deposition, although DHA selectivity remained at ≈85% [62].

3.4. Conclusions

Screening commercial catalysts for the selective oxidation of glycerol to DHA under base-free conditions revealed significant differences in catalytic performance. This study confirmed that adding Bi to Pt nanoparticles enhances DHA formation. Among the tested catalysts, Pt5-Bi1.5/AC from Johnson Mattey was the most promising, achieving the highest DHA yield (36%). As expected from the results reported in the literature, a low Bi load was preferable for DHA production, with Pt5-Bi1.5/AC outperforming Pt5-Bi5/AC. Au1/ZnO also exhibited good performance for DHA production; however, it was less stable than the Pt5-Bi1.5/AC catalyst since it promptly deactivated when higher glycerol concentrations were tested (1 M) and could not be reused after washing or reactivation (not even for glycerol concentrations of 0.1 M).

On the other hand, the Pt5-Bi1.5/AC catalyst from Johnson Mattey showed a stable catalytic performance over four consecutive cycles, performing only a washing stage between them.

Due to the high DHA yield, Pt5-Bi1.5/AC and Au1/ZnO were selected for further kinetic studies, detailed in Chapter 4. The solution obtained from glycerol oxidation over Pt5-Bi1.5/AC after 1.5 hours of reaction will be a reference for designing the DHA separation process in a continuous chromatographic unit, as discussed in Chapters 5 and 6.

3.5. Notation

Abbreviations

OXA, TTA, GCA, GCO, GLY, DHA, GLAD	Oxalic acid (OXA), Tartronic acid (TTA), Glyceric acid (GCA), Glycolic acid (GCO), Glycerol (GLY), Dihydroxyacetone (DHA), Glyceraldehyde (GLAD)
AC	Activated carbon
BJH	Barrett-Joyner-Halenda method
BET	Brunauer, Emmett, and Teller method
DFT	Density Functional Theory method
EDS	Energy-Dispersive Spectroscopy
EDX	X-ray spectroscopy
HPLC	High-Performance Liquid Chromatography
TEM	Transmission electron microscopy

Variables

GLY/w	GLY/dry catalyst mass (wt.%)
GLY/Pt (GLY/Au)	Initial molar ratio of glycerol to platinum (or Au) (mol/mol)
$P(O_2)$	Partial pressure of oxygen (bar)
$Q(O_2)$	Oxygen flow rate (STPml/min)
S_{DHA}	DHA selectivity (%)
T	Temperature (K)
V	Volume of liquid phase (L)
w	Dry catalyst mass (g)
wt.%	Mass fraction (%)
X_{GLY}	Glycerol conversion (%)
Y_{DHA}	DHA yield (%)

Greek Letters

ε_p	Particle porosity (-)
ρ_p	Particle (apparent) density (g_{cat}/cm_{cat}^3)
ρ_s	Solid density (g/cm^3)

3.6. References

1. Villa, A., Jouve, A., Sanchez Trujillo, F.J., Motta, D., Prati, L., and Dimitratos, N., *Exploring the effect of au/pt ratio on glycerol oxidation in presence and absence of a base.* Catalysts, 2018. **8**(2): p. 54.
2. Garcia, R., Besson, M., and Gallezot, P., *Chemoselective catalytic oxidation of glycerol with air on platinum metals.* Applied Catalysis A: General, 1995. **127**(1-2): p. 165-176.
3. Villa, A., Veith, G.M., and Prati, L., *Selective oxidation of glycerol under acidic conditions using gold catalysts.* Angewandte Chemie International Edition, 2010. **49**(26): p. 4499-4502.
4. Katryniok, B., Kimura, H., Skrzyńska, E., Girardon, J.-S., Fongarland, P., Capron, M., Ducoulombier, R., Mimura, N., Paul, S., and Dumeignil, F., *Selective catalytic oxidation of glycerol: perspectives for high value chemicals.* Green Chemistry, 2011. **13**(8): p. 1960-1979.
5. Kimura, H., Tsuto, K., Wakisaka, T., Kazumi, Y., and Inaya, Y., *Selective oxidation of glycerol on a platinum-bismuth catalyst.* Applied Catalysis A: General, 1993. **96**(2): p. 217-228.
6. Mounzer, H.N., Wood, J., and Stitt, E.H., *Heterogeneous oxidation of 2-octanol on 5wt%Pt–1wt%Bi/Carbon catalyst.* Chemical Engineering Science, 2010. **65**(1): p. 179-185.

7. Yanli, X., Zhendong, Z., Yang, B., and Yanfeng, L., *Studies on the synthesis of PtM/C multi-metallic bimetallic catalysts and their catalytic properties on the selective oxidation of glycerol [J].* Journal of Hainan Normal University (Natural Science), 2007. **3**: p. 013.

8. Brandner, A., Lehnert, K., Bienholz, A., Lucas, M., and Claus, P., *Production of biomass-derived chemicals and energy: chemocatalytic conversions of glycerol.* Topics in Catalysis, 2009. **52**(3): p. 278-287.

9. Hu, W., Knight, D., Lowry, B., and Varma, A., *Selective oxidation of glycerol to dihydroxyacetone over Pt− Bi/C catalyst: optimization of catalyst and reaction conditions.* Industrial & Engineering Chemistry Research, 2010. **49**(21): p. 10876-10882.

10. Liang, D., Shiyu, C., Jing, G., Junhua, W., Ping, C., and Zhaoyin, H., *Glycerol oxidation with oxygen over bimetallic Pt-Bi catalysts under atmospheric pressure.* Chinese Journal of Catalysis, 2011. **32**(11-12): p. 1831-1837.

11. Xiao, Y., Greeley, J., Varma, A., Zhao, Z.J., and Xiao, G., *An experimental and theoretical study of glycerol oxidation to 1, 3-dihydroxyacetone over bimetallic Pt-Bi catalysts.* AIChE Journal, 2017. **63**(2): p. 705-715.

12. Feng, S., Yi, J., Miura, H., Nakatani, N., Hada, M., and Shishido, T., *Experimental and Theoretical Investigation of the Role of Bismuth in Promoting the Selective Oxidation of Glycerol over Supported Pt–Bi Catalyst under Mild Conditions.* ACS Catalysis, 2020. **10**(11): p. 6071-6083.

13. Ning, X., Li, Y., Yu, H., Peng, F., Wang, H., and Yang, Y., *Promoting role of bismuth and antimony on Pt catalysts for the selective oxidation of glycerol to dihydroxyacetone.* Journal of Catalysis, 2016. **335**: p. 95-104.

14. Nie, R., Liang, D., Shen, L., Gao, J., Chen, P., and Hou, Z., *Selective oxidation of glycerol with oxygen in base-free solution over MWCNTs supported PtSb alloy nanoparticles.* Applied Catalysis B: Environmental, 2012. **127**: p. 212-220.

15. Rodrigues, E.G., Pereira, M.F., Chen, X., Delgado, J.J., and Órfão, J.J., *Selective oxidation of glycerol over platinum-based catalysts supported on carbon nanotubes.* Industrial & Engineering Chemistry Research, 2013. **52**(49): p. 17390-17398.

16. Motta, D., Trujillo, F.J.S., Dimitratos, N., Villa, A., and Prati, L., *An investigation on AuPt and AuPt-Bi on granular carbon as catalysts for the oxidation of glycerol under continuous flow conditions.* Catalysis Today, 2018. **308**: p. 50-57.

17. Dodekatos, G., Schünemann, S., and Tüysüz, H., *Recent Advances in Thermo-, Photo-, and Electrocatalytic Glycerol Oxidation.* ACS Catalysis, 2018. **8**(7): p. 6301-6333.

18. Liu, B. and Gao, F., *Navigating glycerol conversion roadmap and heterogeneous catalyst selection aided by density functional theory: a review.* Catalysts, 2018. **8**(2): p. 44.

19. Ishida, T., Murayama, T., Taketoshi, A., and Haruta, M., *Importance of size and contact structure of gold nanoparticles for the genesis of unique catalytic processes.* Chemical reviews, 2019. **120**(2): p. 464-525.

20. Carrettin, S., McMorn, P., Johnston, P., Griffin, K., and Hutchings, G.J., *Selective oxidation of glycerol to glyceric acid using a gold catalyst in aqueous sodium hydroxide.* Chemical Communications, 2002(7): p. 696-697.

21. Carrettin, S., McMorn, P., Johnston, P., Griffin, K., Kiely, C.J., and Hutchings, G.J., *Oxidation of glycerol using supported Pt, Pd and Au catalysts.* Physical Chemistry Chemical Physics, 2003. **5**(6): p. 1329-1336.

22. Porta, F. and Prati, L., *Selective oxidation of glycerol to sodium glycerate with gold-on-carbon catalyst: an insight into reaction selectivity.* Journal of Catalysis, 2004. **224**(2): p. 397-403.

23. Bianchi, C.L., Canton, P., Dimitratos, N., Porta, F., and Prati, L., *Selective oxidation of glycerol with oxygen using mono and bimetallic catalysts based on Au, Pd and Pt metals.* Catalysis today, 2005. **102**: p. 203-212.

24. Hutchings, G.J., Carrettin, S., Landon, P., Edwards, J.K., Enache, D., Knight, D.W., Xu, Y.-J., and Carley, A.F., *New approaches to designing selective oxidation catalysts: Au/C a versatile catalyst.* Topics in Catalysis, 2006. **38**(4): p. 223-230.

25. Demirel, S., Lehnert, K., Lucas, M., and Claus, P., *Use of renewables for the production of chemicals: Glycerol oxidation over carbon supported gold catalysts.* Applied Catalysis B: Environmental, 2007. **70**(1-4): p. 637-643.

26. Ketchie, W.C., Fang, Y.-L., Wong, M.S., Murayama, M., and Davis, R.J., *Influence of gold particle size on the aqueous-phase oxidation of carbon monoxide and glycerol.* Journal of Catalysis, 2007. **250**(1): p. 94-101.

27. Sobczak, I., Jagodzinska, K., and Ziolek, M., *Glycerol oxidation on gold catalysts supported on group five metal oxides—A comparative study with other metal oxides and carbon based catalysts.* Catalysis Today, 2010. **158**(1-2): p. 121-129.

28. Rodrigues, E.G., Pereira, M.F., Delgado, J.J., Chen, X., and Órfão, J.J., *Enhancement of the selectivity to dihydroxyacetone in glycerol oxidation using gold nanoparticles supported on carbon nanotubes.* Catalysis Communications, 2011. **16**(1): p. 64-69.

29. Demirel-Gülen, S., Lucas, M., and Claus, P., *Liquid phase oxidation of glycerol over carbon supported gold catalysts.* Catalysis Today, 2005. **102**: p. 166-172.

30. Demirel, S., Kern, P., Lucas, M., and Claus, P., *Oxidation of mono-and polyalcohols with gold: Comparison of carbon and ceria supported catalysts.* Catalysis Today, 2007. **122**(3-4): p. 292-300.

31. Liu, S.-S., Sun, K.-Q., and Xu, B.-Q., *Specific selectivity of Au-catalyzed oxidation of glycerol and other C3-polyols in water without the presence of a base.* Acs Catalysis, 2014. **4**(7): p. 2226-2230.

32. Sullivan, J.A. and Burnham, S., *The selective oxidation of glycerol over model Au/TiO2 catalysts—The influence of glycerol purity on conversion and product selectivity.* Catalysis Communications, 2014. **56**: p. 72-75.

33. Dimitratos, N., Lopez-Sanchez, J.A., Anthonykutty, J.M., Brett, G., Carley, A.F., Tiruvalam, R.C., Herzing, A.A., Kiely, C.J., Knight, D.W., and Hutchings, G.J., *Oxidation of glycerol using gold–palladium alloy-supported nanocrystals.* Physical Chemistry Chemical Physics, 2009. **11**(25): p. 4952-4961.

34. Villa, A., Campisi, S., Chan-Thaw, C.E., Motta, D., Wang, D., and Prati, L., *Bismuth modified Au-Pt bimetallic catalysts for dihydroxyacetone production.* Catalysis Today, 2015. **249**: p. 103-108.

35. Fang, Z., Gongde, W., Keqiang, D., Wen, S., Xianfeng, L., Xiaobo, S., and Xiaoli, W. Method for preparing dihydroxy acetone by selectively oxidizing glycerin with hydrogen peroxide. CN102432445A, 2012.

36. Ai, Y. Method for preparing dihydroxyacetone through glycerol oxidation. CN104098455A, 2014.

37. Spanu, P. and Ulgheri, F. Method For The Selective Oxidation Of Glycerol To Dihydroxyacetone. WO 2014/102840 A1, 2014.

38. Hong, X., Lira, C., McGiveron, O., and Miller, D. Methods for Making 1,3-Dihydroxyacetone (dha) from Glycerol. US2012014889A1, 2012.

39. Dong, W., Ke, Y., Li, D., Liu, C., and Yang, G. Method for producing 1,3-dihydroxyacetone through catalytic oxidation with supported gold catalyst. CN105439831A, 2016.

40. Beltrán-Prieto, J.C., Pecha, J., Kašpárková, V., and Kolomazník, K., *Development of an HPLC method for the determination of glycerol oxidation products.* Journal of Liquid Chromatography & Related Technologies, 2013. **36**(19): p. 2758-2773.

41. Giertyas, C.J., Silva, D.S.d., da Silva, C.L., Meneghetti, M.R., Meneghetti, S.M.P., Almeida, R.M.d., and Bortoluzzi, J.H., *Improvement of an analytical method based on HPLC with refractive index detection for the analysis of glycerol oxidation products.* Química Nova, 2019. **42**: p. 729-735.

42. Nguyen, R., Amouroux, M., Duda, A., and Mouloungui, Z., *Quantification of Mixtures of C2 and C3 Hydroxy Acids and Products of Glycerol Oxidation by High-Performance Liquid Chromatography and Quantitative 13C NMR.* Journal of the American Oil Chemists' Society, 2020. **97**(7): p. 679-689.

43. Kong, H., Gupta, S., Mayer, M.T., Ng, E., Mesa, C.A., Giménez, S., Abdi, F.F., van de Krol, R., and Favaro, M., *Resolving Peak Overlap in HPLC Analysis of Glycerol Oxidation Products by Utilizing Various Detectors: Application to BiVO4 Photoanodes.* ACS Omega, 2025. **10**(12): p. 11786-11795.

44. Kim, S., Lee, C.-G., Kim, Y.T., Kim, K.-H., and Lee, J., *Effect of Pt catalyst on the condensable hydrocarbon content generated via food waste pyrolysis.* Chemosphere, 2020. **248**: p. 126043.

45. Gumbiowski, N., Barthel, J., Loza, K., Heggen, M., and Epple, M., *Simulated HRTEM images of nanoparticles to train a neural network to classify nanoparticles for crystallinity.* Nanoscale Advances, 2024. **6**(16): p. 4196-4206.

46. Uematsu, T., Baba, M., Oshima, Y., Tsuda, T., Torimoto, T., and Kuwabata, S., *Atomic Resolution Imaging of Gold Nanoparticle Generation and Growth in Ionic Liquids.* Journal of the American Chemical Society, 2014. **136**(39): p. 13789-13797.

47. Pan, Y., Wu, G., He, Y., Feng, J., and Li, D., *Identification of the Au/ZnO interface as the specific active site for the selective oxidation of the secondary alcohol group in glycerol.* Journal of Catalysis, 2019. **369**: p. 222-232.

48. Wu, G., Zhao, G., Sun, J., Cao, X., He, Y., Feng, J., and Li, D., *The effect of oxygen vacancies in ZnO at an Au/ZnO interface on its catalytic selective oxidation of glycerol.* Journal of Catalysis, 2019. **377**: p. 271-282.

49. Zhao, G., Wu, G., Liu, Y., He, Y., Feng, J., and Li, D., *Preparation of AuPd/ZnO–CuO for the directional oxidation of glycerol to DHA.* Catalysis Science & Technology, 2020. **10**(18): p. 6223-6234.

50. Wang, Y., Pu, Y., Yuan, D., Luo, J., Li, F., Xiao, F., and Zhao, N., *Selective Oxidation of Glycerol to Dihydroxyacetone over Au/CuxZr1–xOy Catalysts in Base-Free Conditions.* ACS Applied Materials & Interfaces, 2019. **11**(47): p. 44058-44068.

51. Hartadi, Y., Widmann, D., and Behm, R.J., *Methanol synthesis via CO 2 hydrogenation over a Au/ZnO catalyst: an isotope labelling study on the role of CO in the reaction process.* Physical Chemistry Chemical Physics, 2016. **18**(16): p. 10781-10791.

52. Ousmane, M., Liotta, L., Pantaleo, G., Venezia, A., Di Carlo, G., Aouine, M., Retailleau, L., and Giroir-Fendler, A., *Supported Au catalysts for propene total oxidation: study of support morphology and gold particle size effects.* Catalysis today, 2011. **176**(1): p. 7-13.

53. Halasi, G., Gazsi, A., Bánsági, T., and Solymosi, F., *Catalytic and photocatalytic reactions of H2+CO2 on supported Au catalysts.* Applied Catalysis A: General, 2015. **506**: p. 85-90.

54. Tóth, A., Halasi, G., Bánsági, T., and Solymosi, F., *Reactions of propane with CO2 over Au catalysts.* Journal of Catalysis, 2016. **337**: p. 57-64.

55. Ngwenya, T., Nongwe, I., and Jewell, L.L., *Reduction of sulphur dioxide using carbon monoxide over gold supported catalysts.* Gold Bulletin, 2018. **51**(4): p. 153-162.

56. Murzina, E.V., Tokarev, A.V., Kordás, K., Karhu, H., Mikkola, J.-P., and Murzin, D.Y., *d-Lactose oxidation over gold catalysts.* Catalysis Today, 2008. **131**(1): p. 385-392.

57. Pushnov, A.S., *Calculation of average bed porosity.* Chemical and Petroleum Engineering, 2006. **42**(1): p. 14-17.

58. Kimura, H., *Selective oxidation of glycerol on a platinum-bismuth catalyst by using a fixed bed reactor.* Applied Catalysis A: General, 1993. **105**(2): p. 147-158.

59. Mallat, T. and Baiker, A., *Oxidation of alcohols with molecular oxygen on solid catalysts.* Chemical Reviews, 2004. **104**(6): p. 3037-3058.

60. Fordham, P., Garcia, R., Besson, M., and Gallezot, P., *Selective catalytic oxidation with air of glycerol and oxygenated derivatives on platinum metals*, in *Studies in Surface Science and Catalysis*. 1996, Elsevier. p. 161-170.

61. Meng, Y., Zou, S., Zhou, Y., Yi, W., Yan, Y., Ye, B., Xiao, L., Liu, J., Kobayashi, H., and Fan, J., *Activating molecular oxygen by Au/ZnO to selectively oxidize glycerol to dihydroxyacetone.* Catalysis Science & Technology, 2018. **8**(10): p. 2524-2528.

62. Ke, Y., Li, X., Li, J., Liu, C.L., Xu, C., and Dong, W.S., *Conversion of glycerol to dihydroxyacetone over Au catalysts on various supports.* Journal of Chemical Technology & Biotechnology, 2020. **95**(4): p. 1153-1162.

63. Worz, N., Brandner, A., and Claus, P., *Platinum− Bismuth-Catalyzed Oxidation of Glycerol: Kinetics and the Origin of Selective Deactivation.* The Journal of Physical Chemistry C, 2009. **114**(2): p. 1164-1172.

64. Hu, W., Lowry, B., and Varma, A., *Kinetic study of glycerol oxidation network over Pt–Bi/C catalyst.* Applied Catalysis B: Environmental, 2011. **106**(1-2): p. 123-132.

65. Skrzyńska, E., Wondołowska-Grabowska, A., Capron, M., and Dumeignil, F., *Crude glycerol as a raw material for the liquid phase oxidation reaction.* Applied Catalysis A: General, 2014. **482**: p. 245-257.

66. Torbina, V., Vodyankin, A., Ten, S., Mamontov, G., Salaev, M., Sobolev, V., and Vodyankina, O., *Ag-Based Catalysts in Heterogeneous Selective Oxidation of Alcohols: A Review.* Catalysts, 2018. **8**(10): p. 447.

67. Tongsakul, D., Nishimura, S., Thammacharoen, C., Ekgasit, S., and Ebitani, K., *Hydrotalcite-supported platinum nanoparticles prepared by a green synthesis method for selective oxidation of glycerol in water using molecular oxygen.* Industrial & Engineering Chemistry Research, 2012. **51**(50): p. 16182-16187.

68. Tsuji, A., Rao, K.T.V., Nishimura, S., Takagaki, A., and Ebitani, K., *Selective Oxidation of Glycerol by Using a Hydrotalcite-Supported Platinum Catalyst under Atmospheric Oxygen Pressure in Water.* ChemSusChem, 2011. **4**(4): p. 542-548.

69. Zhang, C., Wang, T., Liu, X., and Ding, Y., *Cu-promoted Pt/activated carbon catalyst for glycerol oxidation to lactic acid.* Journal of Molecular Catalysis A: Chemical, 2016. **424**: p. 91-97.

70. Lei, J., Dong, H., Duan, X., Chen, W., Qian, G., Chen, D., and Zhou, X., *Insights into activated carbon-supported platinum catalysts for base-free oxidation of glycerol.* Industrial & Engineering Chemistry Research, 2016. **55**(2): p. 420-427.

71. Ning, X., Zhan, L., Wang, H., Yu, H., and Peng, F., *Deactivation and regeneration of in-situ formed Bismuth-promoted Platinum catalyst for the selective oxidation of glycerol to dihydroxyacetone.* New Journal of Chemistry, 2018.

72. Zope, B.N. and Davis, R.J., *Inhibition of gold and platinum catalysts by reactive intermediates produced in the selective oxidation of alcohols in liquid water.* Green Chemistry, 2011. **13**(12): p. 3484-3491.

4. Glycerol Oxidation Kinetics

This chapter investigates the kinetics of glycerol oxidation into dihydroxyacetone under base-free conditions using a platinum (Pt-Bi/AC) and a gold (Au/ZnO) commercial catalyst. Experimental data was obtained and analysed using both power-law and Langmuir-Hinshelwood types of kinetic models. The latter approach described better glycerol oxidation across a significant range of operating conditions.

4.1. Introduction

The catalytic oxidation of glycerol produces glyceraldehyde (GLAD) and dihydroxyacetone (DHA), depending on whether the terminal or central hydroxyl group is oxidised, respectively. Subsequent oxidation steps yield a wide range of aldehydes and organic acids, namely glyceric acid (GCA), tartronic acid (TTA), hydroxypyruvic acid (HPA), glycolic acid (GCO), and oxalic acid (OXA), with complete oxidation producing carbon dioxide and water. Achieving high selectivity toward desired products requires careful control over the catalyst properties, reaction conditions (e.g., temperature, oxygen pressure, and the absence of base), and reactor design.

The kinetics of bimolecular oxidation reactions over metallic catalysts are frequently described using Langmuir–Hinshelwood–Hougen–Watson (LHHW) models [1, 2], including liquid-phase alcohol oxidation with oxygen [3-7], as detailed in Chapter 2. This approach assumes that both the alcohol and oxygen adsorb on catalyst surfaces and that the reaction rate depends on the product of their surface coverages [3], given by the following expression:

$$r_{dehyd} = k\,\theta_{alcohol}\,\theta_O \tag{4.1}$$

where r_{dehyd} is the alcohol dehydrogenation rate, k is the reaction kinetic constant, and $\theta_{alcohol}$ and θ_O represents the surface coverage by alcohol and oxygen species, respectively. In some cases, including the fraction of available free metallic sites (θ_v) improves model accuracy, reflecting the necessity for an unoccupied site for the reaction to proceed:

$$r_{dehyd} = k\,\theta_{alcohol}\,\theta_O\,\theta_v \tag{4.2}$$

Although this model does not represent a true three-site mechanism, it effectively accounts for surface competitive adsorption, oxygen activation via dissociative adsorption, and site saturation [3]. This approach has proven successful in modelling alcohol oxidation on Pt catalysts, including deactivation and reactivation phenomena [3]. These insights are relevant to glycerol oxidation, whose three hydroxyl groups may oxidise, resulting in multiple oxidation pathways that significantly increase mechanistic complexity.

In reaction kinetic studies, particular care must be taken to exclude or account for mass transfer limitations, depending on whether the reaction occurs under well-defined kinetic control or diffusional control. For this reason, experiments are often performed under conditions that eliminate external and internal diffusion resistances [2].

Two distinct kinetic regimes are commonly observed in aqueous-phase alcohol oxidation over noble metals: an intrinsic kinetic regime, typical of monometallic catalysts such as Pt or Au, and a transport-limited regime often associated with bimetallic systems like Pt-Bi or Pt-Pb [3]. Metallic surfaces are much more active than their oxidised counterparts, so operating under

oxygen-limited conditions, where oxygen availability is kept lower than the alcohol dehydrogenation rate, may be preferable to prevent overoxidation and loss of active sites. In batch reactors, this may be achieved by reducing oxygen concentration or increasing the temperature as glycerol is consumed [5].

Comprehensive kinetic studies of glycerol oxidation, mainly over platinum and gold catalysts, were investigated under basic conditions [8-14] and base-free conditions [15-21], mainly using LHHW-based models. Experimental data collected under various operating conditions ruled out mass transfer limitations for most of these studies, ensuring that the reaction proceeds within the kinetic regime [8, 15, 16, 18].

An investigation focused on studying the solvent effect in the oxidation of glycerol over Pt/CNT catalysts, using density functional theory calculations and isotopic labelling, proposed a kinetic model in which water promotes the formation of reactive OH* intermediates from O_2 dissociation and that the rate-determining step is likely the OH*-assisted terminal C–H bond cleavage [17].

A dual-site LHHW kinetic model described base-free glycerol oxidation over a lab-made Pt-Bi/AC catalyst [15]. Incorporating two types of active sites (Pt and Pt-Bi) allowed the description of GLY, DHA, GLAD, and GCA concentration profiles (at low glycerol conversions), whereas a single-site model failed to describe DHA concentration. Catalyst deactivation was attributed to strong GCA adsorption on Pt-Bi sites, leading to site blockage and loss of activity.

A more detailed microkinetic study by Hu et al. [16] extended the reaction network to include HPA, TTA, GCO, OXA, and CO_2. In their approach, oxidation proceeds via three general steps: (i) alcohol dehydrogenation to aldehyde or ketone, (ii) aldehyde hydration to geminal diol, and (iii) diol dehydrogenation to carboxylic acid. Assuming that the oxidation of each adsorbed species requires two adjacent vacant sites, the reaction rate was generally given by:

$$r_i = k\,\theta_i\,{\theta_v}^2 \tag{4.3}$$

In this model, oxygen is only directly involved in the OXA oxidation step (via dissociative adsorption), while water participates directly in GLAD and GOX oxidation [16]. The reaction network was decomposed into five progressively larger sub-networks with different intermediates as initial reactants to improve the quality of the kinetic parameter estimation. Catalyst deactivation was attributed mainly to the strong adsorption of TTA, a GCA oxidation product. A simplified four-step kinetic model was also studied to accurately predict GLY, DHA, and GCA oxidation, offering a helpful basis for reactor design and process optimisation targeting DHA production [16].

Kinetic studies of glycerol oxidation over gold catalysts under base-free conditions are scarce compared to platinum catalysts. Glycerol oxidation with Au supported on transition metal oxides such as ZnO [18, 22] and CuO [23] relies on oxygen vacancy defects in the support obtained by oxidative thermal activation. In the absence of these defects, the catalysts were inactive. For Au/ZnO, Pan et al. [18] proposed that O_2 undergoes dissociative adsorption at defect sites, forming OOH* species in the presence of water. H-abstraction of glycerol's secondary C–H bond at the Au/ZnO interface was identified as the rate-determining step. A reaction rate expression for GLY oxidation into DHA was proposed based on LHHW kinetics and a nine-step reaction mechanism [18]. In opposition, Meng et al. [22] reported nearly zeroth-order dependence on O_2 pressure, suggesting an Eley–Rideal kinetic model rather than a Langmuir–Hinshelwood mechanism and a non-dissociative O_2 adsorption pathway, with H_2O_2 formation as a by-product.

Building on the findings from Chapter 3, which identified Pt5-Bi1.5/AC from Johnson Mattey and Au1/ZnO from Strem Chemicals as the most effective catalysts for DHA production, the present chapter focuses on the kinetic modelling of glycerol oxidation with oxygen in the aqueous phase over these materials on a semi-batch reactor. Two kinetic models, an empirical power-law model and an LHHW-based mechanistic model, were compared. The aim is to elucidate their respective reaction mechanisms and derive reliable kinetic expressions under base-free conditions.

4.2. Experimental Description

4.2.1. Chemicals and Materials

The following chemicals were used in the kinetic studies: glycerol (GLY, ≥ 99.5%, Fisher Scientific), dihydroxyacetone (DHA ≥ 98%, Merck), glyceric acid (GCA, 20% in water, Tokyo Chemical Industry Co., Ltd.), tartronic acid (TTA, ≥ 97%, Sigma-Aldrich), glycolic acid (GCO ≥ 99%, Fisher Scientific) and oxalic acid (OXA ≥ 99.5%, ACROS Organics). Deionised water was provided from in-house purification systems. N_2 (purity ≥ 99,999% Linde) and O_2 (purity ≥ 99.9995%, AIR LIQUIDE - ALPHAGAZ^{TM}) gases were used throughout all experiments. Glyceraldehyde (GLAD ≥ 90%, Sigma-Aldrich) and hydroxypiruvic acid (HPA ≥ 95%, Sigma-Aldrich) were used exclusively for calibration of the HPLC quantification method and not in reaction experiments.

Two commercial catalysts were investigated. The platinum-based catalyst, 5 wt.% Pt doped with 1.5 wt.% Bi (Pt-Bi/AC), supplied by Johnson Matthey in reduced powder form, was used as received, following the manufacturer's recommendation.

The second catalyst, 1 wt.% Au supported on ZnO (Au/ZnO, AUROlite™), was purchased from Strem Chemicals. It was delivered as dark purple beads (1–2 mm), which were ground and sieved to obtain particles smaller than 100 µm. The sieved catalyst was then dried overnight at 105 °C and subsequently subjected to oxidative thermal activation under airflow (200 mL/min) at 300 °C for 4 hours using a heating ramp of 2 °C/min.

4.2.2. HPLC quantification

Liquid samples were periodically collected and analysed using a Shimadzu Prominence HPLC system equipped with an Alltech Organic Acid OA-1000 analytical column (7.8 × 300 mm, Hichrom, UK) maintained at 333 K. Liquid samples were diluted to be within the calibrated range (1:30 for concentrated solutions, 1:5 for dilute solutions). The analytical method was detailed in Chapter 3. For the kinetic study, calibration curves of GLAD and HPA were also obtained for a more comprehensive analysis.

4.2.3. Oxidation reactions

Oxidation reactions were performed under base-free conditions with a continuous O_2 flow in a 200 ml stainless steel fed-batch reactor custom-designed for this purpose (see Figure 4 in Chapter 3). The procedure was similar to the one described in Chapter 3, changing only certain operating conditions: temperature, oxygen pressure, catalyst load, and initial reactant.

A list of the performed experiments with the Pt-Bi/AC and Au/ZnO catalysts is presented in Table 4.1.

Table 4.1. Experimental runs with Pt-Bi/AC and Au/ZnO for the kinetic study.

#Run	Catalyst	Species	T °C	$P(O_2)$ bar	C_0 M	*w* g	Species/Pt or Au mol/mol
1	Pt-Bi/AC	GLY	80	4.5	1.0	0.82	500
2	Pt-Bi/AC	GLY	**40**	4.5	1.0	0.82	500
3	Pt-Bi/AC	GLY	**60**	4.5	1.0	0.82	500
4	Pt-Bi/AC	GLY	**90**	4.5	1.0	0.82	500
5	Pt-Bi/AC	GLY	**100**	4.5	1.0	0.82	500
6	Pt-Bi/AC	GLY	80	**2.0**	1.0	0.82	500
7	Pt-Bi/AC	GLY	80	**7.5**	1.0	0.82	500
8	Pt-Bi/AC	GLY	80	4.5	**2.0**	0.82	**1000**
9	Pt-Bi/AC	GLY	80	4.5	**0.5**	0.82	**250**
10	Pt-Bi/AC	GLY	80	4.5	**0.5**	**0.40**	**510**
11	Pt-Bi/AC	GLY	80	4.5	**0.1**	0.08	500
12	Pt-Bi/AC	GLY	**90**	4.5	**0.1**	0.08	500
13	Pt-Bi/AC	**DHA**	70	4.5	0.1	0.08	500
14	Pt-Bi/AC	**DHA**	80	4.5	0.1	0.08	500
15	Pt-Bi/AC	**DHA**	90	4.5	0.1	0.08	500
16	Pt-Bi/AC	**GCO**	70	4.5	0.1	0.08	500
17	Pt-Bi/AC	**GCO**	80	4.5	0.1	0.08	500
18	Pt-Bi/AC	**GCO**	90	4.5	0.1	0.08	500
19	Pt-Bi/AC	**OXA**	50	4.5	0.1	0.08	500
20	Pt-Bi/AC	**OXA**	70	4.5	0.1	0.08	500
21	Pt-Bi/AC	**GCA**	70	4.5	0.1	0.08	500
22	Pt-Bi/AC	**GCA**	90	4.5	0.1	0.08	500
23	Au/ZnO	GLY	80	6.5	1.0	1.0	2000
24	Au/ZnO	GLY	80	6.5	0.1	2.0	100
25	Au/ZnO	GLY	**40**	6.5	0.1	2.0	100
26	Au/ZnO	GLY	**60**	6.5	0.1	2.0	100
27	Au/ZnO	GLY	**70**	6.5	0.1	2.0	100
28	Au/ZnO	GLY	**90**	6.5	0.1	2.0	100
29	Au/ZnO	GLY	80	**2.5**	0.1	2.0	100
30	Au/ZnO	**DHA**	70	6.5	0.1	2.0	100
31	Au/ZnO	**DHA**	80	6.5	0.1	2.0	100
32	Au/ZnO	**DHA**	90	6.5	0.1	2.0	100
33	Au/ZnO	**DHA**	80	**2.5**	0.1	2.0	100

4.3. Mass Transfer Evaluation

In three-phase gas–liquid–solid catalytic reactions, assessing mass transfer resistances is essential to establish the operating regime. Conventional criteria such as Weisz-Prater [24] and Mears [25] were used to evaluate the internal and external mass transfer resistance, respectively [2]. Additionally, the influence of external (gas-liquid and liquid-solid) and internal (intraparticle) mass transfer limitations was evaluated following the criteria proposed by Ramachandran and Chaudhari for three-phase catalytic reactors [26]. Mass transfer coefficients may be experimentally obtained or estimated using several correlations available in the literature, including for slurry-agitated reactors. Correlations that do not require power consumption data were used to avoid its determination.

4.3.1. Internal Mass Transfer

The Weisz-Prater criterion [24] is the following, using only measured values:

$$C_{WP} = \frac{\rho_p \, r_{obs,i} \, R_p^2}{D_{e,i} \, C_i} < 1 \tag{4.4}$$

Here, ρ_p is the catalyst (apparent) particle density (kg_{cat}/m_{cat}), R_p is the catalyst radius (m), $D_{e,i}$ is the effective diffusion coefficient in the porous particle (m^2/s), C_i is the bulk concentration (glycerol or dissolved oxygen in the liquid phase, mol/m^3), and $r_{obs,i}$ is the corresponding observed reaction rate ($mol\ kg_{cat}^{-1}\ s^{-1}$), directly obtained from the experimental results.

Additionally, the criteria proposed by Ramachandran and Chaudhari for a first-order reaction in three-phase catalytic reactors was used [26],

$$\phi_{exp} = \frac{d_p}{6}\left[\frac{\rho_p \, r_{obs,i}}{\rho_b D_e C_i^*}\right]^{0.5} < 0.2 \tag{4.5}$$

where, d_p is the catalyst diameter (m), and ρ_b is the catalyst mass per unit volume of reactor (kg_{cat}/m^3). If these criteria are met, internal diffusion limitations can be considered negligible since the reaction is slower than pore diffusion.

4.3.2. External Mass Transfer

4.3.2.1. Mears Criterion

The Mears criterion [2, 25] was used to evaluate external diffusion limitations, namely, if the mass transfer from the bulk gas phase to the catalyst surface can be neglected compared to the observed reaction rate.

$$C_{Mears} = \frac{r_{obs,i}\,\rho_b n\, r_p}{k_{ext} C_i^*} < 0.15 \tag{4.6}$$

Here k_{ext} is the external mass transfer coefficient (m/s), related to the Sherwood number:

$$\mathrm{Sh} = \frac{k_{ext} d_p}{D} \tag{4.7}$$

with D being the molecular diffusivity, in this case for oxygen. Several correlations are available to estimate the Sherwood number. For conservative estimation, a limiting case of *Sh* = 2 (fully diffusional regime) was used [2, 27].

4.3.2.2. Gas-liquid Mass Transfer

The mass transfer resistance across the gas-liquid interface was evaluated for oxygen using [26]:

$$\alpha_{G/L} = \frac{r_{obs,O_2}}{k_L a\, C_{O_2}^*} < 0.1 \tag{4.8}$$

For slurry reactors with catalyst loadings below 10% (w/v), which is the case in this work, $k_L a$ is typically unaffected by the solid phase [26].

Several correlations for the gas-liquid mass transfer coefficient in stirred tank reactors are available in the literature [28]. The volumetric gas-liquid mass transfer coefficient, $k_L a$, was estimated using the Yagi and Yoshida correlation, developed with data of oxygen dissolved in a glycerol aqueous solution [29].

$$\mathrm{Sh}' = 0.060\, Re'^{1.5} Fr'^{0.19} Sc^{0.5} \left(\frac{\mu\, u_s}{\sigma}\right)^{0.6} \left(\frac{N\, d_I}{u_s}\right)^{0.32} \tag{4.9}$$

where $\mathrm{Sh}' = \frac{\mathrm{k_L a}\, {d_I}^2}{\mathrm{D}}$ is the Sherwood number, $\mathrm{Re}' = \frac{\mathrm{N}\,\rho\, {d_I}^2}{\mu}$ is the Reynolds number, $\mathrm{Fr}' = \frac{d_I \mathrm{N}^2}{\mathrm{g}}$ is the Froude number, all modified for the impeller, $\mathrm{Sc} = \frac{\mu}{\rho\, \mathrm{D}}$ is the Schmidt number, $\frac{\mu\, \mathrm{u_s}}{\sigma}$ is the reciprocal of the gas flow number and $\frac{N\, d_I}{u_s}$ is the aeration number. Here, d_I is the impeller diameter (m), σ is the liquid surface tension (N/m), ρ is the liquid density (kg/m^3), μ is the liquid viscosity (Pa.s), N is the rotational speed (rev/s), u_s is the superficial gas velocity (m/s), and g is the gravitational constant (9.80 m/s^2).

4.3.2.3. Liquid-Solid Mass Transfer

Liquid–solid mass transfer limitations for three-phase catalytic reactors were evaluated by [26]:

$$\alpha_{L/S} = \frac{r_{obs,i}}{k_S a_p C_i^*} < 0.1 \qquad \text{with } a_p = \frac{6\rho_b}{\rho_p d_p} \tag{4.10}$$

The liquid-solid mass transfer coefficient, k_S, was estimated using the Storck et al. correlation for agitated tanks, considering the case of mechanical agitation only [30]:

$$k_S = 7.31 \times 10^{-6} N^{0.538} \; [m\, s^{-1}] \tag{4.11}$$

The effective intraparticle diffusion coefficient, $D_{e,i}$ is given by:

$$D_{e,i} = \varepsilon_p \frac{D_i}{\tau_p} \tag{4.12}$$

where ε_p is the particle porosity, τ_p is the particle tortuosity and D_i is the molecular diffusion coefficient (Knudsen diffusion is negligible here) [2].

For glycerol, D_{GLY} was estimated using the Wilke–Chang correlation [31]:

$$D_{GLY} = 7.4 \times 10^{-8} \frac{T(\psi M)^{1/2}}{\mu V_{GLY,nbp}^{0.6}} \; [\text{cm}^2\ \text{s}^{-1}] \tag{4.13}$$

Here, the molecular weight, M (g/mol), and the dynamic viscosity, μ (cP), are specific to the solvent, which is considered to be water (M = 18.02 g/mol, and η = 1.002 cP at 293.15 K), T is temperature (K) and the solvent association factor, ψ, is 2.6 for water [31]. Glycerol molar volume at normal boiling point, $V_{GLY,nbp}$ is 87.5 cm^3/mol [32].

For O_2, the Han–Bartels correlation was used [33]:

$$D_{O_2} = 10^{-4.410 + \frac{773.8}{T} - \left(\frac{506.4}{T}\right)^2} \; [\text{cm}^2\ \text{s}^{-1}] \tag{4.14}$$

Glycerol–water mixture viscosity and density were estimated using empirical correlations proposed by Cheng [34], valid for glycerol mass concentration, $Cm = \frac{m_{GLY}}{m_{GLY}+m_{water}}$, in the range of 0−100% and temperatures varying from 0 to 100 °C:

$$\mu_{mix} = {\mu_{water}}^{\alpha} {\mu_{GLY}}^{(1-\alpha)} \tag{4.15}$$

$$\rho_{mix} = \rho_{GLY} C_m + \rho_{water}(1 - C_m) \tag{4.16}$$

with:

$$\alpha = 1 - C_m + \frac{abC_m(1 - C_m)}{aC_m + b(1 - C_m)} \tag{4.17}$$

where $a = 0.705 - 0.0017\,T$, and $b = (4.9 + 0.036\,T)a^{2.5}$. Pure water and glycerol density data with temperature are available elsewhere [32].

The temperature-dependent viscosities of water and glycerol are:

$$\mu_{water} = 1.79 \exp\left(\frac{(-1230 - T)T}{36100 + 360T}\right) \ [cP] \tag{4.18}$$

$$\mu_{GLY} = 12100 \exp\left(\frac{(-1233 + T)T}{9900 + 70T}\right) \ [cP] \tag{4.19}$$

Surface tension was assumed to match that of water [32].

4.4. Kinetic Modelling

The general reaction network previously proposed in Chapter 3 (Figure 1) was based on preliminary experimental and literature results for base-free glycerol oxidation. The network was refined for the kinetic study, presented in Figure 4.1, which accounts for the relevant species observed: GLY, DHA, GLAD, GCA, HPA, GCO, and OXA.

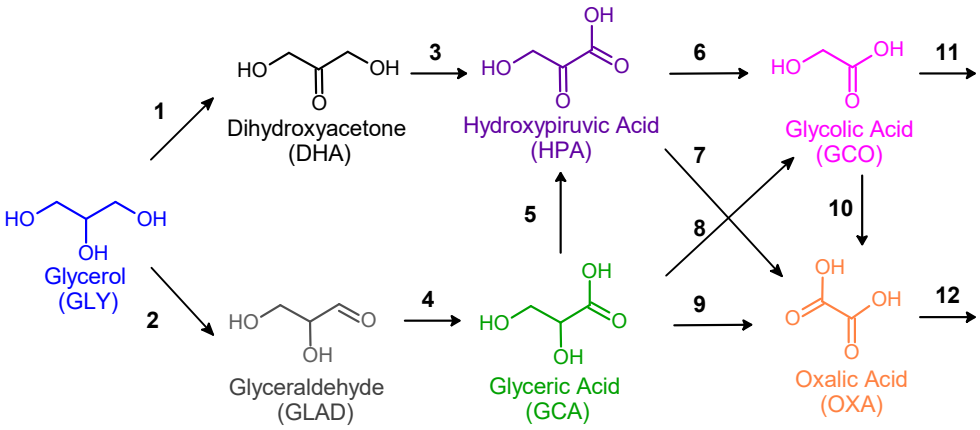

Figure 4.1. Reaction scheme for the glycerol oxidation kinetic study.

Mesoxalic acid and glyoxylic acid were detected at very low concentrations; therefore, they were excluded from the kinetic modelling. A more detailed analysis of the HPLC chromatograms revealed that the previously quantified TTA signal corresponded mainly to HPA. The retention times of TTA and HPA were very close, leading to peak overlap and initial misidentification. Subsequent reanalysis confirmed that TTA concentrations were low. As a result, the initial reaction network proposed in Chapter 3 was herein refined without any impact on the major conclusions withdrawn regarding the production of DHA.

Catalyst screening results using platinum catalysts (see Figure 8 – Chapter 3) indicated that OXA forms early during glycerol oxidation. Since it was unclear whether OXA resulted only from GCO oxidation, additional pathways were considered in the reaction scheme (Figure 4.1): step 7 (HPA → OXA) and step 9 (GCA → OXA). Furthermore, although tartronic acid (TTA), obtained as a product of GCA oxidation, was only detected in trace amounts in the liquid phase,

its oxidative conversion to GCO via mesoxalic acid was reported in the literature. Therefore, step 8 (GCA → GCO) was also included in the proposed mechanism.

Oxidation reactions were conducted in a fed-batch reactor opened for gas flow. Assuming ideal mixing and isothermal operation with negligible mass transfer limitations, the system may be modelled as a perfectly stirred tank reactor. Under these assumptions, energy and momentum balances are neglected, and the mass balance for each species simplifies to:

$$\frac{V}{w}\frac{dC_i}{dt} = \sum_j \upsilon_{ij} r_j \tag{4.20}$$

where V is the reaction liquid volume (L), w is the dry mass of the catalyst (g), C_i is the bulk concentration of species i (mol L^{-1}), r_j is the reaction rate j (mol g_{cat}^{-1} min^{-1}), and υ_{ij} is the stoichiometric coefficient of species *i* in reaction *j*.

The mass balance equations for all carbon-containing species are given by:

$$\begin{aligned}
\frac{V}{w}\frac{d[GLY]}{dt} &= -r_1 - r_2 \\
\frac{V}{w}\frac{d[DHA]}{dt} &= r_1 - r_3 \\
\frac{V}{w}\frac{d[GLAD]}{dt} &= r_2 - r_4 \\
\frac{V}{w}\frac{d[GCA]}{dt} &= r_4 - r_5 - r_8 - r_9 \\
\frac{V}{w}\frac{d[HPA]}{dt} &= r_3 + r_5 - r_6 - r_7 \\
\frac{V}{w}\frac{d[GCO]}{dt} &= r_6 + r_8 - r_{10} - r_{11} \\
\frac{V}{w}\frac{d[OXA]}{dt} &= r_7 + r_9 + r_{10} - r_{12}
\end{aligned} \tag{4.21}$$

Liquid-phase samples were periodically collected at different reaction times and quantified by HPLC. The oxygen concentration was assumed constant, as the reactor was operated at constant oxygen pressure and flow rate. The dissolved oxygen concentration C_{O_2} (mol L^{-1}) as a function of temperature T (K) and oxygen pressure $P(O_2)$ (atm) up to 60 atm was estimated using the Tromans correlation [35] - Eq. (4.22).

$$C_{O_2} = P(O_2)\, exp\left[\frac{0.046T^2 + 203.357T ln\left(\frac{T}{298}\right) - (299.378 + 0.092T)(T - 298) - 20591}{8.3144\, T}\right] \tag{4.22}$$

Although oxygen solubility decreases in aqueous-organic solutions compared to pure water, this effect was considered negligible due to the relatively low initial glycerol concentration (<10 wt.%). A more specific correlation is available for glycerol-water mixtures up to 690 g L^{-1} [36], valid between 273 K and 313 K. For the reference glycerol concentration (≈100 g L^{-1}), the estimated deviation in oxygen solubility at 4.5 bar was approximately 10% (from 4.56 to 4.14 mM). At lower glycerol concentrations (e.g., 0.1 M), this deviation drops below 1%. Even when extrapolated to 353 K, the associated error remains within 6%, justifying the approximation of oxygen solubility using pure water values. This assumption was also considered in similar studies [15].

Two different modelling approaches were considered for describing the kinetics of glycerol oxidation: an empirical power-law model, which assumes that the reaction rate depends only on the concentrations of the reacting species, and a mechanistic model based on the LHHW methodology, incorporating adsorption equilibria and assuming surface reaction as the rate-determining step. These models were compared based on their ability to describe glycerol oxidation experimental data under various operating conditions.

Although not explored in this work, alternative models such as the Eley–Rideal or the Mars–van Krevelen could also be applicable. In the Eley–Rideal model, adsorbed species react directly with gaseous oxygen, also proposed for glycerol oxidation [22], while the Mars–van Krevelen model involves an exchange between the gas phase and lattice oxygen, relevant in selective oxidation over transition metal oxides [1, 2, 6].

4.4.1. Power-Law Kinetic Model

Power-law models, although originally developed for homogeneous systems [2], have been successfully applied to describe heterogeneous catalytic reactions over metal catalysts [1, 7], including glycerol oxidation [11]. Their main advantage lies in their simplicity and reduced number of parameters, typically just the kinetic rate constant *k(T)* and the reaction orders, which facilitates parameter estimation. In this work, the following expression was proposed to describe the oxidation rate of each reaction step:

$$r_j = k_j C_i^n C_{O_2}^m \tag{4.23}$$

where k_j(T) is the kinetic rate constant for step j at a given temperature (L^{m+n} mol^{1-m-n} g_{cat}^{-1} min^{-1}), C_i is the bulk concentration of reactant species *i* (M), C_{O2} is the oxygen concentration in the liquid phase (M), and *n* and *m* are the respective partial reaction orders. Since oxygen pressure was held constant during each experiment, the rate expression can be simplified to a pseudo-nth-order form:

$$r_j = k'_j C_i^n \quad \text{with} \quad k'_j = k_j C_{O_2}^m \tag{4.24}$$

This simplification enables parameter estimation using fewer variables, facilitating model implementation and reducing the number of experiments. However, power-law models lack mechanistic insight and may be less predictive outside the experimental conditions tested.

4.4.2. Langmuir–Hinshelwood–Hougen–Watson Model

A kinetic model based on the Langmuir–Hinshelwood–Hougen–Watson (LHHW) formalism was developed to provide a mechanistic understanding of glycerol oxidation. This approach relies on adsorption–reaction–desorption steps occurring on catalyst surfaces and considers competitive adsorption among the various reactants, with the reaction being the rate-determining step. The general expressions used in the model are as follows:

Kinetic rate expression

$$r_j = k_j \, \theta_i \, \theta_O \, \theta_v \tag{4.25}$$

Surface coverage of species i

$$\theta_i = \frac{K_{ads,i} \, C_i}{1 + \sum K_{ads,i} \, C_i} \tag{4.26}$$

Vacant site coverage

$$\theta_v = 1 - \sum \theta_i \tag{4.27}$$

Oxygen coverage (assuming dissociative adsorption on different sites)

$$\theta_O = \frac{(K_{ads,O2} \, C_{O2})^{1/2}}{1 + (K_{ads,O2} \, C_{O2})^{1/2}} \tag{4.28}$$

Arrhenius law

$$k_j = k_{0,j} \, exp\left(\frac{-E_{a,j}}{RT}\right) \tag{4.29}$$

Van't Hoff law

$$K_{ads,i} = K_{ads,0,i} \, exp\left(\frac{-\Delta H_i}{RT}\right) \tag{4.30}$$

The model assumes that all organic reactants compete for the same type of active site while oxygen adsorbs dissociatively on different active sites. Reaction is assumed to occur between the adsorbed organic species and dissociated oxygen, requiring one additional vacant site to proceed. The temperature dependence of the kinetic rate constant, k, is given by the Arrhenius equation, and the equilibrium constant, K_{ads}, is given by the analogous Van't Hoff equation. E_a and ΔH represent the activation energy and adsorption enthalpy, respectively, and k_0 and $K_{ads,0}$ are the corresponding pre-exponential factors. The full expression of the reaction rate per unit mass of catalyst for each step is derived accordingly:

$$r_1 = k_1\,\theta_{GLY}\,\theta_O\,\theta_v \qquad r_7 = k_7\,\theta_{HPA}\,\theta_O\,\theta_v \tag{4.31}$$

$$r_2 = k_2\,\theta_{GLY}\,\theta_O\,\theta_v \qquad r_8 = k_8\,\theta_{GCA}\,\theta_O\,\theta_v$$

$$r_3 = k_3\,\theta_{DHA}\,\theta_O\,\theta_v \qquad r_9 = k_9\,\theta_{GCA}\,\theta_O\,\theta_v$$

$$r_4 = k_4\,\theta_{GLAD}\,\theta_O\,\theta_v \qquad r_{10} = k_{10}\,\theta_{GCO}\,\theta_O\,\theta_v$$

$$r_5 = k_5\,\theta_{GCA}\,\theta_O\,\theta_v \qquad r_{11} = k_{11}\,\theta_{GCO}\,\theta_O\,\theta_v$$

$$r_6 = k_6\,\theta_{HPA}\,\theta_O\,\theta_v \qquad r_{12} = k_{12}\,\theta_{OXA}\,\theta_O\,\theta_v$$

4.4.3. Model Implementation

The system of ordinary differential equations, Eq. (4.21), describing the glycerol oxidation reaction network, was implemented in MATLAB R2024b (MathWorks, Inc., USA) and integrated using the *ode15s* solver, suitable for stiff systems. Experimental concentration profiles as a function of time and operating conditions (temperature, oxygen pressure, catalyst mass) were used as input for parameter estimation.

Kinetic and adsorption parameters were estimated using the nonlinear least-squares routine *lsqcurvefit*, which minimises the sum of square residuals (SSR) between experimental and model-predicted concentrations.

$$SSR = \sum_{i=1}^{n} \left(C_{i,exp} - C_{i,model}\right)^2 \tag{4.32}$$

where $C_{i,exp}$ and $C_{i,model}$ are the experimental and predicted concentrations of species i, respectively, and n is the total number of data points. Model performance was evaluated quantitatively (via SSR) and qualitatively by visually comparing the experimental and simulated concentration profiles.

Although all parameters could, in principle, be estimated simultaneously, the complexity of the system and the large number of adjustable parameters pose significant challenges for optimisation. In such cases, numerical algorithms may converge to local minima depending on the initial parameter guesses. Moreover, these optimisation methods tend to fail if the number of parameters is too large or if there is a strong correlation between them. While global optimisation techniques exist, they are often computationally demanding and may not guarantee convergence to physically meaningful solutions.

To address these challenges, specific sets of experiments were performed to minimise the number of reactive species involved, reducing the problem's complexity and the number of parameters to be estimated. These results then served as initial guesses for

parameter estimation with the complete reaction network, improving convergence and model reliability.

Additionally, when combining datasets with different initial glycerol concentrations, weighting factors were introduced in the objective function to normalise the influence of each dataset. For example, when fitting two datasets with $C_{GLY,0}$ of 1 M and 2 M, a weight of 0.5 was applied to the latter.

4.5. Mass Transfer Results

Mass transfer resistances were evaluated to determine if glycerol oxidation reactions proceeded under kinetic control. The assessment relied on established dimensionless criteria detailed in Section 4.3 (focusing on the worst-case scenario at 90 °C). The results are summarised in Table 4.2, while the supporting data and selected calculation details are provided in Table C.1 in Appendix C. The reaction rate values used in these calculations will be presented in Sections 4.6.1 and 4.7.1.

Table 4.2. Mass transfer criteria for Pt-Bi/AC and Au/ZnO catalysts at 90 °C.

Criteria	Pt5-Bi1.5/AC	Au1/ZnO
$(-r_{GLY})_0$ (mol kg_{cat}^{-1} s^{-1})	6.7×10^{-2}	1.0×10^{-3}
$(-rO_2)_0$ (mol kg_{cat}^{-1} s^{-1})	3.3×10^{-2}	5.1×10^{-4}
Internal mass transfer resistance		
ϕ_{exp} (O_2) < 0.2	0.20	2.2×10^{-2}
ϕ_{exp} (GLY) <0.2	0.02	7.9×10^{-3}
C_{WP} (O_2) < 1	0.40	4.2×10^{-3}
C_{WP} (GLY) < 1	4.7×10^{-3}	5.7×10^{-4}
External mass transfer resistance		
C_{Mears} (O_2) < 0.15	1.9×10^{-3}	8.8×10^{-6}
C_{Mears} (GLY) < 0.15	2.2×10^{-5}	1.2×10^{-6}
αG/L (O_2) < 0.1	0.9	2.4×10^{-2}
αL/S (O_2) < 0.1	7.9×10^{-2}	1.1×10^{-3}
αL/S (GLY) < 0.1	4.8×10^{-4}	1.0×10^{-4}

Both criteria tested, ϕ_{exp} and Weisz–Prater, indicate negligible internal diffusion limitations for glycerol in both catalysts. Oxygen diffusion within the Pt-Bi/AC particles approached the limit (ϕ_{exp} = 0.20) but remained within acceptable limits. The corresponding Weisz–Prater value for O_2 was 0.40, implying ≈98% reaction efficiency [24], suggesting that intraparticle diffusion is not rate-limiting. Thus, internal mass transfer resistances were considered negligible.

The stirring speed was fixed at 800 rpm to minimise external mass transfer limitations. Higher agitation led to catalyst losses to the reactor headspace and walls. The Mears criterion for external mass transfer was satisfied in all cases, even assuming Sh = 2 (worst case), indicating that external diffusion was not limiting under the tested conditions.

Based on the Ramachandran–Chaudhari criteria, liquid-solid mass transfer resistances for glycerol and oxygen were negligible for both catalysts. The gas-liquid mass transfer was insignificant when using the Au/ZnO. For Pt-Bi/AC, however, $\alpha_{G/L} \approx 0.9$ suggests a possible limitation in oxygen transfer across the gas-liquid interface. Nonetheless, estimating k_La accurately in small lab-scale stirred reactors remains challenging [37], as most correlations available in the literature were developed for larger reactors (0.5–500 L) [26]. For the present setup and N = 800 rpm, typical k_La values range from 0.05-0.1 s^{-1} [26, 38, 39].

Nonetheless, oxygen was supplied via a sintered dip tube, generating fine bubbles that enhanced mixing and gas-liquid contact [40]. Thus, any transfer limitation is likely minor, and external mass transfer resistances were considered negligible. Additionally, catalyst adherence at the gas-liquid interface may allow direct oxygen transfer from the gas phase to the catalyst surface, bypassing the bulk liquid. This phenomenon has been proposed for alcohol oxidation over aqueous noble metal catalysts, including Pt and Pd-Bi, where it was suggested that oxygen diffuses directly into the liquid-filled pores of the catalyst [3].

In summary, no significant internal or external mass transfer resistances are expected across the tested operating range. The system can thus be assumed to operate under kinetic control. Only in the case of Pt-Bi/AC might minor gas–liquid limitations occur, but they are not expected to compromise the reaction kinetics.

4.6. Glycerol Oxidation Kinetics with Pt-Bi/AC

4.6.1. Preliminary Analysis

To obtain initial estimates with physical meaning for parameter estimation and support subsequent kinetic modelling, preliminary experiments were carried out under varying operating conditions and using different reactants to isolate individual reaction steps. A power-law kinetic model was employed to describe the oxidation rate of some species using only the concentration profile of the reactant.

Glycerol and key oxidation products: dihydroxyacetone (DHA), glyceric acid (GCA), glycolic acid (GCO), and oxalic acid (OXA), were each tested as reactants. Although other species, such as glyceraldehyde (GLAD) and hydroxypyruvic acid (HPA), are relevant within the oxidation network, their use was excluded due to prohibitively high costs.

All experiments were conducted in 100 mL of aqueous solution. The initial glycerol concentration was set at 1.0 M, while intermediates were tested at 0.1 M to mimic the concentrations expected for each compound during the reaction and reduce the catalyst needed per experiment. Reference operating conditions were set at an oxygen pressure of 4.5 bar (oxygen flowrate 200 ml/min), stirring speed of 800 rpm and a GLY/Pt initial molar ratio of 500, corresponding to catalyst loadings of 0.82 g for glycerol and ≈ 0.08 g for intermediate oxidation tests.

4.6.1.1. Initial reaction rates and mass transfer evaluation

To evaluate the influence of mass transfer limitations on the observed reaction rates, a series of glycerol oxidation experiments was performed under varying operating conditions:

1. Varying initial glycerol concentrations at fixed catalyst mass;
2. Varying glycerol concentrations at constant GLY/Pt molar ratio;
3. Varying catalyst load at fixed GLY initial concentration.

Initial reaction rates of glycerol consumption, expressed per unit volume ($r''_{0,GLY}$, mmol L^{-1} min^{-1}) were calculated as the first derivative of the experimental concentration-time profile using the centred finite difference method, presented in Figure 4.2.

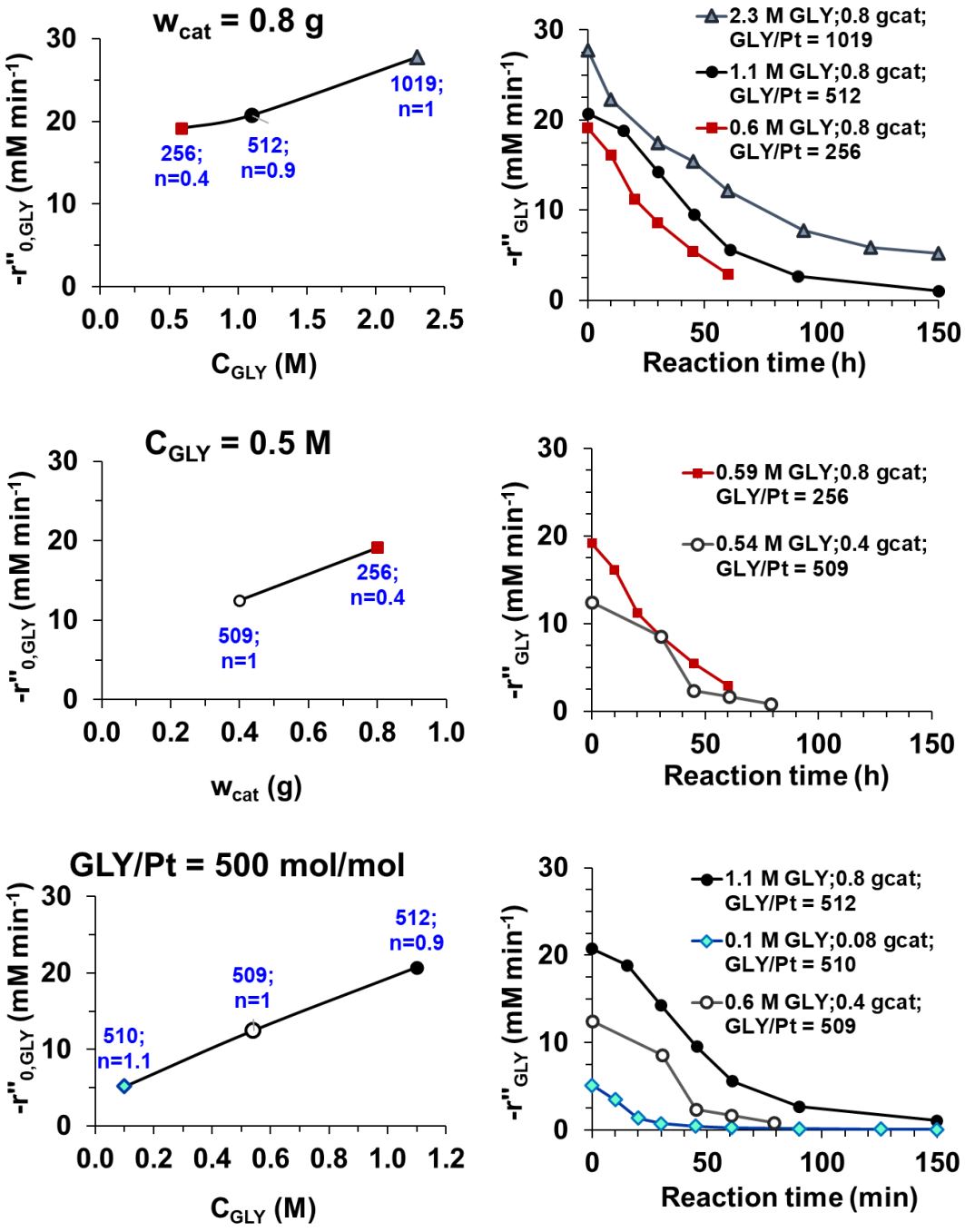

Figure 4.2. Glycerol oxidation over Pt-Bi/AC. Left) Initial reaction rates; Right) reaction rates over time. Top) *w* = 0.8 g; Middle) $C_{GLY,0}$ = 0.5 M; Bottom) GLY/Pt = 500 mol/mol. T = 80 °C, $P(O_2)$ = 4.5 bar, V = 1 L, 800 rpm. Data tags (blue): GLY/Pt (mol/mol) and estimated pseudo-reaction order.

At a fixed GLY/Pt molar ratio of approximately 500, i.e., the same initial ratio of GLY and Pt active sites amounts, the initial reaction rate increased nearly linearly with glycerol concentration in the range of 0.1 to 1.0 M. Moreover, the reaction rate data were well-described by a pseudo-first-order rate law across this concentration range, suggesting that mass transfer limitations were

not significant under these conditions, as previously estimated using mass transfer correlations in Section 4.5.

When the catalyst mass was fixed at 0.8 g, and the initial glycerol concentration increased from 0.5 to 2.0 M, the initial rate also increased, but the relationship was no longer linear. In this case, the apparent reaction order (obtained via the differential method) also increased with glycerol concentration, which is inconsistent with a power-law model and suggests that an alternative kinetic expression might better describe the system.

Conversely, at constant glycerol concentration (≈ 0.5 M), increasing the catalyst mass from 0.4 to 0.8 g resulted in higher reaction rates. However, the corresponding pseudo-order decreased, again implying that a power-law model is inadequate for describing the whole concentration range. Although higher catalyst loads were not tested due to material constraints, the literature indicates that further increases in catalyst amount would eventually lead to a plateau in reaction rate, marking the onset of mass transfer limitations and inefficient catalyst utilisation, as shown in other glycerol oxidation studies [12, 41, 42].

4.6.1.2. Temperature Dependence

The influence of temperature on the catalytic oxidation of glycerol was investigated in the range of 40-100°C under otherwise identical operating conditions. The corresponding concentration profiles of glycerol and its oxidation products at various temperatures are presented in Figure 4.3 (left column). The right column of Figure 4.3 shows the concentration profiles of the reaction products only for easier visualisation.

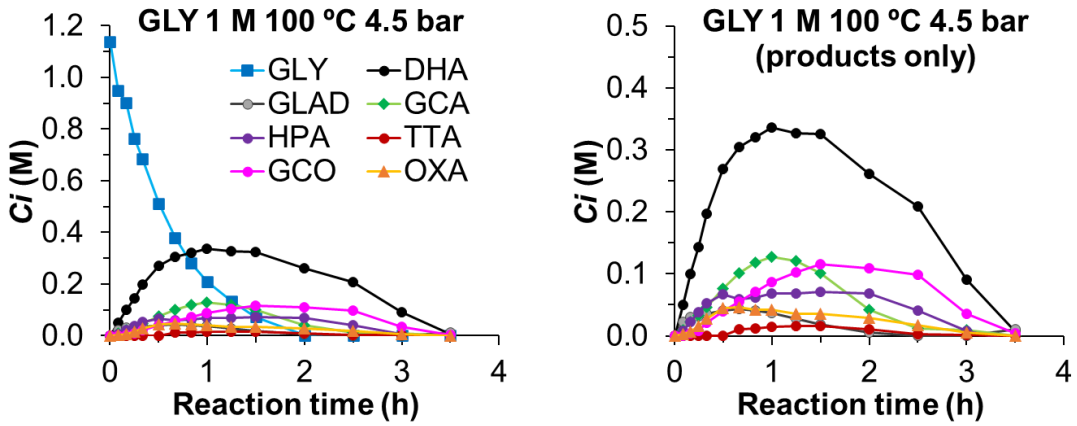

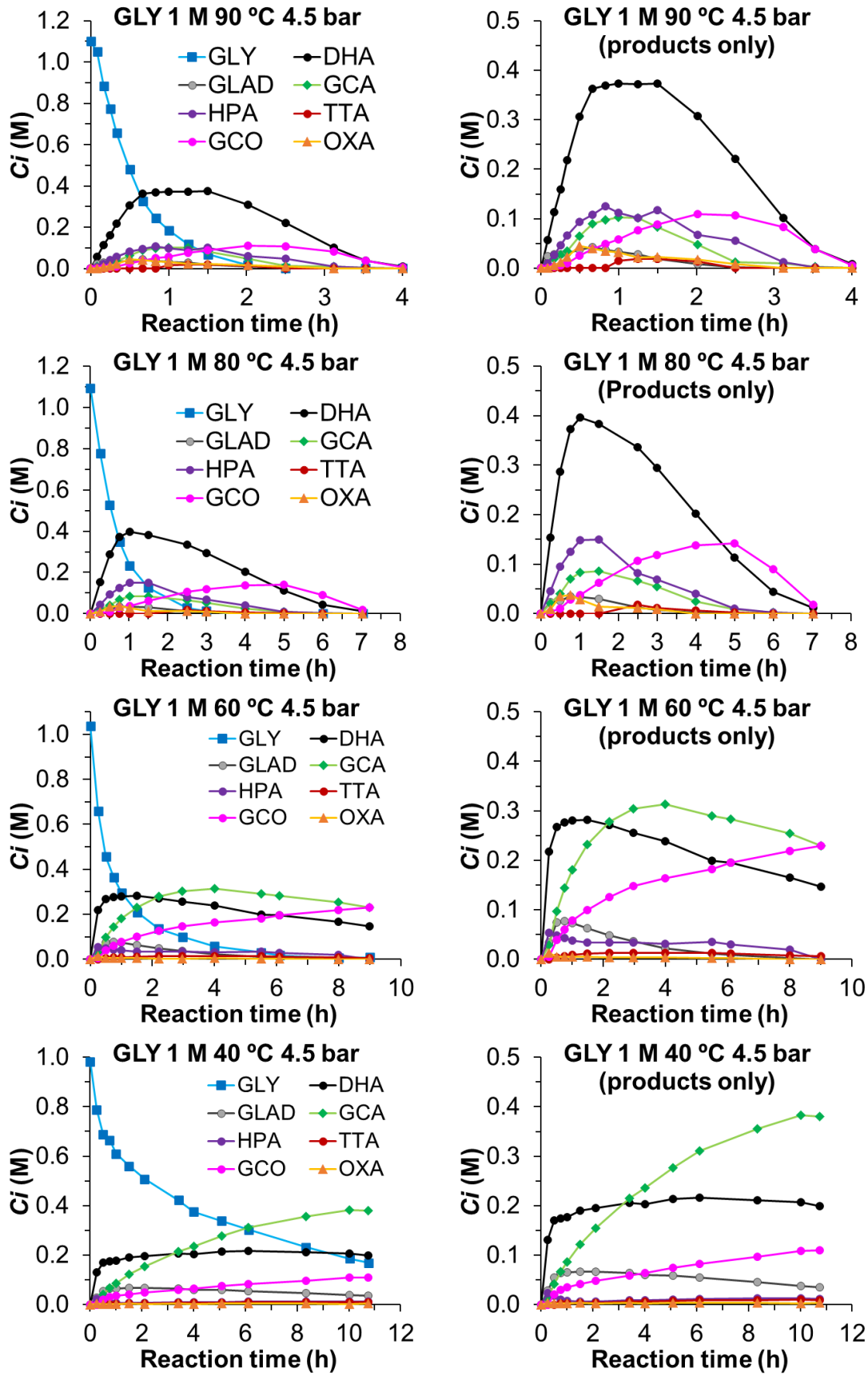

Figure 4.3. Concentration profiles of glycerol oxidation over Pt-Bi/AC at 40–100°C. Left: all species; Right: oxidation products only.

To evaluate the kinetic behaviour of glycerol oxidation independently of product profiles, the differential method was applied by plotting $\ln(-r_{GLY})$ vs. $\ln(C_{GLY})$. As shown in Figure 4.4c, the analysis indicates that the reaction approximates pseudo-first-order kinetics at temperatures ≥ 80 °C. However, at lower temperatures, significant deviations from this behaviour were observed. Specifically, the apparent reaction order increased to approximately 1.5 at 60 °C and 3.0 at 40 °C. Since the reaction order is independent of the temperature, this deviation suggests that a power-law model does not adequately describe the system's behaviour across the whole temperature range. A likely explanation for this deviation is catalyst deactivation at lower temperatures, potentially due to the adsorption of strongly binding species, such as carboxylic acids, that becomes more relevant under these conditions due to the exothermic nature of adsorption.

Assuming pseudo-first-order kinetics, the integral method was used to analyse the data at T ≥ 80 °C (Figure 4.4a). This approach also provided reasonable agreement when applied to the initial reaction data (t ≤ 30 min) at 40 °C and 60 °C, as shown in Figure 4.4b (full dots indicate the data used for linear fitting, represented by solid lines). The corresponding rate constants are summarised in Table 4.3.

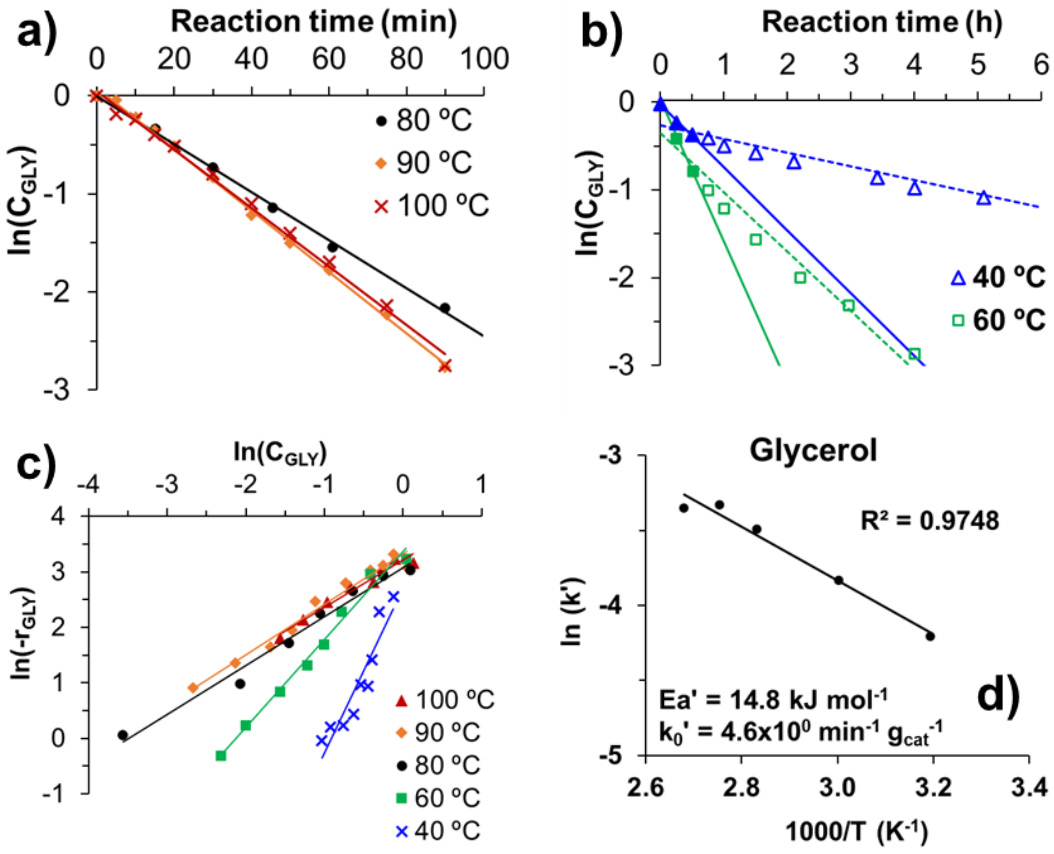

Figure 4.4. Preliminary kinetic study of glycerol oxidation: (a-b) integral method using pseudo-first-order approximation; (c) differential method; (d) Arrhenius plot.

Table 4.3. Glycerol oxidation rate constants (initial data) at different temperatures with Pt-Bi/AC. $P(O_2)$ = 4.5 bar; $C_{GLY,0}$ = 1 M; GLY/Pt = 500 mol/mol; w = 0.8 g; V = 0.1 L.

T (ºC)	PO_2 (bar)	$C_{GLY,0}$ (M)	$[O_2]$ (mM)	k' (L min^{-1} g^{-1})
40	4.5	1.0	4.56	0.0015
60	4.5	1.0	3.78	0.0022
80	4.5	1.1	3.42	0.0030
90	4.5	1.1	3.35	0.0036
100	4.5	1.1	3.32	0.0035

From the Arrhenius plot (Figure 4.4d), an activation energy $Ea'_{GLY,oxi}$ = 14.8 kJ mol^{-1} and a pre-exponential factor $k'_{0,GLY,oxi}$ = 0.46 L min^{-1} g_{cat}^{-1} were estimated. Parameter estimation using MATLAB, considering only glycerol oxidation (GLY → products) at T ≥ 80 °C, showed consistent results: Ea'_{GLY} = 13.6 kJ mol^{-1}; $k'_{0,GLY}$ = 0.31 L min^{-1} g_{cat}^{-1}. The model results, based on a pseudo-first-order reaction ($Ea'_{GLY,oxi}$ = 14.8 kJ mol^{-1} and $k'_{0,GLY,oxi}$ = 0.46 L min^{-1} g_{cat}^{-1}), were represented and show good agreement with experimental data at T ≥ 80 °C while failing at lower temperatures (Figure 4.5).

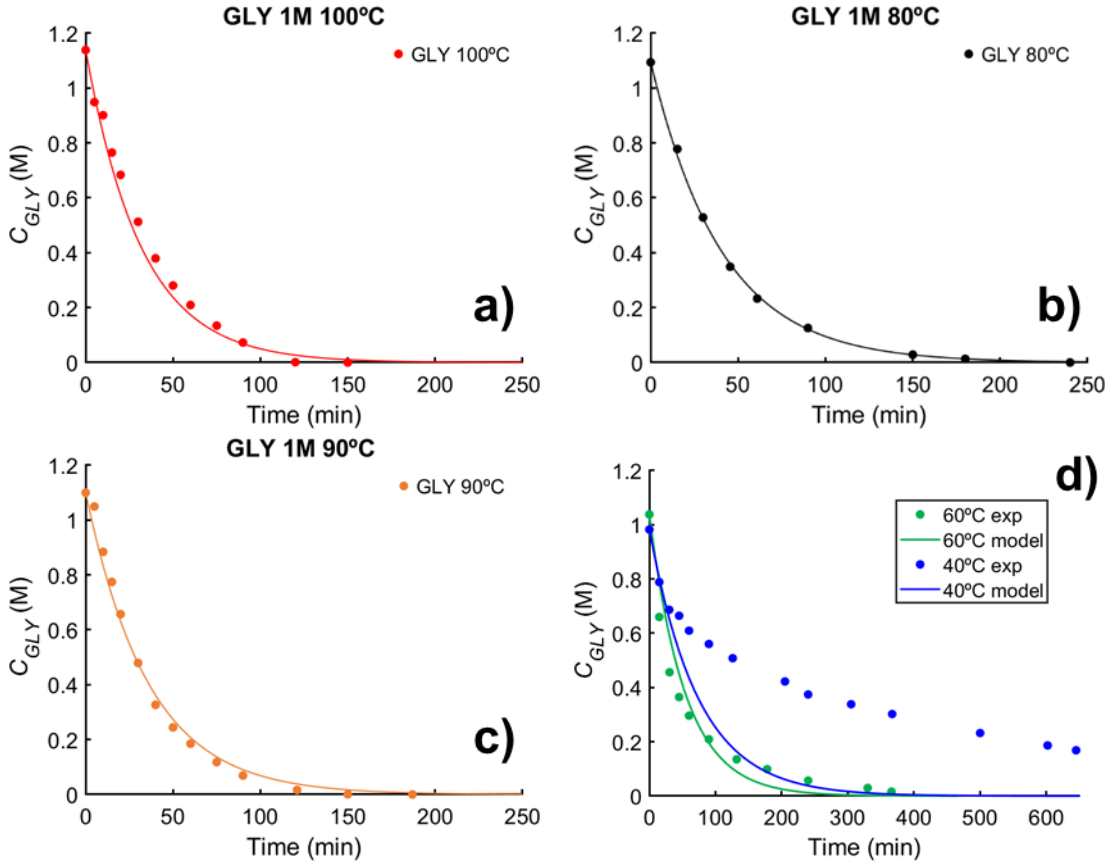

Figure 4.5. Glycerol concentration profiles: experimental (dots) and pseudo-first-order power-law model results (lines) at: (a) 100 °C, (b) 90 °C, (c) 80 °C, (d) 60-40°C. $P(O_2)$ = 4.5 bar; $C_{GLY,0}$ = 1 M; GLY/Pt = 500 mol/mol; w = 0.8 g; V = 0.1 L.

At temperatures below 80 °C, Pt-Bi/AC appears to undergo deactivation, likely due to early-stage poisoning by strongly adsorbing species. This results in lower glycerol conversion and reduced DHA selectivity, accompanied by the accumulation of GCA. Consequently, subsequent kinetic analyses will be restricted to temperatures ≥ 80 °C, where a pseudo-first-order approximation remains valid.

4.6.1.3. Oxygen pressure influence

The influence of oxygen partial pressure on the catalytic oxidation of glycerol was evaluated by conducting experiments at three different oxygen pressures: 2.0 bar, 4.5 bar, and 7.5 bar. All other operating conditions were held constant: temperature = 80 °C, initial glycerol concentration $C_{GLY,0}$ = 1.0 M, GLY/Pt molar ratio = 500 mol/mol, and stirring rate = 800 rpm. The resulting concentration profiles of glycerol and its oxidation products at the different oxygen pressures are presented in Figure 4.6.

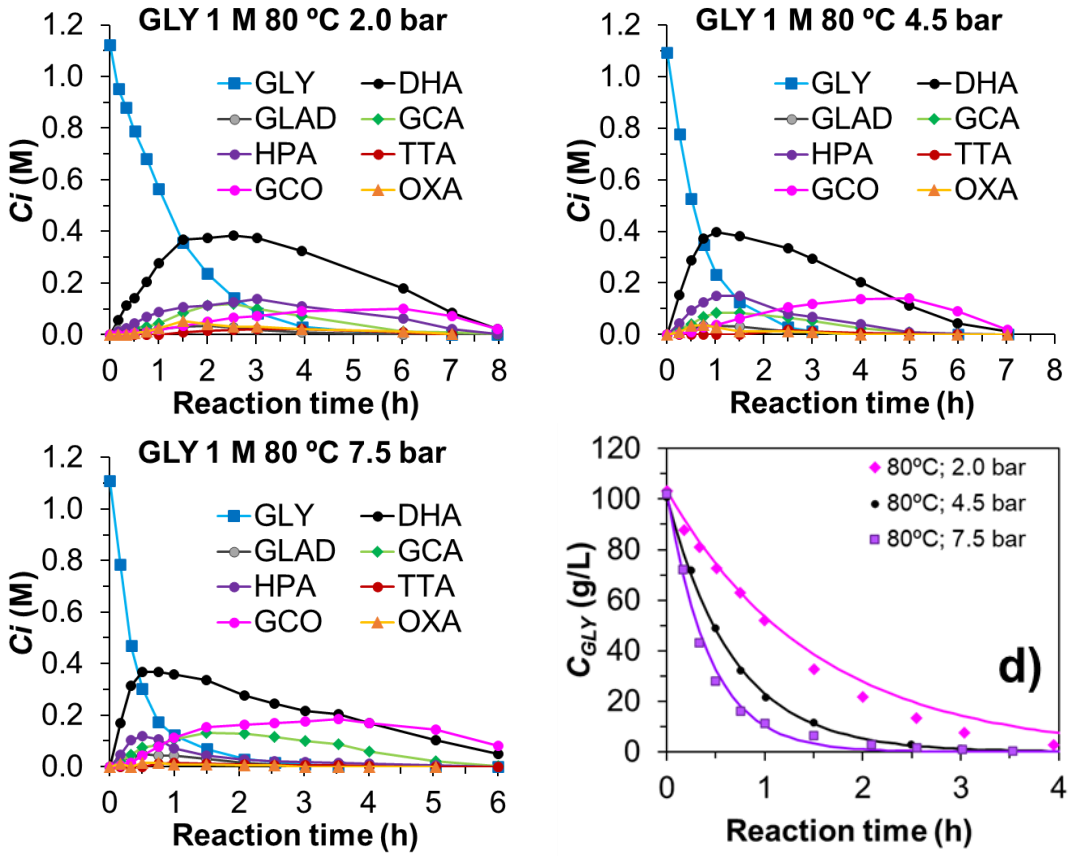

Figure 4.6. Concentration profiles of glycerol oxidation with Pt-Bi/AC at P(O_2) of 2.0 bar, 4.5 bar, and 7.5 bar. d) Model results for second-order power-law (first-order in GLY and O_2). T = 80 °C; $C_{GLY,0}$ = 1.0 M; GLY/Pt = 500 mol/mol, *w* = 0.8 g, V = 0.1 L.

The experimental data were subsequently used to determine the reaction order with respect to oxygen, assuming a power-law rate expression of the form:

$$r_{GLY,oxi} = k_{GLY,oxi} C_{GLY} C_{O_2}^{m} \quad (4.33)$$

The initial reaction rates (r_0) were calculated and are summarised in Table 4.4, along with the corresponding dissolved oxygen concentrations.

Table 4.4. Initial reaction rate of glycerol oxidation using Pt-Bi/AC at $P(O_2)$ of 2.0, 4.5 and 7.5 bar. T= 80 °C; $C_{GLY,0}$ = 1.0 M; GLY/Pt = 500 mol/mol, *w* = 0.8 g, V = 0.1 L.

$P(O_2)$ (bar)	$C(O_2)$ (mM)	r_0 (mol g_{cat}^{-1} min^{-1})
2.0	1.4	9.5×10^{-4}
4.5	3.2	2.4×10^{-3}
7.5	5.4	4.0×10^{-3}

By comparing the reaction rates at different oxygen concentrations while maintaining constant glycerol concentration and temperature, the partial order with respect to oxygen was estimated to be $m \approx 1$. Therefore, under these conditions, glycerol oxidation is well described by a second-order power-law kinetic expression, first-order in both glycerol and oxygen:

$$r_{GLY,oxi} = k_{GLY,oxi} C_{GLY} C_{O_2} \quad (4.34)$$

Model results based on this kinetic expression are shown in Figure 4.6 (bottom-right), demonstrating good agreement with the experimental data.

4.6.1.4. Oxalic acid oxidation

To investigate the oxidation kinetics of reaction intermediates, these compounds were used as initial reactants, dividing the glycerol oxidation network into smaller subnetworks. The effect of temperature was the only variable studied, while all other parameters were maintained constant: $P(O_2)$ = 4.5 bar, 800 rpm and reactant/Pt = 500 mol/mol corresponding to a catalyst load of *w* = 0.08 g. Oxalic acid, the final product of the overall reaction pathway, was tested as the initial reactant at 50 °C and 70 °C. The experimental data are represented in Figure 4.7-left.

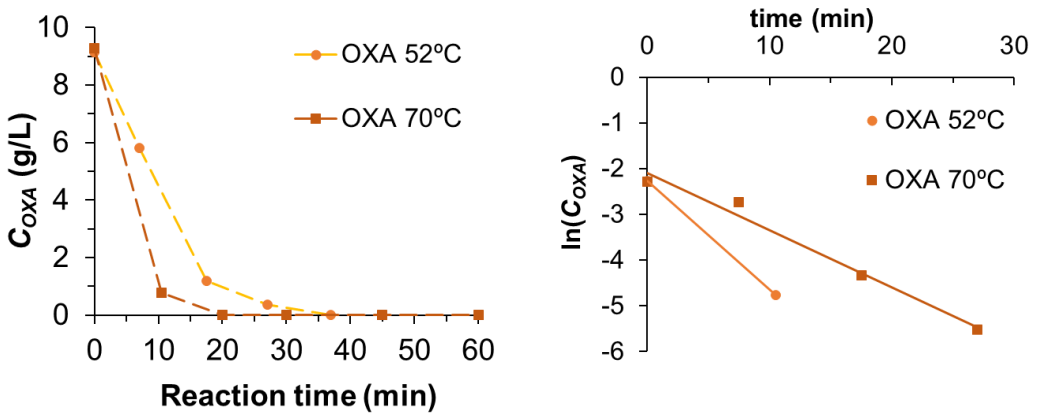

Figure 4.7. Oxalic acid oxidation with Pt-Bi/AC at 50 °C and 70 °C. Left: concentration profiles; Right: integral method assuming pseudo-first-order kinetics. P(O_2) = 4.5 bar; $C_{OXA,0}$ = 0.1 M; OXA/Pt = 500 mol/mol, w = 0.08 g, V = 0.1 L.

As expected, no product was detected in the liquid phase, indicating complete oxidation to CO_2 and water. The reaction proceeded very rapidly, limiting the number of data points collected. Nevertheless, a pseudo-first-order kinetic model was assumed for simplicity, describing the experimental data reasonably well (Figure 4.7-right).

The kinetic constants were obtained from the slopes of the linear adjusts, and despite the limited dataset, the Arrhenius plot still provided a reasonable first approximation. An activation energy Ea'_{OXA} of 35.6 kJ mol^{-1} and a $k'_{0,OXA}$ of 7.7×10^4 L g_{cat}^{-1}min^{-1} was estimated (summarised in Table 4.5 at the end of this Section). These results are summarised in Table 4.5, and the corresponding model fit is shown in Figure 4.8.

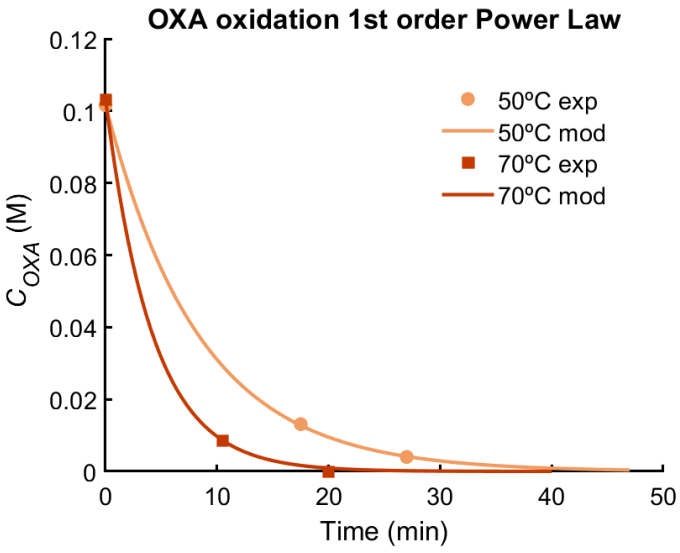

Figure 4.8. OXA oxidation over Pt-Bi/AC: experimental data (dots), pseudo-first-order power-law (lines). P(O_2) = 4.5 bar, $C_{OXA,0}$ = 0.1 M, OXA/Pt = 500 mol/mol, w = 0.08 g, V = 0.1 L.

The model described the experimental data well. Assuming that oxygen follows a first-order reaction, Ea_{OXA} of 41.4 kJ mol^{-1} and $k_{0,OXA}$ of 1.7×10^8 L^2 mol^{-1} g_{cat}^{-1} min^{-1} were estimated.

4.6.1.5. Glycolic acid oxidation

GCO was used as the initial reactant for the oxidation experiments. As expected, OXA was obtained, although only in trace concentrations in the liquid phase, consistent with the high reaction rate of OXA oxidation. The concentration profiles are presented in Figure 4.9 (top-left).

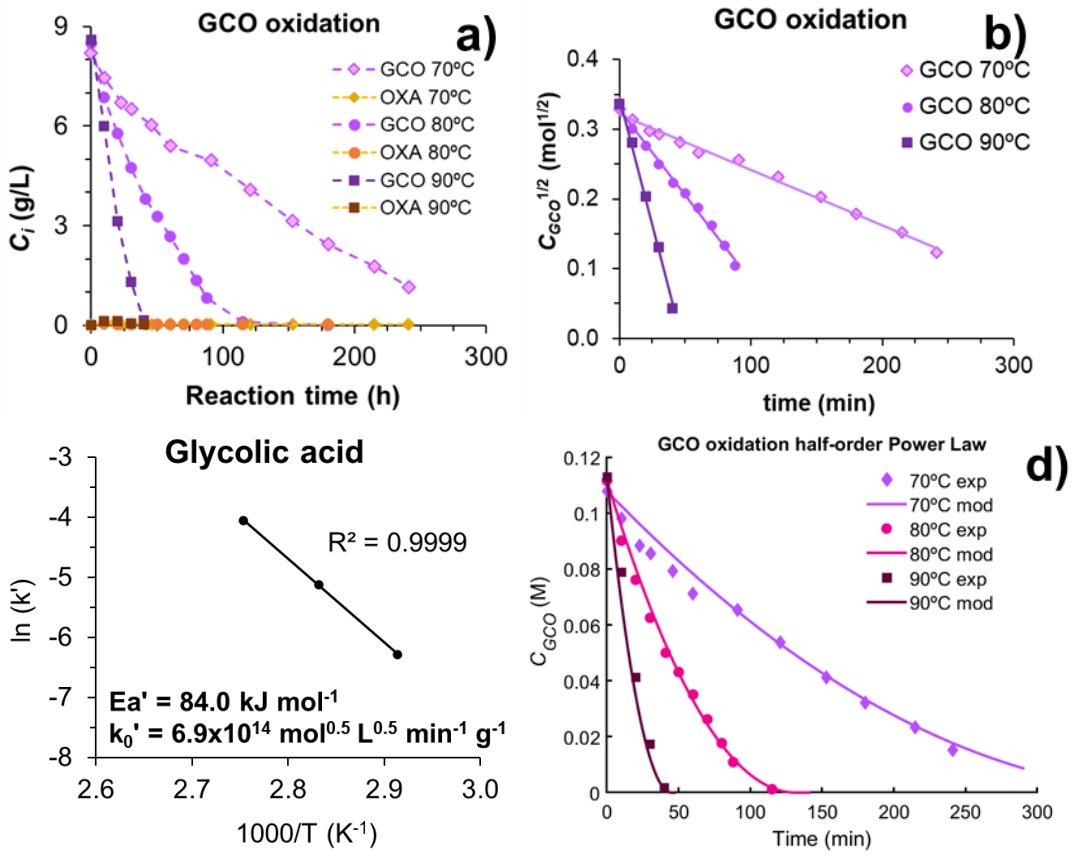

Figure 4.9. Glycolic acid oxidation with Pt-Bi/AC at 70 °C, 80 °C, and 90 °C: a) concentration profiles; b) integral method assuming pseudo-half-order reaction; c) Arrhenius plot; d) experimental data (dots) and model results (lines). P(O_2) = 4.5 bar; $C_{GCO,0}$ = 0.1 M; GCO/Pt = 500 mol/mol, *w* = 0.08 g, V = 0.1 L.

The oxidation of GCO followed a pseudo-half-order oxidation kinetic, represented by $r_{GCO,oxi} = k'_{GCO,oxi}\, C_{GCO}^{0.5}$. A pseudo-first-order oxidation kinetic failed to describe GCO oxidation data at high GCO conversions, as illustrated in Figure D.1 from Appendix D.

From the integral method plot (Figure 4.9 top-right), the kinetic constants were obtained by the slope of the linear fitting and used to obtain the Arrhenius plot (Figure 4.9 bottom-left). An activation energy Ea'_{GCO} of 115.4 kJ mol^{-1}, and a pre-exponential factor of $k'_{0,GCO}$ of 6.9×10^{14} L$^{0.5}$ mol$^{0.5}$ g_{cat}^{-1} min^{-1} were estimated for GCO oxidation (summarised in Table 4.5 at the end of this Section). Assuming that oxygen follows a first-order reaction, an activation energy Ea_{GCO} of 118.3 kJ mol^{-1} and a $k_{0,GCO}$ of 5.5×10^{17} L$^{1.5}$ mol$^{-0.5}$ g_{cat}^{-1} min^{-1} were estimated.

The experimental data and corresponding model fit are represented in Figure 4.9 (bottom-right), showing good agreement between them. None of the kinetic works with Pt-Bi/AC [15, 16]

studied GCO oxidation kinetics; thus, this is the first time GCO oxidation with a Pt-Bi/AC under base-free conditions was investigated.

4.6.1.6. Dihydroxyacetone oxidation

DHA oxidation was studied at 70 °C, 80 °C and 90 °C, presented in Figure 4.10.

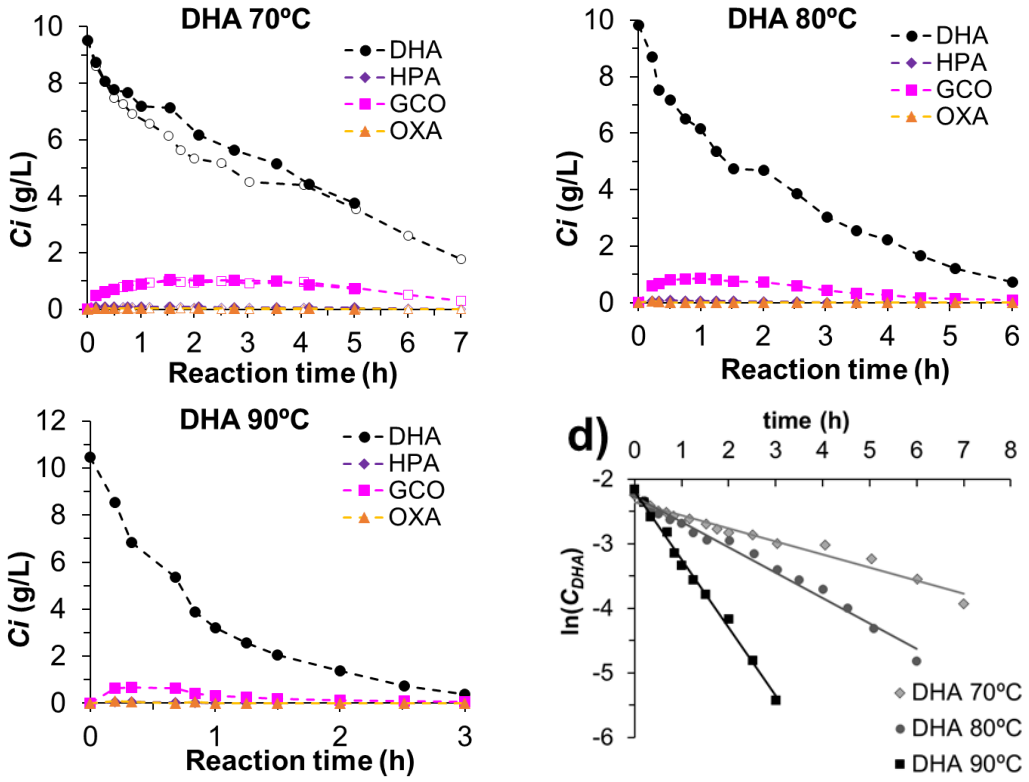

Figure 4.10. (a-c) DHA oxidation over Pt-Bi/AC, T = 70-90 °C. d) integral method for pseudo-first-order power-law. $P(O_2)$=4.5 bar; $C_{DHA,0}$=0.1 M; DHA/Pt=500 mol/mol, w=0.08 g, V=0.1 L.

The main product in the liquid phase was GCO, along with trace amounts of HPA, OXA, and glyoxylic acid (GOX, not shown in the plots). From Figure 4.10-bottom-right, it can be verified that DHA oxidation may be well described by a pseudo-first-order reaction kinetic model: $r_{DHA,oxi} = k'_{DHA,oxi}\, C_{DHA}$. The kinetic constants were obtained from the slopes of the linearised plots (Figure 4.10, bottom-right) and used to get the Arrhenius plot (Figure 4.11, left).

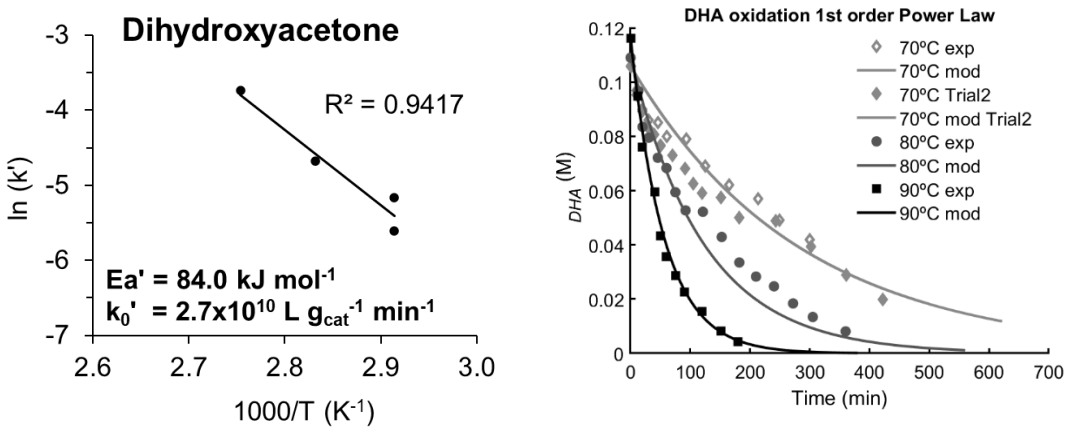

Figure 4.11. DHA oxidation with Pt-Bi/AC. Left: Arrhenius plot; Right: experimental data(dots), power-law model (lines). $P(O_2)$ = 4.5 bar; $C_{DHA,0}$ = 0.1 M; DHA/Pt = 500 mol/mol, w = 0.08 g, V = 0.1 L.

An Ea'_{DHA} of 84.0 kJ mol^{-1} and a $k'_{0,DHA}$ of 2.7×10^{10} L g_{cat}^{-1} min^{-1} were estimated for DHA oxidation (summarised in Table 4.5 at the end of this Section). Assuming that oxygen follows a first-order reaction, an activation energy Ea_{DHA} of 86.9 kJ mol^{-1} and a $k_{0,DHA}$ of 2.2×10^{13} L^2 mol^{-1} g_{cat}^{-1} min^{-1} were estimated. The model results are represented in Figure 4.11 (right), showing good agreement with the experimental data at 90 ºC, while it presents slight deviations for higher DHA conversions at 80 ºC and 70 ºC. Two trials were performed at 70 ºC to check if the data results were reproducible.

4.6.1.7. Glyceric acid oxidation

GCA was used as the initial reactant, but the oxidation did not occur, as shown in Figure 4.12.

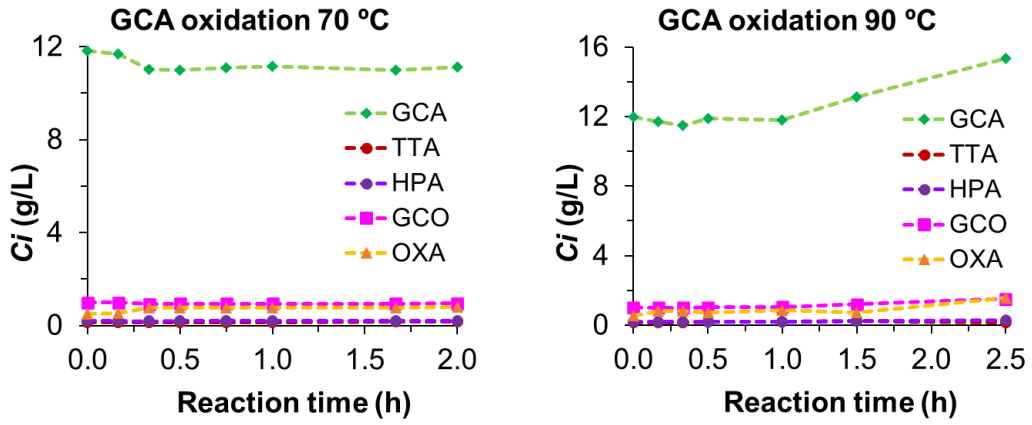

Figure 4.12. GCA oxidation over Pt-Bi/AC at 70 °C (left) and 90 °C (right). $P(O_2)$ = 4.5 bar; $C_{GCA,0}$ = 0.1 M; GCA/Pt = 500 mol/mol, w = 0.08 g, V = 0.1 L.

The commercial GCA solution available was not pure, containing small amounts of other species such as tartronic acid (TTA), hydroxypiruvic acid (HPA), glycolic acid (GCO), oxalic acid (OXA), and trace levels of unidentified compounds (Figure 4.12, t = 0). No GCA oxidation

was observed at either 70 °C or 90 °C. At 70 °C, a slight decrease in GCA concentration was noted without the formation of any new products, suggesting that this may be due to GCA adsorption on the catalyst surface. A similar trend was observed at 90 °C, except that for longer reaction times, GCA concentration increased, most likely due to water evaporation. Interestingly, the reaction solution turned from transparent to yellow after 2 hours, which may be attributed to the formation of trace amounts of glyoxal and glyoxylic acid (C2 products), both of which are yellow in the liquid phase.

The absence of catalytic activity for GCA oxidation was unexpected. This result contrasts with observations from glycerol oxidation experiments at 80 °C, 90 °C, and 100 °C, where GCA is both produced and consumed. At lower temperatures (40 °C and 60 °C), GCA consumption is significantly slower, with GCA remaining the most concentrated product after two hours of reaction (≈40 g/L), whereas at $T \geq 80$ °C, GCA concentrations did not exceed 10 g/L. Reduced catalytic activity was expected for GCA oxidation, as reported for glycerol oxidation in the presence of GCA using a lab-made Pt-Bi/AC catalyst by Worz et al. [15], but still, some catalytic activity was expected. Varma and coworkers [16] also studied GCA oxidation as the substrate using a lab-made Pt-Bi/AC catalyst under similar conditions: $C_{GCA,0}$ = 0.1 M, base-free conditions, 50-90°C, further highlighting the unexpected results obtained in this work with the commercial Pt-Bi/AC catalyst.

4.6.1.8. Summary

The results obtained from the preliminary kinetic analysis are summarised in Table 4.5.

Table 4.5. Preliminary Arrhenius-based parameter estimation for GLY, DHA, GCO and OXA oxidation over Pt-Bi/AC.

	$r_{i,oxi} = k'_{i,oxi} C_i$		$r_{i,oxi} = k_{i,oxi} C_i C_{O2}$	
Oxidised Species	Ea' [kJ mol^{-1}]	k'_0 [L g_{cat}^{-1} min^{-1}]	Ea [kJ mol^{-1}]	k_0 [L^2 mol^{-1} g_{cat}^{-1} min^{-1}]
GLY	14.8	4.6×10^{-1}	22.4	1.8×10^{3}
DHA	84.0	2.7×10^{10}	86.9	2.2×10^{13}
GCO*	115.4	6.9×10^{14}	118.3	5.5×10^{17}
OXA	35.6	7.7×10^{4}	41.4	1.7×10^{8}

*$r_{GCO,oxi} = k'_{GCO} C_{GCO}^{0.5}$; k'_{GCO} [L$^{0.5}$ mol$^{0.5}$ g_{cat}^{-1} min^{-1}]; k_{GCO} [L$^{1.5}$ mol$^{-0.5}$ g_{cat}^{-1} min^{-1}].

The activation energy for glycerol oxidation was lower than that of the subsequent oxidation products. Notably, it was also lower than values reported in the literature (≈50–70 kJ mol^{-1}) using Pt-Bi/AC catalysts under similar operating conditions [15, 16], indicating that glycerol is readily

oxidised under the conditions investigated in this study. These estimated kinetic parameters provided physically reasonable initial guesses for the parameter estimation in the subsequent power-law kinetic modelling Section.

4.6.2. Power Law Kinetics

4.6.2.1. 1 M glycerol oxidation

To develop a kinetic model capable of describing the glycerol oxidation reaction network, 1.0 M glycerol oxidation data were used to estimate the kinetic parameters of other reaction products, namely GLAD, GCA, and HPA. An activation energy Ea = 50 kJ/mol and a pre-exponential factor $k_0 = 1\times10^5$ were assumed for GLAD, GCA and HPA oxidation steps. For the remaining species, the values obtained in the preliminary analysis (Table 4.5) were adopted as initial guesses and allowed to vary within a ± 20% range during parameter estimation in MATLAB. Based on the preliminary study, a first-order power law kinetics was assumed for all species, except for GCO, for which a half-order dependence on its concentration provided a better fit. The resulting model fits are shown in Figure 4.13, and the corresponding estimated kinetic parameters are presented in Table 4.6.

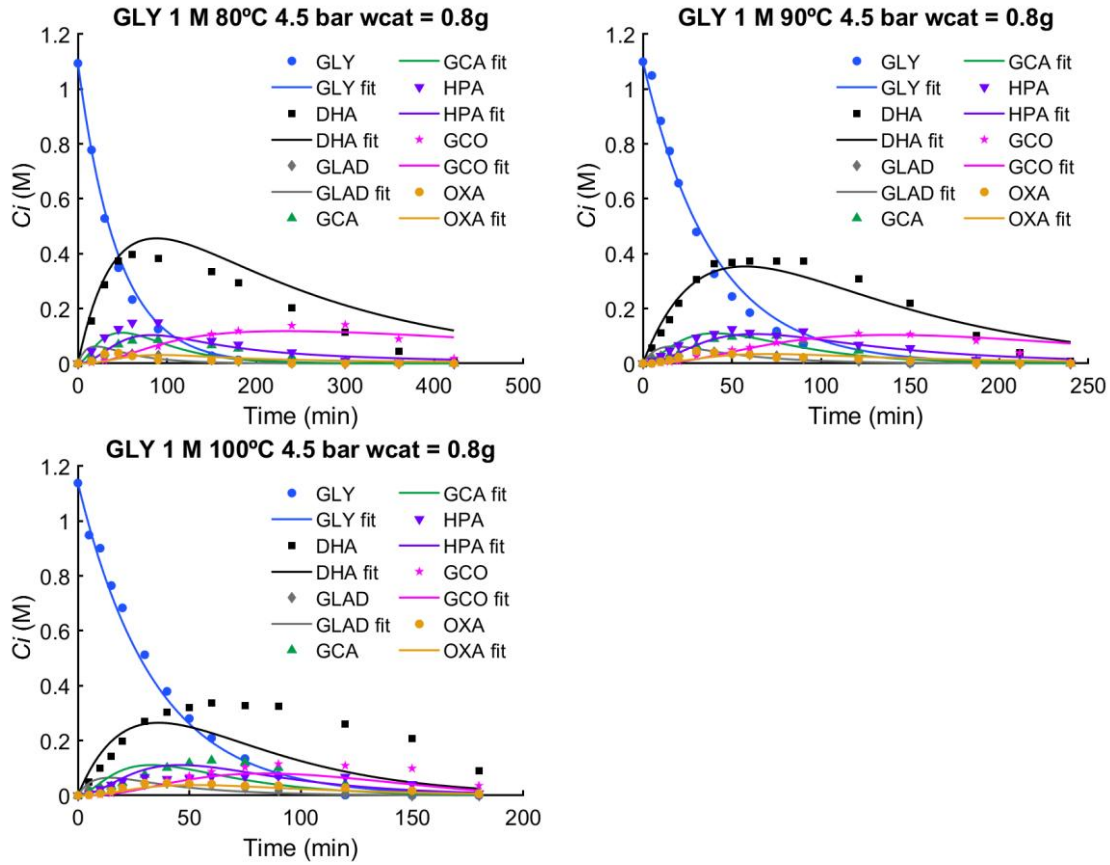

Figure 4.13. GLY oxidation over Pt-Bi/AC at 80 °C, 90 °C and 100ºC, considering first-order power law kinetics for each species, except GCO (half-order reaction). $P(O_2)$ = 4.5 bar; $C_{GLY,0}$ = 1 M; GLY/Pt = 500 mol/mol, *w* = 0.8 g, V = 0.1 L.

Table 4.6. Estimated parameters from power-law kinetic modelling of glycerol oxidation. $C_{GLY,0}$ = 1.0 M, $P(O_2)$ = 4.5 bar, T = 80–100 °C, GLY/Pt = 500 mol/mol. SSR = 0.32.

Reaction/Species	Step #	Ea kJ mol^{-1}	k_0 L^2 mol^{-1} g$_{cat}^{-1}$ min^{-1}	k (90 ºC) L^2 mol^{-1} g$_{cat}^{-1}$ min^{-1}
GLY → DHA	1	14.7	7.4×10^{1}	0.56
GLY → GLAD	2	7.4	4.2×10^{0}	0.37
DHA → HPA	3	95.4	2.0×10^{13}	0.38
GLAD → GCA	4	23.0	8.7×10^{3}	4.29
GCA → HPA	5	29.0	2.5×10^{4}	1.65
HPA → GCO	6	50.4	1.0×10^{7}	0.57
HPA → OXA	7	46.5	1.0×10^{7}	2.05
GCA → GCO	8	35.0	9.8×10^{3}	0.09
GCA → OXA	9	52.8	1.0×10^{4}	3.00×10^{-4}
GCO → OXA	10	106.5	$2.0\times10^{14*}$	0.10
GCO →	11	125.3	$2.0\times10^{14*}$	2.00×10^{-4}
OXA →	12	43.8	1.4×10^{7}	7.10
GLY	1+2	11.8	4.6×10^{1}	0.93
GCA	5+8+9	29.3	2.9×10^{4}	1.74
HPA	6+7	47.3	1.7×10^{7}	2.62
GCO	10+11	106.5	2.7×10^{14}*	0.10*

*$r_{GCO,oxi} = k'_{GCO} C_{GCO}^{0.5} C_{O2}$; k_{GCO} [L$^{1.5}$ mol$^{-0.5}$ g$_{cat}^{-1}$ min^{-1}].

The activation energies for GLY, DHA, GCO and OXA from parameter estimation were similar to the ones obtained in the preliminary analysis (Table 4.5), showing that it provided good initial guess values for parameter estimation. GLY have the lowest activation energy of 12 kJ mol^{-1}, followed by GLAD and GCA (≈ 23-30 kJ mol^{-1}). OXA and HPA showed moderate activation energies of 47 kJ mol^{-1}, while DHA and GCO showed the highest activation energies (> 100 kJ mol^{-1}).

The results in Table 4.6 reveal that the reaction rate constants of step 9 (GCA → OXA) and step 11 (GCO →) were significantly lower than the remaining, indicating that under the studied conditions, GCA is preferentially oxidised to GCO (via TTA) and to HPA rather than directly to OXA, consistent with proposed reaction pathways in the literature [16, 43, 44]. GCO oxidation to C1 products was negligible, so GCO was oxidised to OXA. The low-rate steps (9 and 11) were excluded from further analysis to simplify the model and reduce the number of parameters to be estimated. The new concentration profiles and estimated parameters obtained using this simplified network were nearly indistinguishable from the previous ones (see Table D.1 in Appendix D).

The power-law kinetic model describes the experimental data with relative accuracy under the investigated conditions. However, it fails to describe some reaction product concentration profiles, including DHA (with higher deviations at higher temperatures). Still, the simplicity of

this approach significantly reduces computational efforts, making it an alternative approach for subsequent optimisation and process modelling studies.

4.6.2.2. Extension to different concentrations

As observed in Section 4.6.1.2, the power-law kinetic model does not adequately describe glycerol oxidation at temperatures of 40 °C and 60 °C. The power-law model was evaluated under varying initial glycerol concentrations and catalyst loads to assess the model's applicability further. Initially, the model was tested at a fixed GLY/Pt molar ratio of 500. The results are presented in Figure 4.14.

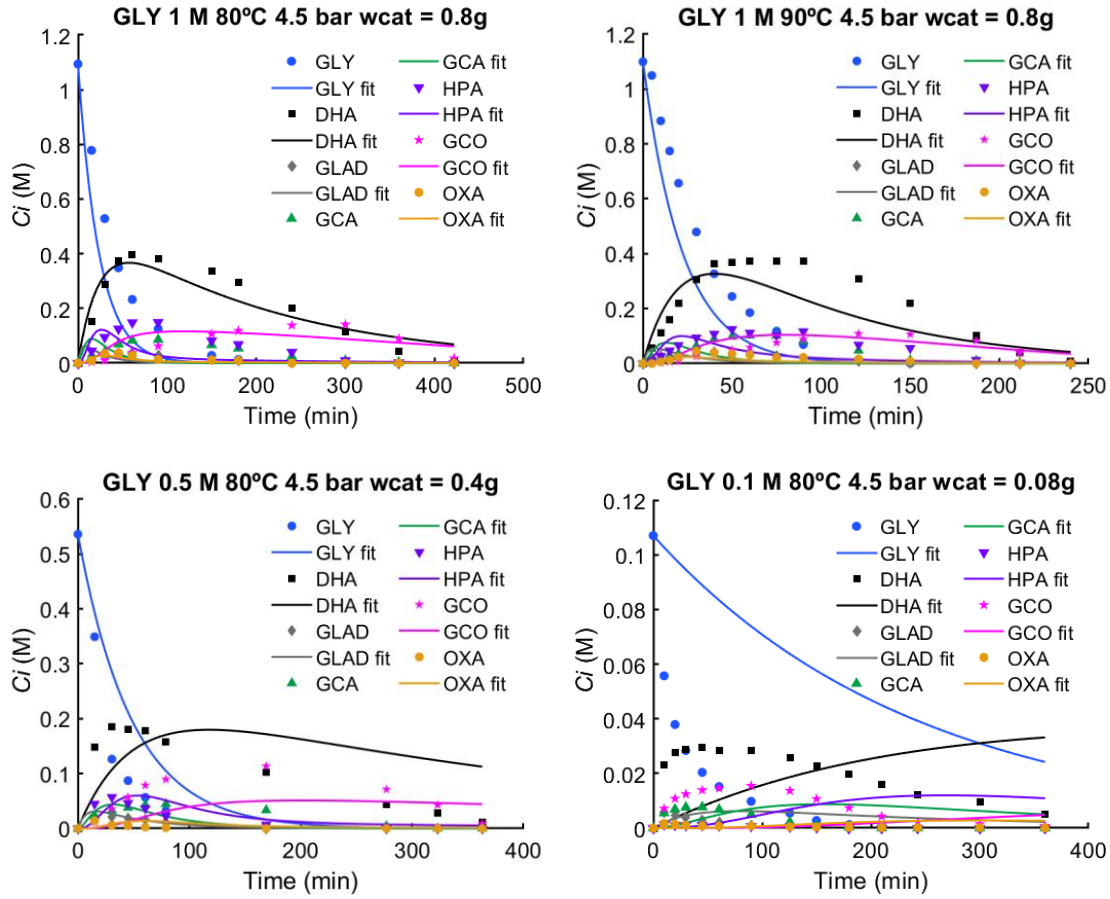

Figure 4.14. Power-law model for GLY oxidation kinetics at T = 80–90 °C, P(O_2) = 4.5 bar, $C_{GLY,0}$ = 0.1–1.0 M, GLY/Pt = 500 mol/mol.

The results indicate that the model fails to describe all experimental datasets simultaneously, with a sum of squared residuals (SSR) of 2.3. While it can adequately fit individual datasets of experiments independently under specific operating conditions (not shown here), the kinetic parameters estimated from one set are not valid across different conditions. This suggests that a power-law kinetic model does not describe the reaction kinetics well. These datasets will be used later for comparison with the LHHW-based model, which is detailed in Section 4.4.2.

4.6.3. LHHW-based Model Kinetics

4.6.3.1. 1 M glycerol oxidation

To evaluate whether a more accurate representation of the glycerol oxidation kinetics could be achieved, the LHHW-based model detailed in Section 4.4.2. was applied. Initial guesses for the kinetic parameters were taken from the power-law analysis (Table 4.6). For adsorption parameters, initial guesses were randomly assigned within physically plausible ranges: adsorption enthalpies (ΔH) between –60 and –40 kJ mol^{-1}, and adsorption pre-exponential factors ($K_{ads,0}$) between 1×10^{-8} and 1×10^{-6} M^{-1}.

As in the power-law study, model fitting was first applied to data from glycerol oxidation experiments conducted with $C_{GLY,0}$ = 1.0 M, GLY/Pt = 500 mol/mol, and temperatures ranging from 80 to 100 °C. The 12-step reaction network (Figure 4.1) was considered, incorporating all studied species. Oxygen was assumed to adsorb dissociatively on different active sites. However, as oxygen concentration was constant, a reliable estimation of parameters associated with oxygen adsorption and reaction was not possible. The model results are presented in Figure 4.15, showing good agreement between experimental data and simulated concentration profiles. The corresponding estimated kinetic and adsorption parameters are summarised in Table 4.7.

Table 4.7. Estimated kinetic and adsorption parameters of glycerol oxidation using the LHHW model. $C_{GLY,0}$ = 1.0 M, T = 80–100 °C, GLY/Pt = 500 mol/mol. SSR = 0.13.

Reaction/ Species	#	Ea kJ/mol	k_0 mol g^{-1} min^{-1}	k(90ºC) mol g^{-1} min^{-1}	ΔH kJ/mol	$Kads_0$ M^{-1}	Kads (90ºC) M^{-1}
GLY → DHA	1	26.2	4.9×10^{3}	0.83	-	-	-
GLY → GLAD	2	17.9	2.3×10^{2}	0.61	-	-	-
DHA → HPA	3	90.9	2.0×10^{14}	17.04	-37.5	1.2×10^{-7}	0.03
GLAD → GCA	4	22.6	1.0×10^{5}	56.64	-32.5	2.8×10^{-6}	0.13
GCA → HPA	5	27.5	3.0×10^{5}	32.70	-	-	-
HPA → GCO	6	56.3	1.0×10^{8}	0.79	-	-	-
HPA → OXA	7	53.0	1.0×10^{8}	2.37	-	-	-
GCA → GCO	8	35.1	1.0×10^{5}	0.88	-	-	-
GCA → OXA	9	55.0	1.0×10^{5}	0.001	-	-	-
GCO → OXA	10	105.1	2.0×10^{14}	0.15	-	-	-
GCO →	11	111.3	2.0×10^{14}	0.02	-	-	-
OXA →	12	57.0	1.4×10^{8}	0.90	-51.9	3.9×10^{-7}	11.4
GLY	1+2	22.6	2.6×10^{3}	1.4	-20.0	1.6×10^{-3}	1.2
GCA	5+8	27.7	3.3×10^{5}	33.6	-34.6	9.1×10^{-7}	0.1
HPA	6+7	53.8	1.7×10^{8}	3.2	-18.7	2.5×10^{-3}	1.3
GCO	10+11	105.8	2.8×10^{14}	0.2	-24.7	8.0×10^{-4}	2.8
O_2	-	-	-	-	-35.0	1.7×10^{-7}	0.02

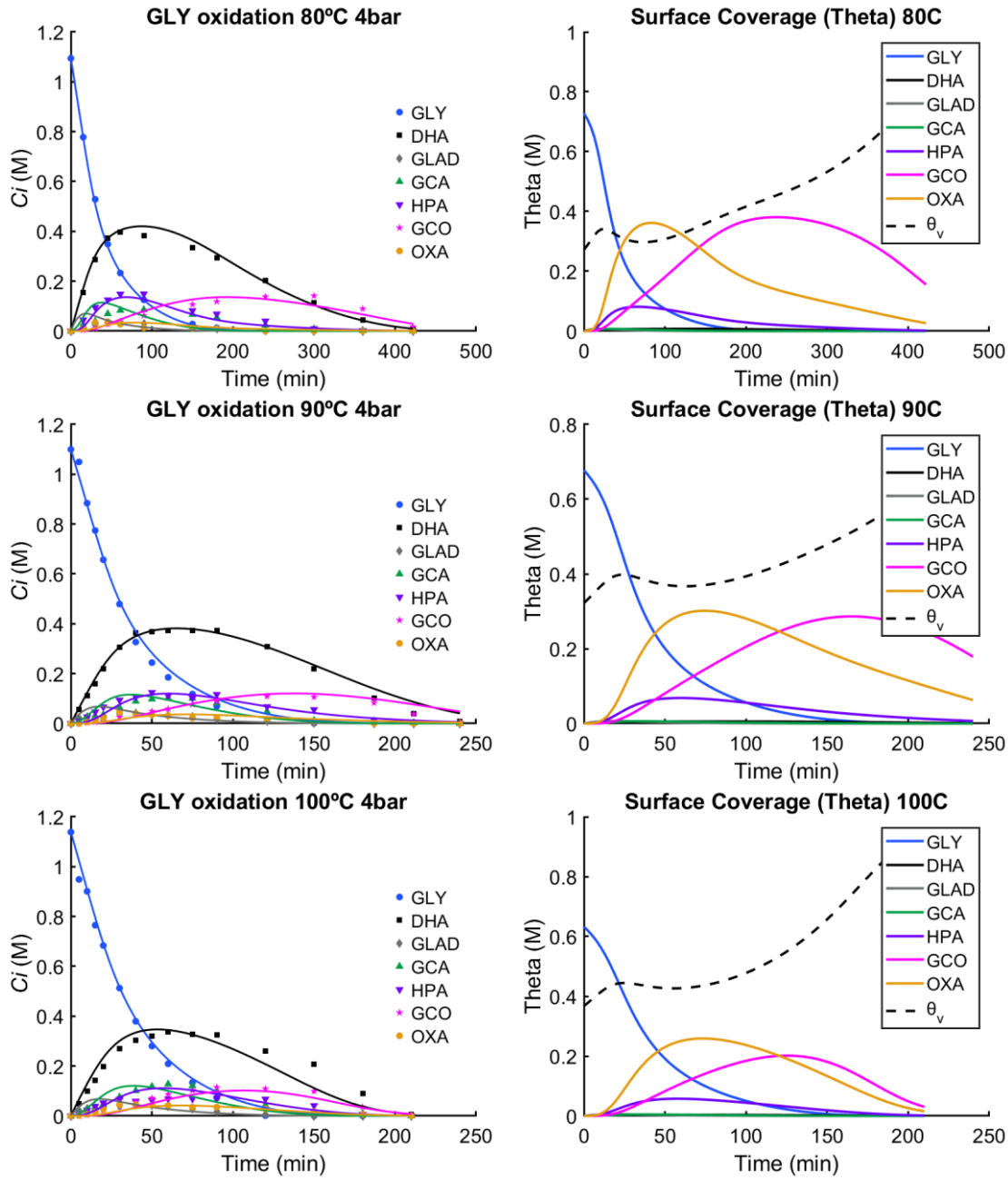

Figure 4.15. Glycerol oxidation at 80 °C (top), 90 °C (middle), 100 °C (bottom). Left: experimental data (dots) and LHHW model results (lines); Right: surface coverage. $C_{GLY,0}$ = 1 M; GLY/Pt = 500 mol/mol, *w* = 0.8 g, V = 0.1 L, 800 rpm.

The estimated activation energies and pre-exponential factors were mostly consistent with the power-law model (Table 4.6), supporting the robustness of the preliminary kinetic analysis. Compared to the power-law model (Figure 4.13), the LHHW model significantly improved the overall model accuracy, reducing the sum of squared residuals from 0.36 to 0.12.

Adsorption parameters obtained from the LHHW model indicated that GCO and OXA were strongly adsorbed on the catalyst surface (K_{ads} at 90 °C of 3.4 and 13.9 M^{-1}, respectively) compared to glycerol (K_{ads} of 1.4 M^{-1}), possibly contributing to site blocking and reducing reaction rate. In contrast, DHA, GLAD, and GCA adsorption were negligible. As oxygen

concentration was maintained constant, its estimated adsorption parameters lack physical interpretability and are not discussed further.

The results in Table 4.7 reveal that the estimated reaction rate constants of step 9 (GCA → OXA) and step 11 (GCO →) were significantly lower than those of the other steps, consistent with the trend observed using the power-law model. The same dataset was fitted using the simplified reaction network, yielding very similar SSR values and estimated parameters, as depicted in Figure D.2 and Table D.2 in Appendix D. Based on these findings, subsequent kinetic parameter estimation studies will adopt the simplified 10-step reaction network. Furthermore, the estimated parameter values in Table D.2 will serve as initial guesses in the following analysis.

4.6.3.2. Extension to different conditions

The LHHW-based kinetic model was evaluated under a broader range of operating conditions to test its robustness and predictive ability. The same datasets used previously with the power law model in Figure 4.14 were considered: glycerol oxidation at various initial concentrations at an initial GLY/Pt molar ratio of 500. The results are presented in Figure 4.16.

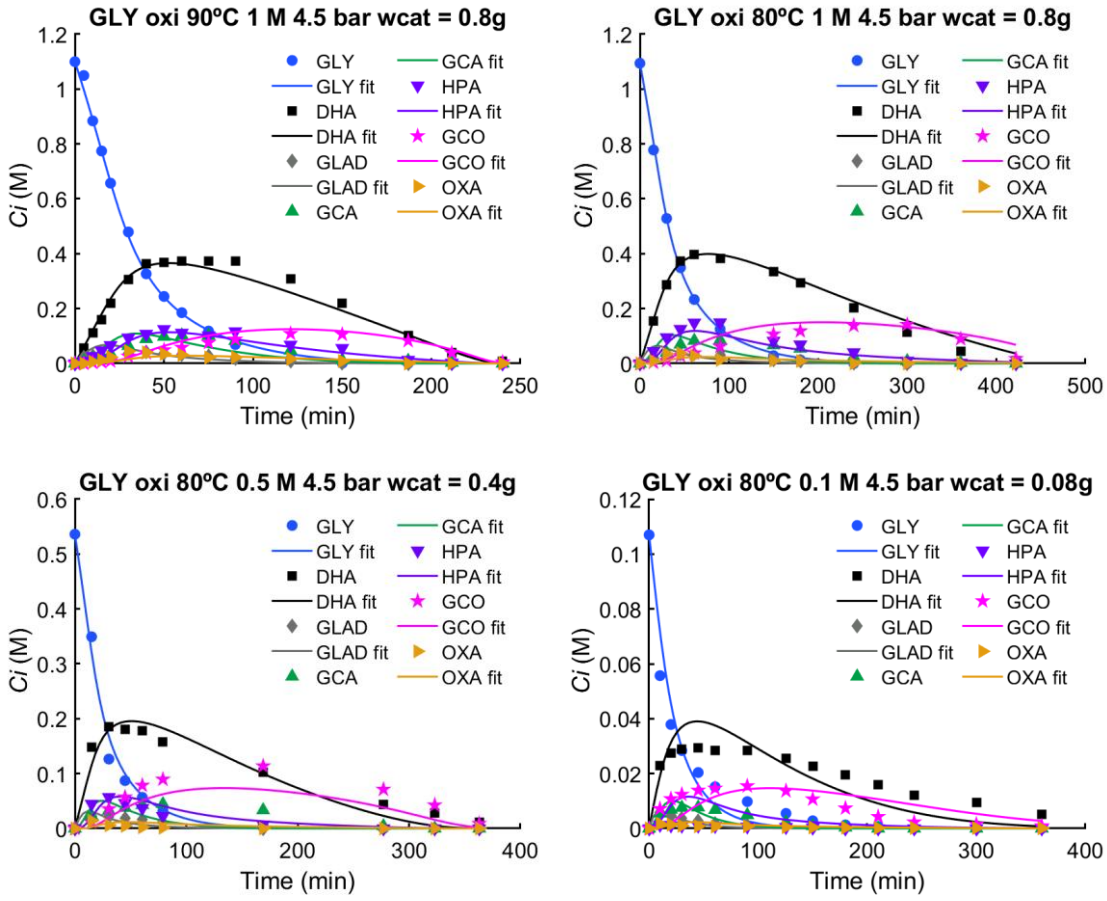

Figure 4.16. LHHW model results for glycerol oxidation with Pt-Bi/AC. T = 80–90 °C; $P(O_2)$ = 4.5 bar; $C_{GLY,0}$ = 0.1–1 M; GLY/Pt = 500 mol/mol.

Unlike the power-law model, which failed to describe the experimental data across varying glycerol concentrations (see Figure 4.14), the LHHW model successfully described all species, regardless of the initial glycerol concentration (Figure 4.16). This improvement highlights the mechanistic model's ability to account for adsorption competition and surface interactions. The estimated parameters slightly changed but remained close to those initially estimated in the first analysis (the values used as model input, which are available in Table D.3 of Appendix D).

Given the promising results obtained for lower concentrations, the LHHW model was also extended across the temperature range between 40 °C and 100 °C, and the results are shown in Figure 4.17.

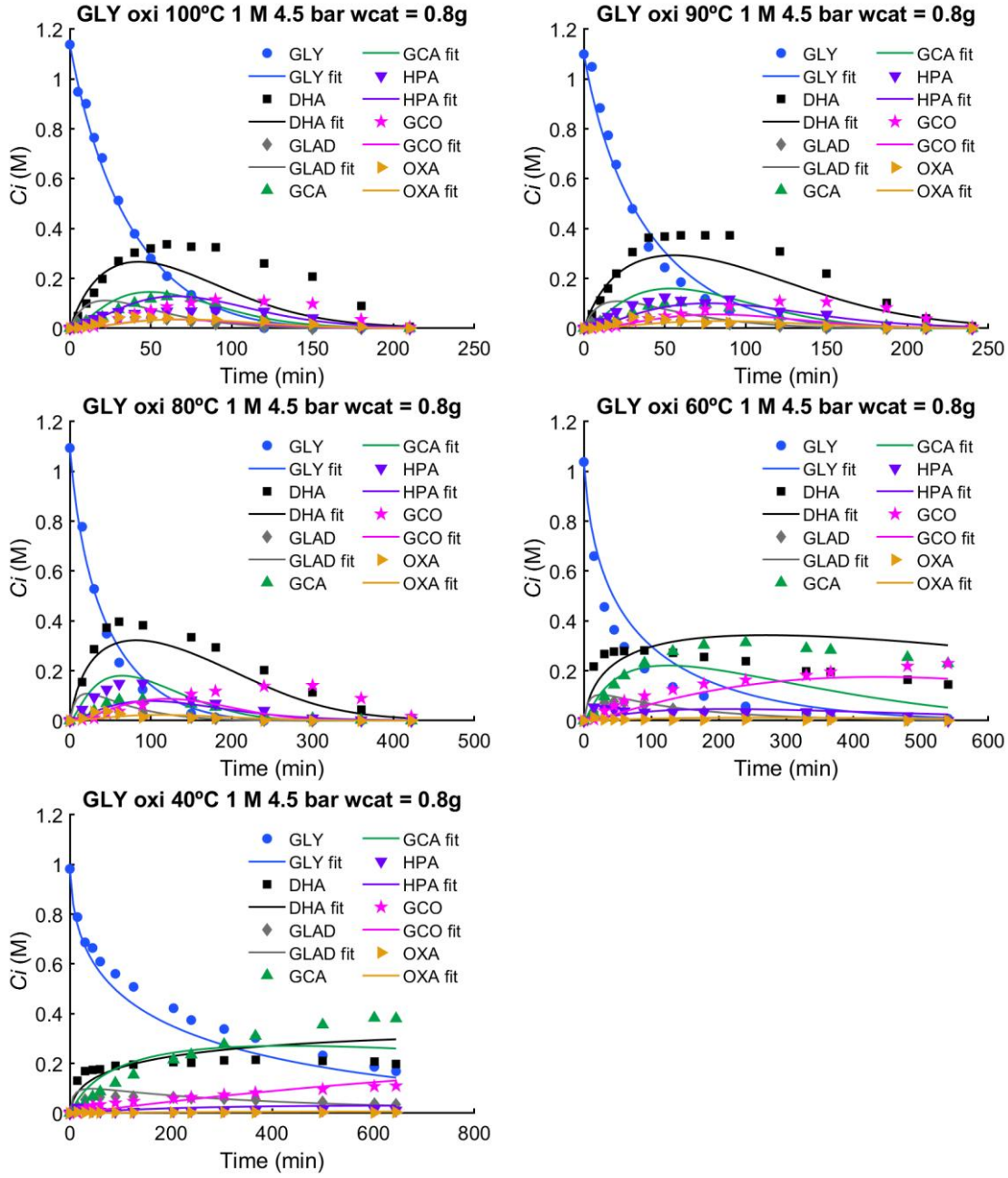

Figure 4.17. LHHW model results for glycerol oxidation with Pt-Bi/AC in the 40–100 °C temperature range. $P(O_2)$ = 4.5 bar; $C_{GLY,0}$ = 1 M; GLY/Pt = 500 mol/mol.

The model demonstrated strong descriptive capability across the studied temperature range, including at lower temperatures (40 °C and 60 °C), where the power-law model had previously shown significant deviations. Although some discrepancies were observed at the lowest temperatures, the model predictions remained within acceptable limits. The corresponding kinetic and adsorption parameters are listed in Table D.4 of Appendix D. The estimated activation energies were within physically meaningful ranges.

4.6.3.3. Final parameter estimation

The LHHW kinetic model was tested for its predictive capacity under a wide range of operating conditions to assess its overall robustness and reliability. A global fit was performed using experimental data spanning glycerol concentrations from 0.1 M to 2.0 M, GLY/Pt molar ratios from 250 to 1000 mol/mol, temperatures between 80 and 100 °C, and oxygen pressures from 2.0 to 7.5 bar. Data collected at 40 °C and 60 °C were excluded from this analysis, as these conditions yielded lower DHA selectivity and are less likely to be used in an optimised process targeting high DHA productivity. The model results are presented in Figure 4.18, and the corresponding estimated parameters are presented in Table 4.8.

Table 4.8. "Global fit" for GLY oxidation using the LHHW kinetic model. T = 80 – 100 °C; $P(O_2)$ = 2.0 – 7.5 bar; $C_{GLY,0}$ = 0.1 – 2 M; GLY/Pt = 250 – 1000 mol/mol. SSR = 1.14.

Reaction/ Species	#	Ea kJ/mol	k_0 mol g^{-1} min^{-1}	k(90ºC) mol g^{-1} min^{-1}	ΔH kJ/mol	$Kads_0$ M^{-1}	Kads (90ºC) M^{-1}
GLY → DHA	1	21.0	4.9×10^{2}	0.47	-	-	-
GLY → GLAD	2	11.5	1.4×10^{1}	0.31	-	-	-
DHA → HPA	3	86.2	2.0×10^{13}	7.99	-44.9	4.6×10^{-8}	0.13
GLAD → GCA	4	21.4	1.0×10^{4}	8.34	-31.5	2.4×10^{-5}	0.83
GCA → HPA	5	25.4	3.0×10^{4}	6.74	-	-	-
HPA → GCO	6	50.6	1.0×10^{7}	0.52	-	-	-
HPA → OXA	7	47.0	1.0×10^{7}	1.72	-	-	-
GCA → GCO	8	32.3	1.0×10^{4}	0.22	-	-	-
GCO → OXA	10	101.8	2.0×10^{13}	0.05	-36.6	8.1×10^{-5}	14.8
OXA →	12	51.2	1.4×10^{7}	0.60	-52.1	1.0×10^{-6}	32.4
GLY	1+2	17.2	2.3×10^{2}	0.78	-27.7	2.7×10^{-4}	2.64
GCA	5+8	25.6	3.4×10^{4}	6.96	-35.2	3.5×10^{-6}	0.41
HPA	6+7	47.8	1.7×10^{7}	2.25	-54.6	4.4×10^{-8}	3.14
O_2	-	-	-	-	-41.7	1.3×10^{-7}	0.13

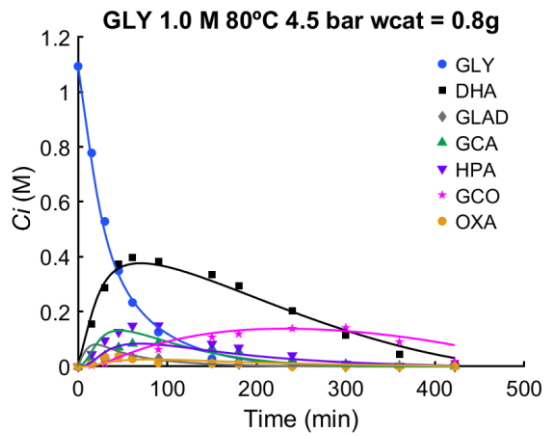
GLY 1.0 M 80ºC 4.5 bar wcat = 0.8g
GLY
DHA
GLAD
GCA
HPA
GCO
OXA
Ci (M)
Time (min)

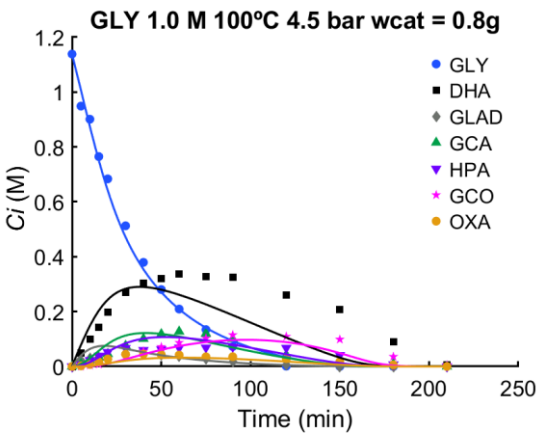
GLY 1.0 M 100ºC 4.5 bar wcat = 0.8g
GLY
DHA
GLAD
GCA
HPA
GCO
OXA
Ci (M)
Time (min)

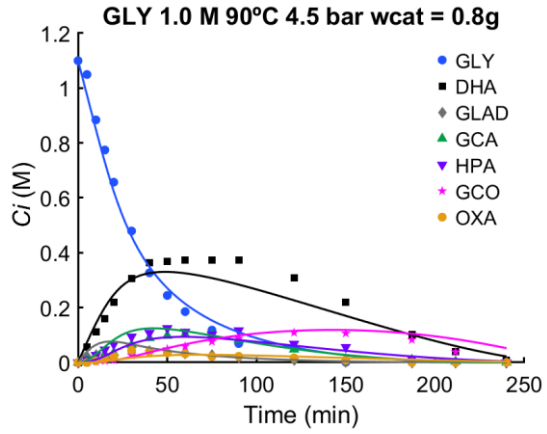
GLY 1.0 M 90ºC 4.5 bar wcat = 0.8g
GLY
DHA
GLAD
GCA
HPA
GCO
OXA
Ci (M)
Time (min)

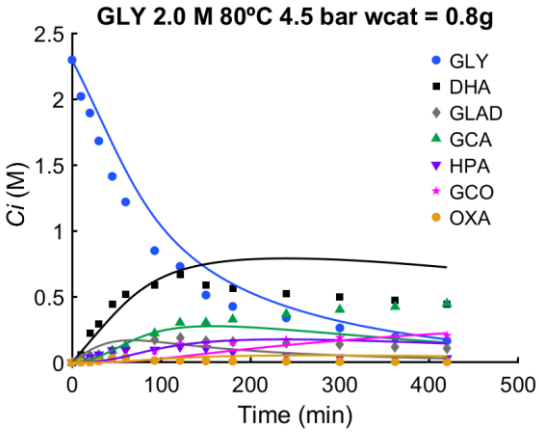
GLY 2.0 M 80ºC 4.5 bar wcat = 0.8g
GLY
DHA
GLAD
GCA
HPA
GCO
OXA
Ci (M)
Time (min)

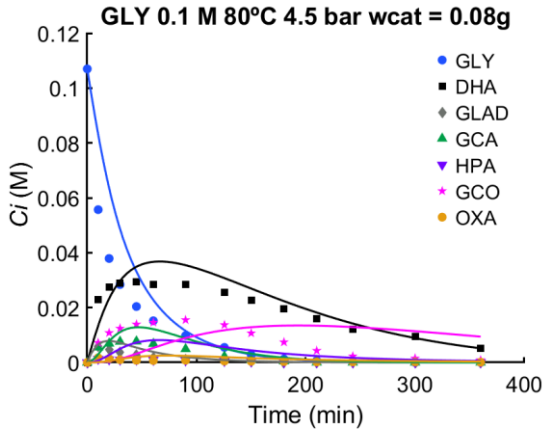
GLY 0.1 M 80ºC 4.5 bar wcat = 0.08g
GLY
DHA
GLAD
GCA
HPA
GCO
OXA
Ci (M)
Time (min)

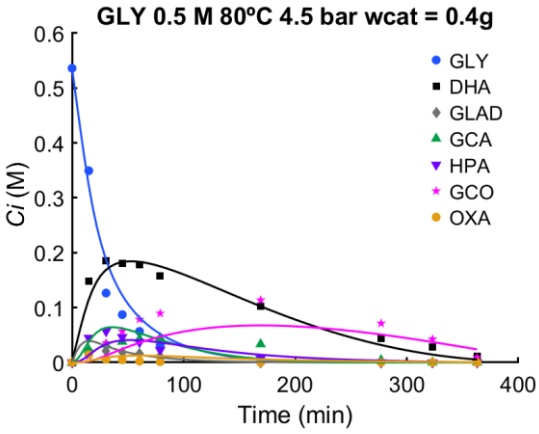
GLY 0.5 M 80ºC 4.5 bar wcat = 0.4g
GLY
DHA
GLAD
GCA
HPA
GCO
OXA
Ci (M)
Time (min)

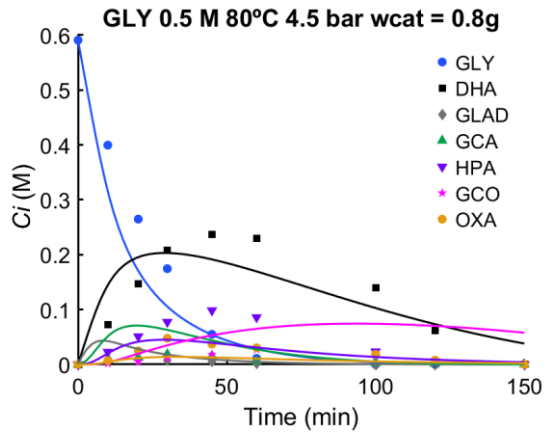
GLY 0.5 M 80ºC 4.5 bar wcat = 0.8g
GLY
DHA
GLAD
GCA
HPA
GCO
OXA
Ci (M)
Time (min)

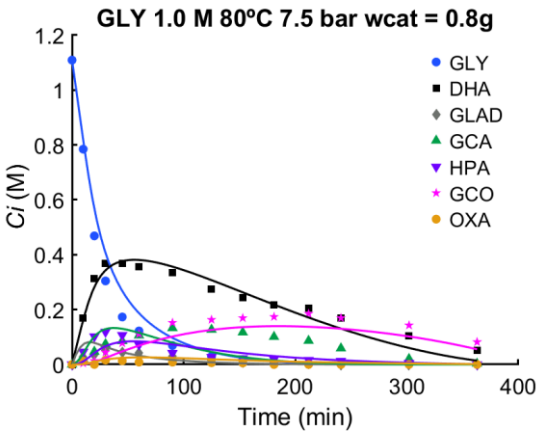
GLY 1.0 M 80ºC 7.5 bar wcat = 0.8g
GLY
DHA
GLAD
GCA
HPA
GCO
OXA
Ci (M)
Time (min)

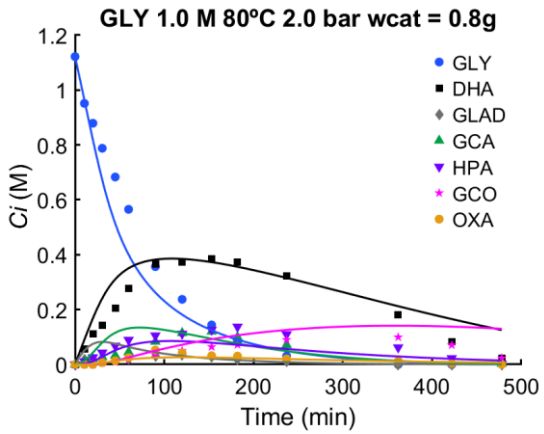

Figure 4.18. LHHW model "global fit" results for glycerol oxidation with Pt-Bi/AC. T=80–100 °C; P(O_2) = 2.0–7.5 bar; $C_{GLY,0}$ = 0.1–2 M; GLY/Pt = 250–1000 mol/mol.

The model successfully described the experimental concentration profiles using a unified set of kinetic and adsorption parameters, confirming the consistency and adaptability of the LHHW model. Its ability to fit data across various operating conditions, including more concentrated glycerol solutions (2.0 M) and varied catalyst loadings, demonstrates its suitability for process modelling, optimisation, and potential scale-up applications.

The results presented in this chapter are particularly noteworthy considering that most kinetic studies in the literature focus on highly diluted glycerol solutions, typically with initial concentrations of 0.1 M, up to 1.0 M [11, 16], or are limited to low glycerol conversions [15], without addressing the simultaneous variation of multiple operating parameters. In contrast, the present work demonstrates the ability of the LHHW model to describe glycerol oxidation kinetics across a broader range of concentrations and catalyst loadings, reinforcing its potential for process optimisation and scale-up.

Oxygen pressure influence was also included in the global parameter estimation. Good results were obtained even using a simplified model for oxygen adsorption and activation. More detailed models, such as the one proposed by the Schouten group [3] for alcohol oxidation, could improve the model's accuracy. However, adapting such a complex framework to a broader reaction network involving multiple species would significantly increase the model's complexity and computational cost.

A simplified kinetic scheme was also tested, including only glycerol, DHA, and GCA (GLAD is assumed to convert rapidly into GCA). This reduced network maintained good predictive accuracy for the key species relevant to DHA production (see Figure D.4 and Table D.5 from Appendix D) despite slightly worse fits due to not accounting for the adsorption of some reaction products that were excluded. Nevertheless, this simplified kinetic scheme offers a trade-off

between model detail and usability, which is particularly valuable for reactor design and process integration studies while still predicting GLY consumption and DHA production.

4.7. Glycerol Oxidation Kinetics with Au/ZnO

4.7.1. Preliminary Analysis

To extend the kinetic investigation beyond Pt-based catalysts, the same methodology was applied to study glycerol oxidation over Au/ZnO. This catalyst had previously demonstrated a high selectivity towards DHA formation under base-free conditions. However, the limited availability of this material (discontinued by the supplier) constrained the experimental scope to reactions involving glycerol and its main oxidation product, DHA.

All experiments were conducted in aqueous medium (V = 100 mL), using an initial substrate concentration of 0.1 M (either glycerol or DHA), an oxygen pressure of 6.5 bar, an agitation rate of 800 rpm, and a GLY/Au molar ratio of 100 (corresponding to a catalyst loading of 2.0 g). This setup was chosen to ensure reliable mass transfer and catalyst activity, following conditions similar to those reported in the literature [18, 22, 23].

A preliminary test was conducted using a more concentrated solution (1.0 M glycerol) and a lower catalyst loading (GLY/Au ≈ 2000, $w \approx 1$ g) to evaluate potential mass transfer limitations. As shown in Figure 4.19-left, glycerol conversion was initially slow (≈5%) with minor DHA formation and trace amounts of GCA, GCO, and OXA. No significant progress was observed after the early reaction stage, and conversion only reached ≈40% after 80 hours. The absence of C2 and C1 oxidation products suggests that a non-catalytic oxidation pathway dominated the reaction under these conditions.

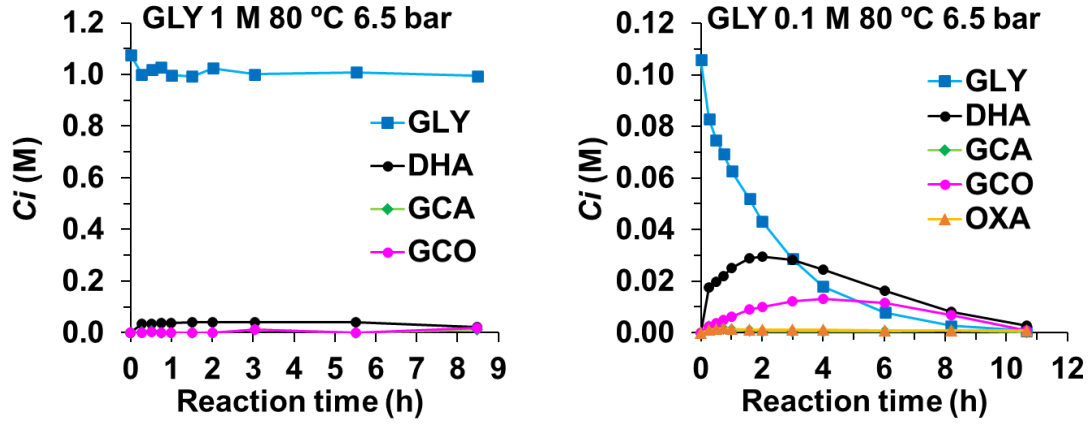

Figure 4.19. Glycerol oxidation over Au/ZnO at 80°C and 6.5 bar O_2: Left) $C_{GLY,0}$ = 1 M; GLY/Au = 2000 mol/mol; Right) $C_{GLY,0}$ = 0.1 M; GLY/Au = 100 mol/mol.

These observations confirmed the importance of operating under favourable reaction conditions to achieve meaningful kinetic insights. For example, at the same temperature of 80 °C and oxygen pressure of 6.5 bar, 0.1 M glycerol oxidation at a GLY/Au = 100 mol/mol proceeds within a reasonable operating time (Figure 4.19-right). Thus, subsequent experiments were performed under those conditions, consistent with most studies using gold catalysts for glycerol oxidation under base-free conditions [18, 22, 23].

4.7.1.1. Temperature Dependence

The influence of temperature on the catalytic oxidation of glycerol was examined in the range of 40–90 °C, maintaining all other operating conditions constant. The corresponding concentration profiles of glycerol and its oxidation products at various temperatures are presented in Figure 4.20 (see Figure 4.19-right for T = 80 °C).

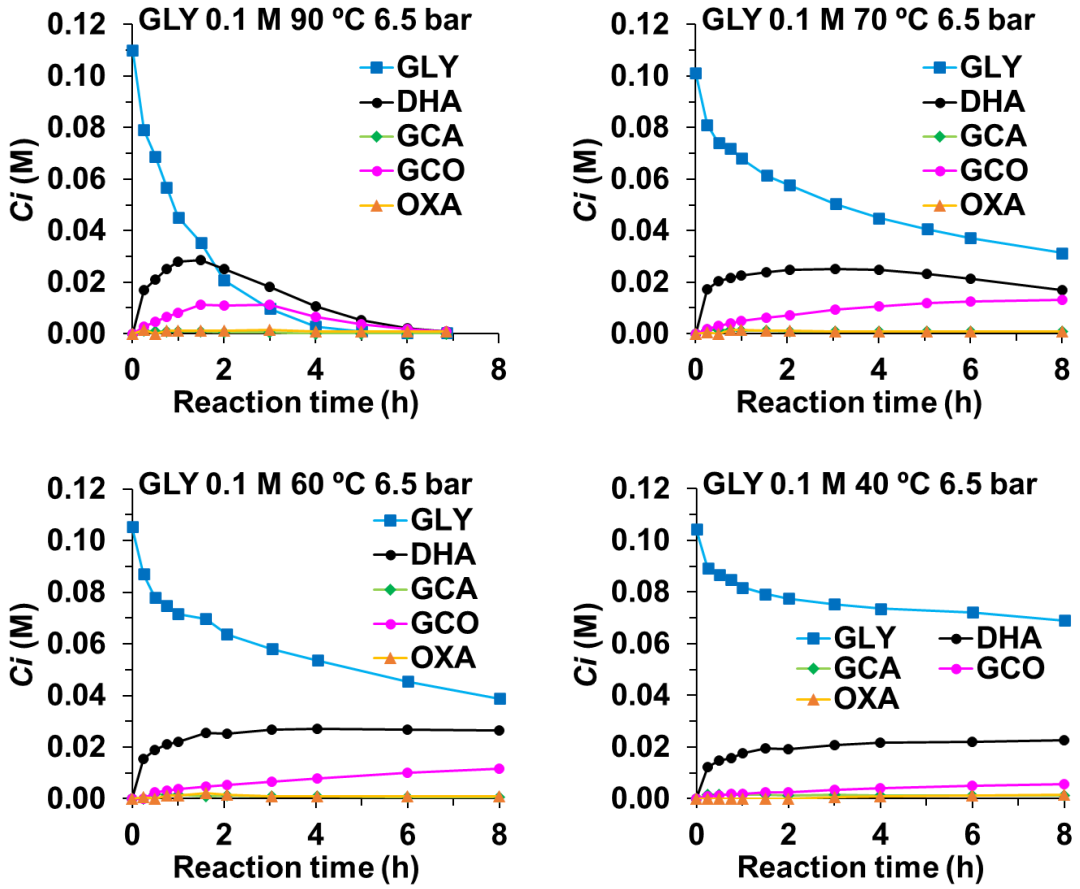

Figure 4.20. Glycerol oxidation concentration profiles at T = 40–90 °C; $P(O_2)$ = 6.5 bar; $C_{GLY,0}$ = 0.1 M; GLY/Au = 100 mol/mol.

DHA and GCO were obtained from glycerol oxidation, while trace quantities of GCA and OXA were detected in the liquid phase. GLAD, TTA and HPA were not detected in the liquid phase. Pan et al. [18] also detected only DHA and GCO during glycerol oxidation over a lab-made Au/ZnO catalyst.

The algorithm applied to Pt-Bi/AC was now applied to the glycerol oxidation data over the Au/ZnO catalyst. Data was first analysed using the differential and integral methods, assuming pseudo-first-order power-law kinetics. The results are depicted in Figure 4.21.

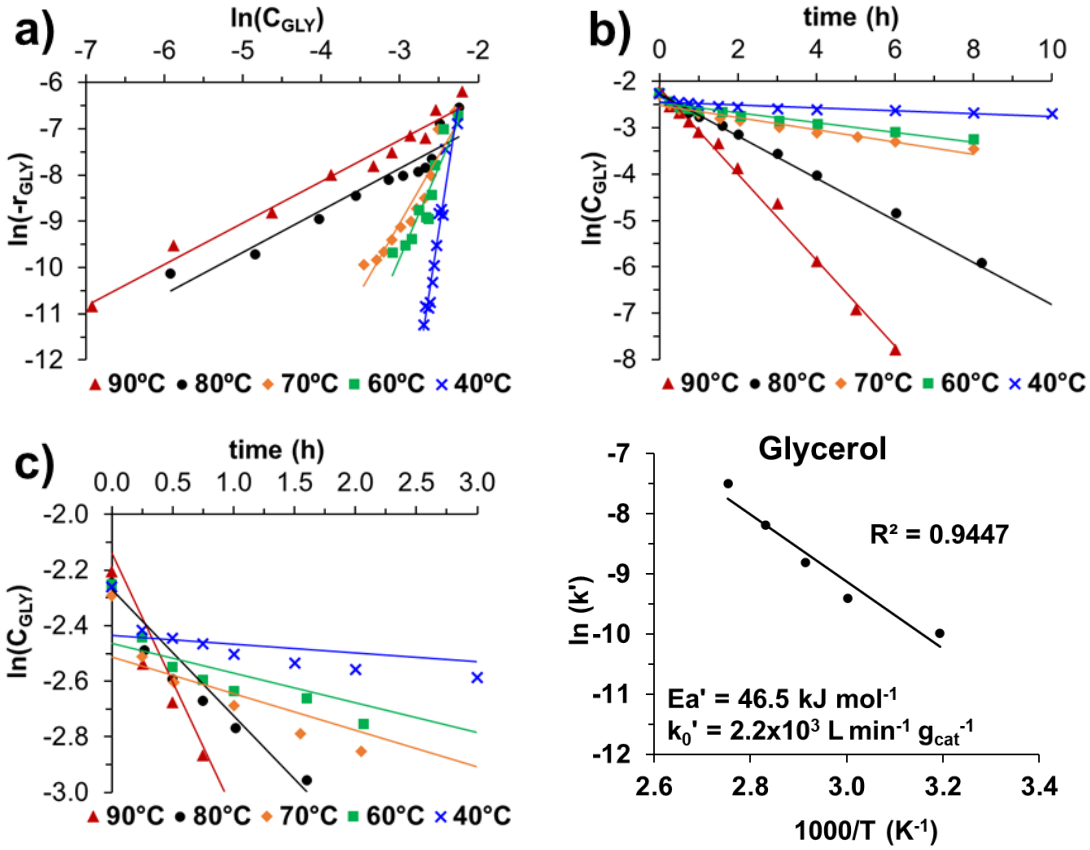

Figure 4.21. Glycerol oxidation with Au/ZnO: (a) differential method; (b-c) integral method with pseudo-first-order approximation; (d) Arrhenius plot.

Differential method analysis (Figure 4.21a) indicated that for T ≥ 80 °C, glycerol oxidation follows a pseudo-first-order power-law kinetics. At lower temperatures, however, the apparent reaction order increased significantly, up to 3 at 60–70 °C and 11 at 40 °C, highlighting the inadequacy of the power-law model at low temperatures. This behaviour may be attributed to the strong adsorption of reaction products, namely carboxylic acids, modifying the catalyst surface. The power law kinetic model does not account for this effect.

For T ≥ 80 °C, integral method analysis showed that pseudo-first-order kinetics described the system reasonably well (Figure 4.21b-c), while for T ≤ 80 °C it failed to describe the reaction data. The kinetic constants obtained considering only the initial reaction are summarised in Table 4.9.

Table 4.9. Temperature effect on glycerol oxidation rate constants (initial data) using Au/ZnO. PO_2 = 6.5 bar; $C_{GLY,0}$ = 0.1 M; GLY/Au = 100 mol/mol; *w* = 2.0 g; V = 0.1 L.

T (ºC)	PO_2 (bar)	$C_{GLY,0}$ (M)	$[O_2]$ (mM)	k' (L min^{-1} g^{-1})
40	6.5	0.1	6.59	5.3×10^{-5}
60	6.5	0.1	5.46	1.3×10^{-4}
70	6.5	0.1	5.15	1.5×10^{-4}
80	6.5	0.1	4.95	3.8×10^{-4}
90	6.5	0.1	4.83	7.6×10^{-4}

The corresponding Arrhenius plot (ln k′ vs. 1/T) is presented in Figure 4.21-d, from which an activation energy $Ea'_{GLY,oxi}$ of 46.5 kJ mol^{-1} and a pre-exponential factor $k'_{0,GLY,oxi}$ of 2.2×10^3 L min^{-1} g_{cat}^{-1} were obtained. These estimated parameters were used to describe glycerol oxidation data in the 40–90 °C temperature range (Figure 4.22).

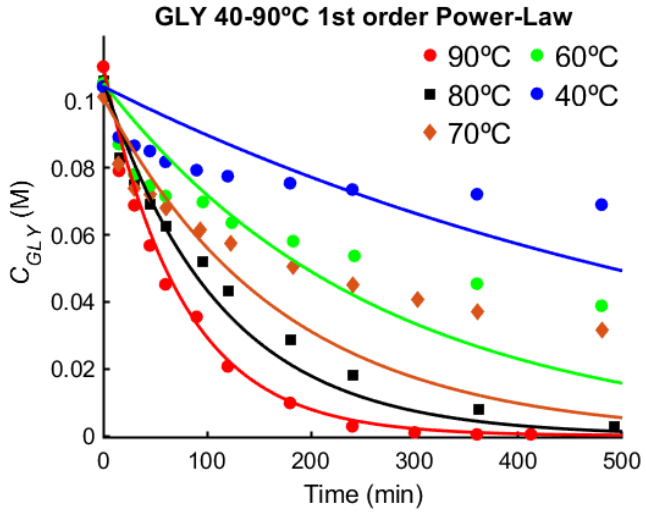

Figure 4.22. Glycerol oxidation with Au/ZnO: experimental data (dots) and model results using pseudo-first-order power-law (lines). T = 40–90 °C; $P(O_2)$ = 6.5 bar; $C_{GLY,0}$ = 0.1 M; GLY/Au = 100 mol/mol; *w* = 2.0 g; V = 0.1 L.

Similarly to glycerol oxidation over Pt-Bi/AC (Section 4.6.1.2), the power law model showed reasonably good agreement with experimental data at T ≥ 80 °C, while it failed to describe glycerol oxidation at 40 ºC, 60 ºC, and 70 ºC.

4.7.1.2. Oxygen pressure influence

To evaluate the influence of oxygen pressure on reaction kinetics, glycerol oxidation was performed at 2.5 bar, and the resulting concentration profiles are shown in Figure 4.23-left. This trial was compared to the reference experiment at 6.5 bar, keeping constant the T = 80 °C, $C_{GLY,0}$ = 0.1 M and GLY/Au = 100 (see Figure 4.19-right).

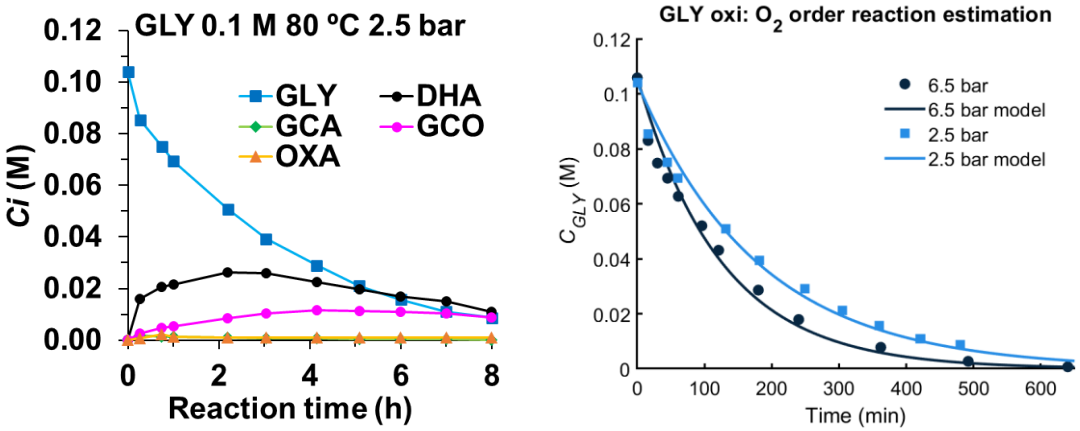

Figure 4.23. Glycerol oxidation over Au/ZnO: Left) $P(O_2)$ = 2.5 bar; Right) experimental data (dots) and first-order power-law model results (lines) at $P(O_2)$ = 2.5 and 6.5 bar. T = 80 °C; $C_{GLY,0}$ = 0.1 M; GLY/Au = 100 mol/mol, w = 2 g, V = 0.1 L.

The initial reaction rate of glycerol oxidation at two different oxygen pressures, 2.5 bar and 6.5 bar, at T = 80 °C, were summarised in Table 4.10.

Table 4.10. Initial reaction rate of glycerol oxidation with Au/ZnO at 2.5 bar and 6.5 bar. T = 80 °C; $C_{GLY,0}$ = 0.1 M; GLY/Au = 100 mol/mol, w = 2 g, V = 0.1 L.

$P(O_2)$ (bar)	$[O_2]$ (mM)	r_0 (mol g_{cat}^{-1} min^{-1})
2.5	1.9	5.8×10^{-5}
6.5	4.9	7.2×10^{-5}

A power-law kinetic model was proposed in the form:

$$r_{GLY,oxi} = k_{GLY,oxi} C_{GLY} C_{O_2}^{m} \quad (4.35)$$

Comparing initial reaction rates from Table 4.10, a reaction order with respect to oxygen of 0.2 was obtained. Parameter estimation in MATLAB estimated a m value of 0.33 (see Figure 4.23-right). Therefore, under these conditions, glycerol oxidation may be described by the following power-law kinetic expression:

$$r_{GLY,oxi} = k_{GLY,oxi} C_{GLY} C_{O_2}^{1/3} \quad (4.36)$$

Considering this power law rate expression, an activation energy $Ea_{0,GLY,oxi}$ = 48.5 kJ mol^{-1} and a pre-exponential factor $k_{0,GLY,oxi}$ = 2.5×10^4 $L^{4/3}$ $mol^{-1/3}$ min^{-1} g_{cat}^{-1} were estimated.

4.7.1.3. Dihydroxyacetone oxidation

DHA oxidation was investigated using Au/ZnO to complement the kinetic study. Experiments were conducted to evaluate the influence of temperature (70°C, 80°C, and 90 °C) and oxygen pressure (2.5 bar and 6.5 bar), while maintaining the remaining conditions constant: $C_{DHA,0}$ = 0.1 M, DHA/Au = 100 mol/mol (w = 2.0 g), 800 rpm.

Concentration profiles at different temperatures are presented in Figure 4.24. The main products identified were GCO, GCA, and OXA. GLAD and GCA formation was unexpected; thus, interconversion between DHA and GLAD may be possible, a mechanism also present in the gold-catalysed reaction under basic conditions. Trace amounts of HPA, glyoxylic acid (GOX, not shown) and other products not identified by the current HPLC analytical method were detected during the analysis.

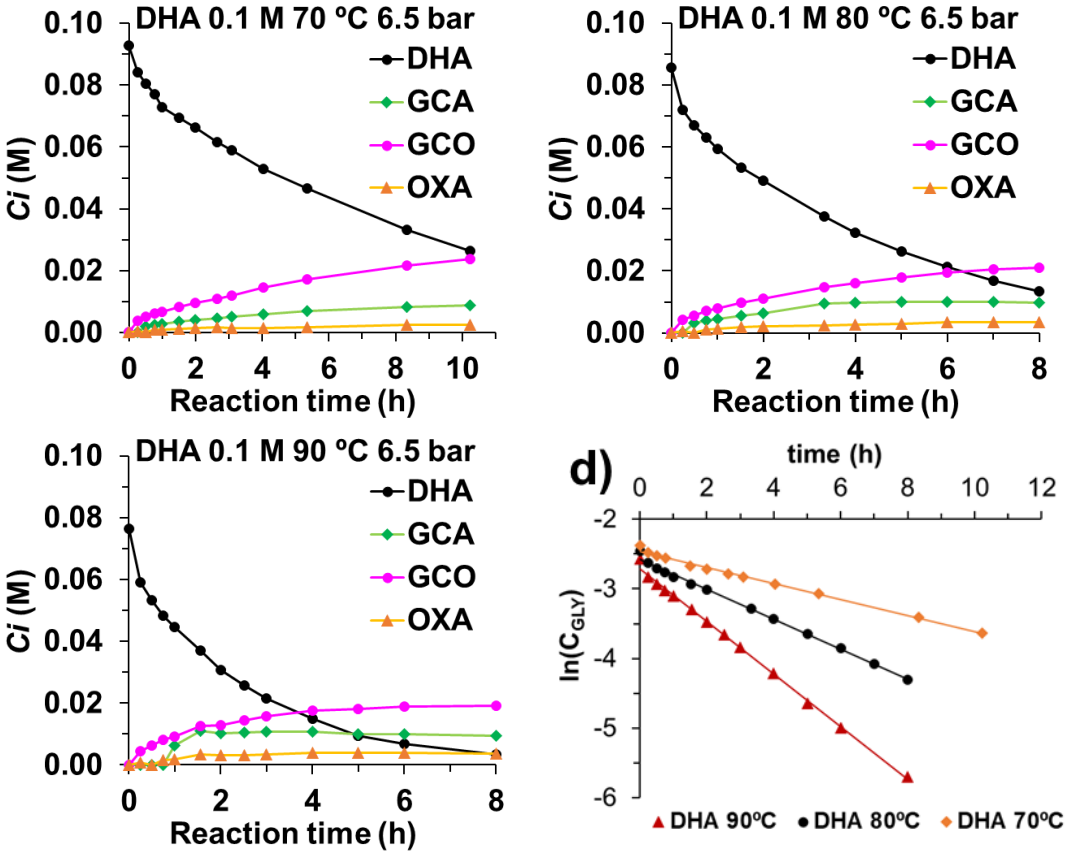

Figure 4.24. DHA oxidation over Au/ZnO at 70 °C, 80 °C, and 90 °C. d) integral method for pseudo-first-order power law kinetics. $C_{DHA,0}$ = 0.1 M; DHA/Au = 100 mol/mol, *w* = 2 g, V = 0.1 L, 800 rpm.

The product distribution from DHA oxidation in this work was consistent with previous studies from the literature. DHA oxidation with a lab-made Au/ZnO [22] and an Au/CuO [23] catalyst showed high GCA selectivity, along with GCO, OXA, and CO_2, the latter with the highest selectivity, indicative of non-selective total oxidation. GCA and GCO were not oxidised over Au/CuO, whereas OXA underwent further oxidation [23]. Oxidation of other C_3 alcohols over Au/CuO showed that the oxidation rate of 2-propanol was two times higher than that of 1-propanol and that 1,2-propanediol oxidation yielded hydroxyacetone, whereas 1,3-propanediol was not oxidised. These results suggested that the active sites on Au/CuO preferentially oxidise secondary hydroxyl groups, consistent with glycerol selective oxidation into DHA and the low GLAD oxidation [23].

So, in this work, despite the presence of multiple oxidation products, only the kinetics of DHA oxidation were modelled, neglecting the reaction products. Integral method analysis (Figure 4.24) showed good agreement with a pseudo-first reaction order for DHA oxidation across the studied temperature range:

$$r_{DHA,oxi} = k'_{DHA,oxi}\, C_{DHA} \tag{4.37}$$

The rate constants were used to obtain the Arrhenius plot (Figure 4.25, left), estimating a Ea'_{DHA} of 59.7 kJ mol^{-1} and $k'_{0,DHA}$ of 1.3×10^5 L min^{-1} g$_{cat}^{-1}$. A comparison of the experimental data and the model predictions is presented in Figure 4.25 (right).

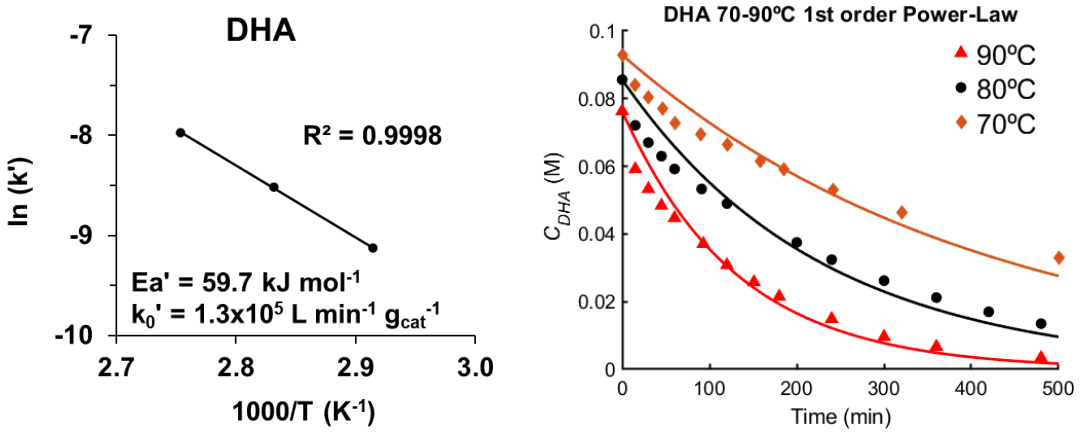

Figure 4.25. DHA oxidation over Au/ZnO: Left) Arrhenius plot; Right) pseudo-first-order power-law. $C_{DHA,0}$ = 0.1 M; DHA/Au = 100 mol/mol.

To assess the role of oxygen in the reaction rate, DHA oxidation was studied at a lower oxygen pressure of 2.5 bar (T = 80 °C), and the experimental concentration profiles are shown in Figure 4.26-left. The initial reaction rates at 2.5 bar and 6.5 bar are summarised in Table 4.11.

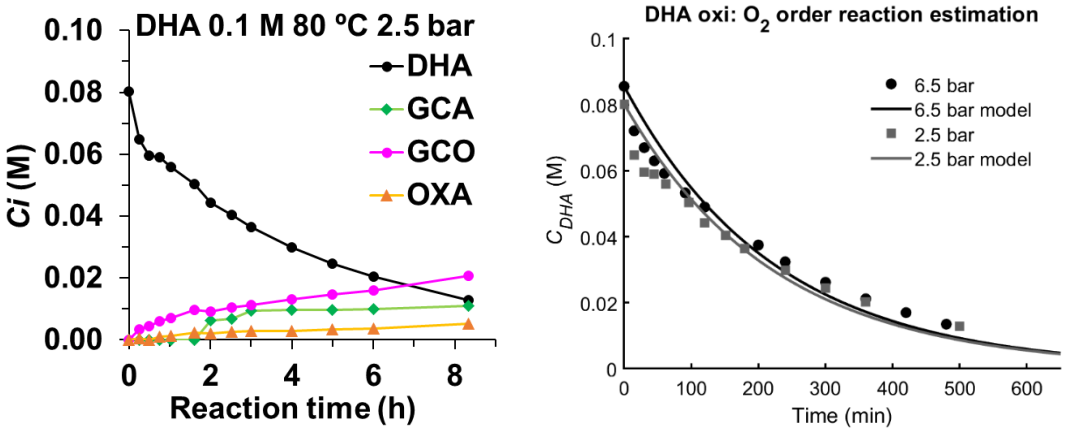

Figure 4.26. DHA oxidation over Au/ZnO: Left) P(O_2) = 2.5 bar; Right) first-order reaction, power-law model. T = 80 °C; $C_{DHA,0}$ = 0.1 M; DHA/Au = 100 mol/mol.

Table 4.11. Initial reaction rate of DHA oxidation with Au/ZnO at 2.5 bar and 6.5 bar. T = 80 °C; $C_{GLY,0}$ = 0.1 M; DHA/Au = 100 mol/mol, *w* = 2 g, V = 0.1 L.

$P(O_2)$ (bar)	$[O_2]$ (mM)	r_0 (mM min^{-1})
2.5	1.9	5.0×10^{-5}
6.5	4.9	4.5×10^{-5}

From Table 4.11 it can be concluded that the DHA oxidation rate was independent of the oxygen pressure; thus, the oxygen reaction order was estimated to be $m \approx 0$ under the studied conditions. These results were further confirmed by parameter estimation in MATLAB (Figure 4.26-right). Accordingly, DHA oxidation can be described by a first-order power-law kinetic model, and $Ea_{DHA} = Ea'_{DHA}$ = 59.7 kJ mol^{-1} and $k_{0,DHA} = k'_{0,DHA} = 1.3\times10^5$ L min^{-1} g_{cat}^{-1}.

$$r_{DHA,oxi} = k_{DHA,oxi} C_{DHA} \tag{4.38}$$

4.7.1.4. Summary

The preliminary kinetic parameters for GLY and DHA oxidation over the Au/ZnO catalyst are summarised in Table 4.12.

Table 4.12. Preliminary Arrhenius-based parameter estimation for GLY and DHA, oxidation over Au/ZnO.

	$k'_{i,oxi}$ [L min^{-1} g_{cat}^{-1}]			$\boldsymbol{r_i = k'_i C_i}$	
Species	70°C	80°C	90°C	Ea' kJ mol^{-1}	k_0' L min^{-1} g_{cat}^{-1}
GLY	1.5×10^{-3}	3.8×10^{-3}	7.6×10^{-3}	46.5	2.2×10^3
DHA	1.1×10^{-3}	2.0×10^{-3}	3.5×10^{-3}	59.7	1.3×10^5

The activation energy for glycerol oxidation over Au/ZnO (49 kJ mol^{-1}) was about two times higher than over Pt-Bi/AC (22 kJ mol^{-1}). The reverse trend was found for DHA (60 versus 84 kJ mol^{-1}). The activation energy for glycerol oxidation over Au/ZnO was similar to the values reported in the literature ≈ 60-70 kJ mol^{-1}, using an Au/ZnO catalyst under identical operating conditions ($C_{GLY,0}$ = 0.1 M, GLY/Au = 100 mol/mol, $P(O_2)$ = 1 bar, 70 – 85 ºC). The estimated kinetic parameters (Table 4.12) provided physically reasonable initial guesses for the subsequent power-law kinetic modelling Section.

4.7.2. Glycerol Oxidation - Power Law Kinetics

The kinetics of glycerol oxidation and its reaction products over Au/ZnO were further analysed through a simplified reaction network model based on the major products consistently

observed in the liquid phase (see Figure 4.20): GLY, DHA and GCO. The concentration of the remaining glycerol oxidation products (OXA, TTA, HPA, GLAD, GCA) was very low, so their oxidation kinetics were discarded from this analysis. The proposed reaction scheme is shown in Figure 4.27.

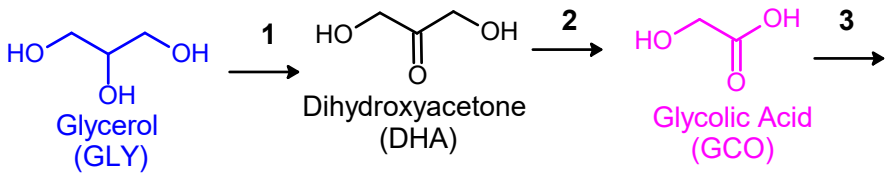

Figure 4.27. Proposed reaction scheme for glycerol oxidation over Au/ZnO catalyst.

The kinetic parameters obtained from GLY and DHA oxidation experiments (Table 4.12) served as initial guesses for the parameter estimation of these two species. Since direct kinetic data for the oxidation of GCO were not available, it was assumed to proceed analogously to DHA oxidation. A zero-order dependence on oxygen concentration was used for both DHA and GCO oxidation steps, and 1/3 with respect to oxygen concentration for the glycerol oxidation step. These assumptions were verified through sensitivity analysis and multiple initial guesses, all converging on the same reaction orders, further supporting the robustness of the selected kinetic expressions.

The rate of each step was modelled using first-order power-law kinetics with respect to the organic substrate, and parameter estimation by nonlinear regression against experimental data at 70°C, 80°C, and 90 °C was performed. The model fitting results are shown in Figure 28, and the corresponding estimated kinetic parameters are summarised in Table 4.13.

Table 4.13. Estimated kinetic parameters for glycerol oxidation over Au/ZnO using a first-order power-law model with respect to the organic species. SSR = 0.003.

Reaction	Step #	Ea kJ mol^{-1}	k_0 L g_{cat}^{-1} min^{-1}	k (90ºC) L g_{cat}^{-1} min^{-1}	O_2 Order (m)
GLY → DHA	1	65.0	8.8×10^{6}	$3.9\times10^{-3*}$	1/3
DHA → GCO	2	55.7	9.2×10^{4}	9.0×10^{-4}	0
GCO →	3	64.0	3.3×10^{6}	2.1×10^{-3}	0

* $L^{4/3}$ $mol^{-1/3}$ min^{-1} g_{cat}^{-1}.

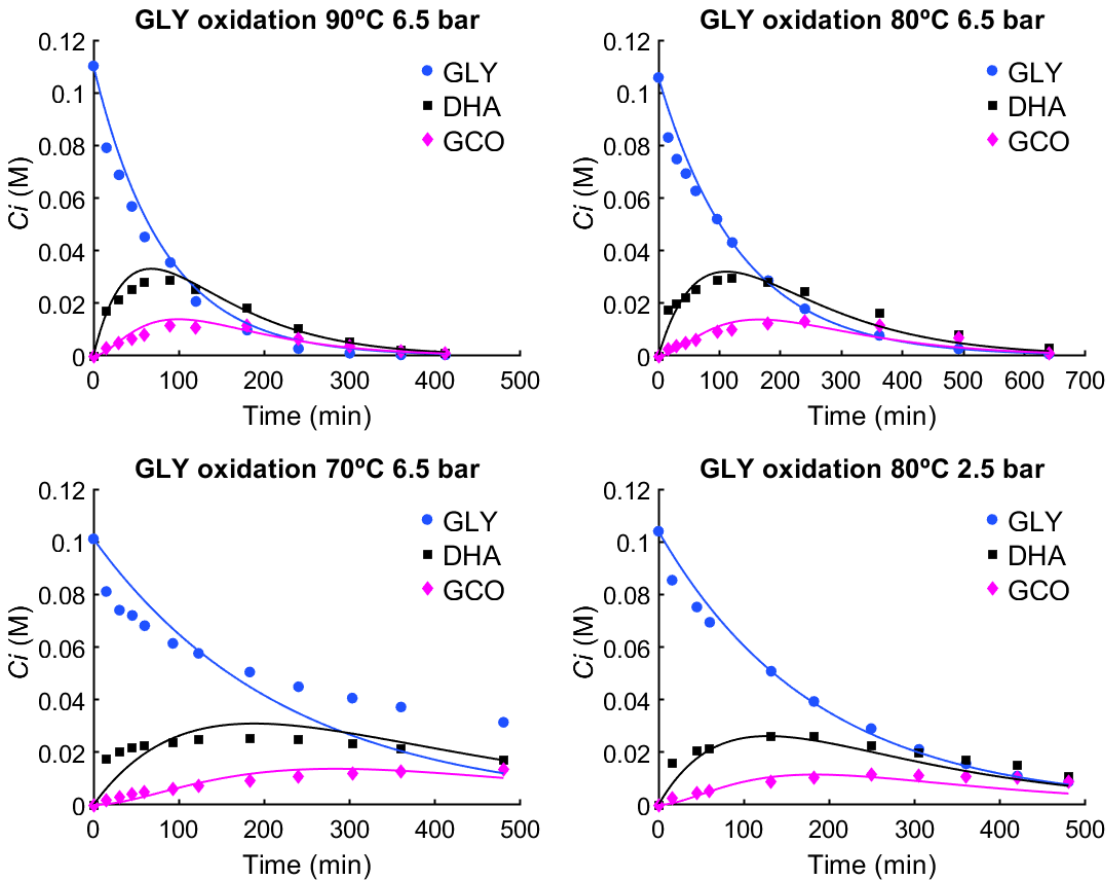

Figure 4.28. GLY oxidation over Au/ZnO at T = 70–90 °C and $P(O_2)$ = 2.5–6.5 bar; experimental results (dots) and model results (lines) for first-order power-law kinetics. $C_{GLY,0}$ = 0.1 M; GLY/Au = 100 mol/mol, *w* = 2 g, V = 0.1 L.

The power-law model described GLY, DHA and GCO concentration profiles well, namely for T ≥ 80 °C and $P(O_2)$ from 2.5 – 6.5 bar, while slightly failing to describe data at 70 ºC. Activation energies ranged between 55 – 65 kJ mol^{-1} for all three steps (Table 4.13), suggesting comparable energy barriers across the oxidation pathways. This dataset will be used in the following Section for direct comparison with the LHHW-based model (detailed in Section 4.4.2).

4.7.3. Glycerol Oxidation - LHHW-based Model

Like in the Pt-Bi/AC kinetic study, an LHHW-based model was used to study glycerol oxidation over Au/ZnO. The same network (Figure 4.27) involving GLY, DHA, and GCO was considered, and the kinetic parameters obtained from the power-law model were used as initial guesses for parameter estimation. Initial guesses were randomly assigned between –60 to –40 kJ mol^{-1} for ΔH and 1×10^{-8} to 1×10^{-6} M^{-1} for $K_{ads,0}$.

The model fitting was performed against the experimental concentration profiles for 2.5 – 6.5 bar and 70 – 90 °C. The model results are presented in Figure 4.29, and the estimated kinetic and adsorption parameters are summarised in Table 4.14.

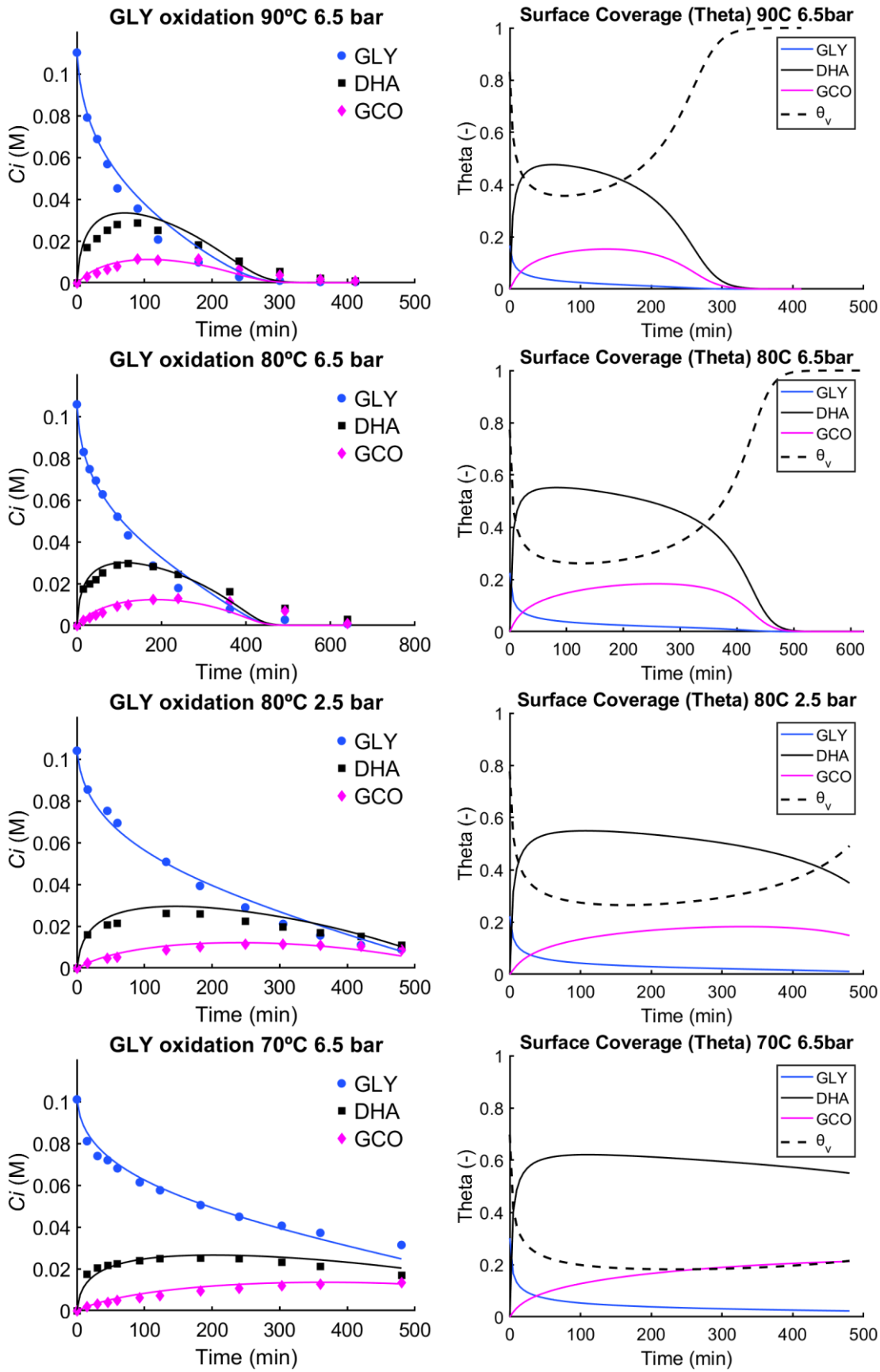

Figure 4.29. GLY oxidation over Au/ZnO at T = 70–90 °C, P(O_2) = 2.5–6.5 bar; using LHHW kinetic model and corresponding surface coverage. $C_{GLY,0}$ = 0.1 M; GLY/Au = 100 mol/mol, *w* = 2 g, V = 0.1 L, 800 rpm.

Table 4.14. LHHW model parameter estimation for GLY oxidation over Au/ZnO. T = 70 – 90 °C and $P(O_2)$ = 2.5 – 6.5 bar. SSR = 0.0014.

Reaction/ Species	#	Ea kJ/mol	k_0 mol^{-1} g^{-1} min^{-1}	k(90ºC) mol^{-1} g^{-1} min^{-1}	ΔH kJ/mol	$Kads_0$ M^{-1}	Kads (90ºC) M^{-1}
GLY → DHA	1	51.4	1.0×10^{5}	4.0×10^{-3}	-44.3	7.8×10^{-7}	2.8
DHA → GCO	2	54.1	1.6×10^{4}	3.0×10^{-4}	-59.7	1.0×10^{-7}	69.7
GCO →	3	57.1	1.3×10^{5}	8.0×10^{-4}	-38.5	1.1×10^{-4}	52.8
O_2	-	-	-	-	-33.2	2.1×10^{-3}	168.9

Figure 4.29 shows that the LHHW showed good agreement between the experimental data and the model predictions, including at T = 70 ºC, for which the power-law model failed. The LHHW model yielded a lower SSR of 0.0014 than the power-law model (0.0033).

The estimated activation energies (Table 4.14) are comparable to those obtained from the power-law model (**Table 4.13**), supporting the consistency of the results. The adsorption parameters suggest that all three species adsorb on the catalyst surface, with the reaction products adsorbing strongly compared to glycerol. The high adsorption strength of GCO may explain the catalyst's strong deactivation after one reaction.

The LHHW-based kinetic model was tested in the 40–90 °C temperature range and 2.5–6.5 bar oxygen pressure. The model results are presented in Figure 4.30, and the estimated kinetic and adsorption parameters are summarised in Table 4.15.

Table 4.15. Estimated parameters ("global fit") for GLY oxidation over Au/ZnO using the LHHW kinetic model. T = 40 – 90 °C and $P(O_2)$ = 2.5 – 6.5 bar. SSR = 0.0023.

Reaction/ Species	#	Ea kJ/mol	k_0 mol^{-1} g^{-1} min^{-1}	k (90ºC) mol^{-1} g^{-1} min^{-1}	ΔH kJ/mol	$Kads_0$ M^{-1}	Kads, (90ºC) M^{-1}
GLY → DHA	1	50.0	9.8×10^{4}	6.3×10^{-3}	-44.1	2.7×10^{-7}	0.9
DHA → GCO	2	57.0	1.2×10^{5}	8.0×10^{-4}	-50.1	5.3×10^{-7}	13.7
GCO →	3	65.2	5.2×10^{5}	2.0×10^{-4}	-60.6	1.3×10^{-7}	121.5
O_2	-	-	-	-	-51.2	5.8×10^{-6}	220.2

The LHHW kinetic successfully described the experimental data across the full range of conditions tested with a low SSR of 0.0023.

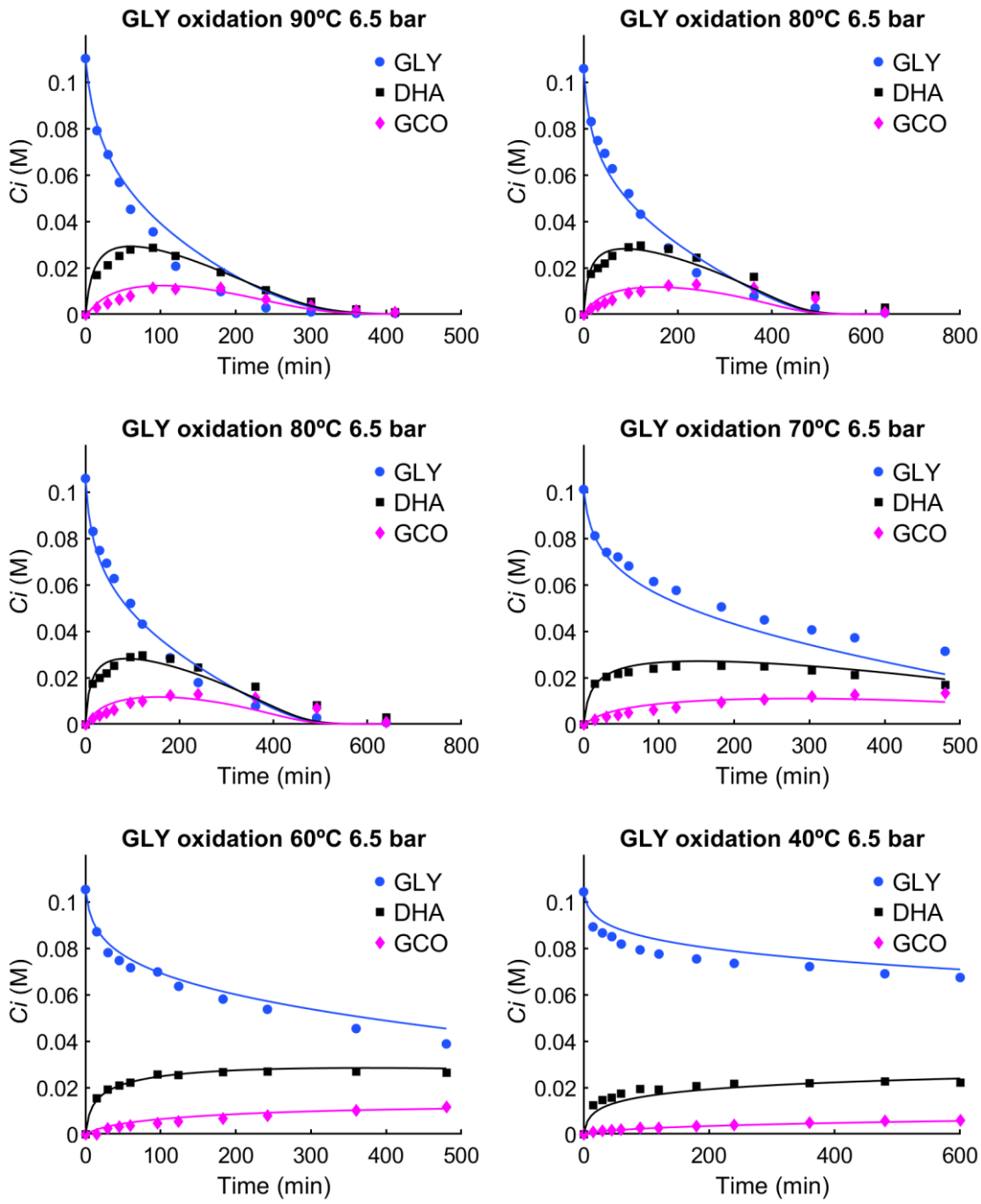

Figure 4.30. GLY oxidation over Au/ZnO at T = 40–90 °C and P(O_2) = 2.5 and 6.5 bar. and the LHHW kinetic model "global fit" results. $C_{GLY,0}$ = 0.1 M; GLY/Au = 100 mol/mol.

Although the Au/ZnO catalyst was not as promising as the Pt-Bi/AC for DHA production, this was the first time that glycerol oxidation kinetics with gold catalysts under base-free conditions were comprehensively studied.

4.8. Conclusions

This chapter presented a comprehensive kinetic analysis of glycerol oxidation over two commercial catalysts, Pt 5 wt.% - Bi 1.5 wt.%/AC and 1wt%. Au/ZnO, under base-free conditions. These catalysts were selected based on their previously demonstrated high activity and selectivity for dihydroxyacetone (DHA) and were studied in detail across varying operating conditions. Emphasis was placed on comparing two modelling strategies: a simple power-law kinetic model and a mechanistic Langmuir–Hinshelwood–Hougen–Watson (LHHW)-based model.

For Pt-Bi/AC, the oxidation network was deconstructed into smaller sub-networks using selected intermediates as starting reactants. The power-law kinetic model provided a reasonable understanding for limited operating ranges: $T \geq 80$ ºC and $C_{GLY} = 1$ M. An Ea_{GLY} of 17 kJ mol^{-1} was estimated, highlighting the high DHA selectivity of Pt-Bi/AC. However, the power-law model failed to describe a broader glycerol concentration range.

In contrast, the LHHW model was capable of describing glycerol oxidation data across a broader range of conditions: temperature of 80–100 °C, oxygen pressure of 2.0–7.5 bar, 0.1–2.0 M glycerol concentration, and GLY/Pt = 250–1000 mol/mol. An Ea_{GLY} of 16 kJ mol^{-1} and a ΔH_{GLY} of -25 kJ mol^{-1} were estimated, showing that DHA is readily obtained from glycerol oxidation and that glycerol is weakly and reversibly adsorbed on the Pt-Bi/AC surface. Glycolic and oxalic acid are strongly adsorbed on the catalyst surface, which may limit active site availability and promote catalyst overoxidation.

For Au/ZnO, glycerol oxidation mainly produced DHA, GCO, and OXA. The power-law model described glycerol oxidation well in the 80-90 °C range but failed for lower temperatures. In contrast, the LHHW model successfully described glycerol oxidation in the 40–90 °C and 2.5–6.5 bar O_2 pressure range. An Ea_{GLY} of 52 kJ mol^{-1} is significantly higher than for Pt-Bi/AC, reflecting the higher energy barrier over Au/ZnO. A ΔH_{GLY} of -43 kJ mol^{-1} indicated stronger glycerol adsorption on Au/ZnO, which may explain the low catalytic activity at higher GLY initial concentration. DHA and GCO also adsorbed strongly on the catalyst surface, which may also result in catalyst deactivation.

Both catalysts exhibited promising activity for the base-free oxidation of glycerol to DHA. However, Pt-Bi/AC outperformed Au/ZnO in catalytic activity, stability, and DHA yield. The LHHW-based model proved more robust and broadly applicable than the empirical power-law model. The mechanistic insights provided by the model, including adsorption effects and pathway selectivity, highlight its value for catalyst evaluation, process development, and scale-up for DHA production from glycerol oxidation.

4.9. Notation

Variables

a, b	Parameters in the Cheng correlation (Eq. 4.17)
C_i	Bulk concentration of species i (mol/L)
C_{WP}	Weisz–Prater criterion
C_{Mears}	Mears external mass transfer criterion
d_I	Impeller diameter (m)
d_p, r_p	Particle diameter/radius (m)
D_i	Molecular diffusion coefficient of compound i (m^2/s)
$D_{e,i}$	Effective diffusion coefficient (m^2/s)
Ea	Activation energy (kJ mol^{-1})
g	gravitational constant (9.80 m/s^2)
GLY/Pt (GLY/Au)	Initial molar ratio of glycerol to platinum (or gold) (mol/mol)
ΔH	Adsorption enthalpy (kJ mol^{-1})
k_0	Pre-exponential factor in Arrhenius equation
k(T)	Reaction rate constant at a given temperature
$K_{ads,0}$	Pre-exponential factor for the adsorption constant
$K_{ads}(T)$	Adsorption constant at a given temperature
k_{ext}	External mass transfer coefficient (m/s)
k_S	Liquid-solid mass transfer coefficient (m/s)
k_L	Gas-liquid mass transfer coefficient (m/s)
$k_L a$	Volumetric gas-liquid mass transfer coefficient (s^{-1})
M	Molar mass of the solvent (g mol^{-1})
m	Reaction order with respect to oxygen concentration (-)
N	Stirring speed (rps or rpm)
$P(O_2)$	Partial pressure of oxygen (bar)
$r_{obs,i}$	Observed reaction rate for species i oxidation (mol kg_{cat}^{-1} s^{-1})
r''_{GLY}	Observed reaction rate (glycerol consumption) per unit volume (mmol L^{-1} min^{-1})
r_j	Reaction rate of kinetic step j (mol g^{-1} min^{-1})
u_s	Superficial gas velocity (m/s)
V	Volume of liquid phase (L)
$V_{i,nbp}$	Molar volume of species i at normal boiling point (cm^3 mol^{-1})
T	Temperature (K)
w	Dry weight of the catalyst (g)

Sh	Sherwood number (particle)
Sh'	Sherwood number modified, $\mathrm{Sh}' = \frac{\mathrm{k_L a}\, {d_I}^2}{\mathrm{D}}$
Re'	Reynolds number modified, $\mathrm{Re}' = \frac{\mathrm{N}\rho\, {d_I}^2}{\mu}$
Fr'	Froude number modified, $\mathrm{Fr}' = \frac{d_I \mathrm{N}^2}{\mathrm{g}}$
Sc	Schmidt number, $\mathrm{Sc} = \frac{\mu}{\rho\, \mathrm{D}}$
α	Factor in the Cheng correlation (Eq. 4.17)
αG/L	Ratio chemical reaction/gas-liquid mass transfer (-)
αL/S	Ratio chemical reaction/liquid-solid mass transfer (-)
ε_p	Particle porosity (-)
θ_i	Surface coverage of species i (-)
θ_O	Surface coverage of oxygen (-)
θ_v	Catalyst vacant site coverage (-)
μ	Dynamic viscosity (Pa.s, or cP in Wilke-Chang correlation)
ρ	Liquid density (kg/m^3)
ρ_b	Bulk density: catalyst mass per unit volume of reactor (kg$_{cat}$/m^3)
ρ_p	Catalyst particle density (kg$_{cat}$/m$_{cat}^3$)
σ	Liquid surface tension (N/m)
τ_p	Particle tortuosity (-)
υ_{ij}	Stoichiometric coefficient of species *i* in reaction *j* (-)
ϕ_{exp}	Experimental Thiele modulus (-)
ψ	Solvent association factor in Wilke-Chang correlation (-)

Abbreviations

GLAD	Glyceraldehyde
MOXA	Mesoxalic acid
GLY	Glycerol
DHA	Dihydroxyacetone
GCO	Glycolic acid
OXA	Oxalic acid
TTA	Tartronic acid
GCA	Glyceric acid
HPA	Hydroxypiruvic acid
HPLC	High-Performance Liquid Chromatography

Pt-Bi/AC	Platinum-Bismuth supported on activated carbon (Johsonn Mattey)
Au/ZnO	Gold supported on zinc oxide (Strem Chemicals)
PL	Power-law (kinetic model)
SSR	Sum of squared residuals
LHHW	Langmuir–Hinshelwood–Hougen–Watson (kinetic model)

4.10.References

1. Figueiredo, J.L., Ribeiro, F.R., de Melo Orfão, J.J., and Lemos, F., *Catálise heterogênea*. 2007.
2. Fogler, H.S., *Elements of Chemical Reaction Engineering*. Vol. 5th edition. 2016, Philadelphia, PA: Prentice Hall.
3. Kluytmans, J., Markusse, A., Kuster, B., Marin, G., and Schouten, J., *Engineering aspects of the aqueous noble metal catalysed alcohol oxidation.* Catalysis Today, 2000. **57**(1-2): p. 143-155.
4. Mallat, T. and Baiker, A., *Oxidation of alcohols with molecular oxygen on platinum metal catalysts in aqueous solutions.* Catalysis Today, 1994. **19**(2): p. 247-283.
5. Mallat, T. and Baiker, A., *Oxidation of alcohols with molecular oxygen on solid catalysts.* Chemical Reviews, 2004. **104**(6): p. 3037-3058.
6. Makwana, V.D., Son, Y.-C., Howell, A.R., and Suib, S.L., *The Role of Lattice Oxygen in Selective Benzyl Alcohol Oxidation Using OMS-2 Catalyst: A Kinetic and Isotope-Labeling Study.* Journal of Catalysis, 2002. **210**(1): p. 46-52.
7. Khan, Y., Kilpiö, T., Marin, M., Russo, V., Lehtonen, J., Karinen, R., and Salmi, T., *Modelling of a microreactor for the partial oxidation of 1-butanol on a titania supported gold catalyst.* Chemical Engineering Science, 2020. **221**: p. 115695.
8. Demirel, S., Lucas, M., Wärnå, J., Salmi, T., Murzin, D., and Claus, P., *Reaction kinetics and modelling of the gold catalysed glycerol oxidation.* Topics in catalysis, 2007. **44**(1-2): p. 299-305.
9. Brainer, J., Sales, D., Medeiros, E., Lima Filho, N., and Abreu, C., *Wet oxidation of glycerol into fine organic acids: catalyst selection and kinetic evaluation.* Brazilian Journal of Chemical Engineering, 2014. **31**(4): p. 913-923.
10. Díaz, J., Skrzyńska, E., Girardon, J.-S., Capron, M., Dumeignil, F., and Fongarland, P., *Glycerol oxidation in the liquid phase over a gold-supported catalyst: kinetic analysis and modelling.* ChemEngineering, 2017. **1**(1): p. 7.
11. Díaz, J.A., Skrzyńska, E., Zaid, S., Girardon, J.S., Capron, M., Dumeignil, F., and Fongarland, P., *Kinetic modelling of the glycerol oxidation in the liquid phase: comparison of Pt, Au and Ag AS active phases.* Journal of Chemical Technology & Biotechnology, 2017. **92**(9): p. 2267-2275.
12. Ntho, T.A., Gqogqa, P., and Aluha, J.L., *Oxidation of Glycerol to Lactic Acid by Gold on Acidified Alumina: A Kinetic and DFT Case Study.* Adv. Chem. Kinet, 2018. **7**: p. 113.
13. Namdeo, A., Jhaveri, J.H., Mahajani, S.M., and Suresh, A.K., *Palladium catalyzed liquid phase oxidation of glycerol under alkaline conditions - Kinetic analysis and modelling.* Chemical Engineering Journal, 2022. **438**: p. 135424.
14. Zhao, M., Sun, Y., Yan, H., Liu, Y., Zhou, X., Chen, X., Feng, X., and Yang, C., *Reaction mechanism and kinetics for Pt/C and Au/C catalyzed aqueous phase glycerol oxidation to various carboxylic acids.* Chemical Engineering Science, 2024. **296**: p. 120237.
15. Worz, N., Brandner, A., and Claus, P., *Platinum− Bismuth-Catalyzed Oxidation of Glycerol: Kinetics and the Origin of Selective Deactivation.* The Journal of Physical Chemistry C, 2009. **114**(2): p. 1164-1172.
16. Hu, W., Lowry, B., and Varma, A., *Kinetic study of glycerol oxidation network over Pt–Bi/C catalyst.* Applied Catalysis B: Environmental, 2011. **106**(1-2): p. 123-132.

17. Ma, Y., Gan, J., Pan, M., Zhang, Y., Fu, W., Duan, X., Chen, W., Chen, D., Qian, G., and Zhou, X., *Reaction mechanism and kinetics for Pt/CNTs catalyzed base-free oxidation of glycerol.* Chemical Engineering Science, 2019. **203**: p. 228-236.

18. Pan, Y., Wu, G., He, Y., Feng, J., and Li, D., *Identification of the Au/ZnO interface as the specific active site for the selective oxidation of the secondary alcohol group in glycerol.* Journal of Catalysis, 2019. **369**: p. 222-232.

19. Chen, W., Wang, J., Zhang, Y., Zhang, J., Duan, X., Si, R., Chen, D., Qian, G., and Zhou, X., *Kinetics decoupling activity and selectivity of Pt nanocatalyst for enhanced glycerol oxidation performance.* AIChE Journal, 2021. **67**(10): p. e17339.

20. Kano, E., Aihara, T., Ghampson, I.T., Nogami, T., Miura, H., and Shishido, T., *Continuous Production of Lactic Acid from Glycerol over Bifunctional Catalysts under Base-Free Conditions Using a Liquid-Phase Flow Reactor.* ACS Sustainable Chemistry & Engineering, 2022. **10**(37): p. 12072-12081.

21. Chida, T., Hiromori, K., Shibasaki-Kitakawa, N., Mimura, N., Yamaguchi, A., and Takahashi, A., *Comprehensive Study on Kinetic Modeling of Liquid-Phase Selective Oxidation Using Au-Supported Catalysts for Efficient Production of Value-Added Chemicals from Glycerol.* Industrial & Engineering Chemistry Research, 2023. **62**(18): p. 6932-6942.

22. Meng, Y., Zou, S., Zhou, Y., Yi, W., Yan, Y., Ye, B., Xiao, L., Liu, J., Kobayashi, H., and Fan, J., *Activating molecular oxygen by Au/ZnO to selectively oxidize glycerol to dihydroxyacetone.* Catalysis Science & Technology, 2018. **8**(10): p. 2524-2528.

23. Liu, S.-S., Sun, K.-Q., and Xu, B.-Q., *Specific selectivity of Au-catalyzed oxidation of glycerol and other C3-polyols in water without the presence of a base.* Acs Catalysis, 2014. **4**(7): p. 2226-2230.

24. Weisz, P. and Prater, C., *Interpretation of measurements in experimental catalysis*, in *Advances in catalysis*. 1954, Elsevier. p. 143-196.

25. Mears, D.E., *Tests for Transport Limitations in Experimental Catalytic Reactors.* Industrial & Engineering Chemistry Process Design and Development, 1971. **10**(4): p. 541-547.

26. Mills, P. and Chaudhari, R., *Multiphase catalytic reactor engineering and design for pharmaceuticals and fine chemicals.* Catalysis Today, 1997. **37**(4): p. 367-404.

27. Cruellas, A., Ververs, W., Annaland, M.v.S., and Gallucci, F., *Experimental investigation of the oxidative coupling of methane in a porous membrane reactor: Relevance of back-permeation.* Membranes, 2020. **10**(7): p. 152.

28. Yawalkar, A.A., Heesink, A.B., Versteeg, G.F., and Pangarkar, V.G., *Gas—liquid mass transfer coefficient in stirred tank reactors.* The Canadian Journal of Chemical Engineering, 2002. **80**(5): p. 840-848.

29. Yagi, H. and Yoshida, F., *Gas absorption by Newtonian and non-Newtonian fluids in sparged agitated vessels.* Industrial & Engineering Chemistry Process Design and Development, 1975. **14**(4): p. 488-493.

30. Storck, A., Brodberger, J., Hutin, D., and Valentin, G., *Mass transfer in agitated vessels: energetic aspects.* Journal of Applied Electrochemistry, 1981. **11**(6): p. 727-733.

31. Wilke, C. and Chang, P., *Correlation of diffusion coefficients in dilute solutions.* AIChE Journal, 1955. **1**(2): p. 264-270.

32. Yaws, C.L., *Yaws' Critical Property Data for Chemical Engineers and Chemists*. 2012, Knovel.

33. Han, P. and Bartels, D.M., *Temperature dependence of oxygen diffusion in H 2 O and D 2 O.* The Journal of physical chemistry, 1996. **100**(13): p. 5597-5602.

34. Cheng, N.-S., *Formula for the Viscosity of a Glycerol− Water Mixture.* Industrial & Engineering Chemistry Research, 2008. **47**(9): p. 3285-3288.

35. Tromans, D., *Temperature and pressure dependent solubility of oxygen in water: a thermodynamic analysis.* Hydrometallurgy, 1998. **48**(3): p. 327-342.

36. Rischbieter, E., Schumpe, A., and Wunder, V., *Gas Solubilities in Aqueous Solutions of Organic Substances.* Journal of Chemical & Engineering Data, 1996. **41**(4): p. 809-812.

37. Meille, V., Pestre, N., Fongarland, P., and de Bellefon, C., *Gas/liquid mass transfer in small laboratory batch reactors: comparison of methods.* Industrial & engineering chemistry research, 2004. **43**(4): p. 924-927.

38. Liu, K., Phillips, J.R., Sun, X., Mohammad, S., Huhnke, R.L., and Atiyeh, H.K., *Investigation and modeling of gas-liquid mass transfer in a sparged and non-sparged continuous stirred tank reactor with potential application in syngas fermentation.* Fermentation, 2019. **5**(3): p. 75.

39. Chaudhari, R. and Ramachandran, P., *Three phase slurry reactors.* AIChE Journal, 1980. **26**(2): p. 177-201.

40. Liu, B., Xiao, Q., Sun, N., Gao, P., Fan, F., and Sunden, B., *Effect of gas distributor on gas–liquid dispersion and mass transfer characteristics in stirred tank.* Chemical Engineering Research and Design, 2019. **145**: p. 314-322.

41. Demirel-Gülen, S., Lucas, M., and Claus, P., *Liquid phase oxidation of glycerol over carbon supported gold catalysts.* Catalysis Today, 2005. **102**: p. 166-172.

42. Zhang, X., Gao, M., Yang, P., Cui, X., Liu, Y., Li, D., and Feng, J., *Insight into the effect of support crystal form on semi-continuous oxidation of glycerol.* Journal of Porous Materials, 2021. **28**(5): p. 1371-1385.

43. Nie, R., Liang, D., Shen, L., Gao, J., Chen, P., and Hou, Z., *Selective oxidation of glycerol with oxygen in base-free solution over MWCNTs supported PtSb alloy nanoparticles.* Applied Catalysis B: Environmental, 2012. **127**: p. 212-220.

44. Villa, A., Campisi, S., Chan-Thaw, C.E., Motta, D., Wang, D., and Prati, L., *Bismuth modified Au-Pt bimetallic catalysts for dihydroxyacetone production.* Catalysis Today, 2015. **249**: p. 103-108.

5. Adsorption Equilibrium and Kinetics of Glycerol and its Derivatives on a Fixed-Bed Column

In this chapter, adsorption data of the main species present in the glycerol oxidation reactive mixture were obtained, providing fundamental insights for designing a dihydroxyacetone purification process. A commercial polystyrene-divinylbenzene ion-exchange resin in acid and calcium forms was used as the stationary phase, with water and 5 mM H_2SO_4 as mobile phases. Single-component adsorption breakthrough experiments were performed to determine adsorption equilibrium data. Additionally, multi-component breakthrough experiments were conducted to evaluate competitive adsorption phenomena.

Part of this chapter was adapted from Walgode, P. M., Coelho, L. C. D., Faria, R. P. V., & Rodrigues, A. E. (2021). Dihydroxyacetone production: from glycerol catalytic oxidation with commercial catalysts to chromatographic separation. Industrial & Engineering Chemistry Research, 60(29), 10551-10565. DOI https://doi.org/10.1021/acs.iecr.1c00275

5.1. Introduction

Glycerol (GLY) catalytic oxidation produces a complex mixture of compounds, as none of the catalysts tested in Chapter 3 or reported in the literature are fully selective toward dihydroxyacetone (DHA). Consequently, a purification step is essential to assess the feasibility of the overall production process. High-purity DHA is required for most commercial applications, particularly in the cosmetics industry, where purity levels above 97% are typically needed [1].

The current industrial production of DHA via microbial fermentation presents significant downstream processing challenges [1-3], including problems associated with DHA sensitivity to heat and strongly alkaline conditions [1, 2]. The downstream process typically involves the use of organic solvents [3] and multiple steps, such as filtration of the broth to remove insoluble matter, use of ion-exchange resin to eliminate inorganic cations and anions, and vacuum distillation for stream concentration [4]. In bioprocesses, downstream operations often account for over 50% of total production costs [5]. A comparative study between bio-fermentation and a catalytic zeolite-based chemical route in the gas phase demonstrated that the latter has significantly lower operating costs and improved environmental performance [6].

Given the structural similarities among glycerol oxidation products, including molecular size, weight, and high boiling points, separation techniques such as membrane separation and distillation may be challenging to implement. Many of these organic compounds degrade near their boiling point, including DHA (188 °C). DHA undergoes slight decomposition at moderate temperatures (≈ 40 °C) [1, 2], reinforcing the importance of working at moderate/room temperatures. Chromatography emerges as a promising solution for such complex separations, building upon its successful use in similar systems [7, 8], including recent commercial applications [9-13].

However, limited studies have addressed DHA purification from glycerol catalytic oxidation reactions. One study explored the separation of DHA from GLY using a commercial polystyrene-divinylbenzene (PS-DVB) ion-exchange resin in calcium form (Purolite PCR), but the separation of organic acids was not studied [14]. However, resins in Ca^{2+} form are unsuitable for direct organic acid separation, as ion exchange between the acids and the resin cations would gradually convert the resin back to its hydrogen form. The operation would be more complex, and steps for resin regeneration would be required.

Selecting an appropriate stationary and mobile phase is crucial for developing an efficient continuous chromatographic purification process. Key resin properties, such as particle size, crosslinking degree, adsorption capacity, and ionic form, directly influence separation performance [15]. PS-DVB ion-exchange resins have been successfully used for chromatographic

separation of short-chain organic acids [16-20] and have also been employed in industrial-scale simulated moving bed (SMB) chromatography for the separation of sugars, amino acids, and organic acids [21-23].

A prior study from our group demonstrated the high potential of strong acid cation-exchange resins for separating glyceric acid (GCA) from tartronic acid (TTA), two glycerol oxidation products [24, 25]. Using a commercial PS-DVB resin in its acid form (Dowex® 50WX) as the stationary phase at 293 K and a 5 mM H_2SO_4 aqueous solution as the mobile phase (to preserve the resin acid properties), it was observed that lower crosslinking (2%) led to higher adsorption capacity and more theoretical plates compared to higher crosslinking levels (4-8%) [24]. These fine-mesh spherical ion-exchange resins offer an excellent balance between flow rate, column packing efficiency, and ease of handling. They are chemically resistant to oxidation and reduction, insoluble in common solvents, and possess high osmotic strength, allowing them to withstand multiple swell/shrink cycles. Additionally, they exhibit high mechanical stability, enabling high flow rates for increased throughput and reliable performance during repeated regeneration cycles [22, 23]. This study was extended to an SMB separation process and experimentally validated for GCA-TTA separation [25], highlighting the potential of continuous countercurrent chromatographic processes for DHA purification.

To design a continuous separation process (later discussed in Chapter 6), adsorption equilibrium data were obtained using frontal analysis, a faster and more accurate method than batch techniques [26]. Breakthrough experiments were conducted in a fixed-bed column packed with Dowex® 50WX-2 resin in both acid (H^+) and calcium (Ca^{2+}) forms. Water was selected as the mobile phase for a more sustainable process, whereas a diluted 5 mM H_2SO_4 solution was used in the H^+ form resin to keep its functional properties.

In the H^+ form resin, adsorption equilibrium and kinetic data were determined for the main species present in the reaction mixture: oxalic acid (OXA), TTA, GCA, glycolic acid (GCO), DHA, and GLY. In the Ca^{2+} form resin, adsorption studies focused only on DHA and glycerol, as organic acids would revert the resin to its acid form. Multi-component adsorption breakthrough experiments were also performed: a six-component mixture in the H^+ resin and a binary DHA-GLY mixture in the resin in Ca^{2+} form.

Although glyceraldehyde (GLAD) and hydroxypyruvic acid (HPA) are relevant products of glycerol catalytic oxidation reactions, particularly HPA, their prohibitive costs (approximately 100 €/g for GLAD and 25 €/mg for HPA) precluded their inclusion in this study. As discussed in Chapter 4, the retention times of TTA and HPA were found to be very similar. Consequently, any HPA potentially present in the reaction mixture was considered as TTA for the separation study. The error introduced by this assumption is expected to be negligible.

5.2. Experimental Description

5.2.1. Chemicals and Materials

In this study, the following chemicals were used to investigate the adsorption of species targeted for separation: oxalic acid (OXA, ≥ 99.5%, ACROS Organics), tartronic acid (TTA, ≥ 97%, Sigma-Aldrich), DL-glyceric acid (GCA, 20% in water, ca. 2 mol/L, Tokyo Chemical Industry Co.), glycolic acid (GCO, ≥ 99%, Fisher Scientific), glycerol (GLY, ≥ 99.5%, Fisher Scientific), and dihydroxyacetone (DHA, ≥ 98%, Merck). Sulfuric acid (H_2SO_4, > 95%, Fisher Scientific) was used to prepare the mobile phase, and calcium chloride dihydrate ($CaCl_2 \cdot 2H_2O$, > 99.5%, HiMedia) was employed for the ion-exchange step. Deionised water, produced by the laboratory purification system, was used.

The stationary phase consisted of a commercial strong cation-exchange resin, the Dowex® 50WX-2 in its acid form (mesh size 200/400, ACROS Organics). This resin is a PS-DVB material functionalized with sulfonic acid groups (SO_3H) and 2% crosslinking. Before use, the resin was thoroughly washed with deionised water and fully hydrated for 48 hours before being packed into a fixed-bed column.

The Dowex® 50WX-2 resin was converted to its Ca^{2+} form via an ion exchange process. A 0.1 M $CaCl_2 \cdot 2H_2O$ solution was continuously pumped into the column until the outlet conductivity and pH matched those of the inlet solution using only detectors. Then, the resin was washed with deionised water to remove any excess cations.

The particle size distribution of the resin in H^+ form and in Ca^{2+} form was measured using a laser diffraction particle size analyser (Beckman Coulter LS230, USA), employing the Fraunhofer light scattering theory.

5.2.2. HPLC Analytical Method

For high-concentration single-component and multicomponent breakthrough experiments, samples were collected from the fixed-bed column outlet and analysed using a Prominence High-Performance Liquid Chromatography (HPLC) system (Shimadzu, Japan). The system was equipped with an Alltech Organic Acid OA-1000 analytical column (7.8 × 300 mm, Hichrom, UK), and the column temperature was maintained at 333 K using a column oven. Detailed information on the HPLC method is provided in Chapter 3.

5.2.3. Breakthrough Experiments

Breakthrough experiments were conducted using a Smartline Knauer HPLC system, which was equipped with an online degasser, pump, column oven (set at 293 K), UV detector (monitoring at 210 and 260 nm), and a refractive index (RI) detector. Two semi-preparative stainless steel columns (100 × 20 mm) were packed with Dowex® 50WX-2 resin, one in the acid (H^+) form and the other in the Ca^{2+} form. The system's dead volume was measured and appropriately accounted for in these experiments.

Single-component breakthrough experiments were performed on the column containing the resin in H^+ form, which was equilibrated with a 5 mM H_2SO_4 aqueous solution as the mobile phase. Aqueous solutions of known concentrations for each of the six species were fed into the column at 3 ml/min using a three-way valve. The experiment continued until the outlet concentration reached a steady plateau equivalent to the inlet concentration, after which desorption was carried out by flushing the column until the outlet concentration dropped to the initial value. For DHA and GLY, breakthrough experiments were similarly performed on the resin in Ca^{2+} form, using deionised water as the mobile phase. In low-concentration experiments, the column outlet concentration was monitored via UV-VIS and RI signals. For high-concentration experiments, in which online monitoring was limited due to signal saturation, periodic outlet samples were collected and subsequently analysed by HPLC.

The mass of each compound adsorbed in the resin, q_i ($g_i/L_{particle}$), was determined by calculating the area above the adsorption breakthrough curve or below the desorption breakthrough curve, described in the modelling Section. Equilibrium isotherms were then obtained by fitting the data to established adsorption models such as the Linear and Freundlich isotherms.

Multicomponent breakthrough experiments were also conducted - one using a six-component mixture in the H^+ resin and another using a binary mixture of DHA and GLY in the Ca^{2+} resin - to evaluate competitive adsorption effects under relevant operating conditions. Outlet liquid samples were periodically collected and analysed by HPLC.

5.3. Fixed-bed Column Modelling

5.3.1. Mathematical Model

A phenomenological model was developed to describe the adsorption phenomena in the fixed-bed column. The model was implemented in the gPROMS Model Builder software V7.0.7 (Process System Enterprise, UK). The orthogonal collocation in finite elements method (OCFEM) was used for the axial discretisation, with 40 finite elements per column and two interior collocation points. To solve the system of ordinary differential and algebraic equations that resulted from the discretisation process, the DAEBDF solver was utilised with a relative error of 10^{-5}.

The model was based on the following assumptions, which are commonly adopted for similar systems [8, 25, 27-29]: 1) an axially dispersed plug flow model describes the fluid flow, 2) mass transfer between the liquid and solid phases follows the linear driving force (LDF) model proposed by Glueckauf [29, 30], 3) the system operates isothermally, 4) the adsorbent consists of homogeneous spherical particles with uniform size, 5) the fluid velocity, bed porosity, and bed length remain constant, and 6) radial concentration gradients in the bed are negligible.

The transient mass balance to the fluid phase is expressed as:

$$\frac{\partial C_i}{\partial t} + \frac{1-\varepsilon}{\varepsilon} k_{h,i}(q_i^* - \bar{q}_i) + \frac{u}{L}\frac{\partial C_i}{\partial z} - \frac{D_{ax}}{L^2}\frac{\partial^2 C_i}{\partial z^2} = 0 \tag{5.1}$$

where the subscript i refers to the component in the mixture, C is the bulk concentration in the liquid phase, $\bar{q}$ is the average adsorbed-phase concentration, q^* is the adsorbed-phase concentration in equilibrium with C, u is the liquid interstitial velocity, z is the normalised axial position, L is the column length, ε is the column bed porosity, D_{ax} is the axial dispersion coefficient, $D_{ax} = \frac{uL}{Pe}$. The parameter k_h represents the homogeneous mass transfer coefficient. Danckwerts' boundary conditions were considered,

$z = 0$

$$u\, C_{i,0} = u\, C_i - \frac{D_{ax}}{L}\frac{\partial C_i}{\partial z}\bigg|_{z=0} \tag{5.2}$$

$z = 1$

$$\frac{\partial C_i}{\partial z}\bigg|_{z=1} = 0 \tag{5.3}$$

The transient mass balance to the solid phase, based on the LDF model, is given by:

$$\frac{\partial \bar{q}_i}{\partial t} - k_{h,i}(q_i^* - \bar{q}_i) = 0 \tag{5.4}$$

The initial conditions were:

$$t = 0 \qquad C_i = C_{i,0} \text{ and } \bar{q}_i = \bar{q}_{i,0} \tag{5.5}$$

For adsorption experiments, the column is pre-equilibrated in eluent, $C_{i,0} = 0$ and $\bar{q}_i = 0$, while for desorption experiments $C_{i,0} = C_{i,feed}$ and $\bar{q}_i = \bar{q}_{feed,i}$.

5.3.2. Model Parameters

The bed porosity and Péclet number (Pe) were determined through tracer experiments. Following the pulse perturbation method, 20 µL of 5 g/L Blue Dextran 2000 (2000 kDa) aqueous solution was injected into the fixed-bed column pre-equilibrated with the mobile phase. Given its large hydrodynamic diameter of approximately 50 nm, the Blue Dextran 2000 molecule is unable to penetrate the pores of the gel-type resin and, therefore, flows exclusively through the interparticle voids of the fixed-bed column [31]. The elution profile was monitored using a UV-VIS detector at 254 nm.

From the residence time distribution theory, the E(t) curve for a pulse injection of a tracer compound in the fixed-bed column was obtained using Equation (5.6). Assuming plug flow with axial dispersion, the first and second moments of the residence time distribution $\mu_n[E(t)] = \int_0^\infty t^n\, E(t)\, dt$, were computed [32]. The first moment of E(t) is the mean residence time ($\bar{t}_r$). For tracer experiments and in the absence of short-circuit or dead zones, $\bar{t}_r$ is equal to the space-time, $\tau = \varepsilon V_c/Q$, where Vc is the empty column volume, Q is the flow rate, and ε is the bed porosity, given by Equation (5.7). The Pe number was calculated from the second statistical moment of the residence time distribution curve using Equation (5.8). Further details regarding these calculations can be found elsewhere [32, 33].

$$E(t) = \frac{C_{out}(t)}{\int_0^\infty C_{out}(t)\, dt} \tag{5.6}$$

$$\varepsilon = \frac{\int_0^\infty t\, E(t)\, dt}{V_c/Q} \tag{5.7}$$

$$Pe = \frac{2\,\bar{t}_r{}^2}{\sigma^2} = \frac{2\,\bar{t}_r{}^2}{\int_0^\infty (t-\bar{t}_r)^2\, E(t)\, dt} \tag{5.8}$$

From the breakthrough curves obtained, it is possible to estimate the stoichiometric time, t_{st}, given by Eq. (5.9), with C_{Feed} being the feed concentration (i.e., the equilibrium concentration):

$$\mathrm{t}_{st} = \int_0^\infty \left(1 - \frac{C_{out}}{C_{Feed}}\right) dt \tag{5.9}$$

In a column pre-equilibrated with eluent, after the adsorption step where it is equilibrated with the feed solution, the quantity of component i, m_i, in the column at equilibrium is given by [26]:

$$m_i = t_{st} Q\, C_{Feed} = \varepsilon V_c C_i^{Feed} + (1-\varepsilon) V_c q_i \tag{5.10}$$

The adsorption data were analysed using different equilibrium isotherm models, depending on the shape of the experimental isotherms [26]. The simplest model is the linear adsorption isotherm, described by Eq. (5.11), with n_i = 1, where the distribution coefficient K_i, increases for more strongly adsorbed species. Non-linear adsorption behaviour was modelled using the Freundlich isotherm, given by equation given by Eq. (5.11) with $n_i \neq 1$.

$$q_i^* = K_i C_i^{1/n_i} \tag{5.11}$$

For differently shaped data, other adsorption isotherm models, such as the Langmuir isotherm, should be considered [26, 29, 34]. Despite their simplicity, Linear and Freundlich isotherms do not account for competitive adsorption effects at active sites or adsorbate-adsorbate interactions. However, using more complex isotherms, such as Langmuir, to data well-described by simpler models can lead to overparameterization, resulting in estimated adsorption parameters with no physical significance, increasing computational effort, and introducing potential modelling errors.

The homogeneous mass transfer coefficient, $k_{h,i}$, was calculated according to the equation proposed by Glueckauf [30], where $D_{h,i}$ is the homogeneous diffusion coefficient and R_p the particle radius.

$$k_{h,i} = \frac{15 D_{h,i}}{R_p^2} \tag{5.12}$$

The value of $D_{h,i}$ may be calculated from the equivalence of the diffusion in the homogeneous particle and the porous particle:

$$D_{h,i} = \frac{D_{e,i}}{\varepsilon_p + K_i} \tag{5.13}$$

$$D_{e,i} = \varepsilon_p D_{p,i} \tag{5.14}$$

$$D_{p,i} = \frac{D_i}{\tau_p} \tag{5.15}$$

where ε_p is the particle porosity, τ_p is the particle tortuosity, $D_{e,i}$ is the effective diffusion coefficient in the particle, $D_{p,i}$ is the diffusion coefficient in the pores of the particle, and D_i is the combined diffusion coefficient [32]. Since Knudsen diffusion can be neglected in liquid systems,

D was assumed to be equal to the molecular diffusion coefficient at infinite dilution, D_i^{∞} (cm^2 s^{-1}), estimated by the Wilke Chang correlation [35].

$$D_i^{\infty} = 7.4 \times 10^{-8} \frac{T(\psi M)^{1/2}}{\eta V_{i,nbp}^{0.6}} \tag{5.16}$$

Here, the molecular weight, M (g/mol), and the dynamic viscosity, η (cP), are specific to the solvent, which is considered to be water (M = 18.02 g/mol, and η = 1.002 cP at 293.15 K), and the solvent association factor, ψ, is 2.6 for water [35]. The Les Bas correlation [36] was used to estimate the molar volume at normal boiling point, $V_{i,nbp}$ (cm^3/mol), except for OXA and GLY, for which experimental data was available [37].

The particle tortuosity, τ_p, is a challenging parameter to estimate, typically ranging between 2 and 10-15 for porous particles [34]. Since tortuosity directly influences the intraparticle diffusion coefficient and, consequently, the mass transfer coefficient for each species, a theoretical tortuosity–porosity correlation was applied. Specifically, the Mackie and Meares model [38], developed for cation-exchange resins with a low degree of crosslinking swollen in water, was considered appropriate for the gel-type resin used in this study.

$$\tau_p = \frac{2 - \varepsilon_p}{\varepsilon_p} \tag{5.17}$$

5.4. Results and Discussion

5.4.1. Resin Properties

The Dowex 50WX-2 resin in H^+ form had an average particle size of 148.0 µm ± 54.28 µm, which decreased to 112.4 µm ± 21.18 µm upon conversion to Ca^{2+} form (see Figure 5.1).

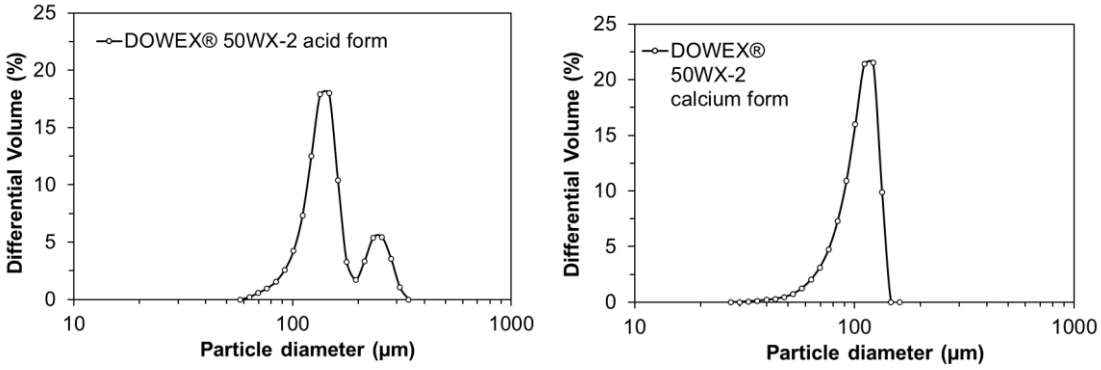

Figure 5.1. Particle size distribution of DOWEX® 50WX-2 resin fully hydrated.

Although classified as a gel-type resin, the Dowex 50WX-2 H^+ form resin swells in polar media, like water, causing morphological changes and forming non-permanent pores [39, 40]. Using Inverse Steric Exclusion Chromatography, the particle porosity, ε_p, of the water-swollen resin in H^+ form was determined to be 0.74 [39]. According to the Ogston model, 27% of the pores have an equivalent diameter of 4.8 nm, while the remaining have a diameter of 2.6 nm. From Eq.(5.17), τ_p is 1.7, slightly below the typical values (2-15).

The resin shrank upon conversion to Ca^{2+} form, reducing the bed volume by 35% compared to its initial volume in H^+ form. Since the resin mass remains unchanged and assuming spherical particles, the particle porosity in Ca^{2+} form was estimated to be 0.41, given by: $\varepsilon_{p,Ca^{2+}} = 1 - \left(1 - \varepsilon_{p,H^+}\right)\left(\frac{R_{p,H^+}}{R_{p,Ca^{2+}}}\right)^3$. From Eq.(5.17), τ_p is 3.9.

Tracer experiments in the fixed-bed column packed with the resin in H^+ form and in Ca^{2+} form, and the results in the form of $E(\theta_c)$ are represented in Figure 5.2.

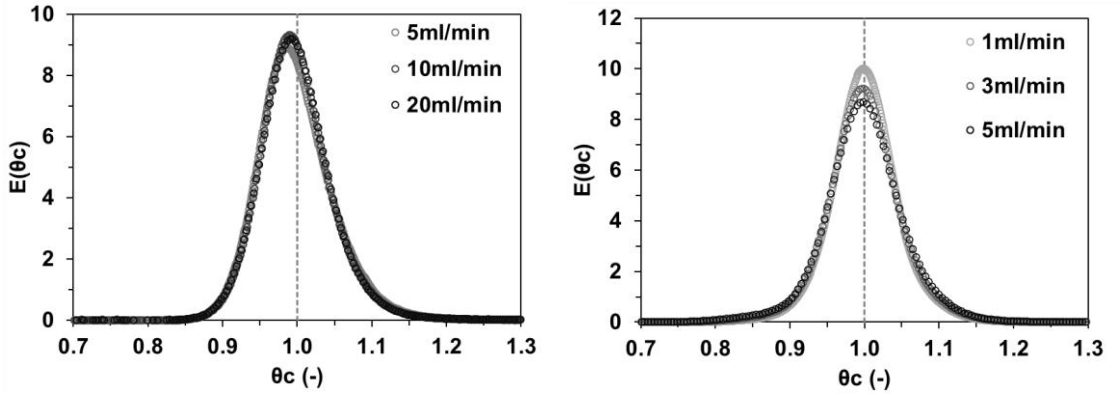

Figure 5.2. Tracer experiments in a fixed-bed column packed with resin in H^+ form (left); Ca^{2+} form (right).

Different flow rates were used to rule out potential effects in bed porosity, as higher flow rates could result in resin compression, decreasing the particles' volume. For the resin in H^+ form, a bed column porosity of 0.36 and a Pe of 608 were determined, while for the resin in Ca^{2+} form, ε of 0.30 and Pe of 527.

5.4.2. Adsorption Equilibrium Isotherms

Adsorption equilibrium data (q *vs* C) were obtained from the single-component breakthrough experiments using the resin in H^+ form at 293 K, with 5 mM H_2SO_4 as the mobile phase. The corresponding adsorption equilibrium isotherms are presented in Figure 5.3. In Figure 5.4, a comparison of the six isotherms in the H^+ resin is available.

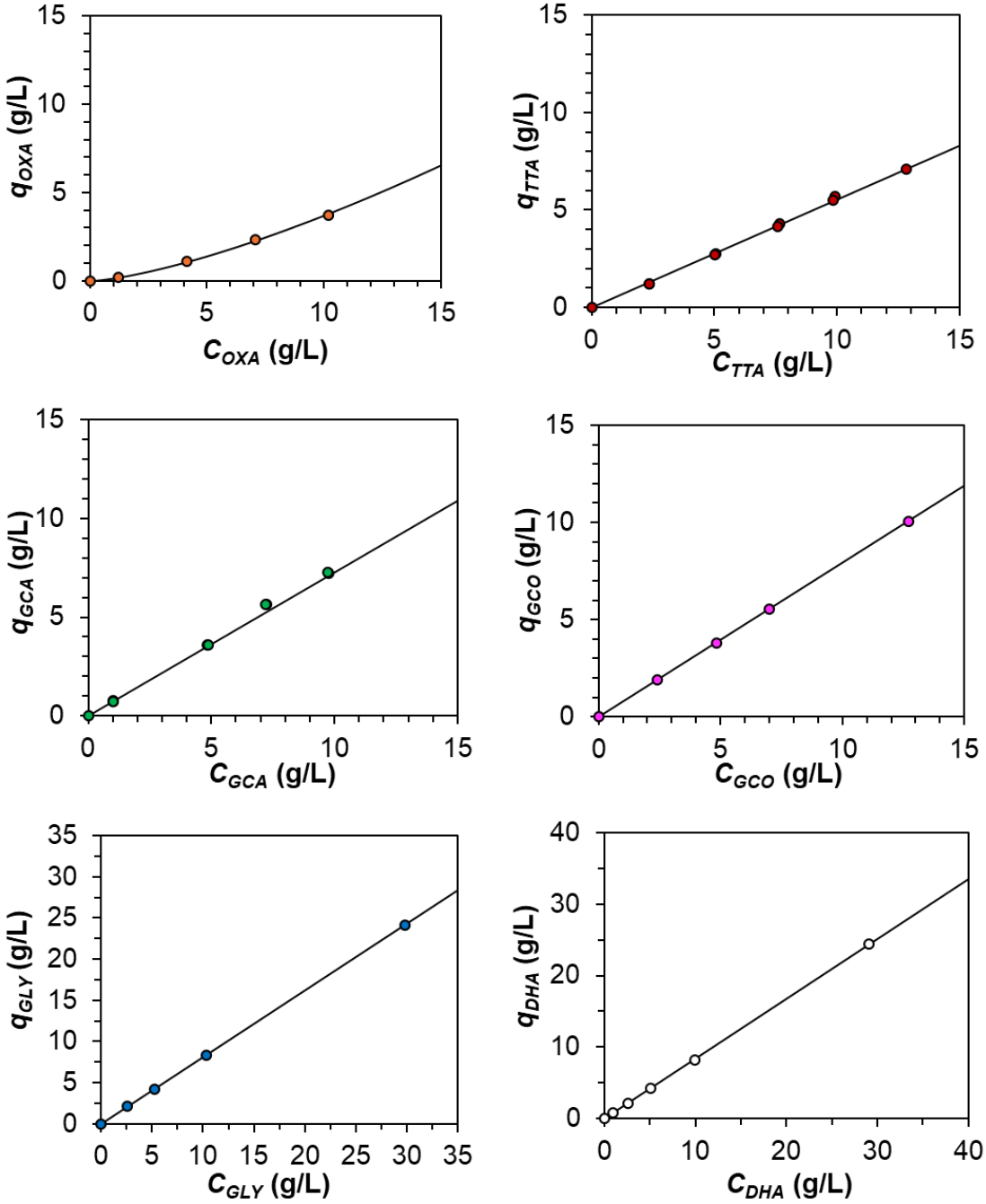

Figure 5.3. Adsorption equilibrium isotherms of (a) OXA, (b) TTA, (c) GCA, (d) GCO, (e) GLY, and (f) DHA on Dowex® 50WX-2 resin in H^+ form at 293 K using 5 mM H_2SO_4 as mobile phase. Experimental data (dots) and isotherms (solid line).

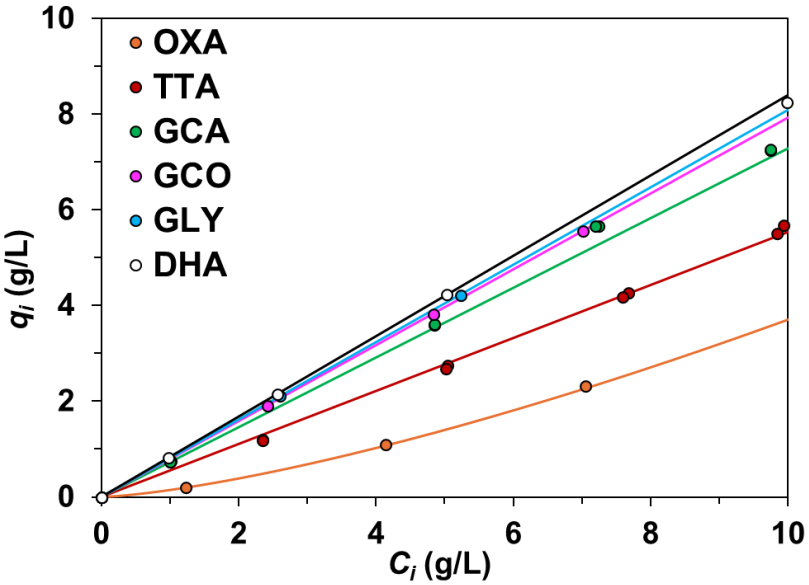

Figure 5.4. Adsorption equilibrium isotherms of six solutes on Dowex® 50WX-2 resin (H^+ form) at 293 K with 5 mM H_2SO_4 as mobile phase. Experimental data (dots) and model isotherms (solid lines).

Within the studied concentration range, the equilibrium isotherms were well described by linear isotherms for all species except OXA, which was better described by the Freundlich isotherm. Figure 5.4 shows that DHA, GLY, and GCO have similar distribution coefficients. The adsorption equilibrium of TTA and GCA on this same resin in H^+ form had also been studied in a previous work of our group [24].

The adsorption data of GLY and DHA on the resin in Ca^{2+} form was well adjusted by a linear isotherm (Figure 5.5). The model parameters for both resins are summarised in Table 5.1.

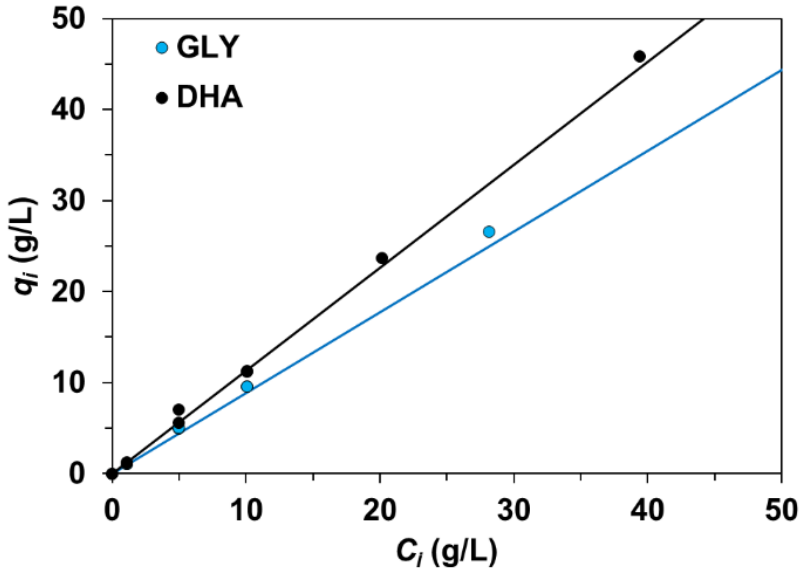

Figure 5.5. Adsorption equilibrium isotherms of DHA (black) and GLY (blue) in Dowex® 50WX-2 resin in Ca^{2+} form at 293 K.

Table 5.1. Distribution coefficients, mass transfer coefficients, and resin properties (Dowex 50WX-2, acid and calcium form) at 293 K. *n_{OXA} = 0.719.

	H^+ form		Ca^{2+} form	
Species	K_i (n_i = 1) (L_{LIQ} L_{SOL}^{-1})	k_h (min^{-1})	K_i (n_i = 1) (L_{LIQ} L_{SOL}^{-1})	k_h (min^{-1})
OXA	0.150*	81.0	-	-
TTA	0.554	50.1	-	-
GCA	0.728	45.4	-	-
GCO	0.792	53.5	-	-
GLY	0.809	46.8	0.887	18.9
DHA	0.840	44.1	1.131	23.4
$\alpha_{(DHA/GLY)}$	1.04		1.28	
ε_p	0.74		0.41	
τ_p	1.7		3.9	

Comparing the two resin forms, retention factors were higher for the Ca^{2+} form than for the H^+ form, with DHA exhibiting the highest retention in both cases. The separation selectivity of DHA from GLY ($\alpha = K_{DHA}/K_{GLY}$) increased from 1.04 in the resin in H^+ form to 1.28 in the resin in Ca^{2+} form, indicating improved selectivity.

5.4.3. Single-Component Breakthrough Experiments

Single-component breakthrough experiments were used to validate the fixed-bed column model described by equations (5.1) to (5.5).

The experimental and simulated outlet concentration profiles for single-component breakthrough experiments in the H^+ resin at 293 K and a volumetric flow rate of 3 ml/min are shown in Figure 5.6. TTA and GCA breakthrough experiments were conducted in a jacketed glass column (Goetec, Germany), 100 x 10 mm, with ε of 0.30 and Pe of 178.

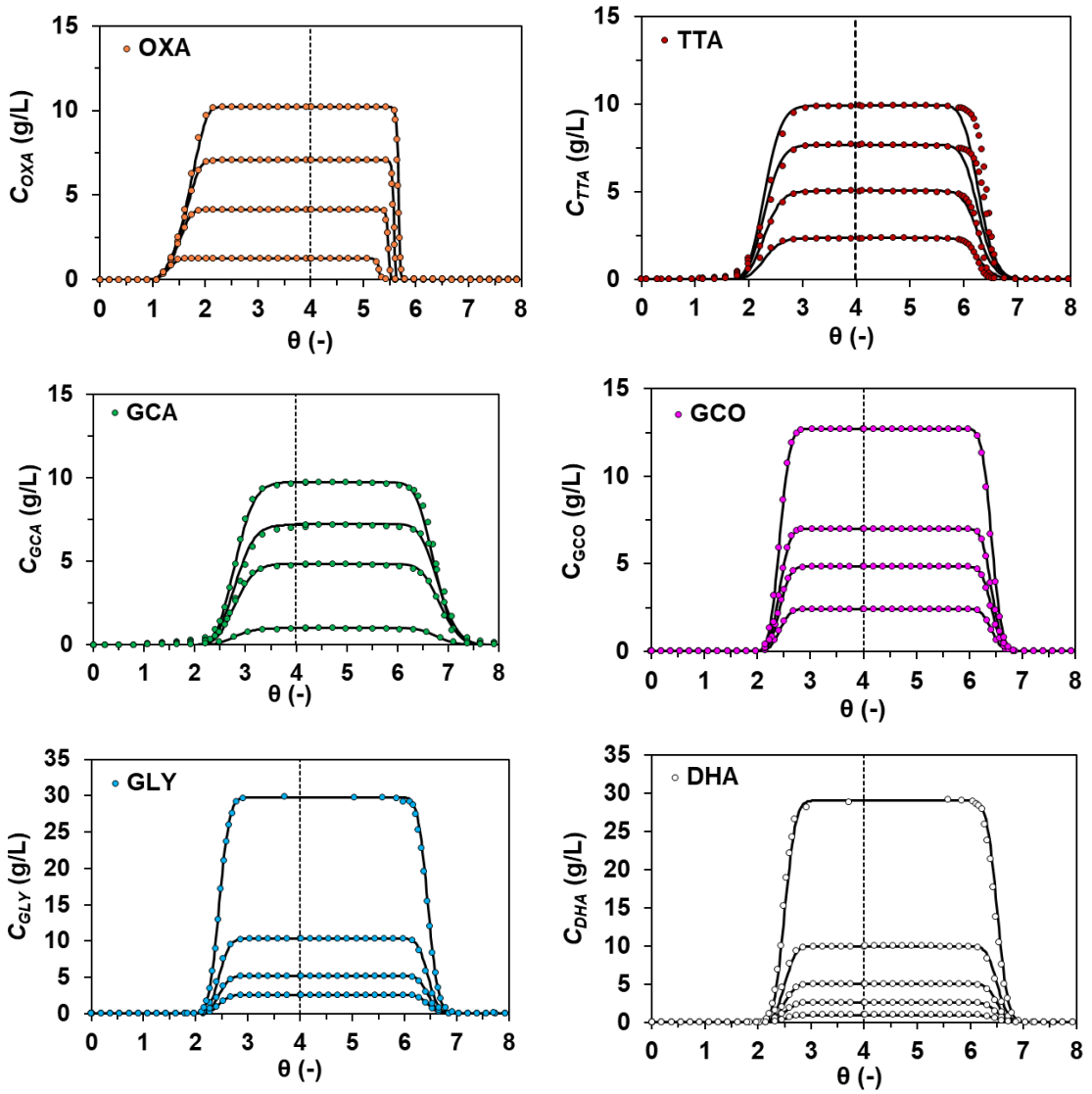

Figure 5.6. Single-component breakthrough experiments in a fixed-bed column packed with Dowex® 50WX-2 in H^+ form at 293 K. Model results (solid lines); desorption step (dashed lines). Feed concentrations (g/L): (a) OXA (orange, 1.1, 4.2, 7.1, 9.8); (b) TTA (red, 2.4, 5.1, 7.3, 9.9); (c) GCA (green, 1.0, 4.9, 7.3, 9.8); (d) GCO (pink, 2.4, 4.8, 7.0, 12.7); GLY (blue, 2.6, 5.2, 10.3, 29.8); DHA (black, 0.9, 2.6, 5.0, 10.0, 29.7).

The same procedure was applied to DHA and GLY using the Ca^{2+} resin at 293 K, with the corresponding experimental and modelled results presented in Figure 5.7. The fixed-bed model accurately described the experimental data across all tested conditions.

For all compounds, similar elution profiles were observed between the adsorption and desorption steps, even at higher concentrations, confirming the linear adsorption behaviour. The only exception was OXA adsorption in the H^+ resin, which the Freundlich model better described. This behaviour was characterised by a dispersive front during adsorption and a compressive front during desorption (see Figure 5.6).

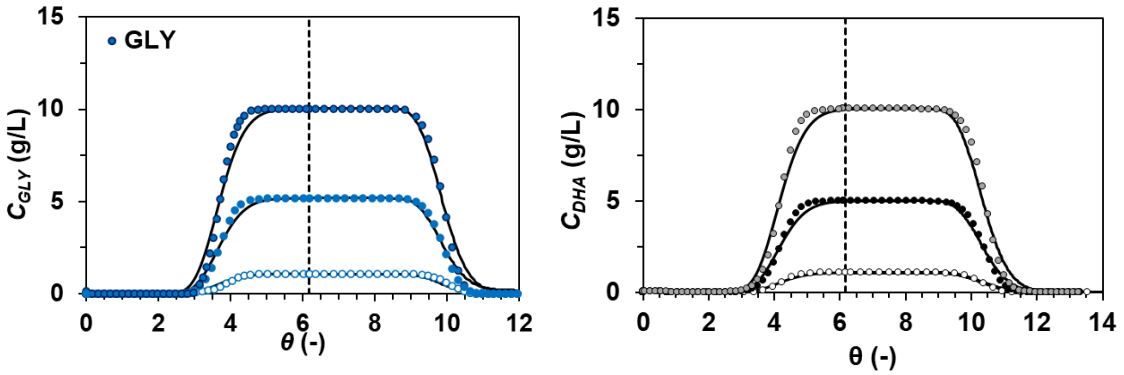

Figure 5.7. Single-component breakthrough experiments in a fixed-bed column packed with Dowex® 50WX-2 in Ca^{2+} form at 293 K. Model results (solid lines); desorption step (dashed lines). Feed concentrations (g/L): a) GLY (blue, 1.1, 5.2, 10.0); DHA (black, 1.1, 5.0, 10.1).

5.4.4. Multi-Component Breakthrough Experiments

Multi-component breakthrough experiments were conducted to assess the model's ability to predict multi-component adsorption behaviour and to identify potential competitive adsorption effects among species. A six-compound solution, matching the composition of the mixture obtained from glycerol oxidation over Pt5-Bi1.5/AC catalysts after 1.5 hours (Chapter 3), was used for the multi-component breakthrough experiment in the column packed with the H^+ resin. The experimental data and the model results are shown in Figure 5.8.

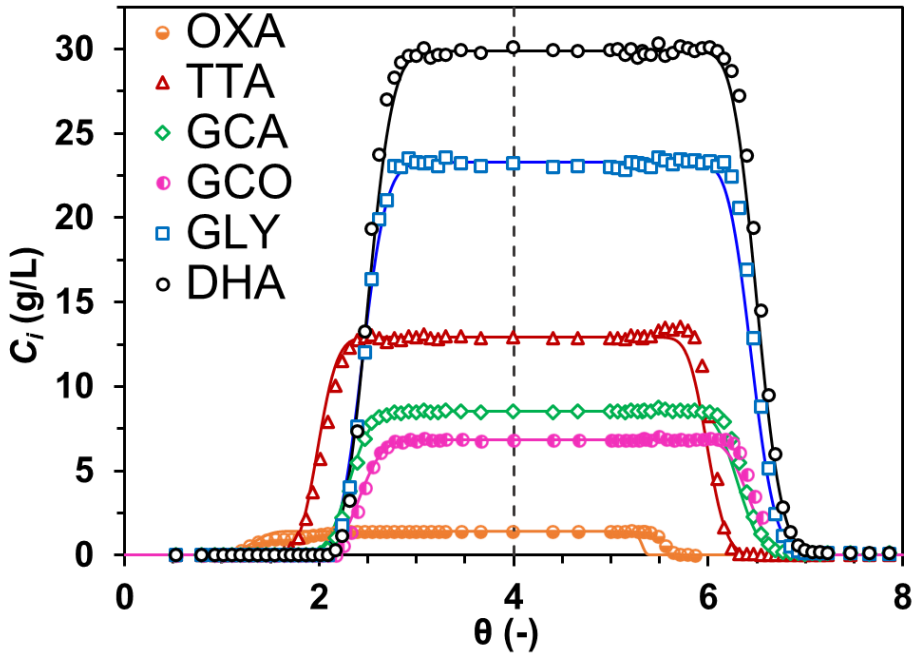

Figure 5.8. Multi-component breakthrough experiment in a fixed-bed column packed with Dowex® 50WX-2 resin in H^+ form at 293 K. Feed composition: OXA (◒, 1.4 g/L), TTA (△, 12.9 g/L), GCA (◇, 8.5 g/L), GCO (◐, 6.8 g/L), GLY (□, 23.3 g/L), DHA (○, 29.9 g/L). Model results (solid lines); desorption step (dashed lines).

As observed in Figure 5.8, the elution times of each compound were consistent with the distribution factors determined from single-component experiments (Table 5.1). During the adsorption step, OXA, the least retained species, was first eluted, followed by TTA and GCA. The most retained compounds (GCO, GLY, and DHA) eluted last, with similar retention times. The absence of significant deviations in elution order or profile suggests that no competitive adsorption effects occurred within the studied concentration range.

To quantify the model's accuracy in predicting multi-component breakthrough behaviour, the correlation coefficient, r^2_{corr}, was computed using equation (5.18), where NC, NE, and NP represent the number of compounds, experiments, and data points.

$$r^2_{corr} = 1 - \frac{\sum_{i=1}^{NC}\sum_{j=1}^{NE}\sum_{k=1}^{NP}\left(C^{exp}_{out,i,j,k} - C^{mod}_{out,i,j,k}\right)^2}{\sum_{i=1}^{NC}\sum_{j=1}^{NE}\sum_{k=1}^{NP}\left(C^{exp}_{out,i,j,k} - \overline{C}^{mod}_{out,i}\right)^2} \tag{5.18}$$

A high r^2_{corr} value of 0.998 was obtained, confirming the model's excellent predictive capability for multi-component breakthrough behaviour.

GLY and DHA binary breakthrough experiments were also performed on a semi-preparative fixed-bed column packed with the resin in Ca^{2+} form. The corresponding experimental and simulated data are presented in Figure 5.9.

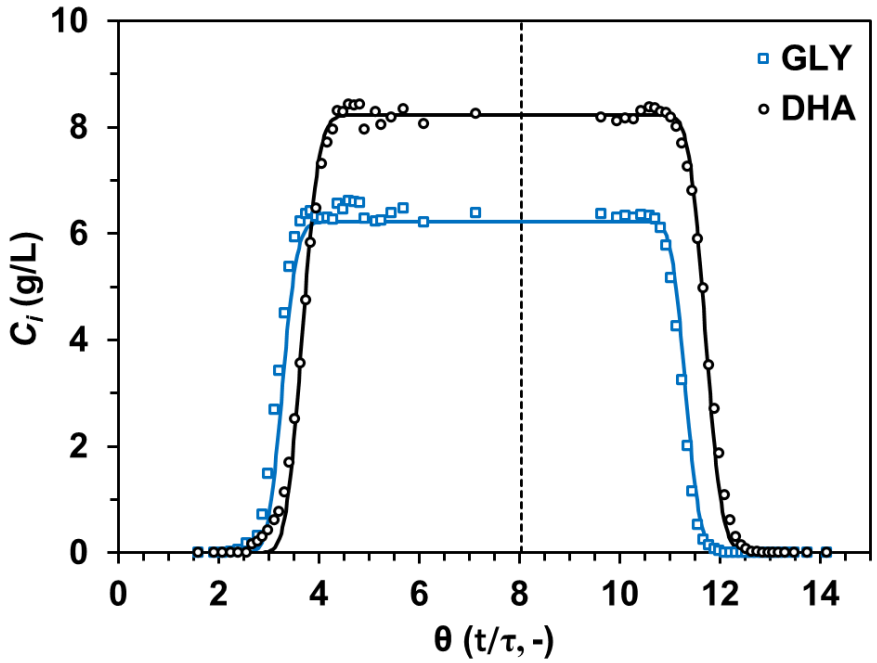

Figure 5.9. Binary breakthrough experiment of GLY and DHA in a fixed-bed column packed with Dowex® 50WX-2 resin (Ca^{2+} form) at 293 K. Feed composition: GLY (□, 6.2 g/L), DHA (○, 8.2 g/L). Model results (solid lines); desorption step (dashed lines).

The binary mixture breakthrough experiments (Figure 5.9) confirmed that GLY and DHA elution times were consistent with the single-component adsorption data. The least retained

compound, GLY, eluted first, while DHA, the most retained species, was the last to elute. Again, no significant interactions between GLY and DHA were observed that would affect resin selectivity. The fixed-bed column model demonstrated strong agreement with the experimental results, with an r_{corr}^2 value of 0.989.

5.5. Conclusions

The adsorption equilibrium and breakthrough behaviour of key compounds on Dowex® 50WX-2 resin in both H^+ and Ca^{2+} forms at 293 K were investigated.

The adsorption equilibrium data for the resin in the H^+ form were well described by the linear isotherm model, with adsorption strength increasing in the order TTA < GCA < GCO < GLY < DHA. Single-component breakthrough experiments confirmed that the adsorption and desorption profiles followed a linear trend for all compounds except for OXA, which exhibited a dispersive front during adsorption and a compressive front during desorption, consistent with the Freundlich model.

In the Ca^{2+} resin, DHA and GLY adsorption equilibrium data were also well-fitted by the linear isotherm, with DHA again being the most retained compound. The retention factors were higher in the Ca^{2+} resin compared to the H^+ resin, and the separation selectivity of DHA from GLY increased from 1.04 in the H^+ resin to 1.28 in the Ca^{2+} resin.

Multi-component breakthrough experiments demonstrated that species eluted in the expected order based on their distribution factors, with OXA eluting first and DHA eluting last. The absence of significant competitive adsorption effects suggests that the resin's selectivity for each compound remains consistent in the concentration range studied. These results confirm the reliability of the fixed-bed column model in describing the adsorption process.

These findings will allow the design of a simulated moving bed separation process for DHA purification from glycerol oxidation products in Chapter 6.

5.6. Notation

Variables

C_i	Concentration of compound i in the liquid phase (g/L)
$C_{i,out}$ (C_{Feed})	Concentration of compound i in the liquid phase (in the feed) / at the column outlet (g/L)
D_c	Fixed-bed column diameter (dm)
$D_{e,i}$	Effective diffusion coefficient ($dm^2\ min^{-1}$)

D_i^{∞}	Molecular diffusion coefficient of compound i at infinite dilution ($dm^2\ min^{-1}$)
D_{ax}	Axial dispersion coefficient ($dm^2\ min^{-1}$) ($D_{ax} = \frac{uL}{Pe}$)
$E(t)$	Residence time distribution (min^{-1})
K_i	Distribuition coefficient ($L_{liquid}\ L_{solid}^{-1}$)
$k_{h,i}$	Homogeneous mass transfer coefficient of compound i (min^{-1})
L	Fixed-bed column length (dm)
M	Molar mass of the solvent ($g\ mol^{-1}$)
n	Freundlich isotherm parameter (-)
Pe	Péclet number (-)
Q	Liquid flow rate in the column ($dm^3\ min^{-1}$)
$\bar{q}_i$	Average concentration of species i adsorbed in the adsorbent ($g_i\ L_{solid}^{-1}$)
q_i^*	Adsorbed concentration of species i in equilibrium with C ($g_i\ L_{solid}^{-1}$)
r_{corr}^2	Correlation coefficient
R_p	Average particle radius (dm)
T	Temperature (K)
$\bar{t}_r$	Mean residence time (min)
u	Liquid interstitial velocity ($dm\ min^{-1}$)
$V_{i,nbp}$	Molar volume of species i at normal boiling point ($cm^3\ mol^{-1}$)
Vc	Column volume (cm^3)
wt.%	Mass fraction (%)
z	Axial position (-)

Greek Letters and Subscript

i	Species i: glycerol (GLY), dihydroxyacetone (DHA), glycolic acid (GCO), glyceric acid (GCA), tartronic acid (TTA), and oxalic acid (OXA)
ε	Column bed porosity (-)
ε_p	Particle porosity (-)
η	Dynamic viscosity of the solvent (cP)
σ^2	Residence time distribution variance (min^2)
τ	Space-time (min)
τ_p	Particle tortuosity (-)
ψ	Solvent association factor (Wilke and Chang correlation) (-)

Abbreviations

PS-DVB	Polystyrene-divinylbenzene (resin)
HPLC	High-Performance Liquid Chromatography
LDF	Linear Driving Force
SMB	Simulated Moving Bed

5.7. References

1. *Opinion on Dihydroxyacetone (DHA) CAS N° 96-26-4*. 03-04 March 2020, Scientific Committee on Consumer Safety.
2. Chen, Q. and Chen, J., *Review of the separation and purification of 1, 3-dihydroxyacetone.* Anhui Med Pharm J, 2013. **17**: p. 1271-1273.
3. Fakley, M.E. and Lindsay, R.J. Process for the isolation of dihydroxyacetone. EP0245976A1, 1987.
4. Charney, W. Process for the production of dihydroxyacetone. US4076589A, 1978.
5. Cheng, K.K., Zhao, X.B., Zeng, J., Wu, R.C., Xu, Y.Z., Liu, D.H., and Zhang, J.A., *Downstream processing of biotechnological produced succinic acid.* Appl Microbiol Biotechnol, 2012. **95**(4): p. 841-50.
6. Lari, G.M., Mondelli, C., Papadokonstantakis, S., Morales, M., Hungerbühler, K., and Pérez-Ramírez, J., *Environmental and economic assessment of glycerol oxidation to dihydroxyacetone over technical iron zeolite catalysts.* Reaction Chemistry & Engineering, 2016. **1**(1): p. 106-118.
7. Sharma, D., *Simulated Moving Bed Technology: Overview and Use in Biorefineries.* Biorefineries-Selected Processes, 2021.
8. Rodrigues, A.E., Pereira, C.S.M., Minceva, M., Pais, L.S., Ribeiro, A.M., Ribeiro, A.E., Silva, M., Graça, N.S., and Santos, J.C., *Simulated moving bed technology: principles, design and process applications*. 1st Edition ed. 2015, Amsterdam: Butterworth-Heinemann. 304.
9. Binder, T., *Simulated moving bed chromatographic purification of amino acids.* Archer-Daniels-Midland Company, 2008: p. 18.
10. Kelliher, A., Morrison, A., Oroskar, A., Rema, R.V.N., and Agarwal, A. Simulated moving bed chromatographic separation process. US9790162B2, 2017.
11. Kelliher, A., Morrison, A., Oroskar, A., Rema, R.V.N., and Agarwal, A. SMB process for producing highly pure EPA from fish oil. US9695382B2, 2017.
12. Koop, E.P., Schwarz, M.J., and Desjonqueres, S. Method of treatment using peroxidized lipids. US6395779B1, 2002.
13. Kelliher, A., Morrison, A., Oroskar, A., Rema, R.V.N., and Agarwal, A. SMB process. US9370730B2, 2016.
14. Xie, Y.-l., Chen, P., Hou, Z.-y., and Zheng, X.-m., *Separation of dihydroxyacetone from partial oxidation product of glycerol by ion exchange resin.* Journal of Zhejiang University, Science Edition, 2007. **34**(1): p. 73.
15. Pedruzzi, I., da Silva, E.A.B., and Rodrigues, A.E., *Selection of resins, equilibrium and sorption kinetics of lactobionic acid, fructose, lactose and sorbitol.* Separation and Purification Technology, 2008. **63**(3): p. 600-611.
16. Walser, P., *New ion-exclusion phase for organic acids.* Journal of Chromatography A, 1988. **439**(1): p. 71-81.
17. Accorsi, C.A. and Blo, G., *Determination of volatile and non-volatile organic acids in technical sugar solutions by ion-exclusion chromatography.* Journal of Chromatography A, 1991. **555**(1): p. 65-71.
18. Shirao, M., Furuta, R., Suzuki, S., Nakazawa, H., Fujita, S., and Maruyama, T., *Determination of organic acids in urine by capillary zone electrophoresis.* Journal of Chromatography A, 1994. **680**(1): p. 247-251.
19. Li, S. and Fritz, J.S., *Organic modifiers for the separation of organic acids and bases by liquid chromatography.* Journal of Chromatography A, 2002. **964**(1): p. 91-98.
20. Nesterenko, P.N., Kebets, P.A., and Volgin, Y.V., *Use of Sulfonated Cation-Exchange Resin Based on Hypercrosslinked Polystyrene for the Separation of Organic Acids.* Journal of Analytical Chemistry, 2001. **56**(8): p. 715-720.

21. Takamatsu, Y., Yamamoto, M., and Sato, Y. Method of purifying amino acid. WO2005097734A1, 2005.

22. Wheaton, R. and Lefevre, L., *Dowex Ion exchange resins: Fundamentals of Ion Exchange.* Dow Liquid Separations, 2000.

23. *DuPont Resins for Downstream Drug Purification* D.W. Solutions, Editor. July 2022, DuPont Water Solutions.

24. Coelho, L.C.D., Filho, N.M.L., Faria, R.P.V., Ribeiro, A.M., and Rodrigues, A.E., *Selection of a stationary phase for the chromatographic separation of organic acids obtained from bioglycerol oxidation.* Adsorption, 2017. **23**(5): p. 627-638.

25. Coelho, L.C.D., Filho, N.M.L., Faria, R.P.V., Ferreira, A.F.P., Ribeiro, A.M., and Rodrigues, A.E., *Separation of tartronic and glyceric acids by simulated moving bed chromatography.* Journal of Chromatography A, 2018. **1563**: p. 62-70.

26. Seidel-Morgenstern, A., *Experimental determination of single solute and competitive adsorption isotherms.* Journal of Chromatography A, 2004. **1037**(1): p. 255-272.

27. Rios, A.G., Ribeiro, A.M., Rodrigues, A.E., and Ferreira, A.F., *Bovine serum albumin and myoglobin separation by size exclusion SMB.* Journal of Chromatography A, 2020. **1628**: p. 461431.

28. Xu, Z., Cai, J.-g., and Pan, B.-c., *Mathematically modeling fixed-bed adsorption in aqueous systems.* Journal of Zhejiang University SCIENCE A, 2013. **14**(3): p. 155-176.

29. Ruthven, D.M., *Principles of adsorption and adsorption processes*. 1984: John Wiley & Sons.

30. Glueckauf, E., *Theory of chromatography. Part 10.—Formulæ for diffusion into spheres and their application to chromatography.* Transactions of the Faraday Society, 1955. **51**: p. 1540-1551.

31. Zelic, B. and Nesek, B., *Mathematical modeling of size exclusion chromatography.* Engineering in Life Sciences, 2006. **6**(2): p. 163-169.

32. Rodrigues, A.E., *Residence time distribution (RTD) revisited.* Chemical engineering science, 2021. **230**: p. 116188.

33. Rodrigues, A., Calo, J., and Sweed, N., *Multiphase Chemical Reactors Volume I–Fundamentals.* Nato Advanced Study Institutes Series, Sijthoff & Noordhoff, Alphen aan den Rijn, The Netherlands/Rockville, Md, USA, 1981.

34. Guiochon, G., Felinger, A., and Shirazi, D.G., *Fundamentals of preparative and nonlinear chromatography*. 2006: Academic Press.

35. Wilke, C. and Chang, P., *Correlation of diffusion coefficients in dilute solutions.* AIChE Journal, 1955. **1**(2): p. 264-270.

36. Poling, B.E., Prausnitz, J.M., and O'Connell, J.P., *The properties of gases and liquids*. Vol. 5. 2001, New York: Mcgraw-hill New York. 768.

37. Yaws, C.L., *Yaws' Critical Property Data for Chemical Engineers and Chemists*. 2012, Knovel.

38. Mackie, J. and Meares, P., *The diffusion of electrolytes in a cation-exchange resin membrane I. Theoretical.* Proceedings of the Royal Society of London. Series A. Mathematical and Physical Sciences, 1955. **232**(1191): p. 498-509.

39. Tejero, M., Ramírez, E., Fité, C., Tejero, J., and Cunill, F., *Esterification of levulinic acid with butanol over ion exchange resins.* Applied Catalysis A: General, 2016. **517**: p. 56-66.

40. Ghim, Y.S. and Chang, H.N., *Adsorption characteristics of glucose and fructose in ion-exchange resin columns.* Industrial & Engineering Chemistry Fundamentals, 1982. **21**(4): p. 369-374.

6. Simulated Moving Bed Separation

This chapter presents the separation of dihydroxyacetone from glycerol oxidation products using simulated moving bed (SMB) technology. The separation process consisted of a cascade of two SMB units designed and optimised using an SMB model implemented in the gPROMS ModelBuilder software. The process was experimentally validated on the lab-scale FlexSMB-LSRE® unit.

This Chapter was adapted from Walgode, P. M., Faria, R. P., & Rodrigues, A. E. (2023). Pseudo-ternary chromatographic separation of dihydroxyacetone from the glycerol oxidation byproducts on a simulated moving bed cascade. Chemical Engineering Journal, 476, 146447. DOI https://doi.org/10.1016/j.cej.2023.146447

6.1. Introduction

Glycerol (GLY) catalytic oxidation produces a complex mixture of compounds, as catalysts are not fully selective towards dihydroxyacetone (DHA). In Chapter 3, commercial catalysts were tested, and at maximum DHA yield, DHA selectivity was ≈ 40%. Given the high purity requirements for DHA in commercial applications, particularly in cosmetics (>97%), efficient purification is essential. In Chapter 5, adsorption data of glycerol oxidation products using Dowex® 50WX-2, a polystyrene-divinylbenzene ion exchange resin, in both acid and calcium forms were obtained, demonstrating the potential of adsorption-based processes for DHA separation from glycerol oxidation. Linear isotherms described the species adsorption in both resins at 293 K, except for oxalic acid (OXA), with DHA being the most retained species. A fixed-bed column model accurately described single and multicomponent breakthroughs, and the latter ruled out competitive adsorption effects.

This chapter extends the batch study to continuous countercurrent chromatographic processes, represented by the True Moving Bed (TMB), where both solid and liquid phases continuously flow countercurrently, maximising the adsorption driving force. This method offers higher productivity levels, more concentrated product streams than batch techniques, lower mobile phase consumption compared with elution chromatography, and performs separations with low selectivity [1-4]. However, practical limitations such as adsorbent abrasion and equipment constraints make TMB operation unfeasible. Those limitations are overcome using the Simulated Moving Bed (SMB) technology, where the countercurrent movement of the solid phase is simulated by periodically shifting inlet and outlet ports in the liquid flow direction. The time interval for this periodic shifting is called the switching time, t^*, defined as $t^* = {}^{L}/_{u_s}$, where L is the column length and u_s is the solid velocity. When the streams return to their initial position, the SMB completes one operating cycle [1].

SMB technology was first patented as the Sorbex process and has been employed in large-scale separations in the petrochemical and sugar industries since the 1960s. In the 1990s, it was adapted for chiral separations, eventually expanding into pharmaceuticals and biomolecule purification. Today, SMB is a well-established technology implemented by numerous companies with various designs, operation modes, and several modelling and optimisation tools have been developed. Detailed information may be found elsewhere [1-4]. The TMB and SMB units are represented in Figure 6.1.

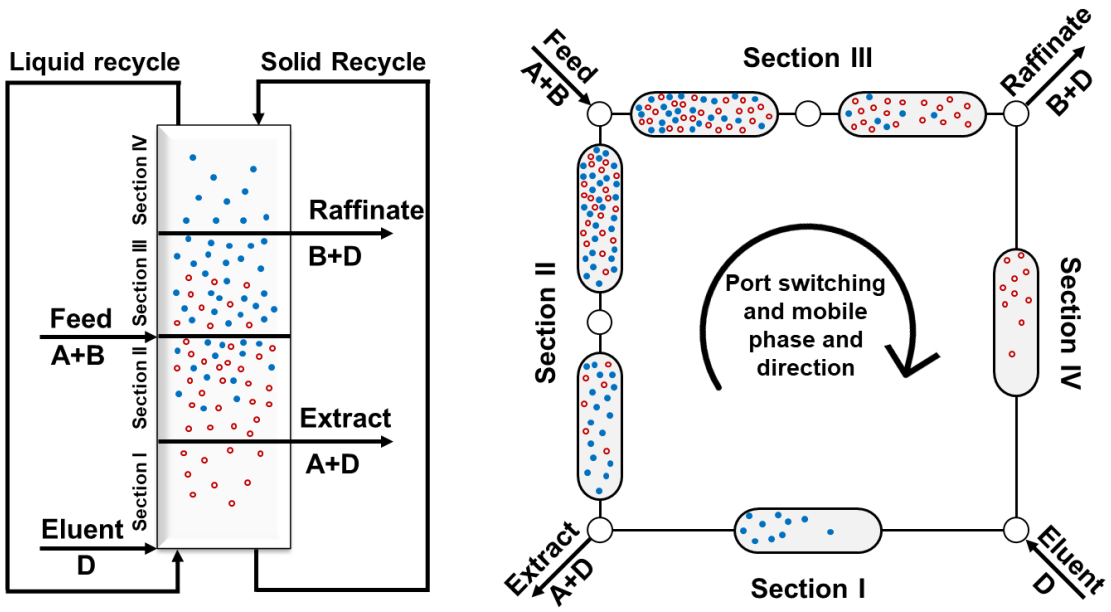

Figure 6.1. TMB and equivalent SMB with six columns in the 1-2-2-1 configuration.

A conventional SMB unit consists of two inlet streams, feed and eluent, and two outlet streams, extract and raffinate, dividing the unit into four sections (see Figure 6.1 left). The feed stream enters between sections II and III, where less adsorbed compounds move with the liquid phase to be collected in the raffinate, while more adsorbed compounds move with the solid and are collected in the extract. Sections I and IV are, respectively, for solid and liquid regeneration before being recycled. In section I, the compounds should move forward with the liquid to be collected in the extract port, while in section IV, they should move backwards with the solid to be collected in the raffinate port. This is achieved by carefully defining the operation flow rates in each section, which are defined by the separation and regeneration regions. These can be determined through methods such as the efficient and straightforward equilibrium theory, the standing wave analysis, or simulation-based search algorithms [5].

Chromatography has proven effective for separating structurally similar compounds [1, 6-11], including industrial-scale simulated moving bed (SMB) processes for sugars, amino acids, and organic acids using ion-exchange resins as the stationary phase [12-14], making it a promising method for DHA purification. Dowex® 50WX-2 in acid form has previously demonstrated success in SMB applications, including the separation of glyceric acid (GCA) from tartronic acid (TTA) using the FlexSMB-LSRE® unit (FlexSMB) [15]. The FlexSMB unit has been employed in chiral [2, 16-20], organic acids [15], and proteins [21-23] separation, but it has never been tested for multiple compound separation.

Several approaches to multicomponent SMB separations exist, including pseudo-SMB units (Japan Organo process) [24], SMB units with five to eight sections [25-29], and SMB cascades

[30-34]. A two-unit SMB cascade was successfully used for separating salts, sucrose, and betaine from sugar crystallisation molasses using strong cation-exchange gel-type resins [32].

A pseudo-binary SMB separation of DHA from GLY and the organic acids (OXA, glycolic acid (GCO), TTA, GCA) over the resin in acid form was initially considered, but DHA-GLY low separation selectivity ($\alpha_{DHA/GLY,}$ = 1.04) may be challenging in a real SMB unit. In contrast, this separation is more easily performed on the Ca^{2+} resin ($\alpha_{DHA/GLY}$ = 1.28). So, a two-step cascade SMB system was designed to separate DHA from GLY oxidation products, schematically represented in Figure 6.2. DHA will be separated from the organic acids ($\alpha_{DHA/GCO}$ = 1.06) on the first SMB unit packed with the resin in acid form, neglecting the extract stream contamination with GLY. This stream will be fed to a second SMB unit packed with the resin in calcium form, separating DHA from GLY. DHA will be collected in the extract stream, and GLY will be collected in the raffinate stream. This approach enables DHA recovery with high purity, while unreacted GLY can be recycled back to the oxidation reactor for further conversion into DHA.

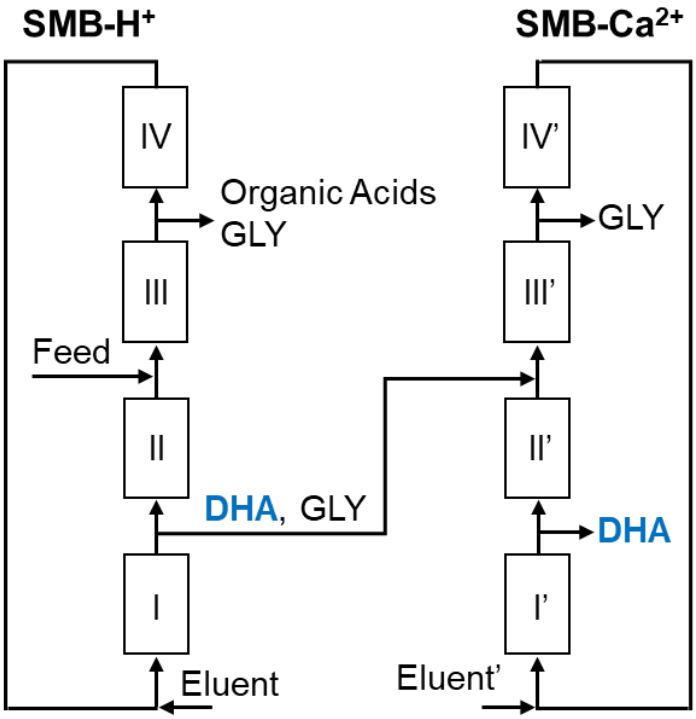

Figure 6.2. Schematic diagram of the proposed SMB cascade for DHA separation from glycerol oxidation products. The first ring (left) is an SMB packed with resin in acid form, while the second unit (right) is packed with resin in calcium form.

In this chapter, the SMB separation process is first modelled in the gPROMS ModelBuilder software based on the TMB concept. Then, the model is extended for the FlexSMB unit and validated experimentally using the FlexSMB unit for the continuous purification of DHA from glycerol and its oxidation products.

6.2. Experimental Description

6.2.1. Chemicals and Materials

In this work, oxalic acid (OXA, ≥ 99.5%, ACROS Organics), tartronic acid (TTA, ≥ 97%, Sigma-Aldrich), DL-glyceric acid (GCA, 20% in water, ca. 2 mol L^{-1}, Tokyo Chemical Industry Co., Ltd.), glycolic acid (GCO, ≥ 99%, Fisher Scientific), glycerol (GLY, ≥ 99.5%, Fisher Scientific), and dihydroxyacetone (DHA, ≥ 98%, Merck), were used to study the species to be separated. Sulfuric acid (H_2SO_4, > 95%, Fisher Scientific) was used for the preparation of the mobile phase, and calcium chloride dihydrate ($CaCl_2 \cdot 2H_2O$, > 99.5%, HiMedia) for the ion exchange step. Deionised water was provided by our laboratory purification systems.

The commercial Dowex® 50WX-2 resin in H^+ form (2% cross-linking, mesh size 200/400, ACROS Organics) was used as the stationary phase for chromatographic separation. When hydrated in water, the resin has an average particle size of 148.0 μm ± 54.28 μm, a porosity ε_p of 0.74, and a tortuosity τ_p of 1.7. After ion exchange to the Ca^{2+} form, the resin's particle size was 112.4 μm ± 21.18 μm, ε_p of 0.41, and τ_p of 3.9. Further details on resin characterisation are available in Chapter 5.

6.2.2. HPLC Analytical Method

The feed solution and the samples collected from the SMB operation (extract and raffinate outlet samples and the internal concentration profile samples) were analysed using a Shimadzu Prominence HPLC system equipped with an Alltech Organic Acid OA-1000 analytical column (7.8 × 300 mm, Hichrom, UK) maintained at 333 K. The analytical method was detailed in Chapter 3.

6.2.3. FlexSMB Setup and Operation

Continuous chromatographic separations were conducted in the FlexSMB-LSRE® (Figure 6.3) unit with six stainless steel columns (20 mm ID × 100 mm length) in a 1-2-2-1 conventional configuration (number of columns per SMB zone). A detailed description is available in Gomes et al. (2010) [16].

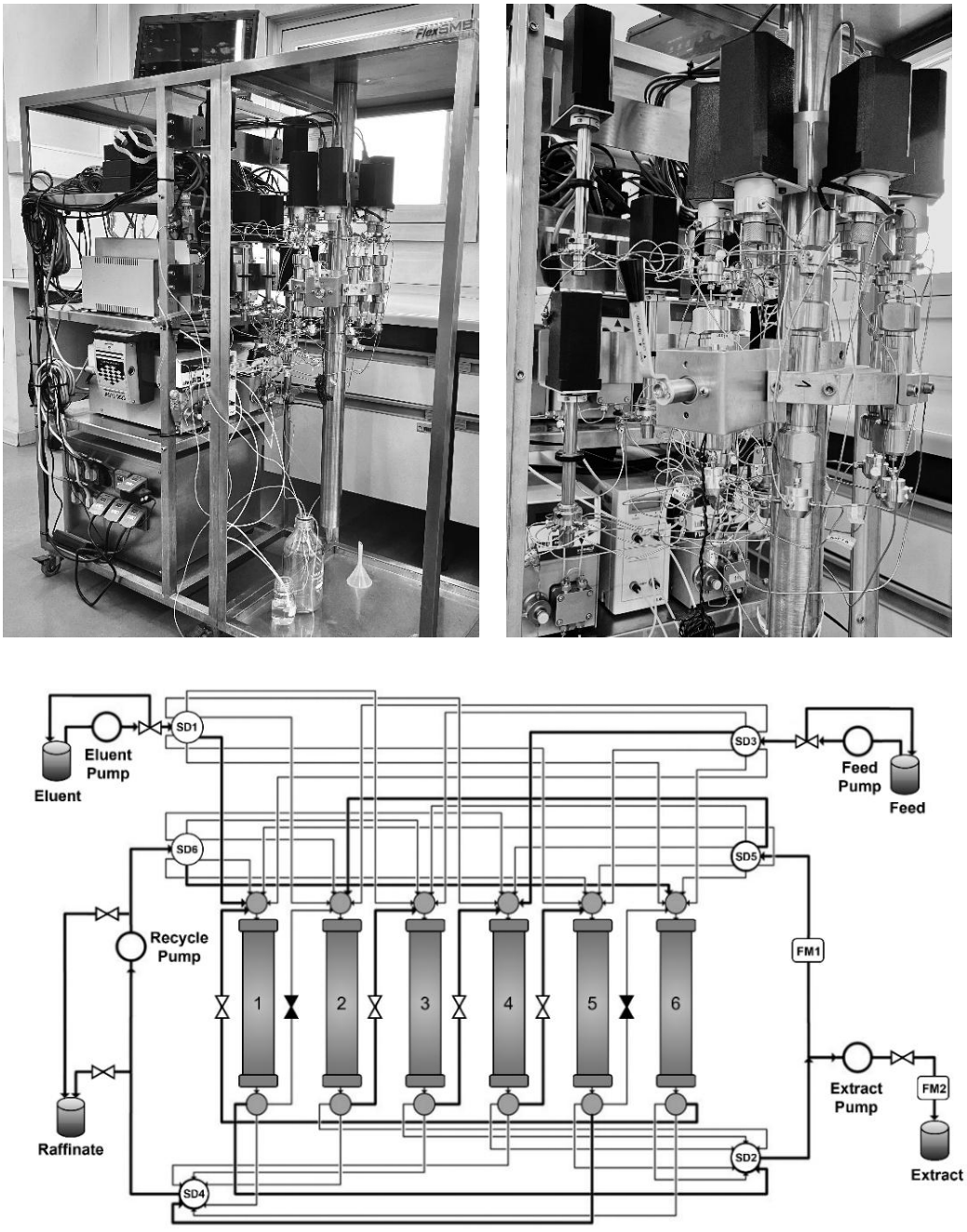

Figure 6.3. FlexSMB-LSRE® unit and a schematic representation adapted from [16].

The FlexSMB is a lab-scale SMB unit capable of operating with up to 12 columns, supporting conventional and non-conventional operation modes, including asynchronous switching (Varicol). A LabVIEW interface (National Instruments, USA) was implemented to simplify the

operation. The unit has four HPLC pumps (VWR International, USA) with 50 ml heads for the eluent, extract, and recycle pumps and 10 ml for the feed pump. Relief valves are installed after each pump to prevent over-pressurisation during valve switching. A purge valve on the raffinate line allows for the system pressure to be regulated. Despite efforts to minimise dead volume, it remained at about 12% of the six-column volume [16].

To initiate SMB operation, the feed and eluent pumps were purged using their respective solutions, and inlet flow rates were measured at the end of every SMB cycle ($6t^*$). Raffinate and extract outlet streams were separately collected during a complete SMB cycle, weighted, and analysed by HPLC. Mass balance was verified by comparing inlet and outlet flow rates. The recycling flow rate was measured using a Coriolis flowmeter placed in SMB section II.

Cyclic steady-state (CSS) conditions were assumed when the species' concentrations in the extract and raffinate streams varied by less than 5% over six consecutive cycles. At this point, internal concentration profiles were obtained by collecting samples at 25%, 50%, and 75% of the switching time using a 0.5 ml loop installed in a 6-port valve between columns 6 and 1, except during switching times 2 and 6 where they were collected in the raffinate and extract port (following the procedure described in the unit's manual of operation).

A two-step SMB separation process was designed to process a feed solution with a composition similar to that obtained from the aerobic oxidation of 1 M glycerol over a Pt5-Bi1.5/AC catalyst (Johnson Matthey) for 1.5 h in a semi-batch reactor (Chapter 3). The solution composition was 1.2 g_{OXA} L^{-1}, 12.9 g_{TTA} L^{-1}, 8.2 g_{GCA} L^{-1}, 6.9 g_{GCO} L^{-1}, 22.0 g_{GLY} L^{-1}, and 29.8 g_{DHA} L^{-1}.

Only one SMB unit was available, so the two experimental separations were conducted sequentially. First, the SMB columns were packed with the resin in acid form (SMB-H) for the pseudo-binary separation of DHA from the organic acids. Then, the columns were repacked with the resin in calcium form (SMB-Ca) for the binary separation of DHA from GLY, using a solution prepared based on the extract from the first SMB. The laboratory, feed, and eluent solutions were maintained at 293 K, at which adsorption isotherms were determined.

6.3. SMB Modelling

6.3.1. Mathematical Model

The phenomenological model developed in Chapter 5 for a single fixed-bed column was extended to describe the columns of the SMB unit. The model was implemented in the gPROMS model builder V7.0.7 (Siemens Process Systems Enterprise, UK), a software designed for chemical engineering process modelling and optimisation, executing both steady-state and dynamic simulations. The orthogonal collocation in finite elements method (OCFEM) was used for the axial discretisation, with 40 finite elements per column and two interior collocation points. To solve the system of ordinary differential and algebraic equations that resulted from the discretisation process, the DAEBDF solver was utilised with a relative error of 10^{-5}.

The model incorporated the following assumptions, considered appropriate for these systems [1, 15, 21, 35, 36]: i) axially dispersed plug flow model to describe the fluid flow, ii) the mass transfer between the liquid and the solid was described by the linear driving force (LDF) model proposed by Glueckauf [36, 37], iii) isothermal operation, iv) homogeneous spherical particles with uniform size, v) constant fluid velocity, bed porosity and bed length and vi) no radial gradients in the bed.

The transient mass balance to the fluid phase may be given by:

$$\frac{\partial C_{i,j}}{\partial t} = \frac{D_{ax,j}}{L_j^2}\frac{\partial^2 C_{i,j}}{\partial z^2} - \frac{1-\varepsilon}{\varepsilon}k_{h,i}\left(q_{i,j}^{*} - \bar{q}_{i,j}\right) - \frac{u_j}{L_j}\frac{\partial C_{i,j}}{\partial z} \tag{6.1}$$

where the subscript i refers to the species in the mixture, the subscript j refers to the column number, C is the concentration in the (bulk) liquid phase, $\bar{q}$ is the average adsorbed-phase concentration, q^* is the adsorbed-phase concentration in equilibrium with C, u is the liquid interstitial velocity, z is the normalised axial position, L is the column length, ε is the bed column porosity, D_{ax} is the axial dispersion coefficient, $D_{ax} = \frac{uL}{Pe}$, and k_h the homogeneous mass transfer coefficient.

The transient mass balance to the solid phase is described by the LDF model,

$$\frac{\partial \bar{q}_{i,j}}{\partial t} = k_{h,i}\left(q_{i,j}^{*} - \bar{q}_{i,j}\right) \tag{6.2}$$

The initial conditions are:

$$t = 0 \qquad C_{i,j} = C_{i,j|0} \text{ and } \bar{q}_{i,j} = \bar{q}_{i,j|0} \tag{6.3}$$

The columns were fully equilibrated with the eluent before starting the experiments, thus $C_{ij|0} = \bar{q}_{ij|0} = 0$. The boundary conditions considered for each column are:

$$z = 0 \qquad u_j C_{ij}^{in} = u_j C_{ij} - \frac{D_{ax,j}}{L_j} \frac{\partial C_{ij}}{\partial z}\Big|_{z=0} \tag{6.4}$$

$$z = 1 \qquad \frac{\partial C_{ij}}{\partial z}\Big|_{z=1} = 0 \tag{6.5}$$

The mass balance equations at the inlet and outlet stream nodes were defined by Equations (6.6) to (6.9) and the global mass balances by Equations (6.10) to (6.14). The subscripts I, II, III, and IV refer to the SMB section, not the column number. Q_E, Q_F to the flow rate of the inlet streams eluent and feed, and Q_X, Q_R to the flow rate of the outlet streams extract and raffinate, respectively. The recycling flow rate, Q_{Rec}, is equal to Q_{IV}. For the nodes between columns in the same SMB section, $C_{i,m-1}^{out} = C_{i,m}^{in}$ and $Q_{m-1} = Q_m$, where m refers to the column number (1 to 6).

- Mass balances at nodes:

Eluent node $$u_{IV} C_{i,IV}^{out} = u_I C_{i,I}^{in} \tag{6.6}$$

Extract node $$C_{i,I}^{out} = C_{i,II}^{in} = C_{i,X} \tag{6.7}$$

Feed node $$u_{III} C_{i,III}^{in} = u_{II} C_{i,II}^{out} + u_F C_{i,F} \tag{6.8}$$

Raffinate node $$C_{i,III}^{out} = C_{i,IV}^{in} = C_{i,R} \tag{6.9}$$

- Global Mass Balances:

Eluent node $$Q_I = Q_{IV} + Q_E \tag{6.10}$$

Extract node $$Q_{II} = Q_I - Q_X \tag{6.11}$$

Feed node $$Q_{III} = Q_{II} + Q_F \tag{6.12}$$

Raffinate node $$Q_{IV} = Q_{III} - Q_R \tag{6.13}$$

SMB $$Q_E + Q_F = Q_E + Q_R \tag{6.14}$$

While the model above describes an ideal SMB unit with zero dead volume, real SMB systems like FlexSMB require adjustments to account for instrumental non-idealities, including the dead volumes introduced by various components such as tubes, equipment, column filters (frits), manifolds, which represent 12% of the system volume, and switching time delays (switch asymmetries), as well as other relevant instrumental aspects [16]. Dead volumes were modelled as additional piping segments following the plug flow assumption, while switching time delays, which represent 0.5% of the switching time, were explicitly included in the SMB model [16].

Although the model above was considered, it is worth mentioning that the group validated a simplified approach to design the SMB separation region by applying a switching time correction to the zero-dead-volume SMB model. The "zero dead volume with t^* correction" and the "FlexSMB" separation regions overlapped, so the switching time correction method could be used with confidence for SMB process design [16].

6.3.2. Model Parameters

The model parameters were consistent with those in Chapter 5, where a detailed description is available. Tracer experiments were performed by injecting Blue Dextran 2000 pulses into each fixed-bed column to characterise bed porosity and Peclet number.

Linear adsorption isotherms $q_i^* = K_i C_i^{1/n_i}$ with $n_i = 1$, were used for all species except OXA on the H^+ resin, which followed a Freundlich isotherm ($n_i \neq 1$). The mass transfer coefficient, $k_{h,i}$, were computed using the equation proposed by Glueckauf [37], and the diffusion coefficients at infinite dilution, D_i^{∞} ($cm^2\ s^{-1}$) were computed by the Wilke Chang correlation [38]. A summary of the model parameters for both resins is available in Table 5.1 in Chapter 5.

6.3.3. SMB Separation Region

To design the separation and regeneration regions, it is convenient to define the ratio of liquid to solid flow rate in each TMB section j, γ_j, [16]:

$$\gamma_j = \left(\frac{1-\varepsilon}{\varepsilon}\right)\frac{Q_j}{Q_s} \tag{6.15}$$

The equivalence of the TMB and SMB models is given by $\gamma_j^* = \gamma_j + 1$, where the superscript * refers to the SMB. To ensure proper SMB operation, the following conditions must be satisfied $\gamma_I^* > \gamma_{III}^* > \gamma_{II}^* > \gamma_{IV}^*$.

The simple equilibrium theory was used as an initial guess for the FlexSMB operation point. This method defines the complete separation and regeneration regions for a binary mixture, assuming negligible mass transfer resistances and instantaneous adsorption equilibrium [1]. For linear adsorption isotherms, the following constraints were defined (for other isotherms, please replace K_i' by $\left(\frac{1-\varepsilon}{\varepsilon}\right)\frac{q_{i,j}}{C_{i,j}}$):

$$\gamma_I \geq K'_{heaviest} \tag{6.16}$$

$$\gamma_{II} \geq K'_{light\ key} \tag{6.17}$$

$$\gamma_{III} \leq K'_{heavy\ key} \tag{6.18}$$

$$\gamma_{IV} \leq K'_{lightest} \tag{6.19}$$

A pseudo-binary separation was performed on the SMB-H; thus, for the regeneration region, $K'_{heaviest} = K'_{DHA}$ and $K'_{lightest} = K'_{OXA}$, while for the separation region $K'_{heavy\ key} = K'_{DHA}$ and $K'_{light\ key} = K'_{GCO}$. For the GLY-DHA binary separation on the SMB-Ca, $K'_{heaviest} = K'_{heavy\ key} = K'_{DHA}$ and $K'_{lightest} = K'_{light\ key} = K'_{GLY}$.

The regeneration regions of the FlexSMB were defined by applying a safety factor of 15% to the respective $\gamma^*_{j,EQ}$, to account for mass transfer limitations and the influence of the unit's dead volumes on the proper regeneration of the liquid and solid phases. It is also convenient to define the relationship between Q^*_j and γ^*_j.

$$Q^*_j = \gamma^*_j \frac{\varepsilon\, V_c}{t^*} \tag{6.20}$$

A simple algorithm based on the FlexSMB model was implemented in the gPROMS model builder to determine the $\gamma^*_{II}, \gamma^*_{III}$ separation regions, following these steps:

1. Fixed values of γ^*_I and γ^*_{IV};

2. Set low feed and extract flow rates;

3. Incrementally increase the extract flow rate until the operation meets the minimum performance criteria (defined in Section 6.3.4).

4. Continue increasing the extract flow rate until the system leaves the separation region, and

5. Reset the extract flow rate, increment the feed flow rate, and repeat the process until the separation region is no longer reached.

This approach ensures that the separation region accounts for mass transfer resistance, axial dispersion, and unit design aspects such as dead volumes and switching delays.

6.3.4. Performance Parameters

Performance parameters are used to evaluate SMB performance and determine the separation regions that achieve high purity and high recovery of the target product. The target species in this study, DHA, was the most retained compound in both resins; thus, it was collected in the extract stream of both units. The extract and the raffinate streams were collected for quantification during

an entire SMB cycle. Therefore, the average species concentration of a species in the outlet stream, e.g., species i in the extract stream at a specific cycle, is given by $C_i^X = \int_t^{t+N_c t^*} C_i^X \, dt / N_c t^*$.

The stream purity is expressed as the ratio of the target species concentration to the total concentration of the species in the outlet stream (on an eluent-free basis). For the first SMB unit, an additional purity criterion was defined to assess DHA separation from organic acids while disregarding GLY contamination, the extract stream purity on a GLY-free basis, $P_{X,GLY-free}^H$. H represents the SMB-H and Ca the SMB-Ca.

$$P_X^H = \frac{C_{DHA}^{X,H}}{\sum_i^n C_i^{X,H}} \tag{6.21}$$

$$P_{X,GLY-free}^H = \frac{C_{DHA}^{X,H}}{\sum_{i \neq GLY}^n C_i^{X,H}} \tag{6.22}$$

$$P_X^{Ca} = \frac{C_{DHA}^{X,Ca}}{C_{DHA}^{X,Ca} + C_{GLY}^{X,Ca}} \tag{6.23}$$

Since DHA holds a significantly higher economic value than the other GLY derivatives, the recovery of the remaining compounds was not considered. The raffinate purity was not considered, as the recovery of organic acids is out of this work's scope. DHA recovery in the extract stream, R_{DHA}, productivity, $Prod_{DHA}$, and eluent consumption, EC, were evaluated for the SMB units and overall cascade: k = H (SMB-H); k = Ca (SMB-Ca), and cascade, as follows:

$$R_{DHA}^k = \frac{Q_X^k \, C_{DHA}^{X,k}}{Q_F^k \, C_{DHA}^{F,k}} \tag{6.24}$$

$$R_{DHA}^{cascade} = R_{DHA}^H \, R_{DHA}^{Ca} \tag{6.25}$$

$$Prod_{DHA}^k = \frac{Q_X^k \, C_{DHA}^{X,k}}{(1-\varepsilon^k) \mathrm{V}_c^k N_c^k} \tag{6.26}$$

$$Prod_{DHA}^{cascade} = \frac{Q_X^{Ca} \, C_{DHA}^{X,Ca}}{\sum_k^n (1-\varepsilon^k) \mathrm{V}_c^k N_c^k} \tag{6.27}$$

$$EC^k = \frac{Q_E^k + Q_F^k}{Q_X^k \, C_{DHA}^{X,k}} \tag{6.28}$$

$$EC^{cascade} = \frac{Q_E^H + Q_F^H + Q_E^{Ca} + Q_F^{Ca}}{Q_X^{Ca} \, C_{DHA}^{X,Ca}} \tag{6.29}$$

The model's predictive accuracy was evaluated using Eq. (5.18) from Chapter 5.

6.4. SMB Results and Discussion

6.4.1. Separation Efficiency

The number of theoretical plates (NTP) of the chromatographic columns was determined to assess bed efficiency and to evaluate the influence of different transport phenomena during SMB operation. The van Deemter equation is commonly employed to characterise chromatographic columns and estimate the height equivalent to a theoretical plate (HETP) as a function of the superficial velocity [36], with $\mathrm{NTP} = \mathrm{L}/\mathrm{HETP}$.

$$\mathrm{HETP} = \mathrm{A} + \frac{\mathrm{B}}{\mathrm{u}_0} + C\mathrm{u}_0 \tag{6.30}$$

Parameter A accounts for Eddy diffusion, which results from multiple flow paths in non-ideal packing and is independent of species properties and flow velocity. Parameter B is related to the molecular diffusion in the longitudinal direction and is inversely proportional to flow velocity. Parameter C relates to the mass transfer resistance between the liquid and the solid phase and is directly proportional to flow velocity. These parameters are defined as follows:

$$\mathrm{A} = 2\,\gamma_2\,d_p \tag{6.31}$$

$$\mathrm{B} = 2\,\varepsilon\,\gamma_1\,D_m \tag{6.32}$$

$$\mathrm{C} = \frac{2}{15}\frac{\varepsilon_p(1-\varepsilon)b^2}{\left(\varepsilon + \varepsilon_p(1-\varepsilon)b\right)^2}\tau_d \tag{6.33}$$

where γ_1 = 55 for liquids and γ_2 = 0.5 are constants [36], D_m is the molecular diffusion coefficient, b the adsorption equilibrium parameter for a linear isotherm, $b = 1 + \{(1-\varepsilon_p)/\varepsilon_p\}K_i$, and τ_d the time constant for diffusion, $\tau_d = \frac{\varepsilon_p {R_p}^2}{D_{e,i}}$, as detailed in [39].

The HETP, NTP, and the relative contributions of each transport mechanism for different species in both SMB units are summarised in Table 6.1. The average internal flow rates were set to match those used during the SMB experiments, as detailed in subsequent Sections: 17.6 ml/min (u_0 of 0.093 cm/s) for SMB-H, and 16.5 ml/min (u_0 of 0.088 cm/s) for SMB-Ca.

Table 6.1. Column efficiency: SMB-H (u_0 = 0.093 cm/s); SMB-Ca (u_0 = 0.088 cm/s).

Parameter	SMB-H						SMB-Ca	
	OXA	TTA	GCA	GCO	GLY	DHA	GLY	DHA
A (x10^2) (cm)	1.5	1.5	1.5	1.5	1.5	1.5	1.1	1.1
B (x10^4) (cm^2 s^{-1})	4.8	3.6	3.7	4.5	4.0	3.8	4.1	3.9
C (s)	0.75	1.07	1.08	0.89	1.01	1.06	2.3	2.7
HETP (cm)	0.09	0.12	0.12	0.10	0.11	0.12	0.22	0.25
NTP (-)	111	84	83	97	88	85	46	40
A (%)	16	12	12	14	13	13	5	4
B (%)	6	3	3	5	4	3	2	2
C (%)	78	84	84	81	83	84	93	94

As shown in Table 6.1, parameters B and C exhibit slight variation among species, which is expected given their similar molecular weights and chemical structures. OXA and GCO, the only C2 compounds in the system, displayed slightly different values. Parameter A remains independent of species. In both SMB units, mass transfer resistance (parameter C) was the dominant contribution, accounting for approximately ≈80-90% of the total resistance. Eddy diffusion (parameter A) had a minor contribution (≈ 5-15%), and molecular diffusion (parameter B) was negligible in all cases (≤ 6%).

An NTP value greater than 20 in preparative chromatography typically indicates good column efficiency [4]. Reasonable NTP values of about 90 in the SMB-H indicate good column efficiency, while lower values of around 40 were found in the columns of the SMB-Ca. At first glance, this trend was unexpected, given that the particle diameter d_p of the resin in calcium form was lower than in acid form (112 μm vs. 148 μm). Typically, a decrease in particle diameter correlates with increased column efficiency [36]. However, the ε_p/τ decreased by 45%, from 0.435 to 0.105, exerting a stronger negative impact on parameter C, thereby reducing column efficiency in the SMB-Ca unit.

6.4.2. SMB-H: Pseudo-binary Separation of DHA

Tracer experiments showed an average porosity ε of 0.365 ± 0.006 and an average Pe number of 600 ± 27 for the six fixed-bed columns packed with the resin in acid form.

A preliminary study used the TMB model to gain insights into unit performance and system dynamics. The TMB model is a continuous representation of the process with a steady-state

solution, while the SMB model requires a transient simulation until cyclic steady-state conditions are reached. Consequently, TMB simulations run significantly faster than those using the transient SMB model [1]. The results offered promising initial indications that SMB separation in both units could be feasible, as detailed in Appendix E. Based on these findings, the study proceeded with the FlexSMB design and experimental validation.

To start, the minimum t^* for the SMB operation should be calculated by defining the maximum flow rate in the first section (i.e., the section with the highest flow rate value within the unit). In the case of the FlexSMB unit, this was set at 41 ml/min to balance hardware limitations and pressure drop constraints [16]. The minimum switching time is defined by [1]

$$t^*_{min} = \frac{\varepsilon\, V_c}{Q^*_I}\gamma^*_I \tag{6.34}$$

The minimum switching time was determined as 48 s, considering a safety factor of 15% and a γ^*_I value of 2.88. However, to mitigate potential fluctuations in the pump's operation, a longer switching time t^* of 1.5 min was selected, ensuring moderate internal flow rates with an average of 17.6 ml/min. The SMB unit operated more stably under mild pressure, ensuring stable pump operation. The system was pressurised to 20 bar (maximum 35 bar) using a relief valve at the raffinate outlet. The stationary phase can withstand these pressures well.

The regeneration region was defined by applying a safety factor of 15%, resulting in γ^*_I = 2.88 and γ^*_{IV} = 1.41. Due to experimental flow rate fluctuations, the actual safety factors applied to $\gamma^*_{I,Eq}$ and $\gamma^*_{IV,EQ}$ were 17% and 12%, respectively. The separation region is represented in Figure 6.4, using the previously described algorithm, ensuring $R_{DHA} \geq 85\%$ and $P^X{}_{GLY-free} \geq 97\%$.

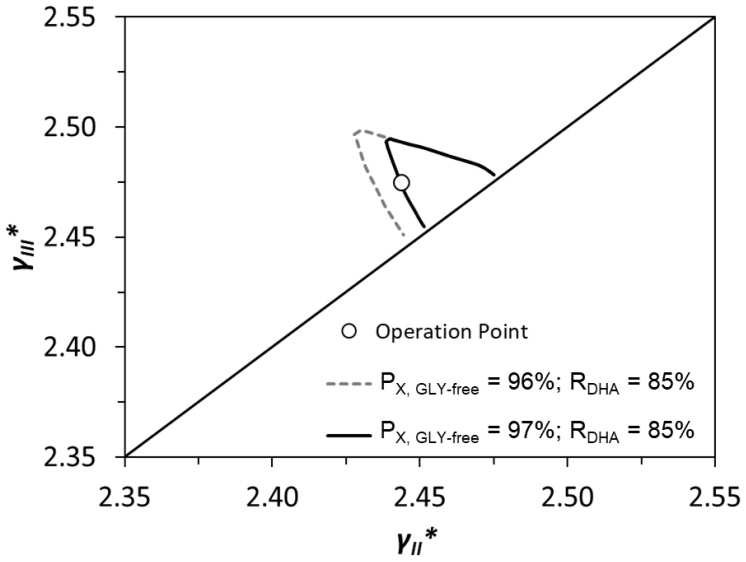

Figure 6.4. Separation region of DHA from organic acids in the SMB-H, considering: $R_{DHA} \geq 85\%$ and $P^X_{GLY-free} \geq 97\%$ (black solid line), and $R_{DHA} \geq 85\%$ and $P^X_{GLY-free} \geq 96\%$ (grey dashed line).

As shown in Figure 6.4, an operation point was positioned at the boundary of the separation region, with values of γ_I^* = 2.88, γ_{II}^* = 2.44, γ_{III}^* = 2.47, γ_{IV}^* = 1.41. A comparison with the separation region for $R_{DHA} \geq 85\%$ and $P^X{}_{GLY-free} \geq 96\%$ is also depicted in Figure 6.4, indicating that a minor shift in the operating point to the left would only slightly reduce purity to 96%. The operating parameters are summarised in Table 6.2.

Table 6.2. Operating parameters for the SMB-H unit.

Operating parameters		Q_{stream}^* (ml/min)	
t^* (min)	1.5	Q_{Rec}^*	10.8
Pe	600	Q_E^*	11.2
ε	0.365	Q_X^*	3.32
D_c and L (cm)	2×10	Q_F^*	0.24
N_c	6	Q_R^*	8.12

The small separation region and the low feed flow rate of 0.24 ml/min resulted in a high number of cycles to develop the concentration fronts and achieve CSS conditions. To accelerate this process, a fast startup methodology was adapted from the approach proposed by Xie, Mun and Wang [40]. During the startup step, the feed solution was pumped to column 3, allowed to flow through column 4, and collected at its outlet through the raffinate port over a complete SMB cycle, while the remaining columns and lines remained filled with eluent.

For the operation point specified, implementing the fast startup reduced the number of cycles required to reach CSS conditions from 28 to 11, representing a reduction of approximately 2.5 hours, as illustrated in Figure 6.5. A feeding volume was optimised for this SMB-H operation, and 19.4 ml was used for the feeding step.

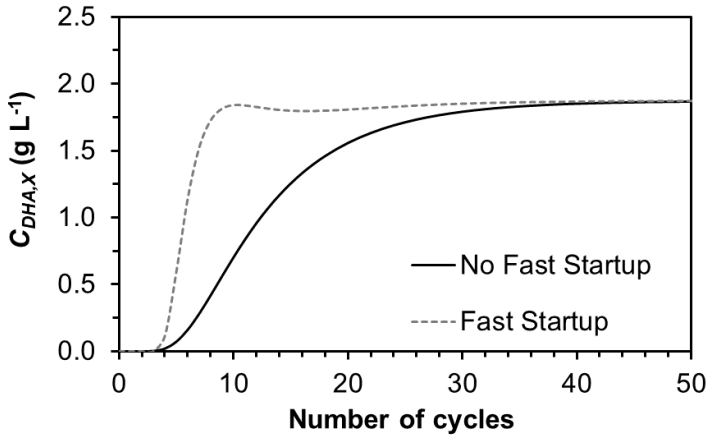

Figure 6.5. DHA concentration history in the extract stream of the SMB-H under different startup strategies: conventional startup (black solid line) and fast startup with a pre-feeding step of 19.4 mL of feed solution (grey dashed line).

The SMB operation thus initiated with the fast startup step, during which the feed solution was pumped at a flow rate of 2.15 ml/min for 9 minutes ($6t^*$). Then, the feed pump was stopped, and conventional SMB operation began. The extract and raffinate streams were collected during each SMB cycle until the CSS conditions were reached, with one cycle of interval to reduce the number of samples for quantification. Figure 6.6 presents the average concentration profiles of the species in the outlet streams, with experimental data shown as open dots and corresponding model predictions depicted as solid lines.

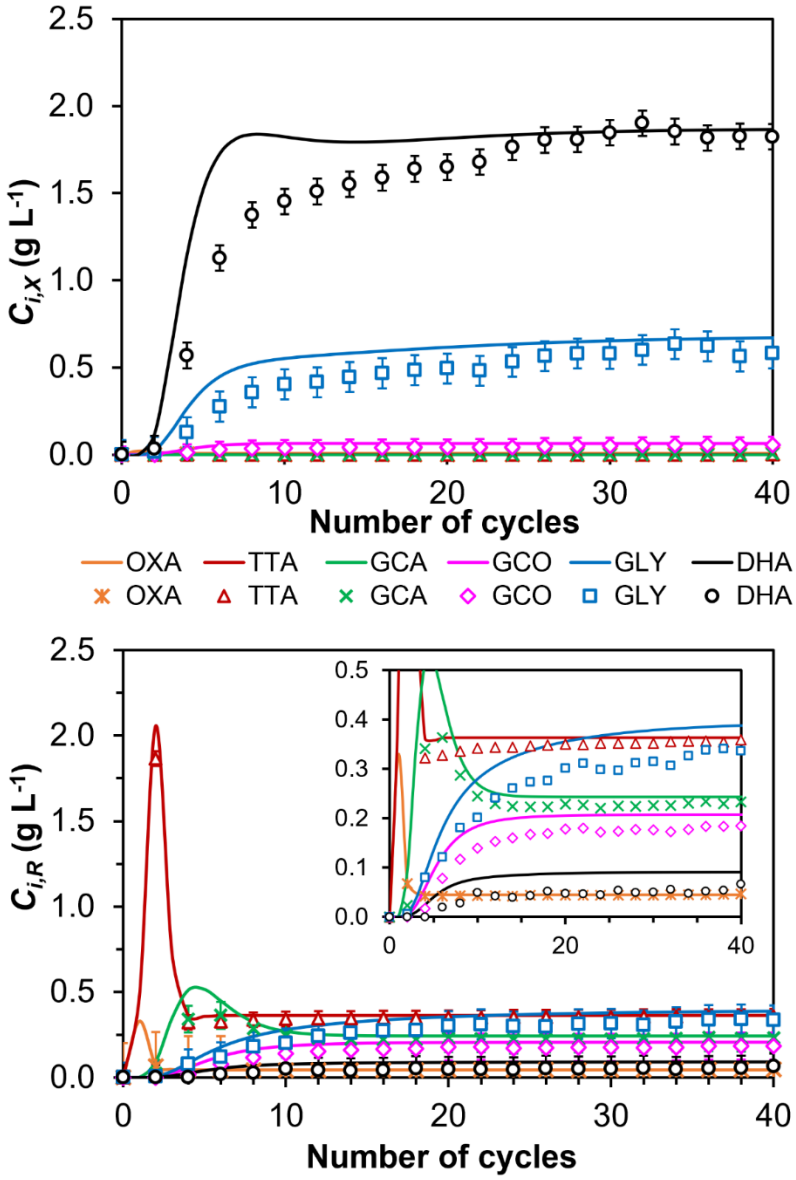

Figure 6.6. Concentration history of the extract (top) and raffinate (bottom) streams of the SMB-H unit. Experimental average concentrations (dots) and model results (lines).

Under CSS conditions, the average composition of the extract stream was 1.82 g/L of DHA and 0.58 g/L of GLY, with the principal contaminant being GCO (0.06 g/L, 2.3% of the total extract composition). The concentration of the remaining organic acids accounted for only 0.2%

of the total extract stream composition (Figure 6.6, top). GCO contamination was attributed primarily to dead volumes within the SMB unit, as evidenced in Figure 6.7, allowing a fraction of GCO to reach the extract stream.

The model effectively describes the species' average concentration in the outlet streams, but the r_{corr}^2 was only 0.781, mainly due to its inability to fully describe the dynamic phase of GLY and DHA concentrations in the extract stream (Figure 6.6, top).

CSS conditions were reached after 30 cycles, though an additional 10 cycles were conducted to ensure the full development of internal concentration profiles. The experimental performance parameters at CSS are summarised in Table 6.3. DHA was collected in the extract stream with a R_{DHA}^H of 87.0%, a P_X^H of 73.8% and a $P_{X,GLY-free}^H$ of 96.8%. The unit showed a $Prod_{DHA}^H$ of 72.9 kg_{DHA} $(m^3_{adsorbent} \cdot day)^{-1}$ with an EC^H of 1.9 m^3_{eluent} kg_{DHA}^{-1}. Model results closely aligned with the experimental ones, with a relative error of -0.4% for the $P_{X,GLY-free}^H$ and 2.2% for the R_{DHA}^H. As expected, the extract purity was lower than the $P_{X,GLY-free}^H$ due to the contamination of the extract stream with GLY.

Table 6.3. Performance parameters of the SMB-H under CSS conditions.

Performance parameter	Experimental	Model
R_{DHA}^H (%)	87.0	89.0
P_X^H (%)	73.8	71.6
$P_{X,GLY-free}^H$ (%)	96.8	96.4

Once CSS conditions were established, internal concentration samples were collected at the 41st, 43rd, and 45th SMB cycles (one interval cycle to ensure no perturbations from sampling). The internal concentration profiles at half-time of the first switching time were represented in Figure 6.7, along with the corresponding model results, plotted against the SMB axial position. Each column of the SMB unit is represented by an axial position ranging from 0 to 1, with column 1 being from 0 to 1, and so on.

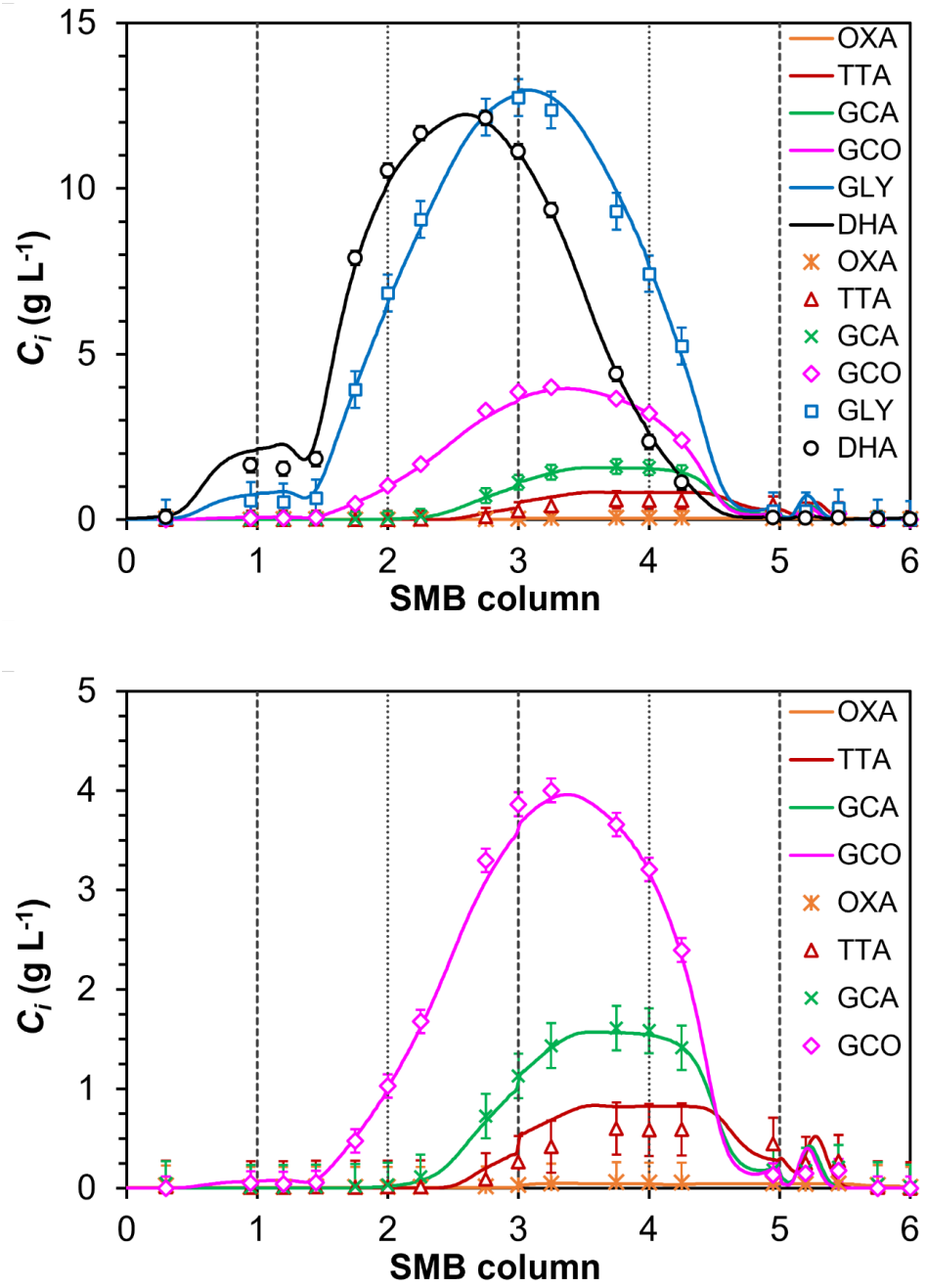

Figure 6.7. Internal concentration profiles of the SMB-H at half-time of the first switching time under CSS conditions, with a 1-2-2-1 column configuration: (Top) all species; (Bottom) organic acids only. Experimental data (dots); model results (lines).

The model fitted the experimental data with a r^2_{corr} of 0.996, with minor deviations observed in the TTA internal concentration profile in Figure 6.7.

The internal concentration profiles reveal that DHA was predominantly transported by the solid phase towards the extract port, while the four organic acids primarily travelled with the liquid phase to the raffinate port. GLY was distributed across both the raffinate and extract streams. Two minor plateaus near the regeneration zones were observed, attributed to dead

volumes and port switching delays inherent to the SMB unit [2]. Those are responsible for the high eluent consumption and reduced productivity, as proper regeneration of zones I and IV must be ensured to prevent species recirculation. Shifting the DHA internal concentration profile leftward by reducing the section I flow rate would increase DHA concentration in the extract stream, but at the expense of decreased recovery due to DHA contamination in the raffinate.

The SMB model was validated as it accurately predicted the experimental data. The separation performance could be enhanced by adjusting the operating point to be closer to the vertex of the separation region, γ_{II}^{*} = 2.44 and γ_{III}^{*} = 2.49, increasing the $Prod_{DHA}^{H}$ to 107.0 kg_{DHA} $(m^3_{adsorbent} \cdot day)^{-1}$ and decreasing the EC^{H} to 1.3 m^3_{eluent} kg_{DHA}^{-1}.

The extract stream was subsequently fed to the second SMB unit, SMB-Ca. A solution with 1.82 g/L of DHA and 0.58 g/L of GLY was prepared for that.

6.4.3. SMB-Ca: DHA-GLY Separation

The same columns used in the SMB-H experiments were repacked with the resin previously exchanged to the Ca^{2+} form. Tracer experiments revealed an average porosity (ε) of 0.384 ± 0.005 and an average Péclet number (Pe) of 607 ± 79.

The FlexSMB model was implemented to simulate a binary separation, where DHA was the most adsorbed species, while GLY was the least adsorbed. A safety factor of 15% was applied to define the regeneration region, resulting in γ_{I}^{*} = 3.33 and γ_{IV}^{*} = 2.07. However, considering the measured flow rates, the actual safety factors applied were slightly higher, at 18% and 14%, respectively.

The $\gamma_{II}^{*}, \gamma_{III}^{*}$ separation region for the SMB-Ca operation is presented in Figure 6.8, where the selected operation point (γ_{I}^{*} = 3.31, γ_{II}^{*} = 2.59, γ_{III}^{*} = 2.81, γ_{IV}^{*} = 2.07) is located inside the black-bordered region, ensuring $P_X^{Ca} \geq 97\%$ and $R_{DHA}^{Ca} \geq 90\%$. This operation point also falls within the grey-bordered region defined by $P_X^{Ca} \geq 99\%$ and $R_{DHA}^{Ca} \geq 90\%$, indicating that extract purities above 99% could be attainable. If the operation point is slightly shifted to the right, it would still be inside the grey-dashed region in Figure 6.8, which defines a $P_X^{Ca} \geq 97\%$ and a $R_{DHA}^{Ca} \geq 85\%$, demonstrating that high DHA recovery rates remain achievable without compromising extract purity.

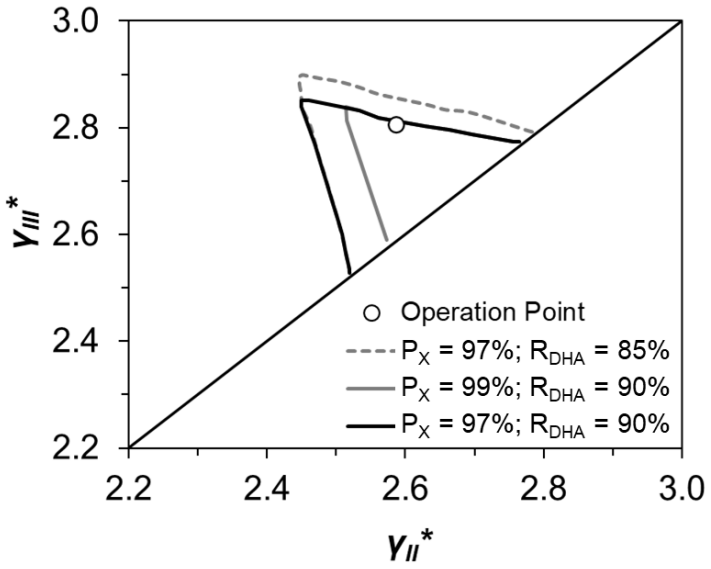

Figure 6.8. DHA-GLY separation regions in the SMB-Ca unit, considering: $P_X^{Ca} \geq 97\%$ and $R_{DHA}^{Ca} \geq 90\%$ (black solid boundary), $P_X^{Ca} \geq 97\%$ and $R_{DHA}^{Ca} \geq 85\%$ (grey dashed boundary) and $P_X^{Ca} \geq 99\%$ and $R_{DHA}^{Ca} \geq 90\%$ (grey solid boundary).

For the SMB-Ca, the t_{min}^* was determined to be 1 min. However, to ensure stable operation and moderate internal flow rates, a t^* of 2 min was chosen, resulting in an average internal flow rate of 16.3 ml/min. This value is similar to the one used during the SMB-H operation. Unlike in the previous SMB-H experiments, the fast startup methodology was not implemented in this case, as it had a negligible impact on the number of cycles required to reach cyclic steady state (CSS) conditions (Figure 6.9).

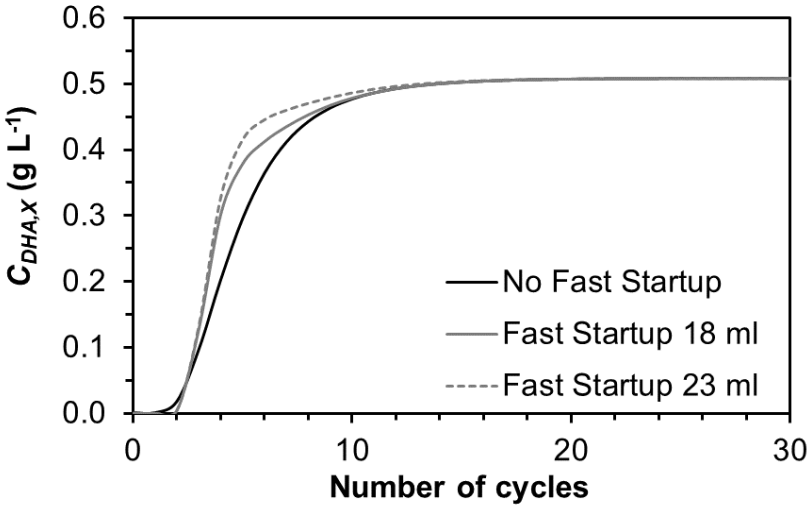

Figure 6.9. DHA concentration history in the extract stream of the SMB-Ca unit under different startup conditions: conventional (black line); 18 ml fast startup step (grey line), and 23 ml fast startup step (grey dashed line).

Furthermore, applying the fast startup protocol would have introduced additional operational complexity and led to unnecessary waste of the feed solution for this specific separation. The detailed experimental operating parameters are summarised in Table 6.4.

Table 6.4. Operating parameters for the SMB-Ca unit.

Operating parameters		Q^*_{stream} (ml/min)	
t^* (min)	2	Q^*_{Rec}	12.6
Pe	607	Q^*_E	7.65
ε	0.384	Q^*_X	4.53
D_c and L (cm)	2×10	Q^*_F	1.34
N_c	6	Q^*_R	4.46

During the initial 10 SMB cycles, extract and raffinate samples were collected during each cycle to capture the transient phase with higher resolution and, after that, with one cycle of interval. Figure 6.10 presents the time evolution of species concentrations in the outlet streams, where experimental data points are shown as open dots and model predictions are represented by solid lines.

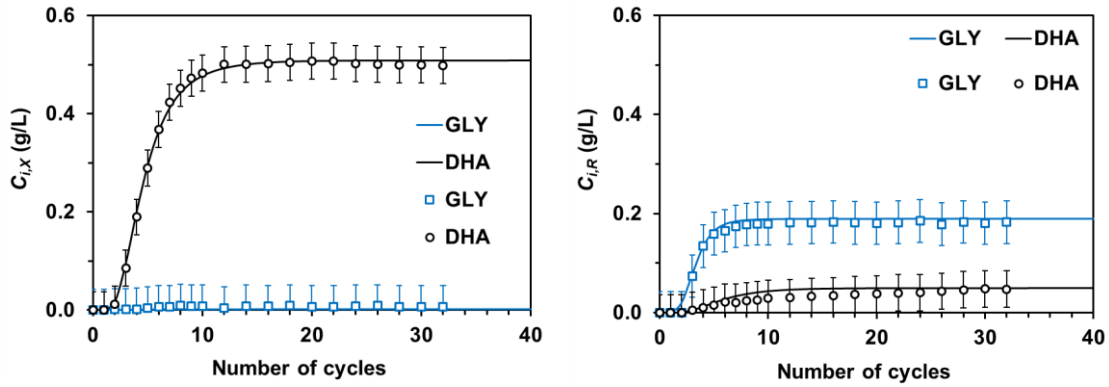

Figure 6.10. SMB-Ca average concentration history in the extract (left) and raffinate (right): GLY (blue squares), DHA (black circles) and model results (lines).

Under CSS conditions, the average composition of the extract stream was 0.50 g/L of DHA and 0.01 g/L of GLY (Figure 6.10 top), while the raffinate stream contained 0.18 g/L of GLY and 0.05 g/L of DHA (Figure 6.10 bottom). The mathematical model accurately described the outlet stream compositions with a r^2_{corr} of 0.992. CSS conditions were achieved after 15 cycles, and the experimental performance parameters are summarised in Table 6.5. The model was able to predict well the experimental results, with relative errors of 1.2% for the P^{Ca}_X and 2.1% for the R^{Ca}_{DHA}.

Table 6.5. Performance parameters of the SMB-Ca under CSS conditions.

Performance parameter	Experimental	Model
R_{DHA}^{Ca} (%)	89.0	90.9
P_{X}^{Ca} (%)	98.6	99.8

Following the establishment of CSS conditions, an additional fifteen cycles were conducted before collecting internal concentration samples during the 33rd, 35th, and 37th SMB cycles. The internal concentration profiles at half-time of the first switching time are plotted against the SMB axial position in Figure 6.11.

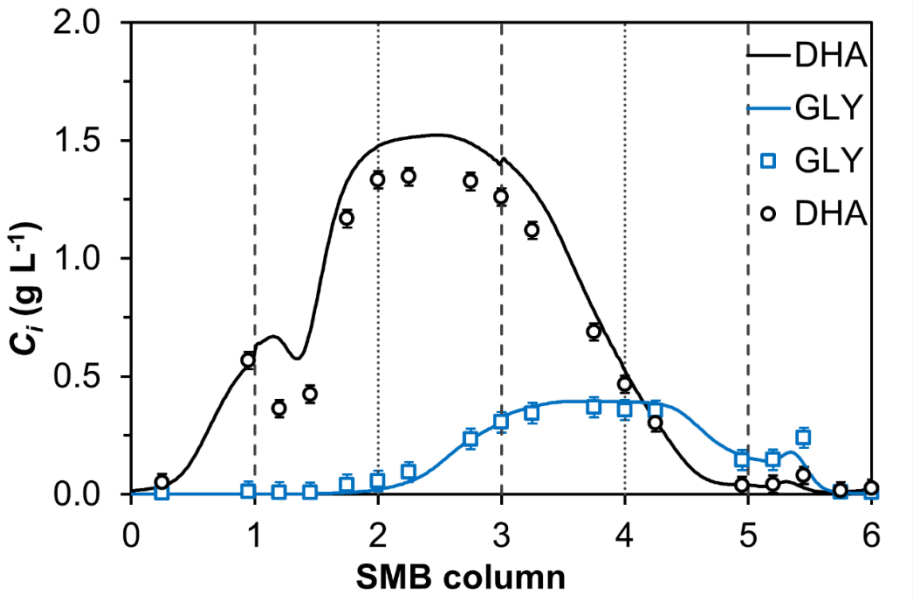

Figure 6.11. Internal concentration profiles of the SMB-Ca at half-time of the first switching time under CSS conditions, with a 1-2-2-1 column configuration. Experimental GLY (blue squares), DHA (black circles) and model results (lines).

The model effectively fitted the internal concentration profiles with a r_{corr}^2 of 0.933. As observed in the SMB-H operation, DHA was primarily transported with the solid phase toward the extract port, with only a minor fraction recirculating and reaching the raffinate port. In contrast, GLY was preferentially carried by the liquid phase toward the raffinate port, resulting in a GLY recovery ($R_{GLY}^{Ca} = \frac{Q_X^{Ca}\, C_{GLY}^{X,Ca}}{Q_F^{Ca}\, C_{GLY}^{F,Ca}}$) of 96.5%. Similar to the SMB-H operation, two plateaus were formed in the regeneration zones near the collecting ports. This required the application of high regeneration safety factors to ensure proper regeneration, highlighting the importance of reducing the unit's dead volumes.

The SMB-Ca operation yielded a $Prod_{DHA}^{Ca}$ of 28.5 kg_{DHA} ($m^3_{adsorbent}$·day)$^{-1}$ with an EC^{Ca} of 4.0 m^3_{eluent} kg_{DHA}^{-1} under the selected operating point. Adjusting it to the vertex of the separation region, γ_{II}^* = 2.46, γ_{III}^* = 2.84, would enhance the $Prod_{DHA}^{Ca}$ to 50 kg_{DHA} ($m^3_{adsorbent}$·day)$^{-1}$ and

reduce the EC^{Ca} to 2.5 m^3_{eluent} kg_{DHA}^{-1}. If higher extract purity is required, the system could be adjusted to achieve purities of up to 99%, although this would reduce the maximum $Prod_{DHA}^{Ca}$ to 39.0 kg_{DHA} $(m^3_{adsorbent} \cdot day)^{-1}$ and an increased EC^{Ca} of 3.0 m^3_{eluent} kg_{DHA}^{-1}.

6.4.4. SMB Cascade Performance

In the experimental run of the two-unit SMB cascade, an extract stream with a DHA purity of 98.6% and a concentration of 0.50 g/L was obtained at a flow rate of 4.5 ml/min. The SMB cascade exhibited a global DHA recovery $R_{DHA}^{cascade}$ of 77.5%, a productivity $Prod_{DHA}^{cascade}$ of 21.7 kg_{DHA} $(m^3_{adsorbent} \cdot day)^{-1}$ and an eluent consumption $EC^{cascade}$ of 9.0 m^3_{eluent} kg_{DHA}^{-1}. Operating both SMB units at the vertices of their respective separation regions would increase $Prod_{DHA}^{cascade}$ to 52.9 kg_{DHA} $(m^3_{adsorbent} \cdot day)^{-1}$ and reduce $EC^{cascade}$ to 4.0 m^3_{eluent} kg_{DHA}^{-1}. Further optimisation could enhance productivity while minimising eluent consumption.

To operate an SMB cascade industrially, two SMB units would be operated simultaneously, with the extract from the first unit being fed into a homogenization tank before entering the second SMB. To maximise productivity, the second SMB would be scaled relative to the first so that its feed flow matches the extract flow rate from the first SMB.

For industrial implementation, two SMB units would be operated simultaneously, with the extract from the first unit being fed into a homogenization tank before entering the second SMB. To maximise productivity, the second SMB would be scaled relative to the first so that its feed flow matches the extract flow rate from the first SMB. The homogenization tank would ensure a consistent and homogeneous feed for SMB-Ca and facilitate in-line acid neutralisation of the 5 mM H_2SO_4 eluent from SMB-H. Calcium hydroxide could be used for neutralisation, leading to the precipitation of calcium sulphate, which could then be removed. Further studies are required to assess the impact of this approach on the separation process.

Alternative SMB configurations could be explored to separate DHA from a six-compound mixture using the H^+ resin. Potential approaches include pseudo-SMB operation or a five-section SMB with two extract streams: one collecting DHA (Extract-I, between sections I and II) and another collecting glycerol (Extract-II, between sections II and III), while the organic acids are directed to the raffinate (between sections IV and V). However, both strategies are limited by the low selectivity of GLY-DHA separation on the H^+ resin, and their implementation was not feasible with the available equipment.

6.4.5. Remarks and Process Considerations

The experiments highlighted the impact of dead volumes in real SMB units, as illustrated in Figure 6.7 and Figure 6.11, reducing separation efficiency compared to an ideal SMB system with zero dead volumes [16, 21]. Nevertheless, SMB technology remains widely used in industry, particularly in the pharmaceutical sector, which requires exceptionally high purities and strict quality standards, proving to be a cost-effective solution for complex separations, including chiral separations. SMB remains a competitive alternative to conventional separation techniques [41]. Key considerations and limitations of this novel separation process include:

Extract Stream Contamination: Under the current experimental conditions, the SMB-H extract stream contained 2.3% GCO and minor organic acid impurities. Feeding directly into the SMB-Ca unit would gradually replace Ca^{2+} with H^{+}. Operational adjustments could help minimise organic acid contamination, and periodic regeneration of the SMB-Ca stationary phase with $CaCl_2$ solution would restore it to its original Ca^{2+} form. A detailed study on stationary phase ageing and its impact on performance and cost is needed, but falls beyond the scope of this thesis.

DHA Purity and Glycerol Presence: The presence of low glycerol concentrations in the DHA stream is not problematic for cosmetic applications, as glycerol is widely used in cosmetic formulations [42, 43].

Eluent Recovery and DHA concentration: While SMB significantly reduces eluent consumption compared to batch chromatography, solvent use remains substantial [1, 41]. Given that DHA is heat-sensitive and the process compounds are non-volatile [44], solvent recovery via falling-film evaporators, reduced-pressure evaporators, or membrane-assisted processes may be viable options [45]. Industrial-scale SMB processes have demonstrated solvent recovery efficiencies of up to 85% [46]. Although solvent recovery involves high operational costs, it simultaneously concentrates product streams [41, 47]. Some industries may utilise concentrated DHA streams directly [48], while others, such as the cosmetics industry, require further processing, including spray drying or freeze-drying, to produce DHA powder, the most common commercial form [44, 48]. Industrial bioprocesses also operate under dilute conditions and require costly downstream processes, including removing organic and inorganic species, multiple water-washing steps, vacuum distillation, and crystallisation [48-51].

Process Integration and Capital Costs: Using different stationary phases in the two SMB units prevents full integration into a single SMB system, leading to higher capital costs than fully integrated SMB processes [34]. Still, SMB separation of DHA from glycerol oxidation products remains an economically attractive alternative compared to bio-fermentation downstream processing [48, 50-52]. A detailed economic evaluation of this chromatographic separation process is needed.

6.5. Conclusions

The purification of DHA from glycerol oxidation products using a Pt-Bi/AC catalyst was successfully achieved using a two-unit SMB cascade on the FlexSMB unit with six columns in the 1-2-2-1 configuration. DOWEX 50WX-2 resin was used as the stationary phase in both the H^+ and the Ca^{2+} form, with 5 mM H_2SO_4 and water as the respective mobile phases at 293 K.

Despite using linear adsorption isotherms for all species except OXA (modelled with a Freundlich isotherm), the mathematical model accurately predicted both the dynamic behaviour and cyclic steady-state performance of the SMB system, suggesting that the added complexity of more advanced adsorption models would provide minimal benefit. Kinetic and equilibrium data determined from fixed-bed column experiments (Chapter 5) were used as model input.

The separation regions for both SMB units were determined considering mass transfer limitations and the dead volumes and time switch asymmetries of the FlexSMB. The first SMB, packed with the resin in H^+ form, separated DHA from organic acids (OXA, TTA, GCA, GCO), reaching CSS conditions after 30 cycles with an experimental DHA recovery of 87.0% and an extract purity (GLY-free basis) of 96.8%. The model accurately described the outlet concentration profiles and internal species distribution at CSS conditions. Implementing a fast startup step reduced the number of cycles required to reach CSS conditions by approximately 10.

The extract stream from the first SMB was then fed into the second SMB unit, packed with the resin in Ca^{2+} form. DHA was successfully separated from GLY, reaching CSS conditions after 30 cycles, with an experimental DHA recovery of 89.0% and an extract purity of 98.6%.

The two-unit SMB cascade produced DHA with a concentration of 0.50 g/L at a flow rate of 4.5 ml/min and with 98.6% of purity, achieving a global productivity of 21.7 kg_{DHA} $(m^3_{adsorbent} \cdot day)^{-1}$ and an eluent consumption of 9.0 m^3_{eluent} kg_{DHA}^{-1}.

The results also provide insights into practical considerations for large-scale implementation. Dead volumes in real SMB units reduce separation efficiency compared to an ideal SMB. Using different stationary phases in the two SMB units prevents full integration into a single system, yet SMB technology remains a cost-effective process for DHA purification. Water recovery will simultaneously concentrate the outlet streams, including the DHA-rich rich-stream, and allow solvent recovery to be reused. These findings demonstrate the successful purification of DHA using a two-unit SMB cascade, validating its potential for large-scale production of high-purity DHA.

6.6. Notation

Variables

C_i ($C_{i,out}$)	Concentration of compound *i* in the liquid phase (at the column outlet) (g L^{-1})
d_p	Particle diameter (μm)
D_i^{∞}	Molecular diffusion coefficient at infinite dilution (dm^2 min^{-1})
D_i	Combined diffusion coefficient of species *i* (dm^2 min^{-1})
$D_{p,i}$	Diffusion coefficient of species *i* in the pores of the particle (dm^2 min^{-1})
$D_{e,i}$	Effective diffusion coefficient of species *i* in the particle (dm^2 min^{-1})
$D_{h,i}$	Homogeneous diffusion coefficient of species *i* (dm^2 min^{-1})
D_{ax}	Axial dispersion coefficient ($D_{ax} = \frac{uL}{Pe}$)
$E(t)$	Residence time distribution (min^{-1})
EC	Eluent consumption (m^3_{eluent} kg_{DHA}^{-1})
K_i (K_i')	Distribution coefficient (L_{liquid} L_{solid}^{-1}) ($K_i' = K_i \frac{1-\varepsilon}{\varepsilon}$, [-])
$k_{h,i}$	Homogeneous mass transfer coefficient (min^{-1})
L	Fixed-bed column length (dm)
M	Molar mass of the solvent (g mol^{-1})
n_i	Freundlich isotherm parameter (-)
N_c	Number of SMB columns
Pe	Péclet number (-)
$Prod_i$	Productivity of compound *i* in the extract or raffinate stream of the SMB [kg_i ($m^3_{adsorbent}$·day)$^{-1}$]
P_i	Purity of compound *i* in the extract or raffinate stream of the SMB (%)
Q_{stream}	Liquid flow rate in the TMB (SMB) stream (dm^3 min^{-1})
(Q^*_{stream})	Recycle (Rec), Eluent (E), Extract (X), Feed (F), Raffinate (R)
Q_j	Liquid flow rate in section *j* (dm^3 min^{-1})
Q_s	Solid flow rate (dm^3 min^{-1})
$\bar{q}_i$	Average concentration adsorbed in the adsorbent (g_i L_{solid}^{-1})
q_i^*	Adsorbed concentration in equilibrium with C (g_i L_{solid}^{-1})
r^2_{corr}	Correlation coefficient (-)
R_i	Recovery of species *i* in the extract or raffinate stream of the SMB (%)
R_p	Average particle radius (dm)
T	Temperature (K)

t^*	SMB switching time (min)
$\bar{t}_r$	Mean residence time (min)
u (u_0)	Liquid interstitial velocity (superficial velocity) (dm min^{-1})
u_s	Solid velocity (TMB) (dm min^{-1})
V_c	Column volume (empty) (cm^3)
$V_{i,nbp}$	Molar volume of species *i* at normal boiling point (cm^3 mol^{-1})
z	Axial position (-)

Greek Letters

α	Separation selectivity (-)
γ (γ^*)	Ratio between the liquid and the solid flow rate in the TMB (SMB) (-)
ε	Bed column porosity (-)
ε_p	Particle porosity (-)
η	Dynamic viscosity of the solvent (cP)
$\mu_n[E(t)]$	*n* moment of the residence time distribution (min^n)
σ^2	Residence time distribution variance (min^2)
τ	Space-time (min)
τ_p	Particle tortuosity (-)
ψ	Solvent association factor (Wilke and Chang correlation) (-)

Abbreviations

CSS	Cyclic Steady State
HETP	Column Height Equivalent to a Theoretical Plate
HPLC	High-Performance Liquid Chromatography
LDF	Linear Driving Force
NTP	Number of Theoretical Plates in chromatography columns
OXA, TTA, GCA, GCO, GLY, DHA	Oxalic acid (OXA), Tartronic acid (TTA), Glyceric acid (GCA), Glycolic acid (GCO), Glycerol (GLY), Dihydroxyacetone (DHA)
Rec, X, R, F, E	SMB streams: Recycle (Rec), Extract (X), Raffinate (R), Feed (F) and Eluent (E)
SMB	Simulated Moving Bed
TMB	True Moving Bed

6.7. References

1. Rodrigues, A.E., Pereira, C.S.M., Minceva, M., Pais, L.S., Ribeiro, A.M., Ribeiro, A.E., Silva, M., Graça, N.S., and Santos, J.C., *Simulated moving bed technology: principles, design and process applications*. 1st Edition ed. 2015, Amsterdam: Butterworth-Heinemann. 304.
2. Sá Gomes, P. and Rodrigues, A.E., *Simulated Moving Bed Chromatography: From Concept to Proof-of-Concept.* Chemical Engineering & Technology, 2012. **35**(1): p. 17-34.
3. Nicoud, R.-M., *Chromatographic Processes: modeling, simulation, and design*. Vol. 1. 2015, Cambridge: Cambridge University Press. 657.
4. Guiochon, G., Felinger, A., and Shirazi, D.G., *Fundamentals of preparative and nonlinear chromatography*. 2006: Academic Press.
5. Tejero, M., Ramírez, E., Fité, C., Tejero, J., and Cunill, F., *Esterification of levulinic acid with butanol over ion exchange resins.* Applied Catalysis A: General, 2016. **517**: p. 56-66.
6. Sharma, D., *Simulated Moving Bed Technology: Overview and Use in Biorefineries.* Biorefineries-Selected Processes, 2021.
7. Binder, T., *Simulated moving bed chromatographic purification of amino acids.* Archer-Daniels-Midland Company, 2008: p. 18.
8. Kelliher, A., Morrison, A., Oroskar, A., Rema, R.V.N., and Agarwal, A. Simulated moving bed chromatographic separation process. US9790162B2, 2017.
9. Kelliher, A., Morrison, A., Oroskar, A., Rema, R.V.N., and Agarwal, A. SMB process for producing highly pure EPA from fish oil. US9695382B2, 2017.
10. Koop, E.P., Schwarz, M.J., and Desjonqueres, S. Method of treatment using peroxidized lipids. US6395779B1, 2002.
11. Kelliher, A., Morrison, A., Oroskar, A., Rema, R.V.N., and Agarwal, A. SMB process. US9370730B2, 2016.
12. Takamatsu, Y., Yamamoto, M., and Sato, Y. Method of purifying amino acid. WO2005097734A1, 2005.
13. Wheaton, R. and Lefevre, L., *Dowex Ion exchange resins: Fundamentals of Ion Exchange.* Dow Liquid Separations, 2000.
14. *DuPont Resins for Downstream Drug Purification* D.W. Solutions, Editor. July 2022, DuPont Water Solutions.
15. Coelho, L.C.D., Filho, N.M.L., Faria, R.P.V., Ferreira, A.F.P., Ribeiro, A.M., and Rodrigues, A.E., *Separation of tartronic and glyceric acids by simulated moving bed chromatography.* Journal of Chromatography A, 2018. **1563**: p. 62-70.
16. Gomes, P.S., Zabkova, M., Zabka, M., Minceva, M., and Rodrigues, A.E., *Separation of chiral mixtures in real SMB units: The FlexSMB-LSRE®.* AIChE journal, 2010. **56**(1): p. 125-142.
17. Ribeiro, A.E., Gomes, P.S., Pais, L.S., and Rodrigues, A.E., *Chiral separation of flurbiprofen enantiomers by preparative and simulated moving bed chromatography.* Chirality, 2011. **23**(8): p. 602-611.
18. Ribeiro, A.E., Gomes, P.S., Pais, L.S., and Rodrigues, A.E., *Chiral separation of ketoprofen enantiomers by preparative and simulated moving bed chromatography.* Separation Science and Technology, 2011. **46**(11): p. 1726-1739.
19. Ribeiro, A.E., Rodrigues, A.E., and Pais, L.S., *Separation of nadolol stereoisomers by chiral liquid chromatography at analytical and preparative scales.* Chirality, 2013. **25**(3): p. 197-205.
20. Arafah, R.S., Ribeiro, A.E., Rodrigues, A.E., and Pais, L.S., *Separation of nadolol racemates by high pH reversed-phase fixed-bed and simulated moving bed chromatography.* Separation and Purification Technology, 2023. **305**: p. 122529.

21. Rios, A.G., Ribeiro, A.M., Rodrigues, A.E., and Ferreira, A.F., *Bovine serum albumin and myoglobin separation by size exclusion SMB.* Journal of Chromatography A, 2020. **1628**: p. 461431.

22. Rios, A.G., Ribeiro, A.M., Rodrigues, A.E., Quadros, P.A., and Ferreira, A.F., *Bovine serum albumin and myoglobin separation on HAp.* Separation and Purification Technology, 2023. **326**: p. 124779.

23. Rios, A.G., Ribeiro, A.M., Rodrigues, A.E., and Ferreira, A.F., *Bovine Serum Albumin and Myoglobin Separation by Ion-Exchange SMB.* Industrial & Engineering Chemistry Research, 2023. **62**(35): p. 13932-13942.

24. Mata, V.G. and Rodrigues, A.E., *Separation of ternary mixtures by pseudo-simulated moving bed chromatography.* J Chromatogr A, 2001. **939**(1-2): p. 23-40.

25. Masuda, T., Sonobe, T., Matsuda, F., and Horie, M., *Process for fractional separation of multi-component fluid mixture*. 1993, Google Patents.

26. Navarro, A., Caruel, H., Rigal, L., and Phemius, P., *Continuous chromatographic separation process: simulated moving bed allowing simultaneous withdrawal of three fractions.* Journal of chromatography A, 1997. **770**(1-2): p. 39-50.

27. Beste, Y.A. and Arlt, W., *Side-stream simulated moving-bed chromatography for multicomponent separation.* Chemical engineering & technology, 2002. **25**(10): p. 956-962.

28. Chiang, A.S., *Continuous chromatographic process based on SMB technology.* American Institute of Chemical Engineers. AIChE Journal, 1998. **44**(8): p. 1930.

29. Wooley, R., Ma, Z., and Wang, N.-H., *A nine-zone simulating moving bed for the recovery of glucose and xylose from biomass hydrolyzate.* Industrial & engineering chemistry research, 1998. **37**(9): p. 3699-3709.

30. Wankat, P.C., *Simulated Moving Bed Cascades for Ternary Separations.* Industrial & Engineering Chemistry Research, 2001. **40**(26): p. 6185-6193.

31. Kang, S.-H., Kim, J.-H., and Mun, S., *Optimal design of a tandem simulated moving bed process for separation of paclitaxel, 13-dehydroxybaccatin III, and 10-deacetylpaclitaxel.* Process Biochemistry, 2010. **45**(9): p. 1468-1476.

32. Heinonen, J., Laatikainen, M., and Sainio, T., *Chromatographic fractionation of a ternary mixture with an SMB cascade process: The effect of ion exchange resin cross-linkage on separation efficiency.* Separation and Purification Technology, 2018. **206**: p. 286-296.

33. Jo, S.H., Kim, J.K., Yoo, C.G., Kim, J.I., Koo, Y.M., and Mun, S., *Comparative Analysis of Single-Cascade Five-Zone and Two-Zone SMB Systems for the Separation of a Ternary Amino Acid Mixture.* The Canadian Journal of Chemical Engineering, 2007. **85**(6): p. 874-882.

34. Park, H., Kim, J.W., Lee, K.B., and Mun, S., *Comparison of the process performances of a tandem 4-zone SMB and a single-cascade 5-zone SMB for separation of galactose, levulinic acid, and 5-hydroxymethylfurfural in agarose hydrolyzate.* Separation and Purification Technology, 2020. **237**: p. 116357.

35. Xu, Z., Cai, J.-g., and Pan, B.-c., *Mathematically modeling fixed-bed adsorption in aqueous systems.* Journal of Zhejiang University SCIENCE A, 2013. **14**(3): p. 155-176.

36. Ruthven, D.M., *Principles of adsorption and adsorption processes*. 1984: John Wiley & Sons.

37. Glueckauf, E., *Theory of chromatography. Part 10.—Formulæ for diffusion into spheres and their application to chromatography.* Transactions of the Faraday Society, 1955. **51**: p. 1540-1551.

38. Wilke, C. and Chang, P., *Correlation of diffusion coefficients in dilute solutions.* AIChE Journal, 1955. **1**(2): p. 264-270.

39. Rodrigues, A.E., *Permeable packings and perfusion chromatography in protein separation.* Journal of Chromatography B: Biomedical Sciences and Applications, 1997. **699**(1-2): p. 47-61.

40. Xie, Y., Mun, S.-Y., and Wang, N.-H.L., *Startup and Shutdown Strategies of Simulated Moving Bed for Insulin Purification.* Industrial & Engineering Chemistry Research, 2003. **42**(7): p. 1414-1425.

41. Nicoud, R.-M., *The amazing ability of continuous chromatography to adapt to a moving environment.* Industrial & Engineering Chemistry Research, 2014. **53**(10): p. 3755-3765.

42. Becker, L.C., Bergfeld, W.F., Belsito, D.V., Hill, R.A., Klaassen, C.D., Liebler, D.C., Marks, J.G., Shank, R.C., Slaga, T.J., Snyder, P.W., Gill, L.J., and Heldreth, B., *Safety Assessment of Glycerin as Used in Cosmetics.* International Journal of Toxicology, 2019. **38**(3_suppl): p. 6S-22S.

43. *Opinion on dihydroxyacetone*. 14 December 2010, Scientific Committee on Consumer Safety.

44. Ciriminna, R., Fidalgo, A., Ilharco, L.M., and Pagliaro, M., *Dihydroxyacetone: An Updated Insight into an Important Bioproduct.* ChemistryOpen, 2018. **7**(3): p. 233-236.

45. Hamende, M., Chatel, M., Rebier, L., and Nicoud, R.-M. Chromatography method and device with recovery of solvent. US6863824B2, 2005.

46. Dapremont, O., *Evolution of Continuous Chromatography: Moving Beyond Chiral Separations.* Pharmaceutical Technology, 2010. **2010 Supplement**(4).

47. Jo, C.Y., Kang, H.-J., and Mun, S., *Optimization studies for improving the throughput and solvent usage levels of a tandem simulated-moving-bed process for recovery of galactotriose from crude galacto-oligosaccharides.* Journal of Industrial and Engineering Chemistry, 2023. **118**: p. 205-215.

48. Lari, G.M., Mondelli, C., Papadokonstantakis, S., Morales, M., Hungerbühler, K., and Pérez-Ramírez, J., *Environmental and economic assessment of glycerol oxidation to dihydroxyacetone over technical iron zeolite catalysts.* Reaction Chemistry & Engineering, 2016. **1**(1): p. 106-118.

49. Charney, W. Process for the production of dihydroxyacetone. US4076589A, 1978.

50. Fakley, M.E. and Lindsay, R.J. Process for the isolation of dihydroxyacetone. EP0245976A1, 1987.

51. Chen, Q. and Chen, J., *Review of the separation and purification of 1, 3-dihydroxyacetone.* Anhui Med Pharm J, 2013. **17**: p. 1271-1273.

52. Cheng, K.K., Zhao, X.B., Zeng, J., Wu, R.C., Xu, Y.Z., Liu, D.H., and Zhang, J.A., *Downstream processing of biotechnological produced succinic acid.* Appl Microbiol Biotechnol, 2012. **95**(4): p. 841-50.

7. Conclusions and Suggestions for Future Work

7.1. General Conclusions

This thesis addressed the development of an integrated process for the selective oxidation of glycerol to dihydroxyacetone (DHA) and its subsequent purification, proposing an alternative to current state-of-the-art bio-fermentation methods. The first part of the work combined a comprehensive literature review, screening of commercial catalysts for DHA production, and experimental and modelling studies of glycerol oxidation kinetics using the most promising catalysts. The second part focused on the downstream purification of DHA from the complex oxidation mixture by obtaining adsorption and kinetic data on a fixed-bed column and designing a simulated moving bed (SMB) chromatography process, which was validated experimentally.

A comprehensive literature review revealed considerable advances in glycerol valorisation, particularly via catalytic oxidation to DHA. Bi-doped Pt and Au-based catalysts have emerged as strong candidates due to their high DHA selectivity and activity. However, critical limitations remain, including catalyst deactivation, scalability issues, and a scarcity of continuous processing studies. In contrast, the purification of DHA has received little attention compared to its synthesis despite the inherent complexity of the resulting reaction mixture. Chromatographic separation, particularly SMB, was identified as a promising strategy due to its efficiency, continuous operation, and flexibility for multicomponent systems.

Experimental screening under base-free conditions confirmed the superior performance of Pt5-Bi1.5/AC (Johnson Matthey) and Au1/ZnO (Strem Chemicals). The former achieved the highest DHA yield (36%) and exhibited excellent reusability over successive batch cycles. While Au/ZnO also demonstrated good selectivity, it suffered from poor stability. These findings justified the selection of both catalysts for in-depth kinetic studies and for generating representative mixtures to support downstream separation development.

The kinetic study and modelling provided deeper insights into glycerol oxidation reactions. The Pt-Bi/AC catalyst exhibited a relatively low activation energy (16 kJ mol^{-1}) for DHA

formation. In comparison, the Au/ZnO catalyst showed a higher activation energy (52 kJ mol^{-1}) and strong adsorption of glycerol and its oxidation products, likely contributing to its reduced activity and faster deactivation. While the power-law kinetic model demonstrated limited applicability and poorer predictive performance, the Langmuir–Hinshelwood–Hougen–Watson model effectively described the reaction kinetics across a broad range of conditions: 80–100 °C, 2.0–7.5 bar O_2, 0.1–2.0 M glycerol concentration, and GLY/Pt molar ratios of 250–1000 for Pt-Bi/AC; 40–90 °C, 2.5–6.5 bar O_2 for Au/ZnO, although the latter was limited to 0.1 M glycerol concentration and GLY/Au = 100 mol/mol.

Adsorption studies at 293 K using Dowex® 50WX2 resin in both H^+ and Ca^{2+} forms provided essential data for SMB design. For the H^+ form, most components followed linear isotherms, while a Freundlich model better described oxalic acid adsorption. The Ca^{2+} form showed enhanced selectivity for the critical separation between DHA and glycerol. Multi-component breakthrough tests confirmed minimal competitive adsorption.

Based on the kinetic and adsorption data, a two-unit SMB cascade was developed to purify DHA from glycerol oxidation products and validated experimentally on a FlexSMB-LSRE® unit with six columns in a 1-2-2-1 configuration, operating at 293 K and an average pressure of 20 bar. The first SMB unit (H^+ resin) effectively removed organic acids, achieving DHA recovery and purity values of 87.0% and 96.8%, respectively. The second SMB unit (Ca^{2+} resin) successfully separated DHA from residual glycerol, resulting in 89.0% DHA recovery and 98.6% purity. Overall, the SMB cascade produced DHA at 0.50 g/L DHA with 98.6% purity and 77.5% recovery, a productivity of 21.7 kg_{DHA} $(m^3_{adsorbent} \cdot day)^{-1}$ and an eluent consumption of 9.0 $m^3_{eluent} \cdot kg_{DHA}^{-1}$.

In conclusion, this thesis demonstrates that coupling a selective catalytic oxidation process with an SMB separation strategy enables the sustainable production of high-purity DHA from glycerol oxidation, enabling its valorisation. The integrated approach has been validated at lab-scale and provides a solid foundation for future development toward pilot-scale and industrial applications.

7.2. Suggestions for Future Work

This Thesis presents a comprehensive investigation into a novel process for DHA production from glycerol, integrating glycerol catalytic oxidation and continuous chromatographic separation. However, several areas remain open for further research to enhance process performance, sustainability, and industrial relevance. Future work should address catalyst development, continuous reactor optimisation, separation efficiency, and process integration.

1. Glycerol Catalytic Oxidation

Catalyst Stability and Reusability

Long-term catalyst stability under continuous operation should be prioritised, as catalyst lifetime significantly impacts process economics. Studies should focus on deactivation mechanisms and reactivation strategies.

Continuous Operation and Reactor Design

Transitioning from batch to continuous operation is essential for process scalability. Optimisation of operation time is needed to ensure high DHA yields. Beyond slurry reactions and bubble column reactors, alternative technologies such as monolithic structured reactors or innovative technologies such as the NETmix® (network-based static mixing reactor) may offer enhanced mass transfer, conversion, and DHA selectivity. Integration of kinetic modelling and computational fluid dynamics (CFD) tools can aid reactor design and optimisation.

Alternative Oxidation Products

While DHA is the primary target, recovering high-value co-products such as hydroxypyruvic and glycolic acids should be explored. It may become more advantageous to selectively produce other glycerol oxidation products depending on market trends.

2. SMB Separation

Recovery of Valuable Byproducts and unreacted glycerol

Organic acids in the raffinate stream of the first SMB unit (glyceric, tartronic, and glycolic acids) have commercial value, which could be separated in subsequent SMB units to improve resource efficiency and process profitability.

Although glycerol can be considered a cheap raw material, the drive for developing more sustainable and environmentally friendly processes, in line with the green chemistry principles, puts additional pressure on minimising chemical consumption. Hence, separating glycerol from the reaction media and subsequent recycling to the conversion step may represent an interesting approach.

Contamination between SMB units

Contaminants from the first SMB extract, especially glycolic or oxalic acid, can compromise the second SMB's performance. Minimising contamination issues and preventing cation exchange (H^+ to Ca^{2+}) should be addressed via operational strategies and periodic calcium regeneration.

Solvent Recovery and Product Concentration

Despite lower than batch chromatography, the eluent consumption of the SMB is significant, 9.0 $m^3_{eluent} \cdot kg_{DHA}^{-1}$. Process optimisation is crucial to operate with lower consumption. Several methodologies have been proposed in the open literature for SMB optimisation.

Furthermore, solvent recovery methods such as falling-film evaporation, vacuum evaporation, or membrane-assisted processes should be evaluated for both DHA concentration and eluent recycling. Additionally, the suitability of concentrated DHA solutions for various end-use applications, ranging from bulk liquids to freeze-dried powders, should be assessed regarding specific quality standards.

SMB Optimisation and Alternatives

Advanced optimisation techniques (e.g. genetic algorithms, particle swarm optimisation) should be applied to the SMB cascade as a unified system, with objective functions targeting increasing DHA productivity and reducing eluent consumption. Moreover, replacing standard SMB units with alternative configurations, such as the pseudo-SMB or intermittent SMB, could minimise equipment footprint and capital costs while maintaining separation efficiency.

3. Global Process Evaluation

Use of Crude Glycerol Feedstock

The valorisation of crude glycerol, a low-cost byproduct of biodiesel production, is economically attractive but requires further investigation to evaluate the need to apply pretreatment techniques due to impurities like methanol, salts, and sulphur compounds. Their effects on catalyst activity, reactor operation, and downstream separation must be assessed to define purification requirements and ensure process robustness.

Techno-Economic Assessment

A comprehensive techno-economic evaluation should integrate potential pretreatment stages, catalytic oxidation, SMB separation, and final product handling stages. This should consider raw material variability, catalyst and resin lifetimes, solvent recovery, capital expenditure, and market prices of DHA and co-products. Such an evaluation will be essential to assess the commercial viability and guide future scale-up.

Appendix A. HPLC quantification method

The main species obtained in the liquid phase from glycerol oxidation were quantified using a High-Performance Liquid Chromatography (HPLC) Prominence system (Shimadzu, Japan) equipped with a diode array detector (set at 260 nm), a refraction index detector (RI), and an Alltech Organic Acid OA-1000 analytical column (7.8 x 300 mm, Hichrom, UK), maintained at 60 °C by a column oven. This temperature represented a compromise between reducing operating pressure (≈37 bar), improving peak resolution, and the recommended maximum operating temperature of 80–85 °C. The mobile phase consisted of a 5 mM H_2SO_4 aqueous solution, as recommended by the manufacturer, previously filtered and degassed, pumped at the maximum recommended flow rate of 0.8 ml min^{-1}. A 20 µL injection loop was used for sample introduction.

Calibration curves for each compound were obtained by injecting individually prepared standard solutions at various concentrations within the relevant working range. These standards were diluted with the eluent (1:30) before injection.

The elution order of the main species, based on their retention times, was as follows: oxalic acid (OXA) > tartronic acid (TTA) > hydroxypyruvic acid (HPA) > glyceric acid (GCA) > glyceraldehyde (GLAD) > glycolic acid (GCO) > dihydroxyacetone (DHA) > glycerol (GLY). Calibration curves obtained using the RI detector- In the case of DHA, the calibration curve for UV-Vis at the wavelength of 260 nm is also shown in Figure A.1. The corresponding standard curve parameters are summarised in Table A.1.

Table A.1. HPLC Standard curves for glycerol oxidation products. $A_{peak} = mC$. * mV·s·L·g^{-1}.

Species	Signal	tr min	*m* mRIU·s·L·g^{-1}	r^2	Concentration range, g/L
OXA	RI	5.61	4160.7	0.9997	0 – 21
TTA	RI	6.65	5335.8	0.9999	0 – 53
HPA	RI	6.95	5544.3	0.9998	0 – 16
GCA	RI	8.82	4141.4	0.9998	0 – 75
GLAD	RI	9.29	6457.1	0.9999	0 – 11
GCO	RI	9.85	4234.2	0.9999	0 – 68
DHA	260 nm	10.53	9660.5*	0.9999	0 – 100
DHA	RI	10.72	5233.1	0.9999	0 – 100
GLY	RI	10.78	5180.7	0.9998	0 – 160

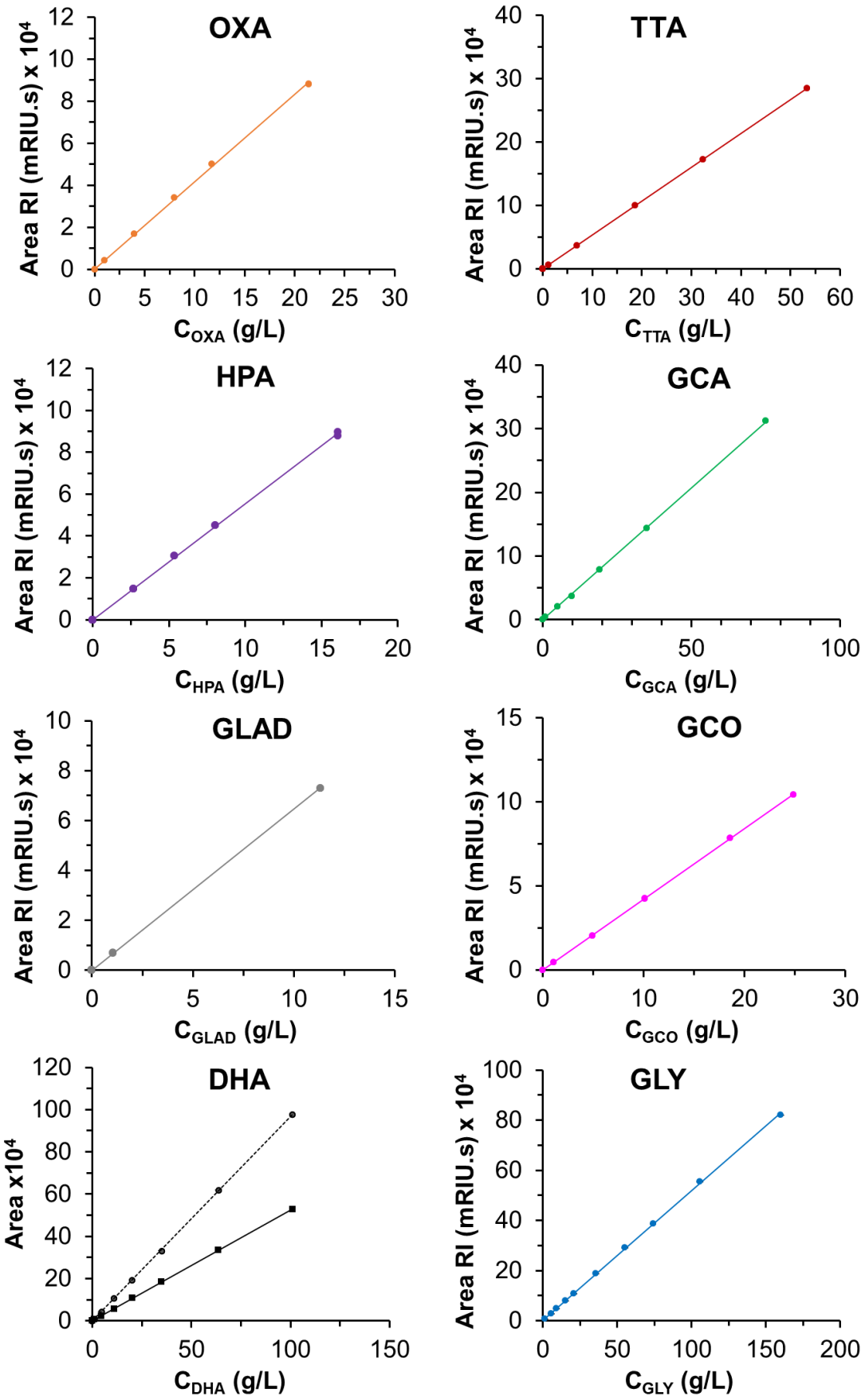

Figure A.1. Calibration curves using the RI detector for all quantified species. For DHA using the UV-Vis detector at 260 nm (dashed line).

All calibration curves exhibited excellent linearity across the studied concentration ranges ($r^2 > 0.999$). Additional compounds, including glyoxylic acid, pyruvic acid, formic acid, and lactic acid, were injected to support peak identification during chromatographic analysis. However, as these appeared only in minor quantities, no calibration curves were established.

Figure A.2 (RI detector) and Figure A.3 (UV-Vis, 260nm) show the respective HPLC chromatograms with all quantified species.

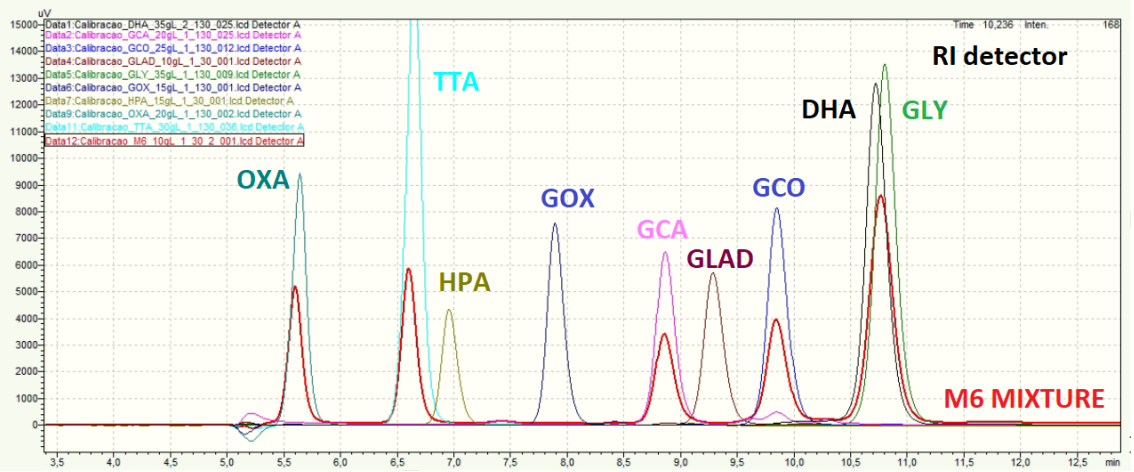

Figure A.2. RI detector signal for all quantified species and other identified peaks (glyoxylic acid, GOX). M6 mixture (red) is a mixture of OXA, TTA, GCA, GCO, DHA, and GLY.

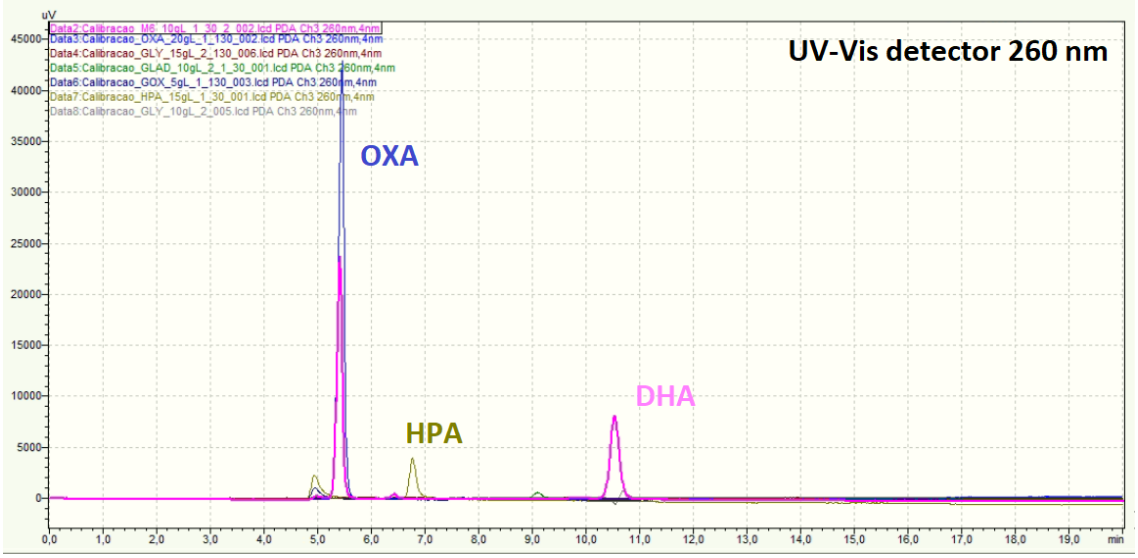

Figure A.3. UV-Vis detector set at a wavelength of 260 nm. M6 mixture in pink, but only OXA and DHA are detected. HPA is also detected, but with a weak response.

It can be seen from Figure A.2 that all peaks have a good resolution in the RI detector chromatogram, except DHA and GLY, which elute at almost the same time. In the case of the UV-Vis detector set at a wavelength of 260 nm, only OXA, HPA and DHA were detected (Figure A.3)

Appendix B. Catalysts Characterisation

The particle size distribution and average particle size of Pt5/AC from Sigma Aldrich and Pt5-Bi5/AC from Evonik are depicted in Figure B.2. and Figure B.2.

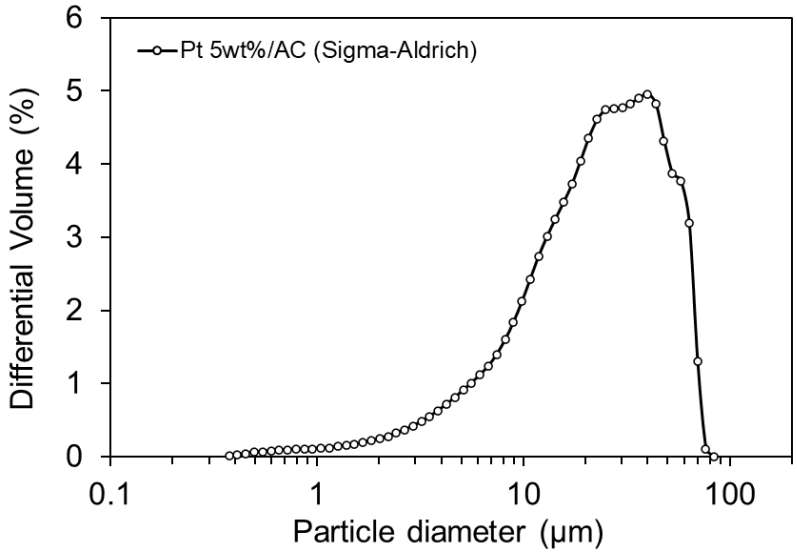

Figure B.1. Particle size distribution of Pt5%/AC from Sigma-Aldrich.

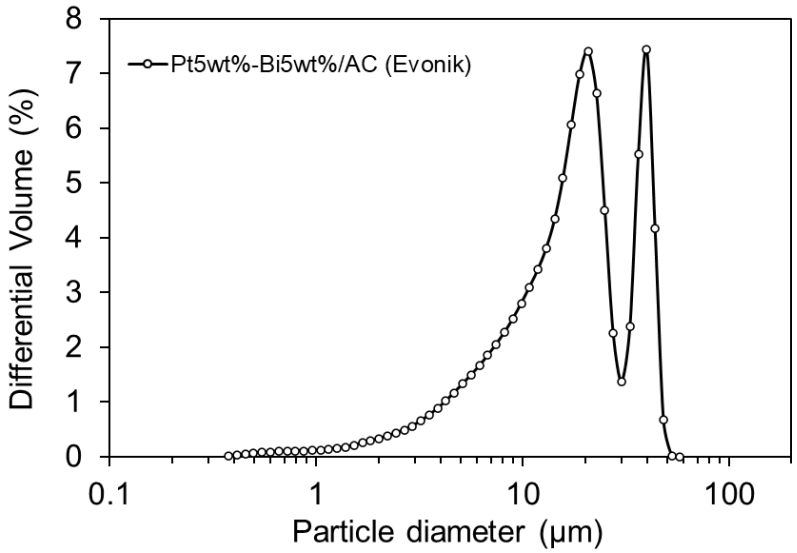

Figure B.2. Particle size distribution of Pt5%-Bi5%/AC from Evonik.

Appendix C. Mass Transfer Resistance

Table C.1 details additional parameters and results employed in the estimation and evaluation of mass transfer coefficients.

Table C.1. Mass transfer resistance: parameters and variables.

Parameter	Pt-Bi/AC	Au/ZnO
Diameter reactor (cm)	5.4	
Diameter agitator (cm)	3	
T (K)	363	
$P(O_2)$ (bar)	4.5	6.5
Vliq (dm^3)	0.1	
Stirring speed (rpm)	800	
C(GLY) (M)	1	0.1
$C(O_2)$ (mol/m^3)	3.3	
$Q(O_2)$ (STP ml min^{-1})	200	
σ (N/m)	0.061	
μ_{mix} (cP)	0.37	0.32
D_{12} (GLY) (m^2/s)	$3.4x10^{-9}$	
D_{12} (O_2) (m^2/s)	$6.0x10^{-9}$	
dp avg (μm)	24	10
ap	3748	6934
ρ_{ap} (kg_{cat} /$m_{particle}^3$)	532	1730
ρ_b (kg_{cat} /$m_{reactor}^3$)	8.0	20
ε_p (-)	0.67	0.36
τp (-)	2	2
De (GLY) (m^2/s)	$1.1x10^{-9}$	$7.0x10^{-10}$
De (O_2) (m^2/s)	$1.9x10^{-9}$	$1.1x10^{-9}$
$(-r_{GLY})_0$ (mol kg_{cat}^{-1} s^{-1})*	$6.7x10^{-2}$	$1.0x10^{-3}$
$(-rO_2)_0$ (mol kg_{cat}^{-1} s^{-1})*	$3.3x10^{-2}$	$5.1x10^{-4}$
Sh modified	12611	13313
Re' (impeller)	$3x10^4$	$4x10^4$
Froude'	0.54	0.54
Sc'	65.0	56.1
1/gas flow number	$7.6x10^{-6}$	$6.5x10^{-6}$
aeration number	326	326
K_La (s^{-1})	0.084	0.088
ks (m/s)	$3x10^{-4}$	$3x10^{-4}$
ks*ap (s^{-1})	1.00	1.85
kext(O_2) (m/s) (Sh=2)	$5.0x10^{-4}$	$1.2\ x10^{-3}$
kext(GLY) (m/s) (Sh=2)	$2.8x10^{-4}$	$7.8x10^{-4}$

Appendix D. Additional data of Glycerol Oxidation Kinetics with Pt-Bi/AC

D.1 Glycolic acid Oxidation: Power Law Kinetics

The oxidation of glycolic acid (GCO) followed a pseudo-half-order kinetic expression, given by $r_{GCO,oxi} = k'_{GCO,oxi}\, C_{GCO}^{0.5}$. In contrast to the oxidation of the other studied species, glycerol, dihydroxyacetone, and oxalic acid were better described by pseudo-first-order kinetics. The pseudo-first-order model failed to adequately describe the GCO oxidation data at high conversions. A comparison of both kinetic models is presented in Figure D.1.

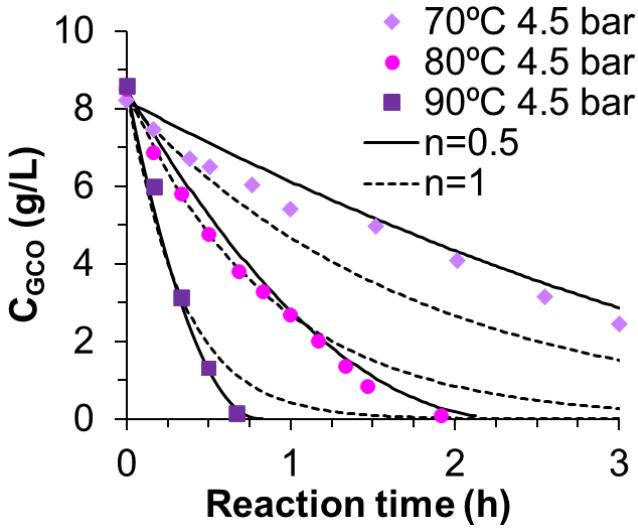

Figure D.1. Comparison of a half-order (n = 0.5) and a first-order (n = 1) power-law kinetics for glycolic acid oxidation over a Pt-Bi/AC catalyst from Johnson Mattey at T = 70 °C, 80 °C, and 90 °C. $C_{GCO,0}$ = 0.1 M; GCO/Pt = 500 mol/mol, *w* = 0.08 g, V = 0.1 L, 800 rpm.

D.2 Network Simplification for Glycerol Oxidation

D.2.1 Power-law kinetic model

The results of the parameter estimation based on the 1.0 M glycerol oxidation data (Table 4.6) revealed that the reaction rate constants for step 9 (GCA → OXA) and step 11 (GCO → C1 products) from the reaction network depicted in Figure 4.1 were significantly lower than those of the other reactions. This suggests that, under the studied conditions, GCA is preferentially oxidised to GCO (via TTA) and to HPA rather than directly to OXA. Moreover, the oxidation of GCO to C1 products was negligible, indicating that GCO primarily oxidises to OXA. To simplify

the kinetic model and reduce the number of estimated parameters, steps 9 and 11 were excluded from further analysis. The resulting concentration profiles and estimated parameters obtained with the simplified reaction network were nearly indistinguishable from those of the network proposed in Figure 4.1. The updated parameters are summarised in Table D.1.

Table D.1. Estimated parameters for glycerol oxidation kinetics considering the power-law model and a 10-step network (removing steps 9 and 11 from the reaction network). T = 80 – 100 °C; $P(O_2)$ = 4.5 bar; $C_{GLY,0}$ = 1 M; GLY/Pt = 500 mol/mol. SSR = 0.33.

Reaction/Species	#	Ea (kJ mol^{-1})	k_0 L^2 mol^{-1} g_{cat}^{-1} min^{-1}	k (90 ºC) L^2 mol^{-1} g_{cat}^{-1} min^{-1}
GLY → DHA	1	14.9	7.9×10^{1}	0.6
GLY → GLAD	2	9.6	9.1×10^{0}	0.4
DHA → HPA	3	95.3	2.0×10^{13}	0.4
GLAD → GCA	4	23.3	9.4×10^{3}	4.3
GCA → HPA	5	29.1	2.5×10^{4}	1.6
HPA → GCO	6	50.3	1.0×10^{7}	0.6
HPA → OXA	7	46.5	1.0×10^{7}	2.0
GCA → GCO	8	35	1.0×10^{4}	0.1
GCO → OXA	10	106.3	2.0×10^{14}*	0.1
OXA →	12	43.8	1.4×10^{7}	7.1
GLY	1+2	12.8	6.4×10^{1}	0.9
GCA	5+8	29.1	2.5×10^{4}	1.6
HPA	6+7	47.4	1.7×10^{7}	2.6

*$r_{GCO,oxi} = k'_{GCO} C_{GCO}^{0.5} C_{O2}$; k_{GCO} [$L^{1.5}$ $mol^{-0.5}$ g_{cat}^{-1} min^{-1}].

D.2.2 LHHW kinetic model

The same simplification discussed in the previous section was considered in the case of the LHHW model. Good results were obtained, depicted in Figure D.2. The estimated parameters are summarised in Table D.2.

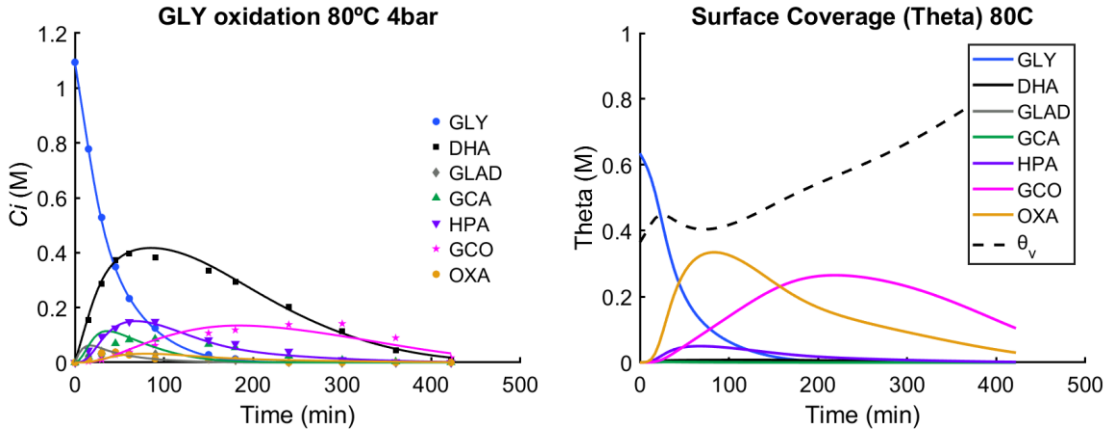

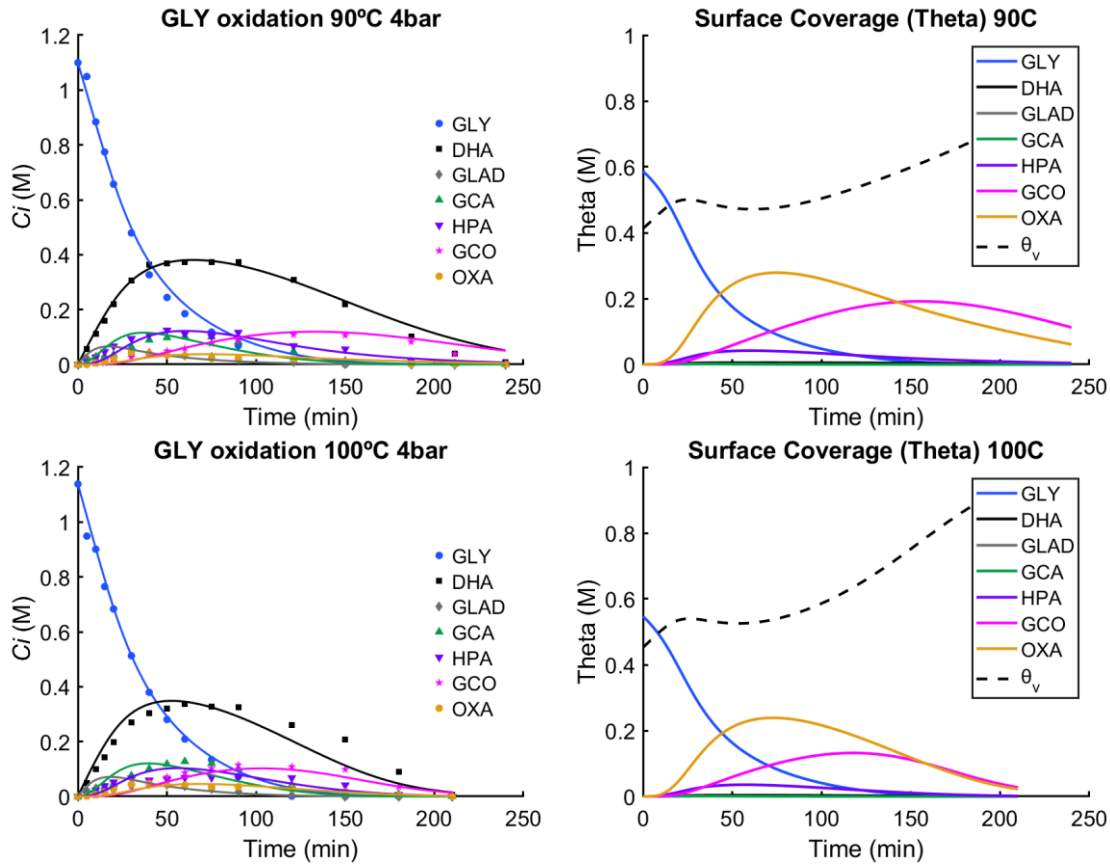

Figure D.2. GLY oxidation at 100 °C (top), 90 °C (middle), 80 °C (bottom): Left) experimental data (dots) and LHHW-based model results (lines); Right) surface coverage. $P(O_2)$ = 4.5 bar; $C_{GLY,0}$ = 1 M; GLY/Pt = 500 mol/mol, w = 0.8 g, V = 0.1 L

Table D.2. Estimated parameters for glycerol oxidation kinetics considering the LHHW model and a 10-step network (steps 9 and 11 removed from the reaction network). T = 80 – 100 °C; $P(O_2)$ = 4.5 bar; $C_{GLY,0}$ = 1 M; GLY/Pt = 500 mol/mol. SSR = 0.13.

Reaction/ Species	#	Ea kJ/mol	k_0 mol g^{-1} min^{-1}	k(90ºC) mol g^{-1} min^{-1}	ΔH kJ/mol	$Kads_0$ M^{-1}	Kads (90ºC) M^{-1}
GLY → DHA	1	26.0	4.9×10^{3}	0.9	-	-	-
GLY → GLAD	2	17.2	2.0×10^{2}	0.7	-	-	-
DHA → HPA	3	90.5	2.0×10^{14}	19.4	-38.4	9.0×10^{-8}	0.03
GLAD → GCA	4	19.7	1.0×10^{5}	144.4	-33.8	9.1×10^{-7}	0.06
GCA → HPA	5	22.9	3.0×10^{5}	150.7	-	-	-
HPA → GCO	6	54.1	1.0×10^{8}	1.7	-	-	-
HPA → OXA	7	50.9	1.0×10^{8}	4.7	-	-	-
GCA → GCO	8	33.7	1.0×10^{5}	1.4	-	-	-
GCO → OXA	10	104.1	2.0×10^{14}	0.2	-29.5	1.6×10^{-4}	2.74
OXA →	12	57.4	1.4×10^{8}	0.8	-53.1	3.6×10^{-7}	15.7
GLY	1+2	22.1	2.4×10^{3}	1.6	-22.2	8.3×10^{-4}	1.29
GCA	5+8	23.0	3.1×10^{5}	152.1	-33.8	3.4×10^{-7}	0.02
HPA	6+7	51.8	1.8×10^{8}	6.4	-11.7	1.5×10^{-2}	0.73
O_2	-	-	-	-	-35.5	1.2×10^{-7}	0.02

D.3 Extension to Different Conditions – LHHW kinetics

The LHHW-based kinetic model was evaluated using glycerol oxidation data for various initial concentrations at a constant initial GLY/Pt molar ratio of 500. The results are presented in Figure 4.16, and the estimated parameters are summarised in Table D.3.

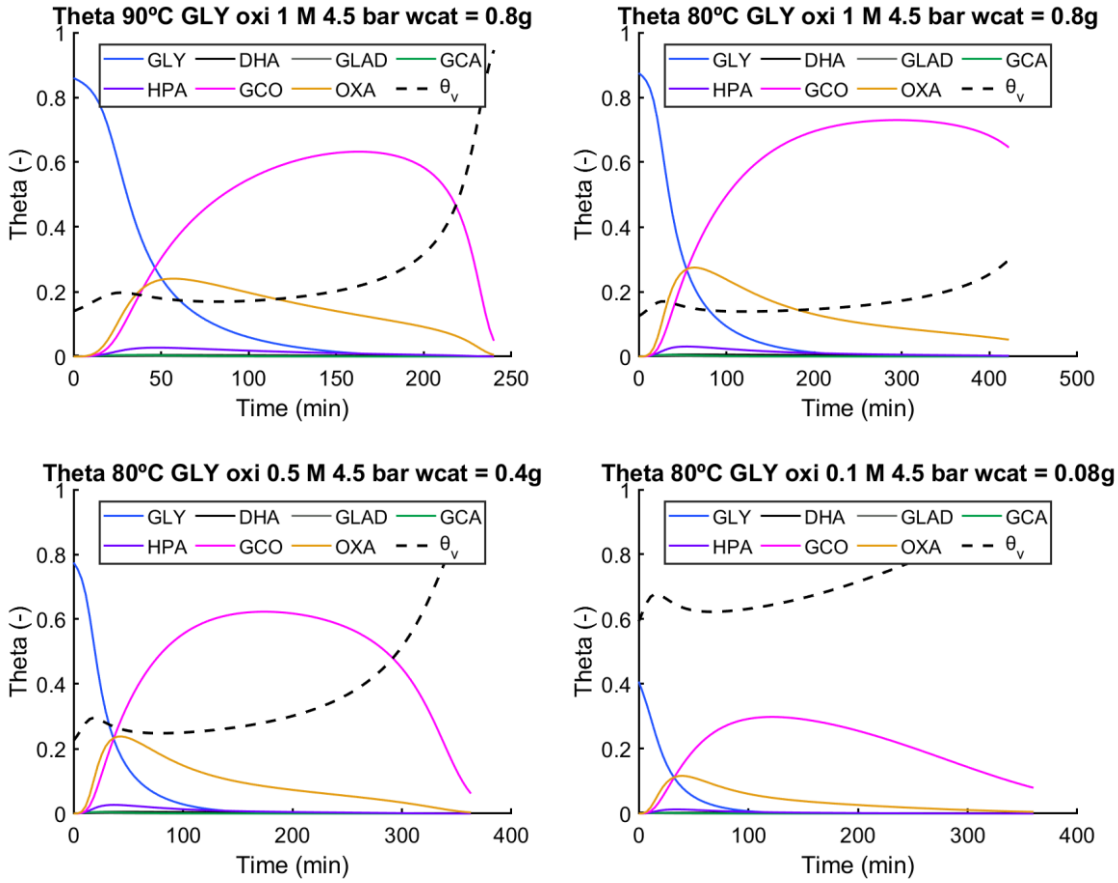

Figure D.3. LHHW kinetic model for glycerol oxidation. T = 80 – 90 °C; $P(O_2)$ = 4.5 bar; $C_{GLY,0}$ = 0.1 – 1 M; GLY/Pt = 500 mol/mol. Left) Experimental data (dots) and model results (lines).

Table D.3. Estimated parameters using the LHHW kinetic model for GLY oxidation. T=80–90 °C; $P(O_2)$ = 4.5 bar; $C_{GLY,0}$ = 0.1–1 M; GLY/Pt = 500 mol/mol. SSR = 0.18.

Reaction/ Species	#	Ea kJ/mol	k_0 mol g^{-1} min^{-1}	k(90ºC) mol g^{-1} min^{-1}	ΔH kJ/mol	$Kads_0$ M^{-1}	Kads (90ºC) M^{-1}
GLY → DHA	1	26.5	3.9×10^{3}	0.6	-	-	-
GLY → GLAD	2	17.5	1.3×10^{2}	0.4	-	-	-
DHA → HPA	3	89.4	2.0×10^{14}	27.2	-37.4	3.1×10^{-7}	0.08
GLAD → GCA	4	20.3	1.0×10^{5}	120.1	-27.0	2.6×10^{-5}	0.20
GCA → HPA	5	26.6	3.0×10^{5}	45.1	-	-	-
HPA → GCO	6	52.2	1.0×10^{8}	3.1	-	-	-
HPA → OXA	7	49.4	1.0×10^{8}	7.9	-	-	-
GCA → GCO	8	33.9	1.0×10^{5}	1.3	-	-	-
GCO → OXA	10	107.2	2.0×10^{14}	0.1	-19.4	4.3×10^{-2}	26.4
OXA →	12	56.7	1.4×10^{8}	1.0	-49.7	3.5×10^{-6}	49.2
GLY	1+2	22.7	1.9×10^{3}	1.0	-15.0	3.9×10^{-2}	5.58
GCA	5+8	26.8	3.3×10^{5}	46.5	-37.1	1.1×10^{-6}	0.23
HPA	6+7	50.2	1.8×10^{8}	11.0	-26.9	1.8×10^{-4}	1.35
O_2	-	-	-	-	-37.1	5.6×10^{-7}	0.12

The LHHW model was extended across the 40–100 °C temperature range. The results are shown in Figure 4.17, and the corresponding kinetic and adsorption estimated parameters are listed in Table D.4.

Table D.4. Estimated parameters using the LHHW kinetic model for GLY oxidation. T = 40 – 100 °C; $P(O_2)$ = 4.5 bar; $C_{GLY,0}$ = 1 M; GLY/Pt = 500 mol/mol. SSR = 0.85

Reaction/ Species	#	Ea kJ/mol	k_0 mol g^{-1} min^{-1}	k(90ºC) mol g^{-1} min^{-1}	ΔH kJ/mol	$Kads_0$ M^{-1}	Kads (90ºC) M^{-1}
GLY → DHA	1	30.2	2.8×10^{3}	0.13	-	-	-
GLY → GLAD	2	17.9	4.5×10^{1}	0.12	-	-	-
DHA → HPA	3	108.9	1.0×10^{14}	0.02	-55.0	1.8×10^{-8}	1.50
GLAD → GCA	4	25.8	5.0×10^{4}	9.80	-28.4	2.4×10^{-6}	0.03
GCA → HPA	5	39.3	1.5×10^{5}	0.33	-	-	-
HPA → GCO	6	59.6	5.0×10^{7}	0.13	-	-	-
HPA → OXA	7	49.5	5.0×10^{7}	3.78	-	-	-
GCA → GCO	8	35.9	5.0×10^{4}	0.34	-	-	-
GCO → OXA	10	101.1	1.0×10^{14}	0.29	-31.1	1.1×10^{-5}	0.33
OXA →	12	44.5	7.0×10^{7}	27.84	-43.3	1.5×10^{-8}	0.02
GLY	1+2	24.1	7.2×10^{2}	0.24	-18.4	7.8×10^{-4}	0.35
GCA	5+8	37.6	1.7×10^{5}	0.68	-22.2	9.2×10^{-5}	0.14
HPA	6+7	49.8	5.8×10^{7}	3.91	-50.7	1.8×10^{-9}	0.03
O_2	-	-	-	-	-46.0	6.7×10^{-7}	2.71

D.4 GLY-DHA-GCA simplified network – LHHW kinetics

A simplified reaction network scheme including only GLY, DHA, and GCA showed good predictive accuracy (see Figure D.4) despite slightly worse results due to neglecting other reaction products' adsorption on the Pt-Bi/AC surface. The estimated parameters are summarised in Table D.5.

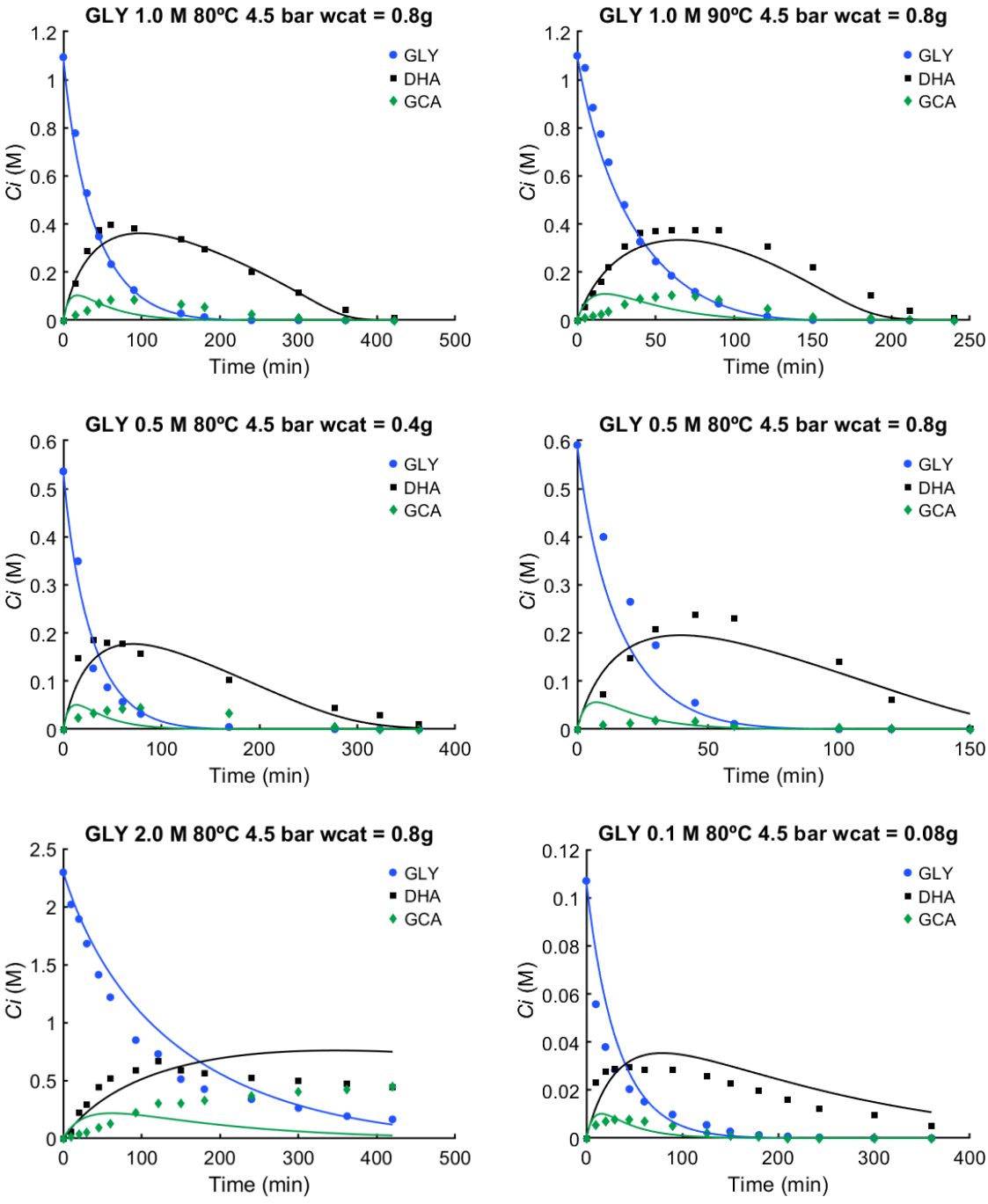

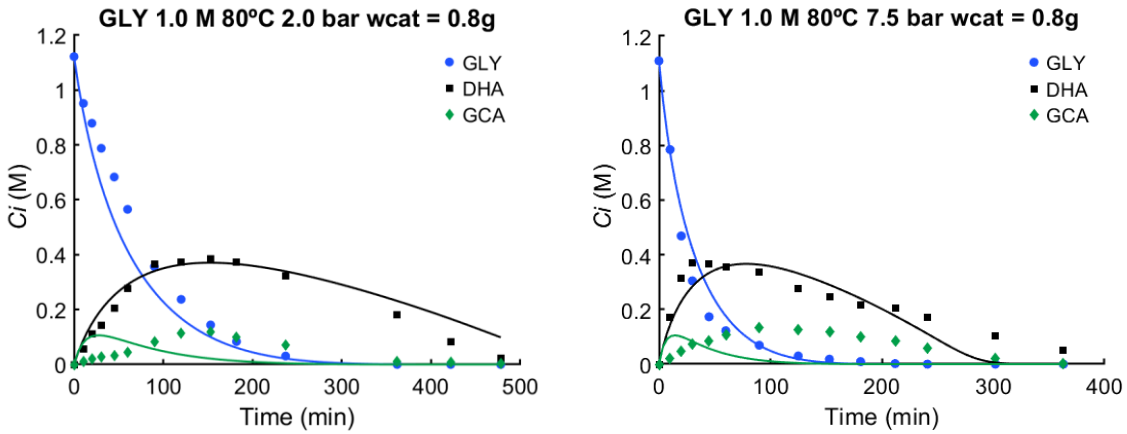

Figure D.4. Glycerol oxidation over Pt-Bi/AC: experimental data (dots) and LHHW model results (lines), considering only GLY-DHA-GCA species. T = 80 – 90 °C; $P(O_2)$ = 2.0 – 7.5 bar; $C_{GLY,0}$ = 0.1 – 2 M; GLY/Pt = 250 – 1000 mol/mol.

Table D.5. Estimated parameters with the LHHW model and the simplified GLY–DHA–GCA network for glycerol oxidation with the Pt-Bi/AC. T = 40 – 90 °C; $P(O_2)$ = 2.0 – 7.5 bar; $C_{GLY,0}$ = 0.1 – 2 M; GLY/Pt = 250 – 1000 mol/mol. SSR = 0.94

Reaction/ Species	#	Ea kJ/mol	k_0 M^{-1} g^{-1} min^{-1}	k (90ºC) M^{-1} g^{-1} min^{-1}	ΔH kJ/mol	$Kads_0$ M^{-1}	Kads (90ºC) M^{-1}
GLY → DHA	1	21.2	5.4×10^{3}	4.8	-	-	-
GLY → GCA	2	8.6	9.3×10^{1}	5.4	-	-	-
DHA →	3	93.2	2.0×10^{13}	0.8	-37.3	3.0×10^{-5}	6.9
GCA →	4	12.7	1.0×10^{4}	155.0	-41.6	5.0×10^{-7}	0.5
GLY	1+2	14.3	1.2×10^{3}	1.9	-27.6	2.5×10^{-4}	2.3
O_2	-	-	-	-	-37.7	5.9×10^{-7}	0.2

Appendix E. Preliminary study of DHA Separation - TMB Model

A preliminary study using the True Moving Bed (TMB) model was conducted to gain insights into unit performance and system dynamics. In TMB operation, a steady state can be achieved in which species concentrations at the extract and raffinate ports remain constant over time.

E.1 TMB Model

The TMB model is similar to the SMB model described in Chapter 6, with the key difference being the mass balance equations, which must account for the movement of the solid phase [1, 2]. In the TMB model, the solid phase is assumed to move in countercurrent flow relative to the liquid phase. This assumption allows the application of continuous boundary conditions. Consequently, the TMB model is more convenient for process simulation since the mass balances remain uniform in each unit zone, which allows direct steady-state results, substantially reducing computational time.

The equivalent TMB model was used as a preliminary study to design the SMB cascade, providing a first approximation of the process before using the time-consuming transient SMB model. The mass balance to the fluid phase in each TMB zone *j* is given by [1, 2]:

$$\frac{\partial C_{i,j}}{\partial t} + \frac{1-\varepsilon}{\varepsilon} k_{h,i}\left(q^*_{i,j} - \bar{q}_{i,j}\right) + \frac{u}{L_j}\frac{\partial C_{i,j}}{\partial z} - \frac{D_{ax}}{L_j^2}\frac{\partial^2 C_{i,j}}{\partial z^2} = 0$$

The mass balance to the solid phase may be given by:

$$\frac{\partial \bar{q}_{i,j}}{\partial t} - k_{h,i}\left(q^*_{i,j} - \bar{q}_{i,j}\right) - \frac{u_s}{L_j}\frac{\partial \bar{q}_{i,j}}{\partial z} = 0$$

where u_s is the solid velocity. The boundary conditions for the TMB model slightly differ from those of the SMB model:

$z = 0$	$u_j C^{in}_{i,j} = u_j C_{i,j} - \frac{D_{ax,j}}{L_j}\frac{\partial C_{i,j}}{\partial z}\Big\vert_{z=0}$
$z = 1$	$\frac{\partial C_{i,j}}{\partial z}\Big\vert_{z=1} = 0$
$j = 1{:}3$	$q_{i,j}\vert_{z=1} = q_{i,j+1}\vert_{z=0}$
$j = 4$	$q_{i,4}\vert_{z=1} = q_{i,1}\vert_{z=0}$

The initial conditions are:

$$t = 0 \qquad C_{ij} = C_{ij,0} \text{ and } \bar{q}_{ij} = \bar{q}_{ij,0}$$

All the remaining model equations were the same as for the SMB unit.

Equivalence between the SMB and the TMB models is established by keeping constant the liquid velocity relative to the solid velocity:

$$v_j^* = v_j + u_s$$

Where v_j and v_j^* are the interstitial liquid velocities in the TMB and SMB, respectively. A more intuitive form of the SMB-TMB equivalence uses the velocity ratio in zone *j*, defined as $\gamma_j = v_j/u_s$, resulting in:

$$\gamma_j^* = \gamma_j + 1$$

Finally, the solid velocity, u_s, is related to the switching time, t^*, in the SMB unit:

$$t^* = \frac{L_c}{u_s}$$

where L_c is the column length. The $\gamma_{II}^*, \gamma_{III}^*$ separation regions for both SMB units were designed using the TMB model.

E.2 SMB-H: DHA pseudo-binary separation

For the first SMB separation, $t^*$was set to 2.45 min, a value previously optimised for the TTA-GCA separation on the FlexSMB unit [3]. The separation region ($\gamma_{II}^*, \gamma_{III}^*$) for SMB-H that ensures $P^X{}_{GLY-free} \geq 99\%$ and $R_{DHA} \geq 90\%$ is outlined by the black contour in Figure E.1. For comparison, the corresponding separation region predicted by equilibrium theory is shown as a grey dashed line.

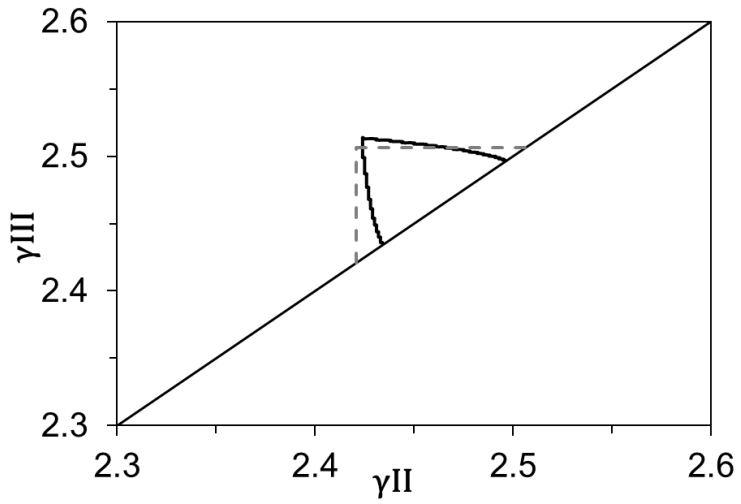

Figure E.1. Separation regions for DHA-GLY in the SMB-H unit: equilibrium theory (grey dashed lines) and SMB model for $Pu^{X}_{GLY\ base\ free} \geq 99\%$ and $R_{DHA} \geq 90\%$ (black line). $\beta_r = 1.2$; $\gamma_I^* = 2.81$; $\gamma_{IV}^* = 1.52$; $t^* = 2.45$ min.

Figure E.1 shows that the separation region defined by the SMB model closely matches the equilibrium theory's triangular region, indicating that mass transfer limitations are not very significant. The maximum productivity corresponds to the vertex point of the lack region in Figure E.1; however, operation at this vertex is not recommended, as minor fluctuations in flow rates could shift conditions outside the separation region, leading to reduced performance and contamination. To mitigate this risk, a safety factor of 1.01 was applied, and the final operating point was selected near the vertex: $\gamma_I^* = 2.81$, $\gamma_{II}^* = 2.44$, $\gamma_{III}^* = 2.50$, $\gamma_{IV}^* = 1.52$. The internal concentration profiles at this operating point are presented in Figure E.2.

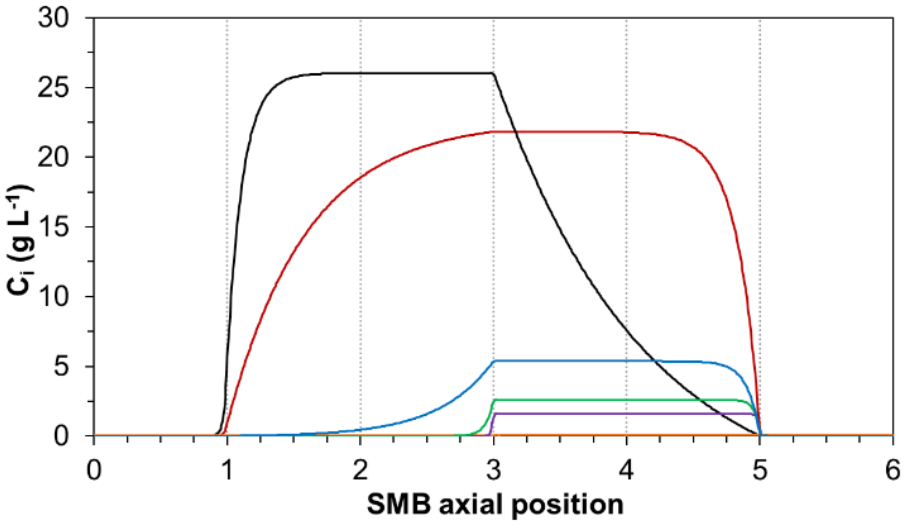

Figure E.2. Internal concentration profile of SMB-H, packed with Dowex® 50WX-2 resin in H^+ form, for the separation of DHA (black) from the remaining compounds: GLY (red), GCO (blue), GCA (green), TTA (orange), and OXA (purple), with $\boldsymbol{Pu^{X}_{GLY\ base\ free}} \geq 99\%$ and $\boldsymbol{R_{DHA}} \geq 90\%$; $\boldsymbol{\gamma_I^*} = 2.81$, $\boldsymbol{\gamma_{II}^*} = 2.44$, $\boldsymbol{\gamma_{III}^*} = 2.50$, $\boldsymbol{\gamma_{IV}^*} = 1.52$.

The SMB-H unit achieved an extract purity of 99% ($P^{X}_{GLY-free}$) with OXA as the main contaminant (0.4 wt.% on a GLY-free basis). Other contaminants in the extract stream were negligible, allowing for a simplified design of the second separation step. The raffinate stream contained organic acids, which could be recovered depending on the technical and economic feasibility of such a process. However, this aspect falls outside the scope of this study.

E.3 SMB-Ca: DHA-GLY separation

The extract stream from the SMB-H unit, containing 6.30 g/L DHA and 1.56 g/L GLY, was fed into SMB-Ca, which was packed with resin in Ca^{2+} form. The higher DHA-GLY separation selectivity resulted in an easier separation than the pseudo-binary separation in SMB-H. The regeneration region was determined based on equilibrium theory with β_r = 1.2. The most adsorbed compound was DHA, while GLY was the least adsorbed, defining the separation limits: γ_I^* = 4.17 and γ_{IV}^* = 2.87. The SMB-Ca feed flow rate was fixed by the SMB-H extract flow rate (1.76 mL/min) to avoid intermediate stream accumulation, resulting in t^* = 2.12 min.

Figure E.3 compares the separation regions from equilibrium theory (grey dashed lines) and the SMB model (black contour), defined for $R_{DHA} \geq 90\%$ and $Pu^X \geq 97\%$. The minimum DHA purity was set based on cosmetic industry requirements, the primary market for DHA. The SMB model predicted a larger separation region than the equilibrium theory, as it did not account for raffinate purity or GLY recovery constraints. A safety factor of 1.03 was applied to improve process robustness. The selected operating point was γ_I^* = 4.17, γ_{II}^* = 3.26, γ_{III}^* = 3.61, γ_{IV}^* = 2.87.

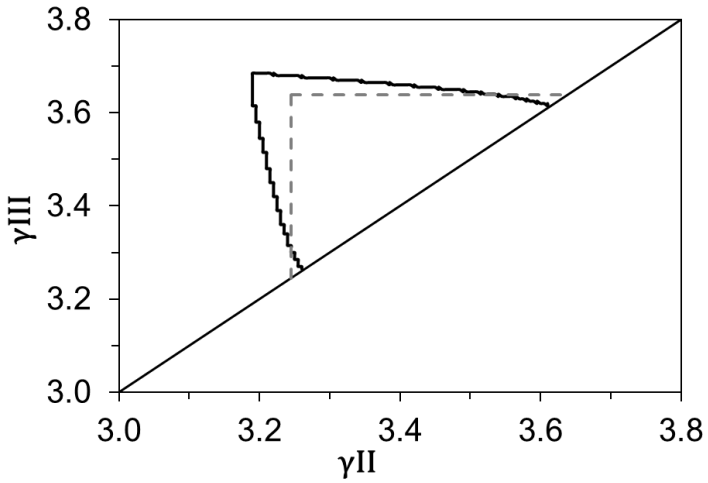

Figure E.3. $\gamma_{II}, \gamma_{III}$ separation regions: equilibrium theory (limited by the grey dashed line) and the SMB model for $R_{DHA} \geq 90\%$ and $Pu^X \geq 97\%$ (limited by black line) for DHA separation from GLY on the SMB-Ca. β_r = 1.2; γ_I^* = 4.17; γ_{IV}^* = 2.87; t^*= 2.12 min.

The internal concentration profiles at this operating point are shown in Figure E.4.

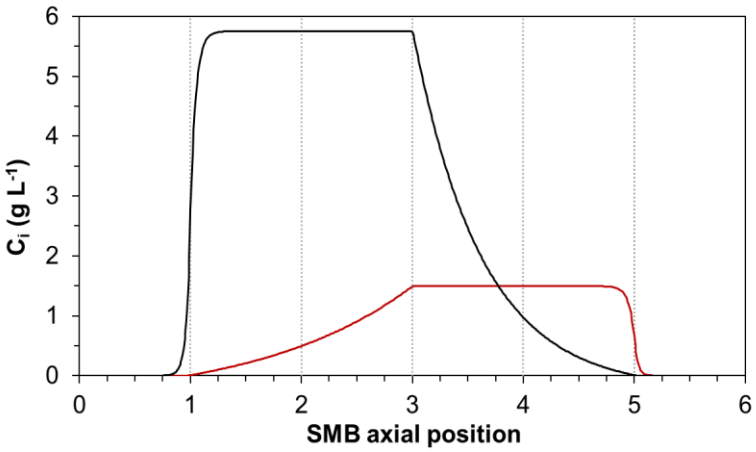

Figure E.4. Internal concentration profile of SMB-Ca for DHA (black) separation from GLY (red). $R_{DHA} \geq 90\%$ and $Pu^X \geq 97\%$; $\gamma_I^* = 4.17$, $\gamma_{II}^* = 3.26$, $\gamma_{III}^* = 3.61$, $\gamma_{IV}^* = 2.87$.

E.4 Performance Summary

Table E.1 summarises the key performance parameters for SMB-H, SMB-Ca, and the SMB-cascade process at their respective separation region vertices based on the TMB model results.

Table E.1. Performance parameters for DHA separation in SMB-H at the separation region vertex $\gamma_I^* = 2.81$, $\gamma_{II}^* = 2.42$, $\gamma_{III}^* = 2.51$, $\gamma_{IV}^* = 1.52$; and SMB-Ca for the binary separation at the separation region vertex: $\gamma_I^* = 4.17$, $\gamma_{II}^* = 3.26$, $\gamma_{III}^* = 3.61$, $\gamma_{IV}^* = 2.87$.

Performance parameters	SMB-H	SMB-Ca
EC (L_{Des}/kg_{DHA})	567	651
Pu^X (%) *GLY free-basis	99.0*	97.2
Pu^R (%)	-	69.2
R_{GLY} (%)	-	88.9
R_{DHA} (%)	90.1	90.6

Although selectivity in the binary separation (SMB-Ca) was higher than in the pseudo-binary separation (SMB-H), the eluent consumption (EC) was more significant in SMB-Ca due to the stronger adsorption of both DHA and GLY on the resin in Ca^{2+} form compared to the H^+ form. GLY was recovered with 69.2% purity in the raffinate stream, making recycling unfeasible. However, when applying a safety factor of 1.03, GLY recovery increased to 98.6%, though at a very low concentration of 0.7 g/L, over 100 times more diluted than the reaction feed concentration of 92 g/L. Given GLY's low market value and the risk of contaminant accumulation, recycling the raffinate stream from SMB-Ca may not be feasible.

The SMB cascade had an EC of 1218 L_{Des} kg_{DHA}^{-1} and a $Prod_{DHA}$ of 69 kg_{DHA} $(L_{Ads} \cdot day)^{-1}$. Although the SMB performance may be lower than the TMB model predictions, these results demonstrate the potential of an SMB cascade for high-purity DHA separation from glycerol oxidation products.

E.5 References

1. Rodrigues, A.E., Pereira, C.S.M., Minceva, M., Pais, L.S., Ribeiro, A.M., Ribeiro, A.E., Silva, M., Graça, N.S., and Santos, J.C., *Simulated moving bed technology: principles, design and process applications*. 1st Edition ed. 2015, Amsterdam: Butterworth-Heinemann. 304.
2. Nicoud, R.-M., *Chromatographic Processes: modeling, simulation, and design*. Vol. 1. 2015, Cambridge: Cambridge University Press. 657.
3. Coelho, L.C.D., Filho, N.M.L., Faria, R.P.V., Ferreira, A.F.P., Ribeiro, A.M., and Rodrigues, A.E., *Separation of tartronic and glyceric acids by simulated moving bed chromatography.* Journal of Chromatography A, 2018. **1563**: p. 62-70.